A Model Study Of Chemistry And Transport In The Arctic Troposphere

Sarah Anne Monks

Submitted in accordance with the requirements for the degree of
Doctor of Philosophy

The University of Leeds
School of Earth and Environment
October 2011

Declaration of Authorship

The candidate confirms that the work submitted is her own, except where work which has formed part of jointly-authored publications has been included. The contribution of the candidate and the other authors to this work has been explicitly indicated below. The candidate confirms that appropriate credit has been given within the thesis where reference has been made to the work of others.

The publication Sodemann et al. (2011), Episodes of cross-polar transport in the Arctic troposphere during July 2008 as seen from models, satellite, and aircraft observations, Atmospheric Chemistry and Physics, 11, 3631–3651, was jointly-authored with H. Sodemann (Norwegian Institute for Air Research (NILU), Kjeller, Norway). The TOMCAT model simulations which make up a significant part of this publication were performed by the candidate, along with the emission analysis for the TOMCAT model used in Table 1 of the publication. The majority of the text was written by the first author of the publication, however the TOMCAT model description was written by the candidate with input and discussion given for the rest of the publication. This work is discussed as past of the model evaluation in Chapter 4.

Abstract

In this thesis the TOMCAT chemical transport model is used to investigate the processes which control the concentrations of CO and O_3 in the Arctic troposphere. Particular focus is on understanding the main sources of CO, O_3 and NO_y species in the Arctic, distinguishing between natural and anthropogenic sources and the current drivers of interannual variability (IAV).

First results from a new version of TOMCAT, with extended hydrocarbon chemistry and heterogeneous uptake of N_2O_5, shows better agreement with observed CO from MOPITT, surface stations and aircraft. Changes in simulated burdens demonstrate the importance of NMHC as a source of CO, O_3 and PAN in the troposphere and show that the complexity of chemical schemes may have contributed to previously reported inter-model differences. The high PAN sensitivity to additional NMHC is particularly important in the Arctic as it is the dominant source of NO_x in the Arctic lower troposphere, producing up to 30% of total O_3 in the summer.

This thesis contains the first source contribution analysis to consider impacts of fire emissions throughout the year in comparison to anthropogenic sources. Anthropogenic emissions are found to be the largest source of Arctic CO (48%), followed by methane (25%) and fires (13%). In summer, fire and anthropogenic sources contribute equally to the total CO burden. Boreal fires are the dominant source of O_3 and NO_x compared to anthropogenic emissions. North America contributes the largest amount (30%) to the total anthropogenic CO burden, followed by East Asia (26%), Europe (23%) and South Asia (9%). In contrast, North America makes the largest contribution (9%) to the Arctic O_3 burden, followed by Europe (7%) and then Asia (6%). Overall, CO shows that the Arctic is most sensitive to emissions changes in Europe, then North America and then Asia.

Fire emissions are the dominant driver of current Arctic CO IAV, causing 84-93% of observed variability. A statistically significant correlation is found between observed CO and the El Niño 3.4 index due to a link with fires. El Niño is strongly associated with increased fire emissions in regions of North, Central and South America, Africa, and Asia. In contrast, El Niño is associated with reduced fire emissions in eastern North America, Europe, southern Asia and Australia. The temperature dependence of fires in several regions indicates that fire activity will increase in a warmer climate.

Model simulations show that meteorology is responsible for 0-25% of Arctic CO IAV. During positive phases of the NAO, Arctic CO is increased in winter but is reduced in summer. This is the first time that the effect of the NAO on transport to the Arctic has been considered throughout the year, showing a seasonal evolution in the Arctic response. El Niño is shown to increase transport from South Asia during winter and spring.

Acknowledgements

I would like to express a large thank you to my project supervisors Stephen Arnold and Martyn Chipperfield, whose constant guidance and support have given me the ability to complete this thesis. Many helpful discussions and emails will not be forgotten.

Thanks is also due to my research group and ICAS who have helped me in many ways, including Doug Parker for his contribution on my RSG.

Thanks is also due to the POLARCAT community, in particular Kathy Law and Louisa Emmons, who have helped me greatly from start to finish with useful discussions and provision of data that has been used in this thesis. I would also like to acknowledge Paul Young and the ExTC/QUAAC group for the provision of the chemical mechanism which has been used in this thesis. I also wish to acknowledge funding support from EPSRC and EUFAR.

I would like to say a big thank you to all my friends, who have shown me great kindness and support throughout and have always been there to listen. I owe an especially large thank you to Chris, who has kept me smiling (and sane!) throughout. Last, but not least, I would like to say a huge thank you to my family who have always encouraged and believed in me.

Contents

List of Figures

List of Tables

Abbreviations

ARCTAS	**A**rctic **R**esearch of the **C**omposition of the **T**roposphere from **A**ircraft and **S**atellites
BL	**B**oundary **L**ayer
CTM	**C**hemical **T**ransport **M**odel
ENSO	**E**l **N**iño-**S**outhern **O**scillation
FLEXPART	A Lagrangian Particle Dispersion Model
FT	**F**ree **T**roposphere
IPY	**I**nternational **P**olar **Y**ear
ITCZ	**I**nter**T**ropical **C**onvergence **Z**one
IUPAC	**I**nternational **U**nion of **P**ure and **A**pplied **C**hemistry
LRT	**L**ong-**R**ange **T**ransport
MODIS	**MO**derate **R**esolution **I**maging **S**pectroradiometer
MOPITT	**M**easurements **O**f **P**ollution **I**n **T**he **T**roposphere
MOZART	**M**odel for **OZ**one **A**nd **R**elated **T**racers
NAO	**N**orth **A**tlantic **O**scillation
NMHC	**N**on **M**ethane **H**ydro**C**arbons
POLARCAT	**Pol**ar Study using **A**ircraft, **R**emote Sensing, Surface Measurements and Models, of **C**limate, Chemistry, **A**erosols, and **T**ransport
POLMIP	**POL**ARCAT **M**odel **I**ntercomparison **P**roject
PNA	**P**acific-**N**orth **A**merican Oscillation
STE	**S**tratosphere-**T**roposphere **E**xchange
TOMCAT	A Global Chemical Transport Model
TOPSE	**T**ropospheric **O**zone **P**roduction about the **S**pring **E**quinox
WCB	**W**arm **C**onveyor **B**elt

Chapter 1

Motivation and aims

1.1 Motivation

Since the industrial revolution, emissions of trace gases from the combustion of fossil fuels have resulted in increased atmospheric concentrations of greenhouse gases such as carbon dioxide (CO_2) and methane (CH_4). Greenhouse gases absorb outgoing long-wave radiation and therefore concentration changes in these gases can affect global temperatures. Observed global surface temperatures have increased by 0.74°C since 1906, during this period of industrialisation, providing evidence that human activities are perturbing the Earth's radiation budget (IPCC, 2007).

Figure 1.1 shows observed sea surface temperature (SST) anomalies averaged over the whole globe and over different latitude bands relative to the 1880-1890 mean SST. There is a positive trend in all regions, however, the 60°N-90°N latitude band clearly exhibits a much higher temperature anomaly, with an overall increase of 2.25°C. In the Arctic, the periods of warming and cooling prior to 1970 have been attributed to natural climate variability. However, the post-1970 warming has been shown to be caused by increased concentrations of greenhouse gases (Johannessen et al., 2004; ACIA, 2005). Analysis of observed SSTs, during this period of human-induced warming, revealed that temperatures in the region north of 60°N have been increasing at a rate of 0.09°C per decade during the 20^{th} century compared to 0.06°C per decade for the whole of the Northern Hemisphere (ACIA, 2005). This faster rate of warming in the Arctic has been termed 'polar amplification' and is due to feedback mechanisms, such as sea-ice-albedo feedbacks, where melting ice leads to increased absorption of solar radiation, which further enhances warming in the Arctic (Serreze and Francis, 2006). Climate model projections performed as part of the IPCC (Intergovernmental Panel on Climate Change) report are shown in Figure 1.2. The amplified rate of warming is clearly seen in the Arctic and suggest that this increased rate of warming is likely

Figure 1.1 Area-weighted mean observed surface temperature anomalies (°C), relative to the 1880-1890 mean, for different latitude bands (adapted from Shindell and Faluvegi (2009)). The observations are from the Met Office Hadley Centre's sea Ice and Sea Surface Temperature data set, HadISST1 (Rayner et al., 2003).

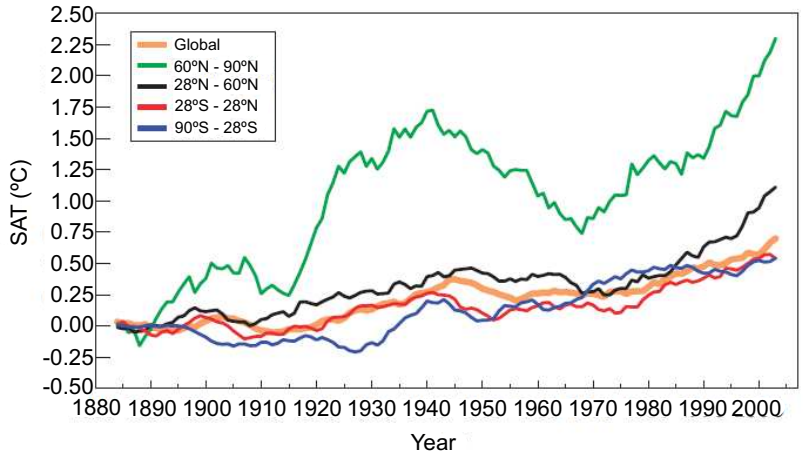

to continue throughout the 21st century with a temperature increase of up to 6°C in the Arctic by 2100 (Christensen et al., 2007).

Climatic changes such as increased precipitation, reduced sea-ice and snow cover, increased river discharge to the ocean and melting of permafrost have already been observed in the Arctic (ACIA, 2004). The Arctic climate is intrinsically linked to the rest of the globe and therefore the observed changes have global implications. Reduced surface albedo, due to less ice and snow, results in increased absorption of short-wave radiation increasing temperatures further (Christensen et al., 2007). The formation of cold dense water in the Arctic is also important as it causes deep downwelling which drives part of the global oceanic circulation known as the thermohaline circulation (Clark et al., 2002). Increased input of freshwater into the Arctic ocean from increased precipitation and river discharge reduces its salinity and density, thereby reducing this downwelling (Rahmstorf, 2000). This also has implications for global atmospheric circulation which is linked to ocean currents. Any shift in oceanic and atmospheric circulation will affect temperature and precipitation patterns globally as they both act to transport moisture and heat poleward from the equator. Melting of glaciers is also expected to cause a rise in sea level (Bindoff et al., 2007). As a whole, increased temperatures in the Arctic are expected to have wide-reaching consequences, affecting the whole of human society, animal populations and plant species (ACIA, 2004).

For this reason, it is vital for anthropogenic emissions to be reduced in order to mitigate the impacts of climate change, allowing time for populations to adapt to regional changes. CO_2, the largest contributor to radiative forcing, has a very long lifetime and therefore the benefits of emission reductions will not be seen for a long time (Forster et al., 2007; Quinn et al., 2008). It has

Figure 1.2 Mean projected surface temperature change (°C) for 2020-2029 (left) and 2090-2099 (right) from multi-model simulations for different IPCC emissions scenarios: B1 (top), A1B (middle) and A2 (bottom) (taken from Solomon et al. (2007)). The emission scenarios represent different partitioning between the usage of fossil fuel and renewable energies, with B1 being equally reliant on both and A2 being most reliant on fossil fuel.

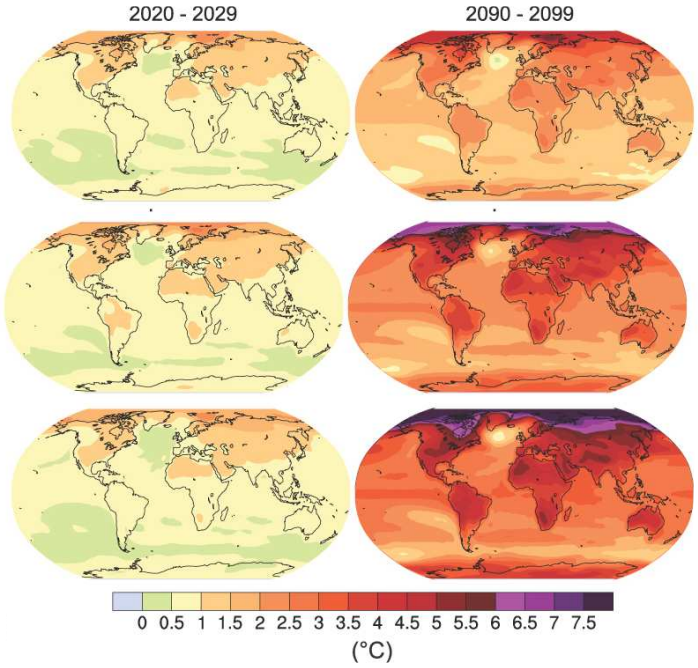

been suggested that emission reduction policies should firstly target precursors of relatively short-lived greenhouse gases, such as CH_4 (9-12 years) (Prinn et al., 1995; Forster et al., 2007) and ozone (O_3) ($\sim$22 days) (Stevenson et al., 2006), to mitigate immediate climate change, whilst also reducing CO_2 concentrations for future benefits (Quinn et al., 2008). Tropospheric O_3 is the third most important greenhouse in terms of its contribution to global radiative forcing (Forster et al., 2007) and has been estimated to have contributed 0.3°C to total global warming and $\sim$0.4-0.5°C to Arctic warming during winter and spring since 1880 (Shindell et al., 2006a). O_3 is produced photochemically in the atmosphere and processes which control its abundances in the Arctic are poorly understood (Shindell et al., 2006a; Law and Stohl, 2007; Jacob et al., 2010). Other gases which do not trap outgoing longwave radiation can also contribute to increasing temperatures indirectly. For example, increased emissions of carbon monoxide (CO) and non-methane hydrocarbons (NMHC) can affect the oxidising capacity of the atmosphere by reducing hydroxyl radical (OH) concentrations, increasing the lifetime of gases such as CH_4 and O_3 (Forster et al., 2007).

It is therefore important to understand the sources and sinks of pollution in the Arctic which are contributing to the changing climate in order to mitigate global increases in temperature. Particular emphasis should be on which anthropogenic regions are contributing the most to concentrations of trace gases in the Arctic. This will allow the implementation of effective emission reduction

polices to be put in place to curb the impacts of climate change. Due to the location of the boreal regions, fires have the potential to affect Arctic composition. Boreal fires are largely caused by lightning strikes to the ground and modelling studies have shown that a doubling of CO_2 is likely to increase the frequency of lightning across the northern hemisphere and lead to dryer and warmer climatic conditions, increasing overall fire risk (Flannigan and Van Wagner, 1991; Stocks, 1993; Price and Rind, 1994; Stocks et al., 1998; Flannigan et al., 2001). It is not well known how fires impact the Arctic and therefore an understanding of how current levels of biomass burning affects Arctic composition will also allow us to understand how the climate may be affected in the future. Understanding how fire emissions and anthropogenic emissions affect the Arctic overall will allow us to understand whether anthropogenic emission reduction policies will reduce concentrations in the Arctic.

Three-dimensional (3-D) global chemical transport models (CTMs) are useful tools for studying issues such as these, where the problem is dominated by long-range transport of pollution from a wide range of sources. The Arctic is characterised by very low temperatures, a stable boundary layer, snow/ice-covered surfaces and a strong seasonal solar radiation cycle. Modelling Arctic composition is particularly challenging due to these complexities. Previous assessments, using spatially limited observations only at the surface, identified that CTMs show large deviations from both the observed and simulated means of short-lived pollutant concentrations, such as CO and O_3, in the Arctic (Shindell et al., 2008). This suggests a lack of understanding in terms of the chemical and transport processes controlling such budgets. This has implications for more complex climate models which are used to predict Arctic and global climate response to emission changes using the chemical mechanisms from CTMs. Models need to be constantly evaluated with in-situ data so we can better understand and reduce model limitations and errors, making more accurate simulations of global climate and atmospheric composition possible in the future.

1.2 Aims

The main focus of this thesis is to improve our understanding of the main sources of Arctic CO and O_3 using a global chemical transport model, TOMCAT, to simulate the export of pollution polewards. The specific research aims are to:

1. **Evaluate the ability of chemical transport models to simulate Arctic tropospheric composition**. The TOMCAT model is compared to newly available trace gas measurements from the POLARCAT-summer 2008 aircraft campaign in combination with surface observations and satellite measurements to better understand model weaknesses. Particular focus is paid to CO, O_3 and NO_y species.

2. **Quantify the main sources of trace gases within the Arctic**. Novel CO tracer experiments are used to track mid-latitude pollution emissions from anthropogenic, fire and biogenic emissions to quantify their contributions to Arctic burdens between 1997-2009. The major Northern Hemispheric anthropogenic emission regions are differentiated between, along with natural and man-made fire contributions. The impact of the regional anthropogenic and boreal fire emissions are then also estimated for O_3 and NO_y species.

3. **Investigate the processes which control observed interannual variability of CO in the Arctic.** An integral part of understanding future changes in the burdens of atmospheric trace gases in the Arctic is to better understand the current processes which lead to recent observed variability. A range of model simulations are used to compare the impact of meteorology and fire emissions on the interannual variability in CO between 1997-2009. Changes in transport to the Arctic during different modes of naturally occurring climate oscillations, such as the NAO, PNA and El Niño are also considered. Drivers of fire emissions variability are also studied.

1.3 Layout of this thesis

Background descriptions of the atmosphere, long-range transport, tropospheric chemistry and climate of the Arctic are given in Chapter 2, along with a discussion of the current state of knowledge and literature, which are relevant to the work presented in this thesis. The TOMCAT CTM, which is used throughout this thesis, is described in Chapter 3. Model updates which have been developed and tested as part of this thesis are also discussed here, including 1) newly implemented emission estimates, 2) an extension of organic chemistry and 3) a treatment of heterogeneous uptake of N_2O_5 by aerosol. Testing and evaluation of the newly updated version of the TOMCAT model, in comparison to surface observations of CO, NO_y and O_3, and satellite measurements of CO, are shown in Chapter 4. Contributions to Arctic burdens of CO and O_3 from anthropogenic and fire sources are estimated in Chapter 5. This chapter also considers how the Arctic sensitivities to anthropogenic regional sources vary seasonally due to different transport pathways. The sources of inter-annual variability of CO are discussed in Chapter 6, focusing on meteorological variations in transport patterns and changes in emissions from biomass burning. The influence of climate modes on both transport and fire emissions are also further investigated in this chapter. Chapter 7 compares TOMCAT to aircraft data from the POLARCAT campaign and investigates the sensitivity of O_3 to Arctic PAN. Finally all results are summarised in Chapter 8 along with a discussion of how they have addressed the aims presented in Section 1.2 and suggestions of possible future work.

Chapter 2

Background

2.1 The atmosphere

The atmosphere is a layer of gases which lies above the Earth's surface, mostly composed of nitrogen ($\sim$78%), oxygen ($\sim$21%) and argon ($<$1%). Water vapour is the fourth most abundant gas, which is mostly present in the lower atmosphere, varying in concentration due to evaporation and precipitation. Trace gases and particles make up the rest of the atmosphere, which are affected by both natural and human emissions from the surface of the Earth. The atmosphere can be separated into different layers characterised by changes in temperature and pressure. The lowermost part of the atmosphere is called the troposphere, which is defined by a decrease in temperature with altitude. The troposphere contains 80% of the mass of the atmosphere and experiences rapid vertical mixing due to surface heating. Above the troposphere lies the stratosphere, which is defined by an increase in temperature with altitude due to absorption of ultraviolet (UV) radiation by the ozone layer. The tropopause is where these two regions meet. The height of the tropopause is determined by the extent of vertical mixing in the troposphere, with an average height of $\sim$18 km in the tropics and $\sim$8 km at the poles. Due to the stable conditions of the tropopause (warm air in the stratosphere overlying colder denser air), air is mixed very slowly between the two layers. Above these layers, are the mesosphere, thermosphere and exosphere.

The troposphere can be further separated into the free troposphere (FT) and the boundary layer (BL). The BL is the lowest part of the troposphere, defined as the region of air which is influenced by the Earth's surface and responds more quickly to surface temperature changes than the FT. The FT is the region of air above the boundary layer extending up to the tropopause. The height of the boundary layer depends on the meteorological conditions, with lower boundary layer heights in stable conditions. In general, the boundary layer extends from the surface up to 500 m to 3,000 m altitude.

Emissions of trace gases from human activities, such as combustion and land-use change, perturb the natural state of the atmosphere. This can be seen in global atmospheric concentrations of gases such as carbon dioxide (CO_2) and methane (CH_4), which have long enough lifetimes (>9 years) to accumulate in the atmosphere and have shown marked increases since the pre-industrial times (IPCC, 2007). Observations suggest that other shorter lived gases such as ozone (O_3) have also increased (Hough and Derwent, 1990; Vingarzan, 2004). Concentrations of O_3 are affected through anthropogenic emissions of nitrogen oxides (NO_x=NO+NO_2), carbon monoxide (CO) and non-methane hydrocarbons (NMHC). Modelling studies suggest that greater anthropogenic emissions of O_3 precursors are the cause of the observed increase (Wang and Jacob, 1998; Vingarzan, 2004). These increasing concentrations have important implications for both air quality and climate. Most trace gases are emitted in the BL, once emitted their fate is controlled by chemical processes and the general circulation of the atmosphere. These are now described in Sections 2.2 - 2.4.

2.2 General atmospheric circulation

The circulation of the troposphere can be generalised into three cells which have formed as a result of uneven heating of the Earth's surface and the rotation of the Earth. The influx of solar radiation at the equator is greater than at the poles and results in a surplus of energy at the equator and a net loss of energy at the poles. Atmospheric and oceanic circulation acts to transport excess energy poleward. This alone would result in a single circulation cell known as the Hadley cell, however, the rotation of the Earth results in an affect known as the Coriolis force causing two additional cells, the Ferrel cell and the Polar cell. As the Earth is a rotating sphere, points on the Earth's surface move at different speeds depending on their latitude. It can be generalised to result in a deflection of air to the right of its travel direction in the Northern Hemisphere (NH) and to the left in the Southern Hemisphere (SH). The three cells are shown in Figure 2.1 and are now described in more detail.

Hadley cell

Strong surface heating at the equator causes the air to become buoyant and rise. This air then moves along the tropopause northward to around 30°N or southward to around 30°S, where it cools and descends. This creates an area of low pressure at the equator and an area of high pressure at around 30°N and 30°S. This pressure gradient drives air along the surface back towards the equator and completes the Hadley cell (see Figure 2.1). Due to the Coriolis force, the winds travel in an east to west direction, creating what are known as the trade winds. Air from the SH and the NH converges at the equator forming the Intertropical Convergence Zone (ITCZ). This convergence also acts to

intensify uplift in the equatorial region which is characterised by extensive cloud and rainfall due to high rates of evaporation and uplift.

Ferrel cell

At 30°N and 30°S descending air, which does not move equatorward as part of the Hadley cell, moves towards the high latitudes. This air is deflected from the west to the east due to the Coriolis force, resulting in the so-called westerlies. At around 60°N/S warm, moist air rises which then moves equatorward along the tropopause back to the region at 30°N/S, where it sinks back down to the surface. This generalised cell of rising and sinking air is known as the Ferrel cell (see Figure 2.1).

When there is sufficient instability caused by large north-south temperature gradients and very strong upper levels winds, the general westerly flow breaks downs into large-scale eddies. This is known as baroclinic instability and generates the mid-latitude weather systems which characterises this region's weather. Alternating high and low pressure systems move slowly eastwards creating a wavelike flow known as Rossby waves. Troughs and ridges formed in this flow transport cold air equatorward and warmer air poleward.

Figure 2.1 Schematic of global circulation taken from Seinfeld and Pandis (2006).

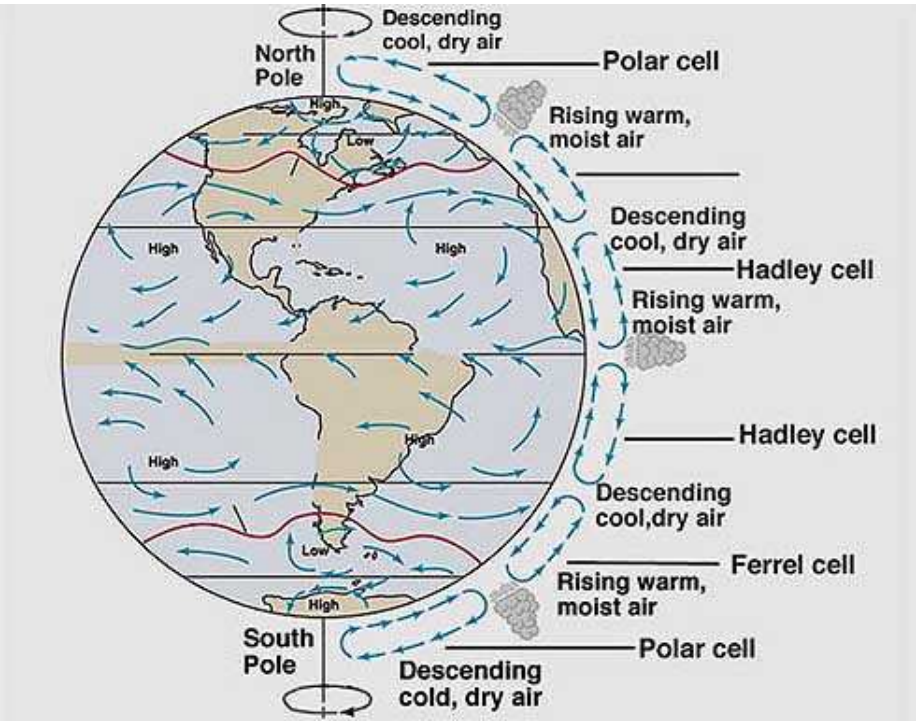

Polar cell

At around 60°N/S some air moves along the tropopause towards the poles where it cools and descends to the surface, forming the polar high. Air at the surface completes the polar cell by moving back along the surface towards 60°N/S to the region of divergence (see Figure 2.1). The Coriolis force deflects the surface winds towards the west forming the polar easterlies. This cell is the weakest of all three cells. At the surface where the mild mid-latitude westerlies meet the cold polar easterlies a region of convergence is formed known as the polar front.

2.3 Atmospheric transport of anthropogenic trace gases

Interest in long-range transport of emissions largely began when O_3 concentrations were found to be at their highest downwind of source regions (White et al., 1976; Parrish et al., 1993). This, along with modelling studies, suggested that emissions from one continent could influence another (Berntsen et al., 1999; Jaffe et al., 1999). The fact that emissions could cross political boundaries meant that increasing anthropogenic emissions was a global problem. The major anthropogenic emissions regions of North America, Asia and Europe are all located in the NH (see later in Figure 3.1). For this region, the majority of research to date has focused on the transport pathways of emissions from these regions. Most gases are emitted in the BL, therefore processes which mix air out of the BL to the FT prevent the build-up of harmful gases. However, once in the FT, these gases can be transported globally by large-scale advection. The processes that enable boundary venting and long-range transport are now described.

2.3.1 Advection

Advection is the horizontal movement of air by wind that can transport gases and aerosols over both small and large distances. Winds are generated by pressure gradients where air moves from regions of high pressure to areas of low pressure. The gradient in pressure controls the strength of the wind and the balance between this pressure gradient force and the Coriolis force determines the direction of the wind. In winter in the NH, when land and sea temperature gradients are at their greatest, winds are at their strongest. As mentioned previously, the Hadley cell, Ferrel cell and Polar cell experience different prevailing wind directions. It is this that determines the dominant export pathways for long-rang transport of emissions once in the FT.

The majority of export from North America and East Asia occurs in the FT where the prevailing westerlies in the mid-latitudes cause emissions from North America to be transported to the

Atlantic and Europe and emissions from East Asia to be transported to the Pacific and North America (Stohl, 2001). Due to the positioning of Europe near the exit of the jet stream, the region is dominated by subsidence resulting in low-level transport being more important (Stohl, 2001). In winter, the dominant export pathway of emissions from Europe are in the BL polewards towards the Arctic due to the lack of convection (Stohl, 2001; Duncan and Bey, 2004). Upper level transport is important in the summer for Europe when deep convection exists to lift emissions to the FT (Fischer et al., 2003; Huntrieser et al., 2002).

2.3.2 Convection

Convection acts to rapidly transfer energy, gases and particles vertically. Two types of convection exist, free and forced. Forced convection is the upward or downward movement of air caused by the convergence/divergence of winds which forces air to rise/sink or the horizontal flow over topographic features which force the air to be lifted. The movement of air over topographical barriers can result in swirling motions known as eddies. They mix air in the BL and multiple eddies of different sizes generate turbulence. Free convection occurs from heating of the ground from solar radiation which is conducted to the air, making the air buoyant, causing it to rise.

Studies have shown convection to be an important process for venting the BL during summer over both North America and Europe, and in some cases, the dominant process to export emissions of CO, O_3, NMHC and NO_y to the FT (Thompson et al., 1994; Purvis et al., 2003; Choi et al., 2005; Kiley and Fuelberg, 2006). Convection is particularly important over South Asia where export of pollutants is largely controlled by the seasonally varying monsoon. During the NH summer deep moist convection, caused by the wet phase of the monsoon, lifts emissions into the upper troposphere (UT) where they can then be transported large distances with the prevailing easterlies (Liu et al., 2003; Lawrence, 2004; Park et al., 2009). With the lack of deep convection during the winter dry phase of the monsoon, export of emissions occurs mostly in the BL towards the ITCZ, which can take several days (de Gouw et al., 2001; Phadnis et al., 2002). Convection is also an important mechanism for the export of fire emissions from the Earth's surface, where intense heat creates so-called pyro-convection, lifting emissions high into the UT (Fromm and Servranckx, 2003; Damoah et al., 2006). Once in the UT, fire emissions can be transported on hemispheric scales (Forster et al., 2001; Dirksen et al., 2009).

2.3.3 Warm conveyor belts

In the mid-latitudes, baroclinic instability leads to the formation of cyclones. An air-stream, known as a warm conveyor belt (WCB) makes up the eastern part of a typical mid-latitude cyclone, which moves ahead of the surface cold front. The WCB draws air from the surface northward, causing

it to ascend into the mid to upper troposphere. It is this process that is believed to be responsible for the majority of pollution export from the BL throughout the year in North America and East Asia (Stohl and Trickl, 1999; Cooper et al., 2001; Stohl, 2001; Stohl et al., 2002; Cooper et al., 2004). WCBs over Europe have also been observed to export emissions from Europe to the lower and mid troposphere (Bethan and Vaughan, 1998), however, the formation of such air-streams are more infrequent and shallower compared to North America and East Asia (Eckhardt et al., 2003) and are therefore deemed to be less important.

2.4 Background chemistry

Once pollutants have been emitted into the atmosphere the concentrations are also affected by chemical reactions, which are influenced by temperature and availability of sunlight. This section gives an overview of the chemical species and reactions in the troposphere, which will be discussed in this thesis. The summary is largely based on the description given in Seinfeld and Pandis (2006).

2.4.1 Ozone

Ozone is a reactive gas which is found in the greatest concentrations in the stratosphere. In the troposphere, the largest sources are transport from the stratosphere or photochemical production from NO_x, NMHC and CO and CH_4. O_3 is important as it is a greenhouse gas and irritant to humans, therefore there is much interest in understanding its sources and sinks. Table 2.1 shows the global tropospheric budget of O_3 calculated by two different chemical transport models. This shows that O_3 is balanced by equal sources and sinks, with photochemical production and loss being the largest terms.

Ozone is also important in the troposphere because it is the main source of the hydroxyl radical (OH). The OH radical is highly reactive and its abundance controls the atmospheric lifetime of most species in the troposphere (Logan and McElroy, 1981). It is formed when O_3 is photolysed at wavelengths less than 330 nm which yield an excited oxygen atom ($O(^1D)$) (reaction 2.1). The excited state oxygen atom has enough energy to react with water vapour (H_2O) to yield two OH radicals (reaction 2.2):

$$O_3 + h\nu \rightarrow O_2 + O(^1D) \tag{2.1}$$

$$O(^1D) + H_2O \rightarrow OH + OH \tag{2.2}$$

Ozone formation is largely dependent on the availability of NO_x. Most NO_x is emitted as NO and is rapidly converted to NO_2. NO_2 is photolysed by wavelengths <424 nm to produce NO and atomic oxygen, O (reaction 2.3). The oxygen atom then reacts with molecular oxygen to form O_3 (reaction 2.4). O_3 can then react with NO to reform NO_2 and O_2 (reaction 2.5). During the day, background tropospheric concentrations of O_3 are much larger than NO_x, which means that O_3 is not depleted by this reaction apart from in cities due to very high NO_x concentrations.

$$NO_2 + h\nu \rightarrow NO + O \tag{2.3}$$

$$O + O_2 + M \rightarrow O_3 + M \tag{2.4}$$

$$NO + O_3 \rightarrow NO_2 + O_2 \tag{2.5}$$

During the daytime the main sink of NO_x is by reaction with OH to form nitric acid (HNO_3) (reaction 2.6). HNO_3 is efficiently lost from the atmosphere by wet deposition. At nighttime, reaction 2.3 no longer occurs which means the photochemical source of O_3 is eliminated. If emissions of NO_x still occur at night then O_3 will be depleted quickly by reaction with NO (reaction 2.5). Therefore at night the majority of NO_x is in the form of NO_2. NO_2 also reacts with O_3 to form nitrate (NO_3) (reaction 2.7). This can then react with NO_2 to form dinitrogen pentoxide (N_2O_5) (reaction 2.8). The heterogeneous reaction of N_2O_5 on aerosol forms nitric acid (HNO_3) through reaction 2.9. Reaction 2.9 is one of the major removal mechanisms of NO_x along with reaction 2.6 and is particularly important in the Arctic in winter (Tie et al., 2003).

$$NO_2 + OH + M \rightarrow HNO_3 + M \tag{2.6}$$

Table 2.1 Estimates of the global tropospheric O_3 budget (in $Tg(O_3)/yr$). The first column is taken from the study by Wang and Jacob (1998) and the second column was calculated by the TOMCAT model from Breider (2010).

Reference	Wang and Jacob (1998)	Breider (2010)
Sources		
In-situ production	4100	4334
transport from the stratosphere	400	644
Total sources	4500	4978
Sinks		
In-situ chemical loss	3680	3420
Dry deposition	820	1554
Total sinks	4500	4974

Figure 2.2 O_3 concentrations (ppbv) simulated by a photochemical model shown as a funtion of hydrocarbon and NO_x emissions. The thick black line demonstrates the non-linear production efficiency of O_3. Taken from Jacob (1999b).

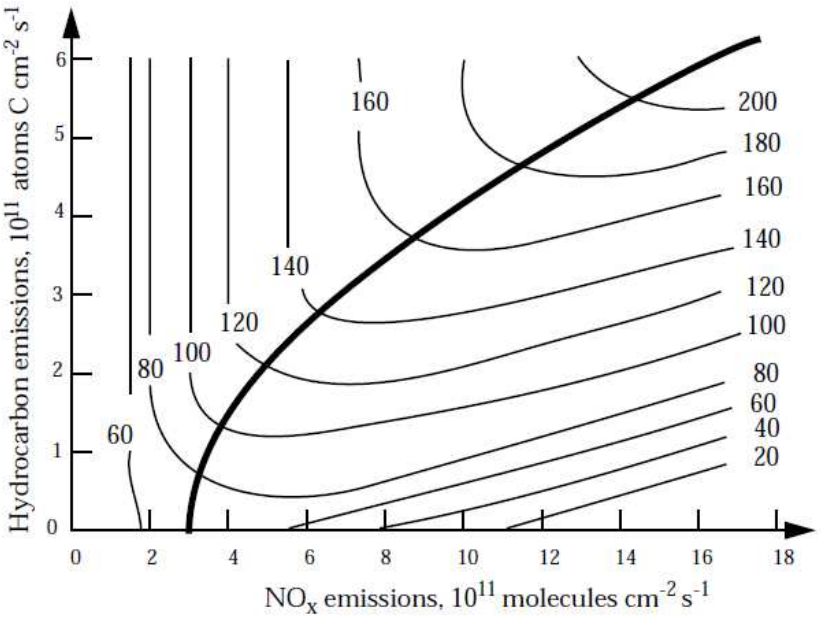

$$NO_2 + O_3 \rightarrow NO_3 + O_2 \tag{2.7}$$

$$NO_2 + NO_3 + M \rightarrow N_2O_5 + M \tag{2.8}$$

$$N_2O_5(g) + H_2O(aerosol) \rightarrow 2HNO_3 \tag{2.9}$$

When NO_x is available, ozone production can be further enhanced by the presence of CO, CH_4 and NMHC. The production of O_3 from NO_x is not linear and for very high concentrations of NO_x the production efficiency of O_3 is reduced. This is shown in Figure 2.2 by the thick black line which represents the production of O_3 as a function of NO_x and NMHC. This is the reason why higher rates of O_3 production are found downwind of large urban centres, where the NO_x concentrations are lower (Parrish et al., 1993).

2.4.2 Carbon monoxide

CO is an important trace gas in the atmosphere due to its interaction with OH. Increased emissions of CO can reduce the global tropospheric OH concentrations, increasing the lifetime of the greenhouse gas methane (CH_4) (Isaksen and Hov, 1987). CO oxidation can also lead to the formation of O_3, another important greenhouse gas (Logan and McElroy, 1981). Even though CO is not a

greenhouse gas, it is still considered to have an indirect global warming potential (GWP) due to its influence on CH_4 and O_3 (Forster et al., 2007). CO is a useful tracer of combustion and is used in studies to understand impacts of anthropogenic and biomass burning sources (e.g. Jaeglé et al. (2003); Fisher et al. (2010); Sodemann et al. (2011)).

CO can be both emitted directly from natural and anthropogenic sources or produced in the atmosphere from chemical reactions. Table 2.2 shows different estimates of the major sources and sinks of the global tropospheric CO budget. Direct emission at the Earth's surface and in-situ production of CO in the atmosphere are estimated to be of equal importance in terms of total global tropospheric sources. Oxidation of methane by OH and direct emission from biomass burning are major sources of CO, each accounting for ∼30% of the total global source. Another major source is direct emission of CO from fossil fuel combustion and industrial processes which accounts for ∼23% of total sources. These sources vary in importance depending on location. Biomass burning and methane oxidation are particularly important in the tropics and SH (Duncan et al., 2007) due to high rates of methane oxidation (Bloss et al., 2005) and large fire emissions (van de Werf et al., 2004). In the NH, fossil fuel sources dominate due to large anthropogenic emissions (Duncan et al., 2007). Oxidation from naturally emitted isoprene, terpenes and methanol also contribute a reasonably large portion to the budget of CO according to the estimates shown. Other sources of CO are oxidation of both natural and anthropogenic NMHCs which can be oxidised by OH to CO and minor direct emissions from oceans and vegetation.

The main sink of CO is reaction with OH and to a lesser extent through dry deposition by uptake in soils. When CO reacts with OH it forms CO_2 and a hydrogen atom (H), which then reacts very quickly with O_2 to form HO_2. As the second part of the reaction is so fast it can be shortened to:

$$CO + OH + O_2 \rightarrow CO_2 + HO_2 \tag{2.10}$$

The hydroperoxy radical (HO_2) formed from this reaction is particularly important in controlling the ratio of NO and NO_2 when they are present:

$$HO_2 + NO \rightarrow NO_2 + OH \tag{2.11}$$

NO_2 formed from this reaction can then take part in reactions 2.4-2.5 to produce O_3. Otherwise HO_2 can react with itself to form H_2O_2, which is a temporary reservoir of HO_x (OH + HO_2):

$$HO_2 + HO_2 \rightarrow H_2O_2 + O_2 \tag{2.12}$$

Table 2.2 Estimates of global tropospheric CO budget (in Tg(CO)/yr).

Reference	Hauglustaine et al. (1998)	Bergamaschi et al. (2000)	Ehhalt et al. (2001)	Duncan et al. (2007)
Sources				
In-situ production				
Oxidation of CH_4		795	800	778-861
Oxidation of Isoprene		268	270	170-184
Oxidation of Terpene		136	0	68–71
Oxidation of industrial NMHC		203	110	72–76
Oxidation of biomass NMHC			30	45–57
Oxidation of acetone			20	21
Oxidation of methanol				95–103
Sub-total in-situ oxidation	881	1402	1230	1279–1403
Direct emission				
Vegetation		100	150	
Oceans		49	50	
Biomass burning		768	700	
Fossil and domestic fuel		641	650	
Sub-total direct emissions	1219	1458	1550	
Total sources	2100	2860	2780	
Sinks				
Surface deposition	190			
OH reaction	1920			
Total sinks	2110			

$$H_2O_2 + h\nu \rightarrow OH + OH \tag{2.13}$$

$$H_2O_2 + OH \rightarrow HO_2 + H_2O \tag{2.14}$$

Reaction 2.13 yields two OH molecules and reaction 2.14 produces one molecule of HO_2. Overall, reaction 2.14 results in a loss of one HO_x molecule. H_2O_2 is soluble and can therefore be lost through wet deposition resulting in a loss of two HO_x molecules from the atmosphere.

2.4.3 Methane oxidation

A similar mechanism to the CO oxidation route also exists for methane. CH_4 reacts with OH to form the methyl radical (CH_3) (reaction 2.15), which reacts very quickly with O_2 to form the methyl peroxy radical (CH_3O_2) (reaction 2.16). CH_3O_2 then reacts with NO to form NO_2 (reaction 2.17), which can then be involved in the cycle of reactions 2.3 to 2.5. CH_4 has a very long lifetime

(approximately 9-12 years), which is determined by OH , however, due to its high concentrations it is still important in tropospheric chemistry.

$$CH_4 + OH \rightarrow CH_3 + H_2O \tag{2.15}$$

$$CH_3 + O_2 + M \rightarrow CH_3O_2 + M \tag{2.16}$$

$$CH_3O_2 + NO \rightarrow CH_3O + NO_2 \tag{2.17}$$

The methoxy radical (CH_3O) reacts with O_2 to form formaldehyde (HCHO) and HO_2. This is so fast that this is often shortened with reaction 2.17 to:

$$CH_3O_2 + NO + O_2 \rightarrow HCHO + HO_2 + NO_2 \tag{2.18}$$

The CH_3O_2 radical produced in reaction 2.16 can also react with NO_2, HO_2 or another CH_3O_2 radical.

Formaldehyde is a common product of hydrocarbon oxidation and undergoes two main reactions in the atmosphere; one with OH and the other by photolysis. The photolysis of HCHO has two channels, reaction 2.19 and 2.20. Reaction 2.19 results in formation of H and HCO. H reacts rapidly with O_2 to form HO_2 (see Section 2.4.2) and HCO can also react quickly with O_2 to form CO and HO_2. Reaction 2.20 results in the formation of CO and H_2.

$$HCHO + h\nu \rightarrow H + HCO \tag{2.19}$$

$$HCHO + h\nu \rightarrow H_2 + CO \tag{2.20}$$

Reaction with OH results in HCO and H_2O:

$$HCHO + OH \rightarrow HCO + H_2O \tag{2.21}$$

All pathways of HCHO result in the formation of CO, explaining why in-situ production is a large source of CO (see Table 2.2).

2.4.4 Reactive nitrogen

Reactive nitrogen (NO_y) is the sum of NO_x and all compounds that are products of the atmospheric oxidation of NO_x. This includes HNO_3, N_2O_5 and peroxyacetyl radical ($CH_3CO_3NO_2$) (PAN). As

already mentioned HNO_3 formation is the dominant sink of NO_x in the atmosphere due to rapid wet deposition. PAN is an important reservoir species as it has a lifetime of up to a few months in cold temperatures compared to NO_x, which has a lifetime of the order of a fews days near the surface (Moxim et al., 1996). This means PAN can be transported long distances in the free troposphere due to the low temperatures. PAN is formed in the atmosphere from the oxidation of many NMHC. Production from acetaldehyde (CH_3CHO) with OH is detailed below:

$$CH_3CHO + OH \rightarrow CH_3CO + H_2O \tag{2.22}$$

$$CH_3CO + O_2 + M \rightarrow CH_3CO_3 + M \tag{2.23}$$

$$CH_3CO_3 + NO_2 \rightleftarrows CH_3CO_3NO_2 \tag{2.24}$$

Reaction 2.24 is temperature dependent and when temperatures are sufficiently high, PAN decomposes and releases NO_2 back into the atmosphere. It has been shown that PAN is an efficient mechanism for transporting NO_x to remote locations where it can affect the regional O_3 budget (Moxim et al., 1996).

2.5 The Arctic climate

The Arctic is commonly referred to the as the area north of the Arctic Circle at 66°33' N. This is an imaginary line which is the southern most point where the sun does not set on the summer solstice. Other definitions also exist, for example the area north of the tree line (the northern limit of upright tree growth) or the area where the average daily summer temperature does not rise above 10°C. These three definitions are shown in Figure 2.3. It is the high latitude location of the Arctic that shapes the climate. The Arctic shows a strong latitudinal dependence on the amount of incoming radiation, with the length of the polar day (complete daylight) and the polar night (complete darkness) ranging from 1 day at the Arctic circle to 6 months at the North Pole. The highest elevation of the sun at noon is much shallower than at lower latitudes and accounts for the fact that the poles receive much less solar radiation causing strong latitudinal temperature gradients. The Arctic region consists of ocean surrounded by two large land masses, Eurasia and North America, and many islands, the largest being Greenland (see Figure 2.3). The Arctic Ocean is covered by floating sea-ice year-round, with a maximum coverage in winter and a minimum in summer. Permanent land ice also covers large parts of Greenland and some smaller mountainous regions in Siberia, Canada, Svalbard and Iceland. Permafrost (perennially frozen soil) is also present over most of the land areas. Snow covers much of the ground, permanent sea ice and land ice throughout the year. Snow and ice are particularly important for the Arctic climate for three reasons. Firstly, they have a high albedo, reflecting a large amount of incoming solar radiation,

reducing the amount absorbed in comparison to land and ocean, lowering the ground and surface air temperature (SAT). Secondly, they have a high emissivity, allowing strong surface cooling through the efficient loss of infrared radiation. Thirdly, they have high insulating properties. If the snow or ice are suitably thick, they can completely prevent heat transfer between the air and the land/ocean. This allows strong cooling of air at the surface.

Figure 2.3 Map showing three definitions of the Arctic region: the tree line (green line), the 10 degrees Celsius isotherm (red line) and the Arctic Circle at 66°33' N (purple line). Taken from http://nsidc.org/arcticmet/basics/arctic_definition.html

2.5.1 Temperature and precipitation

The seasonality in solar radiation controls the seasonal evolution of temperature and precipitation and the ice/snow coverage results in particularly strong regional gradients. For example, in January the mean SAT in parts of Siberia, the central Arctic Ocean and Iceland are approximately -40°C, -25 to -32°C and 0°C, respectively (Serreze and Barry, 2005). Over Siberia, extensive surface cooling in the snow-covered regions results in a high pressure system forming over most of the region. Topographical features of the regions and subsidence in the high pressure system cause very low temperature to form in valleys. Over the central Arctic Ocean, the presence of snow and ice limits the amount of heat transported to the atmosphere allowing the surface air to cool. However, the SATs are modulated through the formation of leads and polynyas (regions of open water where the sea-ice separates). In these regions, heat and moisture exchange between the air and the ocean prevents the temperature from dropping even lower. Near Iceland, the ocean remains largely uncovered allowing heat and moisture exchange to occur keeping the SAT above freezing. This is also the region of the North Atlantic storm track which transports heat from the more southerly latitudes. In the summer, temperatures over the central Arctic Ocean reach near 0°C and snow-covered land can reach between 10-20°C (Serreze and Barry, 2005). Increased incoming radiation causes some of the snow and ice to melt. Uncovered land and ocean has a much lower albedo and therefore more absorbed solar radiation increases the SAT through conduction.

Tropospheric inversions refer to meteorological conditions where warm air is overlying cooler air the near the surface. They are a common occurrence in the Arctic winter due to strong surface cooling but can also occur in the warmer seasons. Inversions create stable conditions where turbulence is suppressed reducing dry deposition of gases and aerosols at the surface.

Due to cold temperatures, humidity (the amount of moisture in the air) is also low. In summer, increased temperatures increase humidity, however it still remains below the global average (Serreze and Barry, 2005). Like temperature, precipitation shows a strong seasonal and regional dependence. Cloud cover is at a minimum in winter ($\sim$60%) and a maximum in summer ($\sim$80%) (Serreze and Barry, 2005). In summer, most clouds are low-level stratus which is associated with drizzle and higher rates of wet deposition (Barrie, 1986). Regional differences exist with an annual mean of around 200 mm around parts of the Canadian Arctic and 1000 mm in the Northern Atlantic (Serreze and Barry, 2005). In the Atlantic, high rates of precipitation are associated with the location of the Atlantic storm track, with a minimum in summer and maximum in winter.

2.6 Atmospheric transport to the Arctic

To understand the transport pathways to the Arctic, it is useful to consider the mean state of atmospheric circulation and how this can change with season. Figure 2.4 shows the climatological circulation patterns at 1000 hPa for winter (December to February) and summer (June to August) which control pollution transport to the Arctic. During the winter months there are three pronounced pressure centres; intense low pressure systems over Iceland and the north Pacific and a high pressure system over north-eastern Siberia. In the NH air moves anticlockwise round a low pressure system and clockwise round a high pressure system. This causes the Icelandic low and the Siberian High to collectively draw air from parts of Europe and Siberia directly into the Arctic. The importance of anti-cyclonic transport of air into the Arctic was highlight by Raatz and Shaw (1984) and Raatz (1989). Due to low precipitation rates around high pressure systems (due to subsidence) pollutants which would undergo wet deposition can be transported to the Arctic. Consideration of this meteorology led scientists to conclude that Eurasia is likely to be the dominant source of Arctic pollution in the winter and spring (Barrie, 1986). The low pressure centre over the Pacific leads to transport of emissions from East Asia to western North America, which can eventually be transported to the Arctic over western Canada along with any emissions from western North America. Emissions from the eastern region of North America will be transported along the more southerly portion of the Icelandic low to Europe which can eventually join emissions from this region to be transported into the Arctic. During the summer, horizontal advection is not as intense due to weaker pressure gradients (as indicated by the more widely spread isobars). The Icelandic low becomes much weaker and moves to the northwest, the Azores High becomes stronger, Asia is dominated by a extra-tropical low pressure system and the Pacific low is replaced by a high pressure system. The weaker circulation and positioning of the pressure centres means that transport of pollution to the Arctic will be slower and less efficient in the summer.

Stohl (2006) used a Lagrangian model to study the seasonal transport pathways to the Arctic from the three major emissions regions of North America, Europe and Asia. The study identified three main pathways of transport to the Arctic which varied in terms of importance depending on the source region and season. The three pathways were:

1. Low-level transport followed by ascent in the Arctic
2. Low-level transport alone
3. Uplift outside the Arctic followed by descent in the Arctic

They found that European emissions can follow all three pathways during the winter and the first and second pathway during the summer. However, Asian and North American emissions tended

Figure 2.4 1000 hPa climatological height field (in Dams=Decimetre) for January, December and February (top) and June, July and August (bottom). Arrows represent the dominant transport pathway of air. Taken from Bottenheim et al. (2004).

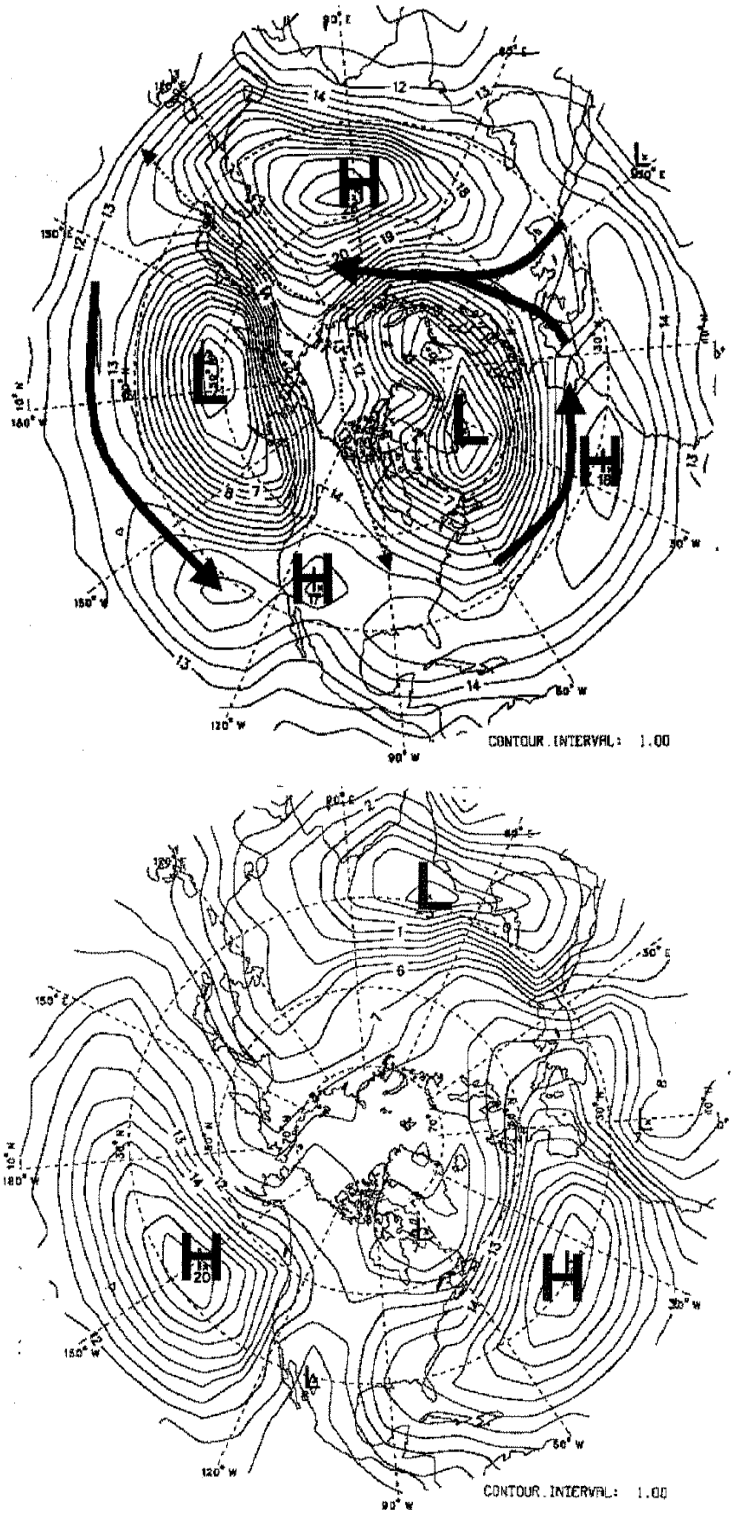

to only follow the third pathway due to export mechanisms which vent the polluted BL and higher potential temperatures which cause the air parcels to rise as they follow lines of constant potential temperature (isentropes) poleward. The different transport mechanisms cause a vertical structure in the Arctic atmosphere where higher altitudes are more easily affected by emissions from North America and Asia and the lower altitudes are more easily affected by emissions from Europe and Siberia (Klonecki et al., 2003). Stohl (2006) found that an important characteristic of the different transport pathways was varying deposition rates related to the thermodynamic signatures of the air parcel. For example, European emissions tended to have low potential temperature values which meant that the air was more easily transported at low levels. Air parcels from Asia tended to take a lot longer to reach the Arctic and travel at much higher altitudes where they experienced repeated ascending/descending motions. This motion meant that the Asian air masses experienced high levels of wet deposition prior to reaching the Arctic. In contrast, low-level transport of European air masses was followed by ascent in the Arctic resulting in high levels of wet deposition within the Arctic. The different rates of deposition along transport pathways was also previously highlighted in a review by Barrie (1986). Figure 2.5 shows the January mean precipitation rates in the NH with the dominant transport pathways of air from North America, Europe and East Asia. Air originating from North America experiences the largest precipitation rates, air originating from East Asia experiences less but still large precipitation rates and air from Europe experiences very low precipitation rates. This highlights an important consideration when evaluating models. The ability of the model to reproduce the observed concentrations of trace species in the Arctic will be closely related to the accuracy of modelled transport pathways. The model will need to diagnose precipitation rates if it is to capture the wet deposition of gases such as HNO_3. Also, the model must be able to capture different transport patterns in order to be able to reproduce the vertical structure of trace gases and pollutants.

2.6.1 Atmospheric blocking

The pressure systems shown in Figure 2.4 represent the mean state of atmospheric transport to the Arctic. On a time-scale of days, the mid-latitude weather patterns are determined by fluctuations between states of baroclinic stability and instability which drive the formation of cyclones and anticyclones (low and high pressure regions). In periods of high baroclinic instability, meridional atmospheric exchange increases and has been associated with larger Arctic concentrations of pollutants in spring (Iversen and Joranger, 1985). One atmospheric state that is believed to increase transport to the Arctic is that of blocking (Iversen and Joranger, 1985). This occurs when a high pressure ridge forms above a low pressure trough, which 'blocks' the westerlies in the mid-latitudes. The pressure systems cause the westerly jet stream to split into two sections, one with a poleward flow and the other with a southward flow (Austin, 1980). This poleward flow can exist

for up to 15 days (Austin, 1980) and has a maximum occurrence in the North Atlantic in winter and autumn (Tyrlis and Hoskins, 2008) encouraging direct flow into the Arctic.

2.6.2 Polar dome

Another feature of Arctic meteorology that is important in terms of atmospheric transport from lower latitudes is seasonal evolution of the 'polar dome' or 'polar front'. Due to the lack of sunlight in winter, extremely low surface temperatures form within the Polar cell resulting in large temperature gradients between the Arctic and the mid-latitudes. This large temperature contrast results in lines of constant potential temperature forming a closed dome around the Arctic (Barrie, 1986). This suggests that transport from sources south of the polar front will have a limited impact on the lower tropospheric composition of the Arctic and direct emissions into the polar dome will be particularly important (Iversen, 1984). During the winter, the polar front extends as far as 40°N, over the cold snow covered areas of Siberia and Canada and moves to around 70°N in summer when temperatures in the Arctic increase (Bottenheim et al., 2004) (see Figure 2.6). This is why air from North America and Southern Asia has a limited impact on the surface in winter and European and Siberian emissions, which are directly emitted into the polar dome, provide a large source of pollutants to the Arctic (Rahn, 1981; Barrie, 1986; Klonecki et al., 2003).

2.6.3 North Atlantic Oscillation and transport to the Arctic

Some recent studies have shown that transport to the Arctic can be influenced by the North Atlantic Oscillation (NAO) (Eckhardt et al., 2004). Positive and negative phases of the NAO represent changes in the gradient in pressure between the semi-permanent Icelandic low and Azores High in the North Atlantic region. During positive phases, anthropogenic emissions of CO have been shown to be elevated in the Arctic in a modelling study by Eckhardt et al. (2004). This will be discussed in more detail in Chapter 6.

2.7 Arctic air pollution

The Arctic has very few local pollution sources due to a small human population. However some sources exist from industrial processes such as mining (e.g. Norilsk in Russian Arctic). As seen in Figure 2.3, the Arctic is surrounded by North America and Eurasia, making these the most likely source of pollution in the Arctic. This section now describes previous studies documenting the discovery of the spring Arctic haze and Arctic atmospheric composition research.

Figure 2.5 Monthly mean January precipitation (mm) in the NH with average transport pathways to the Arctic from North America, Europe and Asia depicted with the arrows. Taken from Barrie (1986).

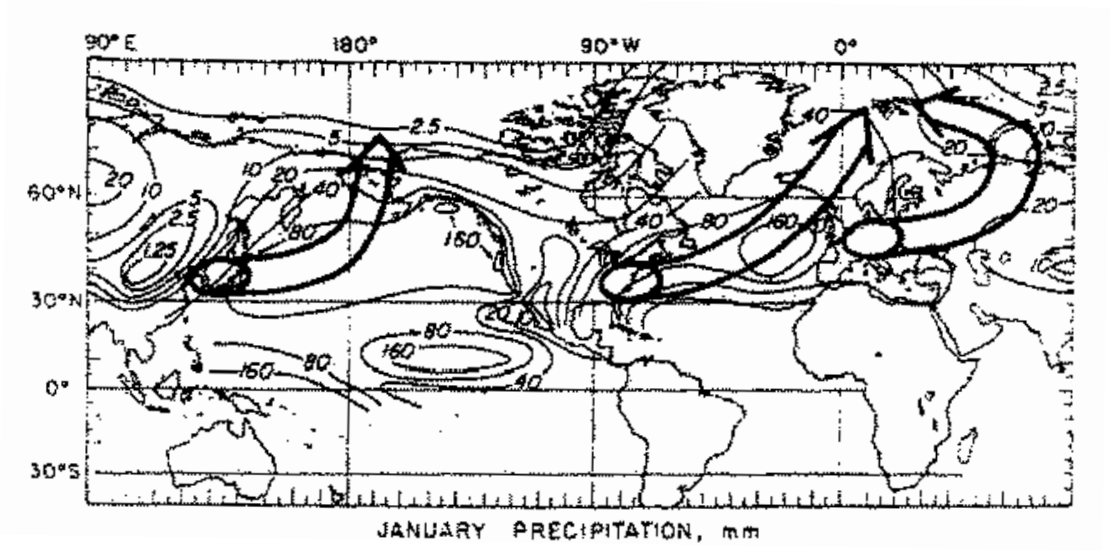

Figure 2.6 Average Location of the Arctic front in January and July. Taken from Bottenheim et al. (2004).

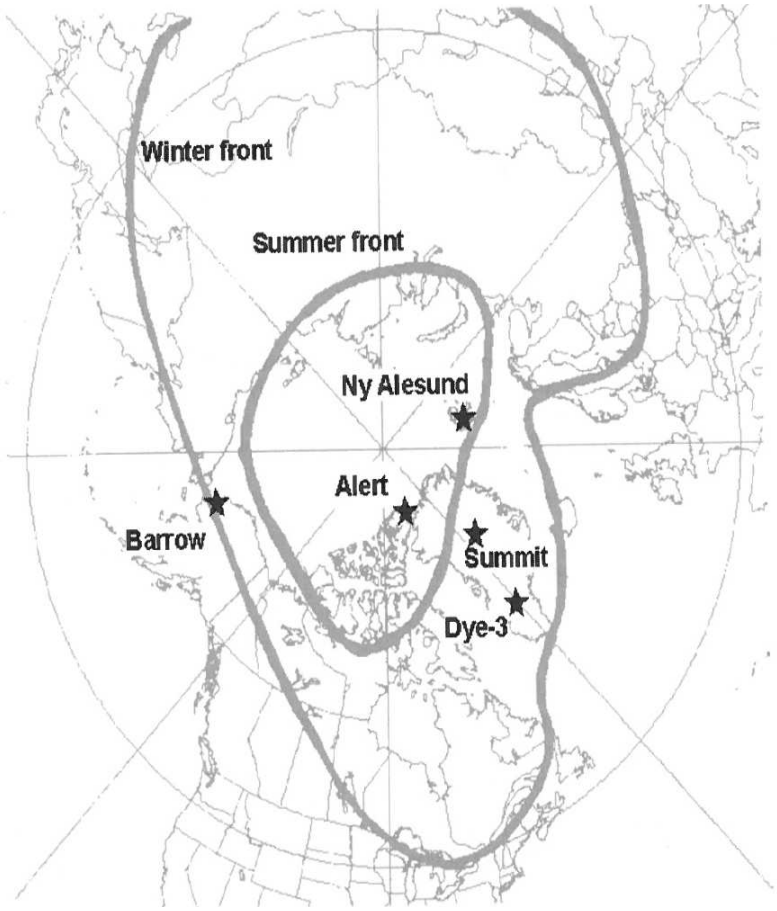

2.7.1 Discovery of the Arctic haze

The Arctic was previously believed to be a clean unpolluted region of the world with only small local emission sources. However, in the 1950s pilots observed layers of haze in the Arctic during spring, indicating that the Arctic was a receptor of atmospheric pollution from some unknown source (Shaw, 1995). Later studies suggested that this haze came from anthropogenic emissions at lower latitudes (Rahn, 1985). To properly understand the so-called spring Arctic Haze, scientists began to investigate the likely sources of the haze, what it consisted of and what controlled its occurrence. This was aided by analysis of surface measurements and aircraft campaigns, such as AGASP (Arctic haze and the Arctic Gas and Aerosol Sampling Program), which took place throughout the 1980s with particular focus on the spring (e.g. Schnell (1984)). This confirmed that the Arctic Haze occurred throughout the Arctic in distinct layers throughout the troposphere (Schnell and Raatz, 1984). The most abundant component of the haze was found to be sulphate aerosols (formed mostly from sulphur dioxide emissions) (Rahn, 1985; Pacyna, 1995). Surface observations showed a strong seasonality in sulphate concentrations with maximum concentrations occurring during the spring and minimum concentrations during the summer. They also found elevated concentrations of other aerosols within the haze, such as black carbon (BC) and nitrate (Heintzenberg, 1989). Trace gases such as CO, CO_2, CH_4, O_3, PAN and other organic species were also found to be elevated within haze layers (Khalil and Rasmussen, 1984b; Hov et al., 1984; Rahn, 1985; Conway et al., 1985; Pacyna, 1995).

2.7.2 Early source contribution studies

Due to the dominant component of Arctic haze being sulphate, most early source contribution studies focused on understanding the sources of this aerosol. Rahn (1981) used ratios of manganese (Mn) and vanadium (V) measured at the surface in the Arctic to differentiate between anthropogenic and natural air masses of different origins, assuming V will be enriched in air which has come from an anthropogenic origin. This method was also used by Raatz and Shaw (1984) and Rahn (1985). All three of these studies suggested Eurasia to be the dominant source of anthropogenic pollution in the Arctic during spring, with North America contributing very little to Arctic haze. However, some debate still exists to whether this method is accurate due to unaccounted sources of V (Przybylak, 2003). Barrie et al. (1989) used a chemical transport model to study the main sources of sulphur throughout the year and found that North America only contributed 6% to the Arctic sulphur burden with the rest from Eurasian sources. Overall, it was generally accepted that Arctic haze was a product of inefficient removal processes in the stable cold Arctic atmosphere coupled with efficient transport patterns in the winter and spring from Eurasia (Barrie, 1986; Shaw, 1995).

2.7.3 Recent source contribution studies

Trend analysis of observed trace species at surface stations in the Arctic indicate there may have been a change in the anthropogenic source contributions to the Arctic. Quinn et al. (2007) showed that surface concentrations of sulphate at Arctic stations in the 1990s decreased by 30 to 70%. This was attributed to a reduction in emissions with the breakup of the Soviet Union. However, more recently between 1997 and 2003, aerosol light scattering has increased by 50% (Quinn et al., 2007). Analysis of O_3 observations at surface stations in the Arctic showed a reduction in O_3 during the 1980s to the mid-1990s but have since shown a small increase after that (Oltmans et al., 1998, 2006; Helmig et al., 2007). However, O_3 trend analysis is difficult to draw statistically significant evidence from due to the lack of long-term observations. Together, these recent trends suggest that the amount of pollution reaching the Arctic has begun to increase again after a decline. Total energy consumption in Asia is estimated to have more than doubled between 1980 and 2003, resulting in a large increase in Asian emissions (Ohara et al., 2007). In particular, increases of 28% for BC, 64% for CO, 108% for NMHC, 119% for sulphur dioxide (SO_2), and 176% for NO_x have been estimated by Ohara et al. (2007). This may have an important influence on the amount of aerosols and trace gases found in the Arctic. A modelling study by Koch and Hansen (2005) showed South Asia to be the dominant source of BC in the Arctic due to the recent emission increases in Asia in contrast to emission reductions in Europe and North America. However, Stohl (2006) argued that the presence of the polar dome limited the impact of South Asia on the Arctic and found Europe to be a more important source of BC in winter and summer. As with first source contribution studies, these two studies are both concerned with the main sources of Arctic aerosol.

There are currently very few studies that have estimated the regional contributions to the Arctic burdens of trace gases. Trace gases which have different sources, different lifetimes and are not efficiently lost by wet deposition may exhibit different sensitivities to source regions. For this reason, it is important to also estimate the source contributions for important gases such as O_3 and its precursors, considering the seasonality of sources due to changing transport patterns. A large fraction of early source contribution studies have focused on winter and spring due to the general belief that emissions were not efficiently transported to the Arctic during summer and concentrations of aerosols and trace gases generally exhibiting a summer minimum (Barrie et al., 1989; Jaffe et al., 1991) due to more efficient wet and dry deposition with increased precipitation and turbulence (Shaw, 1995). However, observations have shown that European, Asian and North American emissions along with natural sources (such as fires) can affect the Arctic throughout the year (Pacyna and Ottar, 1985, 1989; Harriss et al., 1992).

The only source contribution study to consider O_3 and CO throughout the year was conducted by Shindell et al. (2008). They used output from several CTMs to study the source contributions from anthropogenic emissions from North America, Europe and Asia. Using CO as a tracer for

anthropogenic pollution, they found European emissions to be most important in the lower troposphere and North American emissions to be most important in the upper troposphere. To study the sensitivity of Arctic O_3 to emissions from North America, Europe and Asia they reduced emissions of NO_x by 20% in all the CTMS. They found that O_3 was most sensitive to North America, followed by Europe and then East Asia. Only one other study has considered trace gas transport to the Arctic. Fisher et al. (2010), also used CO as a tracer of mid-latitude pollution sources in April 2008 and found Asian anthropogenic emissions to dominate the total column of CO.

2.7.4 Biomass burning as a source of Arctic pollution

Biomass burning is another potential source contributor to the Arctic. Due to the proximity of the boreal forests in Canada and Siberia, they have the potential to contribute a large fraction to observed trace gases during the summer boreal fire season. Biomass burning emits large quantities of CO, NO_x and aerosols to the atmosphere and can result in O_3 production downwind of emissions (Kasischke et al., 2005; Real et al., 2007). Chemical signatures of biomass burning have been found in ice cores, indicating that fire emissions at lower latitudes can be transported to the Arctic (Legrand et al., 1992; Whitlow et al., 1994). Plumes of biomass burning emissions have also been observed within the Arctic in the 1990s during the ABLE-A (Arctic Boundary Layer Experiment) and ABLE-B aircraft campaigns that took place in July-August in 1988 and 1990 (Wofsy et al., 1992; Harriss et al., 1992, 1994). During these campaigns, efficient conversion of NO_x to PAN was observed in fire plumes (Wofsy et al., 1992), which resulted in low production of O_3 due to low NO_x concentrations (Wofsy et al., 1992). However, the biomass burning sourced PAN transported to the Arctic could then decompose to release NO_x and produce O_3 at a later date. This impact of fires on O_3 has not been well studied and warrants further examination. Due to increased temperatures and drying in the boreal regions, it is thought that fires will increase in the future (Flannigan and Van Wagner, 1991; Stocks, 1993) and it is believed that this may already be occurring (Soja et al., 2007). Therefore there is a need to better understand the overall impact that fires have on the Arctic. Emissions from agricultural burning in spring from eastern Europe have also been observed to perturb concentrations of gases in the Arctic (Stohl et al., 2007). Any changes in agricultural practices in the mid-latitudes of the NH could also be important for the Arctic.

2.7.5 Radiative importance of ozone in the Arctic

Radiative forcing is used to assess and compare the anthropogenic and natural drivers of climate change (Forster et al., 2007). A recent study by Quinn et al. (2008) demonstrated the Arctic response to gases and aerosols found in the Arctic. They calculated seasonally averaged values

of the surface temperature response in the Arctic to concentrations of O_3 and showed that O_3 contributes significantly to the surface temperature response throughout the year. Hansen et al. (1997) demonstrated that the O_3 response is greater at higher altitudes. This has implications for O_3 transported from different regions which are believed to show a strong altitudinal dependency.

2.7.6 Tropospheric ozone within the Arctic

Due to the radiative importance of O_3 and its suspected increase in the Arctic, many studies have focused on trying to understand what controls the abundance of O_3 in the Arctic. Like many other trace species, O_3 exhibits a spring maximum and a summer minimum in the Arctic. Most past studies have focused on the springtime maximum. There have been several hypotheses regarding the cause of this feature at high-latitudes. Some studies have suggested that an accumulation of O_3 and its precursors occurs over the winter due to a lack of removal processes (Honrath and Jaffe, 1992). It has also been suggested that the springtime maximum is caused by an increase in the influx of stratospheric O_3 (Logan, 1985). During February and March 2000, the TOPSE (Tropospheric Ozone Production about the Spring Equinox) campaign was undertaken to study the transition from winter to spring between 40°-80°N to try and understand the driving processes of the springtime maximum (Atlas et al., 2003). Measurements in conjunction with models have shown that even though the transport of stratospheric O_3 to the troposphere is larger in the spring (Dibb et al., 2003; Browell et al., 2003; Emmons et al., 2003), the O_3 maximum is driven by increased rates of photochemistry (Emmons et al., 2003; Stroud et al., 2003). However, one study also showed that during the TOPSE campaign latitudes between 60°-80°N experienced net destruction of O_3 along the flight tracks and therefore transport of O_3 from lower latitudes is particularly important (Wang et al., 2003). This is also in agreement with Stroud et al. (2004) who found net import of O_3 was required to reproduce the observed ozone concentrations in their model. However, all studies showed that O_3 production was sensitive to the concentrations of NO_x and HO_x. Very little is known about what controls the abundances of these species in the Arctic (Jacob et al., 2010).

An important reservoir of NO_x is PAN, which is formed from NO_2 and the peroxyacetyl radical (CH_3CO_3) (see Section 2.4.4). PAN is stable at low temperatures and has been observed to be the dominant NO_y species in the Arctic during winter and spring (Singh et al., 1992; Bottenheim et al., 1993). Compared to NO_x, which is relatively short-lived, PAN is capable of undergoing long-range transport which means it can contribute to the O_3 budget at remote locations by acting as a source of NO_x when it thermally decomposes. It has been suggested that PAN may be an important source of O_3 in spring in the Arctic when temperatures increase (Penkett and Brice, 1986). It has also been suggested that enhanced NO_x during stratospheric intrusions may drive production of O_3 in the upper troposphere, acting as an important source of O_3 (Liang et al., 2009). It is clear that

our understanding of what controls the concentrations of O_3 in the Arctic is still not complete. In particular, O_3 during other seasons apart from spring have not been well studied.

O_3 chemistry is further complicated in the Arctic due to the occurrence of what have been termed ozone depletion events (ODEs). During spring, when sunlight increases in the Arctic, but temperatures are still low (below -20°C), ODEs are a common occurrence observed every year, generally between March and May (Simpson et al., 2007). These events were first witnessed in the 1980's when O_3 was shown to be depleted to near zero levels during polar sunrise (Bottenheim et al., 1986; Barrie et al., 1988; Oltmans et al., 1989). Measurements showed that air with depleted ozone also contained elevated levels of bromine compounds with back-trajectories suggesting the air to have originated over the Arctic Ocean (Sturges et al., 1993). It is now generally understood that bromide (Br^-) coming from sea salt releases reactive bromine (Br) which reacts with O_3 rapidly. Generally most of the ODEs are observed below 400 m in the boundary layer, however, some events have been observed where O_3 is depleted up to 4 km (Solberg et al., 1996) and can also have extend over a horizontal distance of up to 2 km (Ridley et al., 2007). As O_3 is the primary source of OH, this can have important implications for the oxidising capacity of the atmosphere (Simpson et al., 2007). There is the need for this to be included in models to properly understand O_3 and tropospheric chemistry in the Arctic.

2.8 Atmospheric modelling of the sources and chemistry of the troposphere

2.8.1 Modelling studies of carbon monoxide

A recent study by Shindell et al. (2006b) showed that in general models are able to capture the features of CO observed by a satellite instrument. However, all models were unable to capture the high concentrations of CO during winter and spring in the Northern Hemisphere. This was largely attributed to an underestimate of emissions from Asia in the inventory used. They also found errors in biomass burning to contribute to model-observation biases. Model-to-model differences were also found to be quite large, with a spread of 35 ppbv (45% of the mean) and were partly attributed to differences in the models treatment of wet deposition, OH concentrations, NMHC emissions and NMHC chemistry scheme complexity.

2.8.2 Modelling studies of ozone

A recent study by Wild (2007) compared results from several CTMs to understand what causes the biggest differences in simulated O_3 budgets. The study found emission inventories to result in the

biggest differences amongst models with the models using more recent emission inventories comparing better to ozonesonde data. The next largest difference was found to be lightning emissions showing that better constraints on this would improve our ability to model O_3 in the troposphere. Models with coarser grids (a range 300 to 600 km were considered) also overestimated the stratospheric influx of O_3 and underestimated dry deposition. This study did not consider differences between the chemical schemes used in the models, which are also likely to cause model-to-model differences.

2.8.3 Modelling the Arctic troposphere

Shindell et al. (2008) compared seventeen different models and found large differences between simulated CO and O_3 in the Arctic. They found that model variability for O_3 was largely due to differences in chemical schemes. In particular, models were unable to capture the low spring concentrations at Barrow, in Alaska, if they did not include bromine chemistry. Causes of CO model variability differed depending on altitude. Surface Arctic CO differences were dominated by East Asian emissions and at higher levels model-to-model variability was due to transport and chemistry. This demonstrates that our ability to accurately model Arctic climate and composition is still limited and indicates we do not yet fully understand the processes that are important within the Arctic. It is worth noting here, that due to the limited availability of observations, comparisons were only done at two surface stations. The recent international aircraft campaign POLARCAT (Polar Study using aircraft, remote sensing, surface measurements and models of climate, chemistry, aerosols and transport), which took place in 2008, aimed to provide a valuable dataset to assess models within the Arctic. This dataset is described and used in Chapter 7 to evaluate the TOMCAT model during the summer.

2.9 Summary

If we are to reduce concentrations of O_3 and trace gases in the Arctic to offset further enhanced warming then there is a need to have a better understanding of the different seasonal source contributions from different anthropogenic regions. Most of our understanding of the main source regions is based on old emission inventories of sulphur dioxide from the 1980s. It is clear that there have been large changes in the distribution of emissions, with Asia quickly becoming a large source of trace gases in the Northern Hemisphere. Also, Arctic sensitivity to O_3 produced from different regions is likely to vary to that of aerosols due to complicated chemistry and NO_x reservoir species such PAN, which are able to be transported to this remote region. Therefore, there is a need to quantify the impact of the industrialised regions in the Northern Hemisphere to estimate the efficiency of emission reduction policies on O_3. One possible source of Arctic O_3 is from

natural sources such as fires in the boreal regions. It is important to gain an understanding of how sensitive the Arctic is to emissions from fires because their frequency and intensity are predicted to increase in the future as the climate warms. This will help us to distinguish possible increasing trends in trace gases due to natural and anthropogenic sources. In this thesis, these questions are addressed using the chemical transport model, TOMCAT, which will be described more detail in Chapter 3.

Chapter 3

The TOMCAT chemical transport model

3.1 Introduction

Offline chemical transport models (CTMs) are useful tools for studying how different processes affect the chemical composition of the atmosphere on varying spatial and temporal scales. They resolve the movement of chemical species through large-scale horizontal and vertical advection and smaller sub-grid scale processes such as convection and boundary layer mixing. Meteorological analyses read in by the model are used to resolve these transport mechanisms. As well as transport, the concentrations of chemical species in the atmosphere are also affected by emission fluxes at the surface, chemical loss and production and wet and dry deposition. Emissions from both natural sources and anthropogenic activities are usually obtained from emissions inventories which provide regional or global estimates of fluxes of different species. CTMs can be applied to many problems. They are often used in combination with in-situ observations to help understand the transport and chemical mechanisms which control concentrations of chemical species leading to new understanding of certain processes (e.g. Emmons et al. (2003); Jacob et al. (2005); Mao et al. (2010)). They are also commonly used to study source-receptor relationships which is useful for understanding the sensitivity of a region to different sources (e.g. Wild and Akimoto (2001); Cook et al. (2007)). Regional and global budgets of atmospheric species can also be estimated (e.g. Duncan et al. (2007)).

One such CTM, TOMCAT, has been used throughout this thesis to understand the chemical and transport processes which are important in influencing the chemical composition of the Arctic atmosphere. This chapter describes the TOMCAT model and several updates which have been implemented as part of this thesis. The standard version of TOMCAT is outlined in Section 3.2.

Updates to the standard TOMCAT chemistry scheme are discussed in Section 3.3. New emissions datasets which have been processed for use in this thesis are presented in Section 3.4

3.2 TOMCAT: A global chemical transport model

The TOMCAT model is a Eulerian three-dimensional (3-D) global CTM (e.g. Stockwell and Chipperfield (1999); Chipperfield (2006)). The model calculates the transport of mass between grid boxes across 6 faces. Large-scale horizontal and vertical motion is calculated from fields which are read in and interpolated to the TOMCAT grid from the European Centre for Medium-Range Weather Forecasts (ECMWF) analyses. The use of offline analyses mean that the model is constrained by observational data, which is assimilated into the reanalyses. To avoid inconsistencies between horizontal and vertical winds after this interpolation, the vertical motion is diagnosed from horizontal divergence instead of using vertical velocity fields from the analyses. Tracer advection in the meridional, zonal and vertical direction is based on the Prather (1986) scheme which conserves the second-order moments. This scheme conserves mass and maintains tracer gradients (Chipperfield, 2006). Gas-phase chemical loss and production, wet and dry deposition, treatment of moist convection, and boundary layer mixing are all treated in TOMCAT. The model extends from the surface up to 10 hPa and for tropospheric studies uses a σ - p coordinate system, with near-surface levels following the terrain (σ) and higher levels ($>$100 hPa) using pressure levels (p). All simulations used in this thesis have 31 vertical levels and a horizontal resolution of 2.8°$\times$ 2.8° (128 longitudes and 64 latitudes).

3.2.1 Sub-grid scale parameterisations

The Holtslag and Bolville (1993) scheme is used for sub-scale boundary layer mixing. The inclusion of this scheme into a CTM is described by Wang et al. (1999). The parameterisation determines the height of the planetary boundary layer (PBL) explicitly and includes transport by eddies in unstable conditions and entrainment of air at the top of the PBL. When convection is absent, vertical diffusion is included up to 3 km. Moist convection is based on the Tiedtke (1989) scheme, which calculates tracer mass flux rates due to convective updrafts, entrainment/detrainment in clouds, large-scale subsidence and turbulent mixing, which is forced from the large-scale horizontal winds (u and v), temperature (T) and humidity (q).

3.2.2 Wet and dry deposition

Dry and wet deposition are important loss channels for gas-phase species in the atmosphere and need to be considered by CTMs. Dry deposition describes the uptake of atmospheric species at the surface of the Earth. The efficiency of uptake is dependent on species, meteorological conditions and surface type. Wet deposition is the scavenging of trace gases from the atmosphere by precipitation and depends on cloud formation, precipitation rates and the solubility of gases. TOMCAT uses the dry and wet deposition scheme which were shown to perform better than other schemes in the study by Giannakopoulos et al. (1999). The rate of dry deposition (r_d (s^{-1})) is calculated as a function of the deposition velocity (V_d, (ms^{-1})) of the relevant species (which are included in the model as a look-up table, and are dependent on season and surface type) and the height of the lowest model level (H):

$$r_d = \frac{V_d}{H} \tag{3.1}$$

V_d is extrapolated to the middle of the lowest model level using the vertical diffusion coefficient which is a function of wind velocity, surface roughness and stability of the boundary layer and is calculated within the PBL scheme. The vertical diffusion coefficient is a function of wind speed, surface roughness and boundary layer stability which means this is also factored into the deposition rates.

Wet deposition is parameterised according to the proportionality of the removal rate (R) to the concentration of the species (C) as follows:

$$R = -rC \tag{3.2}$$

where r is the local removal frequency (s^{-1}) and is taken from the model-derived large-scale and convective precipitation.

3.3 Updates to the TOMCAT chemistry scheme

3.3.1 Standard chemistry scheme

TOMCAT contains a detailed tropospheric chemistry scheme which includes O_x-HO_x–NO_x-CO-CH_4 chemistry and C1-C3 hydrocarbons (Law et al., 1998; Arnold et al., 2005). TOMCAT also includes the oxidation of isoprene based on the Mainz Isoprene Mechanism scheme (Pöschl et al., 2000). The implementation of this scheme into TOMCAT is described by Young (2007). The

chemical reactions are implemented via a software package, ASAD (Carver et al., 1997). There are a total of 62 species with 42 being advected. Shorter lived species are grouped into families for advection between grid boxes (i.e. NO_x and O_x). ASAD is provided with a set of 122 bimolecular, 16 termolecular and 37 photolysis reactions. The bimolecular and termolecular kinetic rates are mostly taken from the International Union of Pure and Applied Chemistry (IUPAC)[1] and the Leeds Master Chemical Mechanism (MCM)[2]. Photolysis rates are calculated online using the code of Hough (1988) which considers both direct and scattered radiation. Within TOMCAT, this scheme is supplied with surface albedo, monthly mean climatological cloud fields and ozone and temperature profiles.

3.3.2 Addition of monoterpene and C2-C7 hydrocarbon chemistry

As part of this work the model's chemistry scheme was updated to account for missing sources of carbon from higher hydrocarbons which were not previously emitted in the model. The model was developed to include ethene (C_2H_4), propene (C_3H_6), butane (C_4H_{10}) and toluene (C_7H_8) emissions. The degradation of these species and subsequent products were based on the ExTC scheme based on Folberth et al. (2006). Biogenic emissions and oxidation of monoterpenes were also included based on the MOZART-3 scheme (Kinnison et al., 2007). A full list of reactions is given in Appendix A. The chemistry was implemented by Dr Stephen Arnold[3] and evaluation of the new scheme was done as part of this thesis. First results and comparisons to the standard model are shown in Chapter 4.

3.3.3 Addition of heterogeneous uptake of N_2O_5 by aerosols

Heterogeneous chemistry is known to affect the global concentrations of O_3, OH and NO_x in the troposphere (Jacob, 2000). One important reaction is the reaction of N_2O_5 on the surface of aerosols to form HNO_3:

$$N_2O_5(g) + H_2O(aerosol) \rightarrow 2HNO_3 \tag{3.3}$$

This is important in the troposphere when there is no sunlight to photolyse NO_3 therefore allowing time for the formation of N_2O_5 (See reactions 2.7-2.9 in Section 2.4). This makes this reaction particularly important in the Arctic during winter (Tie et al., 2003). HNO_3 is highly soluble and is therefore efficiently lost through wet deposition making this an important loss channel for NO_x

[1] http://www.iupac-kinetic.ch.cam.ac.uk/
[2] http://mcm.leeds.ac.uk/MCM/
[3] University of Leeds, Leeds, UK

Table 3.1 List of γ values used in TOMCAT for heterogeneous uptake of N_2O_5 by aerosol based on Evans and Jacob (2005) with the uptake coefficient on dust reduced from 0.1 to 0.02 based on Mogili et al. (2006).

Aerosol Type	**Reaction Probability** (T=temperature (K), RH= relative humidity (%))
Sulphate	$\gamma = \alpha \times 10^{\beta}$ $\alpha = 2.79 \times 10^{-4} + 1.3$ $\times 10^{-4} \times RH - 3.43$ $\times 10^{-6} \times RH^2 + 7.52$ $\times 10^{-8} \times RH^3$ $\beta = 4 \times 10^{-2} \times$ (T$-$294) (T$\geq$ 282K) $\beta = -0.48$ (T$<$ 282K)
Organic Carbon	$\gamma = RH \times 5.2 \times 10^{-4}$ (RH$<$ 57%)
Black Carbon	$\gamma = 0.005$
Sea Salt	$\gamma = 0.005$ (RH $< 62\%$) $\gamma = 0.03$ (RH $\geq 62\%$)
Dust	$\gamma = 0.02$

from the atmosphere. The standard version of TOMCAT only included the gas-phase form of the above reaction using an upper limit reaction rate. A scheme has been included in TOMCAT to account for this heterogeneous reaction based on the parameterisation of Evans and Jacob (2005). The parameterisation was adapted for TOMCAT and used by Breider (2010) who used the newly developed coupled TOMCAT-GLOMAP CTM with online aerosol and gas phase chemistry, considering loss by sea-salt and sulphate aerosol. However, as the work presented here only uses the TOMCAT CTM, which does not include aerosols, it was necessary to use prescribed monthly mean aerosol fields. These were calculated by the aerosol model GLOMAP (Mann et al., 2010) and read in offline. This method is computationally cheaper but means that the version used in this thesis will not have co-located aerosol and gases in plumes for heterogeneous reactions, which will likely introduce some error in the loss rates of NO_x in highly polluted cases. However, it is assumed that the overall monthly loss of NO_x will provide a better estimate of NO_x concentrations in the Arctic than not accounting for this process in the model.

When a gas molecule strikes the surface of a particle not every collision will lead to a reaction. Therefore, an estimate of the probability of collision resulting in a reaction is needed when considering heterogeneous chemistry in a model. This is represented by the reactive uptake coefficient (γ) which has a value between 0 and 1 and is estimated through laboratory experiments. There is large uncertainty in the values of γ for different aerosol types and better quantification of these

are still required (Macintyre, 2010). This uncertainty has important implications for modelling with simulated OH and NO_x concentrations being sensitive to the chosen (γ) value (Macintyre and Evans, 2010). The scheme included in TOMCAT considers externally mixed sulphate, organic carbon, black carbon, sea salt and dust. The γ values that are used in TOMCAT for the simulations shown in this thesis are given in Table 3.1. They are the same as used by Evans and Jacob (2005), except for dust, and vary as a function of temperature, humidity and aerosol composition. The overall γ value used is weighted according to mass of each aerosol type. Adapting the scheme used by Breider (2010) for TOMCAT was done by Dr Stephen Arnold. The evaluation and development of the scheme was done as part of this thesis and first results are discussed in Chapter 4.

3.4 Emissions

The standard version of TOMCAT uses emissions created for the Third Assessment Report of the Intergovernmental Panel on Climate Change (IPCC TAR) (Houghton et al., 2001). These emission files include surface continental anthropogenic emissions, ship emissions, aircraft emissions and biomass burning emissions. The biomass burning emissions are a climatology of monthly biomass burning emissions calculated from the Global Fire Emissions Database (GFED) (van de Werf et al., 2006) (referred to in this thesis as the climatological emissions). Emissions of NO_x from lightning are coupled to convection in the model and therefore vary in space and time according to the seasonality and spatial pattern of convective activity (Stockwell et al., 1999). Biogenic isoprene and acetone emissions were taken from the POET inventory (Granier et al., 2005) which calculates emissions using a vegetation canopy model. Isoprene emissions are scaled according to the diurnal cycle online. Biogenic monoterpene emissions are not treated directly in the model, however, an additional 7 Tg of acetone is emitted to account for production from the oxidation of monoterpenes based on Jacob et al. (2002). Methane in the model is emitted and then scaled up to a global mean concentration of 1800 ppbv. This gives regional differences due to emissions whilst maintaining the concentration of methane globally. All emissions are read into TOMCAT on a $1°\times1°$ grid and are regridded within the model to the TOMCAT grid.

3.4.1 Anthropogenic and ship emissions

As part of this thesis, the anthropogenic emissions used in TOMCAT were updated. Two different datasets were implemented into TOMCAT and are described here. The first is a newly available inventory created for the IPCC Fifth Assessment Report (AR5) which gives an estimate of emissions for the year 2000 (Lamarque et al., 2010). The second inventory, Streets v1.2, was updated for

Table 3.2 Global annual total anthropogenic and natural emissions used in the TOMCAT model (in Tg(species)/yr)) from different inventories: AR5 anthropogenic only (1st column), Streets v1.2 anthropogenic only (2nd column), natural POET emissions only (3rd col.), AR5+POET (4th col.), Streets v1.2 + POET (5th col.) and the standard TOMCAT emissions prior to updates (TAR+Natural) (6th col.).

	Emissions (Tg(species)/yr)					
	Anthropogenic only		**Natural**	**Anthropogenic and Natural**		
Species	**AR5**	**Streets**	**POET**	**AR5+POET**	**Streets+POET**	**TAR+Natural**
NO_x	104.87	107.70	26.32	131.19	134.02	113.85
CO	609.46	595.08	180.40	789.86	775.48	567.52
C_2H_4	7.72	6.81	5.02	12.74	11.84	7.26
C_2H_6	3.33	6.34	1.01	4.34	7.35	6.56
C_3H_6	3.46	3.04	1.00	4.46	4.04	-
C_3H_8	4.03	5.68	1.83	5.86	7.50	7.67
C_4H_{10}	10.38	41.49	-	10.38	41.49	-
C_5H_8	-	-	536.79	536.79	536.79	568.66
C_7H_8	7.03	25.34	-	7.03	25.34	-
$C_{10}H_{16}$	-	-	81.68	81.68	81.68	-
CH_2O	3.18	2.99	-	3.18	2.99	0.75
CH_3OH	5.69	0.93	230.04	235.73	230.97	4.46
CH_3CHO	1.92	2.00	-	1.92	2.00	2.23
CH_3COCH_3	2.85	0.54	23.82	26.67	24.36	22.23

modelling studies associated with the POLARCAT campaign which took place in 2008 [4]. These datasets are described in more detail in Sections 3.4.1.1 and 3.4.1.2 and total annual emissions for all species are shown in Table 3.2. The distribution of annual emissions for CO and NO_x are shown in Figures 3.1 and 3.2 showing any regional differences.

3.4.1.1 IPCC Fifth Assessment Report emissions (AR5)

This dataset provides monthly mean estimates of emissions on a $0.5° \times 0.5°$ horizontal grid for the year 2000 and is described in detail by Lamarque et al. (2010). The ship emissions vary from month to month, although the land-based anthropogenic emissions do not. Regional inventories EMEP, EPA and REAS were used for Europe, North America and Asia, respectively. Where evaluated regional inventories were not available, the EDGAR-v4 global anthropogenic inventory was used. The anthropogenic emissions include contributions from the sectors shown in Table 3.3 and the ship emissions include fishing, international and domestic shipping. These emissions were downloaded in netcdf format from ftp://ftp-ipcc.fz-juelich.de/pub/emissions and processed them for TOMCAT. All the sectors in Table 3.3 and the ship emissions were added together for each species and regridded to $1° \times 1°$. In some cases, not all of the TOMCAT species

[4] http://www.cgrer.uiowa.edu/arctas/emission.html

Figure 3.1 Total annual anthropogenic and natural CO (Gg/yr) emissions from the standard model based on TAR (top, left), the Streets v1.2 2008 and POET inventories (top, right) and the AR5 2000 and POET inventories (bottom).

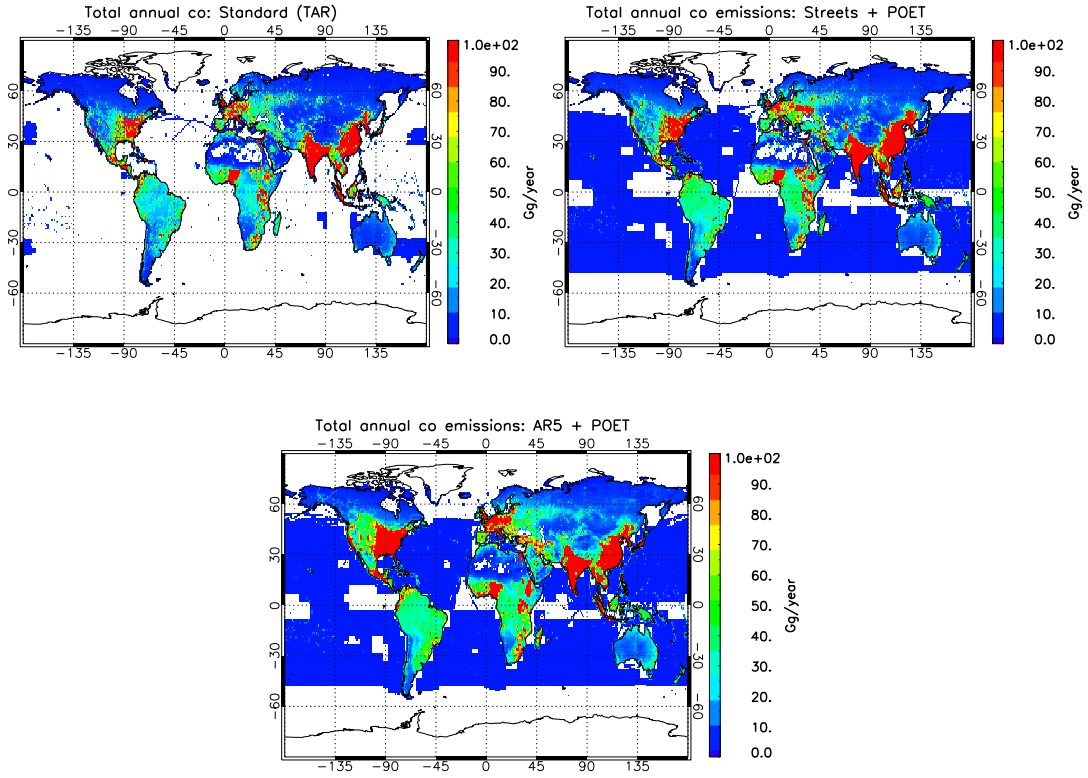

were available therefore lumped groups were used instead. This was the case for TOMCAT emitted species methanol, acetaldehyde and acetone, where the alcohols, alkanals and ketones IPCC lumped groups were used, respectively.

3.4.1.2 Streets v1.2 anthropogenic emissions

For the POLARCAT campaign, an inventory was created by David Streets[5] and Qiang Zhang[6] which consolidated emission estimates from the most up to date published regional inventories to account for regional changes in emissions, similar to that described in Zhang et al. (2009). The inventory uses CAC 2005, EMEP 2006 and USNEI 2002 for Canada, Europe and North America, respectively. Asian emission estimates are described by Zhang et al. (2009) based on the year 2006. Where regional datasets were not available or suitable the inventory uses the EDGAR v3.2 FT2000 global inventory which is scaled to the year 2000 from 1995 according to trends. The

[5] Argonne National Laboratory, US
[6] Argonne National Laboratory, US

Figure 3.2 Total annual anthropogenic and natural NO_x (Gg/yr) emissions from the standard model based on TAR (top, left), the Streets v1.2 2008 and POET inventories (top, right) and the AR5 2000 and POET inventories (bottom).

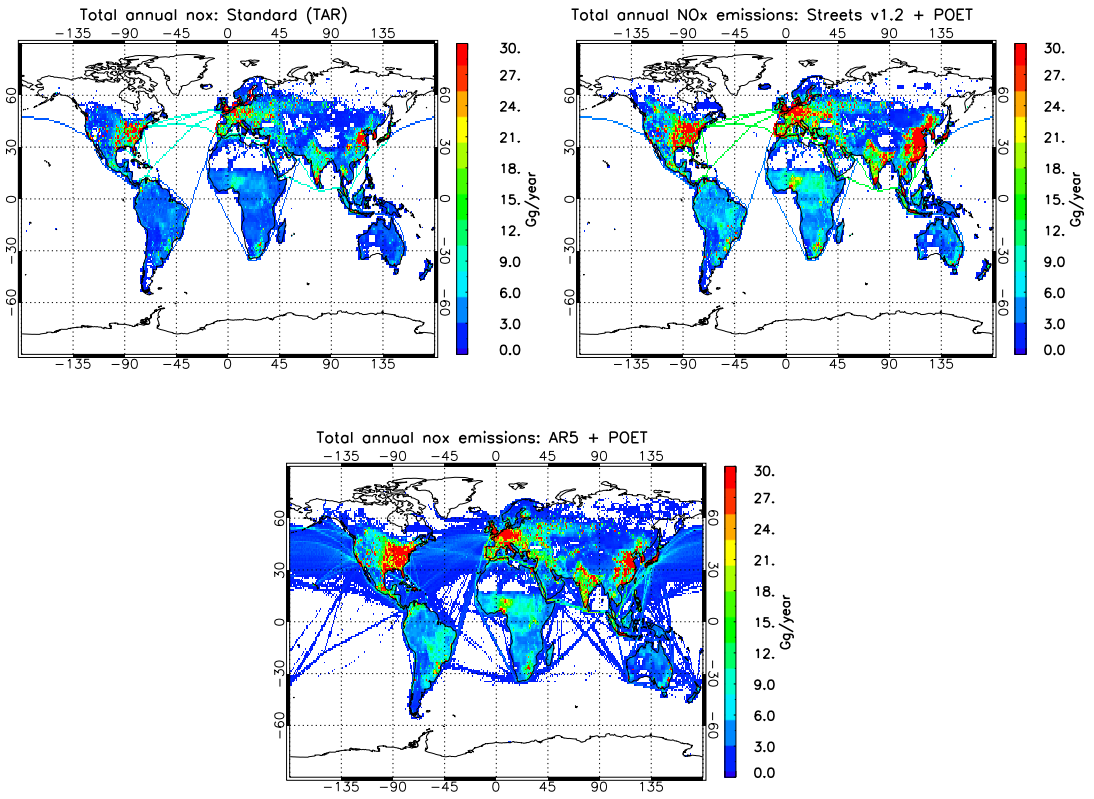

Streets v1.2 inventory is available for download[7] and provides emissions of CO, NO_x and VOCs. The VOCs were speciated by Louisa Emmons[8] according to the method used by Lamarque et al. (2010) for the AR5 emissions. These emissions were received from Emmons and formatted them for TOMCAT.

3.4.2 Natural emissions

Natural emissions account for a large quantity of trace gases found in the atmosphere (e.g., Guenther et al. (2006)). The AR5 and Streets v1.2 anthropogenic inventories therefore required natural emissions to be added to them. Emission estimates for natural sources such as NO_x from soils and CO from oceans were taken from the POET inventory (Granier et al., 2005). Isoprene and monoterpene emissions were calculated by the Model of Emissions of Gases and Aerosols from Nature (MEGAN) as described by Emmons et al. (2010). These were provided by Louisa Emmons

[7] http://www.cgrer.uiowa.edu/arctas/emission.html
[8] National Center for Atmospheric Research, USA

Table 3.3 List of anthropogenic sectors for AR5 anthropogenic emissions

Sector number	Sector name
1	Energy production
2	Industry
3	Land transport
4	Maritime transport
5	Aviation
6	Residential and commercial
7	Solvents
8	Agriculture
9	Agricultural waste burning on fields
10	Waste

Table 3.4 Global total CO biomass burning emissions for July 2008

	Emissions (Tg(species)/month)		
Species	**GFEDv2**	**GFEDv3**	**FINNv1**
CO	381.1	276.6	418.5

along with the Streets v1.2 emissions. Previously, TOMCAT did not include emissions of biogenic methanol which is believed to be a large source of carbon in the atmosphere (Jacob et al., 2005) and this was also added to the model.

3.4.3 Biomass burning emission inventories

Biomass burning emission estimates are commonly derived following the relationship described by Seiler and Crutzen (1980):

$$E = A \times B \times CE \times EF \tag{3.4}$$

where A is the area burned, B is the fuel loading (mass of biomass per unit area), CE is the combustion efficiency (ratio of biomass burnt to total available biomass), EF is the emission factor for the species in question (kg of species released per kg of dry matter (DM) burned). These parameters can be obtained from observational data, model data and laboratory experiments. All of the emission inventories used in this thesis were regridded to $1° \times 1°$ horizontal resolution and converted to molecules/cm^2 for use in this thesis. The total annual CO emissions for 2008 for each inventory are shown Table 3.4 and the distribution of emissions is shown in Figures 3.3.

Figure 3.3 Total CO biomass burning emissions (Tg(CO)/year) for 2008 from GFED v2 (top, left), GFED v3.1 (top, right) and FINN v1 (bottom).

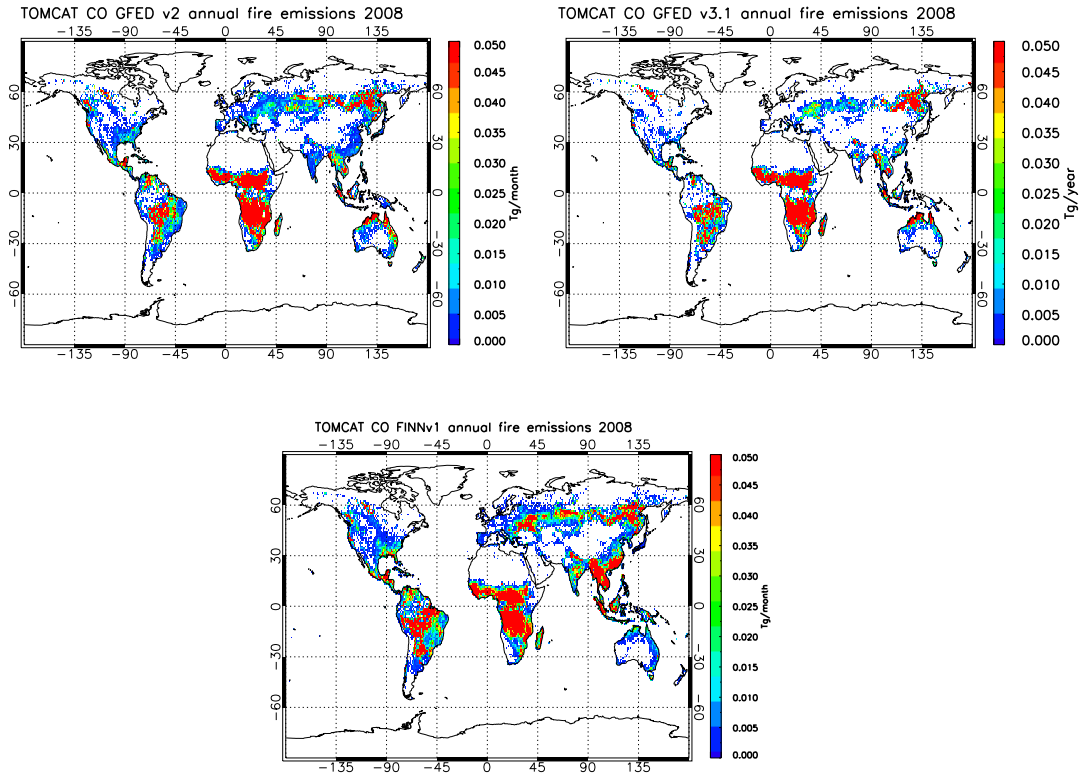

3.4.3.1 Global Fire Emission Database version 2 (GFED v2)

Version 2 of the Global Fire Emission Database (GFED v2) combines modelling tools and satellite data to estimate fire emissions. A detailed description of the dataset is given by van de Werf et al. (2006). Burned area was calculated from MODIS retrievals based on Giglio et al. (2006). Fuel loads were calculated by considering net primary productivity (NPP) and losses within a biogeochemical model. Combustion completeness was prescribed in their model and considered both seasonal effects and differences among fuel type based on observations. For this thesis, monthly mean carbon emission estimates on a $0.5° \times 0.5°$ horizontal resolution were downloaded from http://www.falw.vu/ gwerf/GFED/GFED2/. The carbon emissions were converted to dry matter burned by multiplying by 0.45, assuming carbon emitted was 45% of dry matter burned (DM) according to van de Werf et al. (2006), which was then use to calculate emissions for three different vegetation types. A vegetation map provided with the carbon emissions online allowed 3 types of forest to be distinguished; savannah/grasslands, temperate forest and boreal forest. After DM was calculated it was then multiplied by emission factors (shown in Table 3.5) to get emissions for the species emitted in TOMCAT. The emissions factors are based on Andreae and Merlet

Table 3.5 Emission factors for different vegetation types used to calculate GFED v2 emissions.

Species	Emissions Factors (g/kg DM)		
	Savannah/Grasslands	Tropical Forest	Extratropical Forest
NO_x	2.12	2.26	3.41
CO	61.5	100.9	105.6
C_2H_4	0.82	1.48	1.18
C_2H_6	0.32	1.12	0.72
C_3H_6	0.34	1.14	0.57
C_3H_8	0.09	1.04	0.27
C_4H_{10}	0.025	0.056	0.128
C_5H_8	0.026	0.218	0.103
C_7H_8	0.177	0.241	0.403
$C_{10}H_{16}$	0.014	0.000	0.223
CH_2O	0.71	2.22	2.155
CH_3OH	1.47	2.95	1.88
CH_3CHO	0.5	2.26	0.979
CH_3COCH_3	0.48	0.63	0.673

(2001) but were updated in 2008 by Andreae Merlot[9], provided by Guido van de Werf[10].

3.4.3.2 Global Fire Emissions Database version 3 (GFED v3.1)

GFED v3.1 uses the same method and model as GFED v2 to derive carbon emission estimates. However, some minor differences do exist and are described by van de Werf et al. (2010), the main one is the use of updated burned area estimates (Giglio et al., 2010). Giglio et al. (2010) compared GFED v3 area burned estimates to GFED v2 and found they increased by about 15% when averaged globally, with some substantial regional differences ($>$50%). Europe area burned is substantially lower whereas Middle East area burned is substantially higher compared to GFED v2. They also show that when they compare GFED v3.1, GFED v2 and other area burned estimates to independent observational area burnt data for USA and Canada, GFED v3.1 has the highest correlation, giving a higher confidence in the newer version. Another development in GFED v3.1 dataset now means that emissions are estimated for six different fires types; Savannah, woodland, deforestation, forest, agriculture and peat. The dominant fire type in each 0.5°$\times$0.5° grid-box is shown in Figure 3.4.

[9]Max Planck Institute for Chemistry, Mainz, Germany.
[10]VU University (Vrije Universiteit), Amsterdam, Netherlands.

Figure 3.4 The dominant fire type in each 0.5°×0.5° grid-box in the GFED v3.1 fire emissions inventory taken from van de Werf et al. (2010).

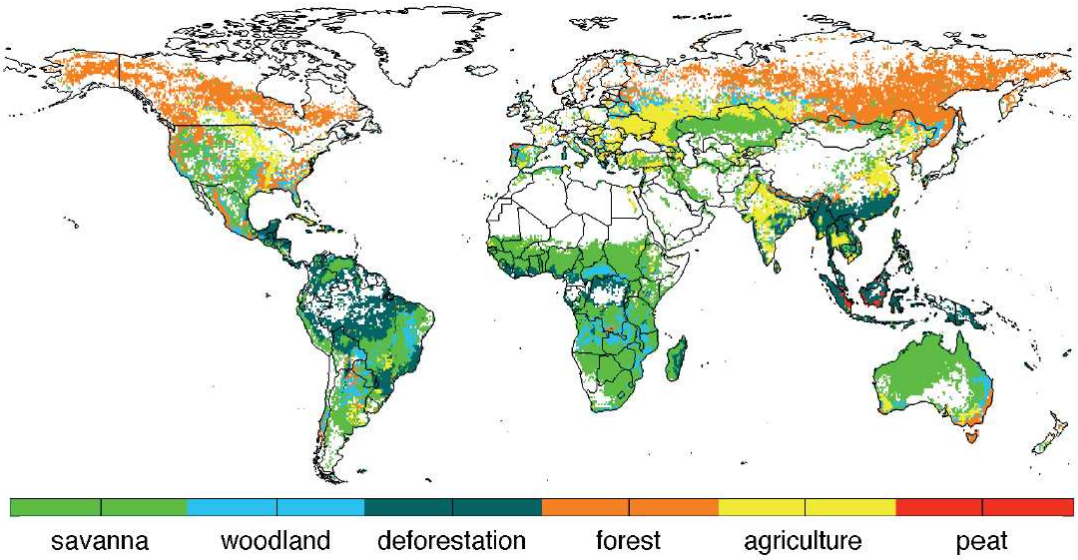

3.4.3.3 FINN v1 inventory

The FINN dataset was first described and used in Wiedinmyer et al. (2006). MODIS Fire and Thermal Anomalies Product (Giglio et al., 2003) were used to identify fire locations which use both MODIS sensors onboard two polar orbiting satellite platforms, Aqua and Terra. Each provides daily thermal observations over nearly the entire globe on both daytime and nighttime passes. Satellite datasets which identify land use, vegetation types, and percentage vegetative cover were used in combination with available regional data to assign fuel loadings for pixels in which fires were identified. Land cover was assigned by the Global Land Cover Dataset for 2000 (GLC2000) which gives 29 land cover types, emission factors for each of these types were assigned based on the currently available estimates in the literature (Wiedinmyer et al., 2006). An updated version of this inventory was created for the POLARCAT campaign at a daily temporal resolution (Wiedinmyer et al., 2011) and is used for this thesis. The inventory was processed by Louisa Emmons and formatted for use in TOMCAT as part of the work for this thesis.

3.4.4 Summary

In this chapter the standard version of the TOMCAT chemical transport model has been described. As part of this thesis several developments have been implemented into the model to better simulate the troposphere. The new extended hydrocarbon chemistry scheme has been described, now including ethene, propene, butane and toluene emissions. Natural monoterpene emissions and

chemistry have also been included explicitly. A scheme for uptake of N_2O_5 onto aerosol has been adapted for the purposes of this thesis. The impacts of these updates have been tested and are discussed in Chapter 4. The standard emission inventories have also been updated with natural emissions from methanol are now included along with the implementation of two new anthropogenic inventories (Streets v1.2 and AR5) and three new biomass burning emission inventories. These new inventories are used throughout this thesis for simulations with the TOMCAT model.

Chapter 4

TOMCAT model development and evaluation

4.1 Introduction

First simulations of the standard version of the TOMCAT model performed for this thesis showed that the model underestimated tropospheric CO in the Northern Hemisphere (NH). In-situ chemical production is an important source of CO accounting for approximately 50% of the total global tropospheric source (Hauglustaine et al., 1998; Bergamaschi et al., 2000; Ehhalt et al., 2001; Duncan et al., 2007). Oxidation of industrial non methane hydrocarbons (NMHC) has been estimated to contribute up to 14% (203 Tg(CO)/yr) to this global production of secondary CO, which is 7% of the total global source (Bergamaschi et al., 2000). The major anthropogenic emission regions are located in the NH and therefore emissions of hydrocarbons that are not accounted for in the standard version of the TOMCAT model would lead to an underestimation in the production of secondary CO in this region, contributing to the NH underestimate. As CO is used as a tracer of anthropogenic and natural sources in this thesis, this underestimate was partly addressed by developing the TOMCAT model to account for some of the missing sources of carbon by including additional NMHC emissions and subsequent chemical processing. Anthropogenic sources of ethene, propene, butane and toluene have been implemented in this work and contribute an additional 28.6 Tg(C)/yr on top of the already emitted 21.0 Tg(C)/yr of NMHC, increasing the total mass of carbon from anthropogenic NMHC emissions by 136%. Emissions of monoterpenes from vegetation are another important source of carbon. Most emissions occur in the tropics due to the high temperatures and abundance of vegetation, however, they are also emitted during the summer in the mid-northern latitudes and boreal regions and therefore could be important in the NH. Bergamaschi et al. (2000) estimated that oxidation of terpenes (including monoterpenes) can contribute up to 10% (136 Tg(CO)/yr) to secondary CO and 5% to the total global sources of CO. By

adding natural monoterpene emissions, which emit an extra 72 Tg(C)/yr, along with natural emissions for the new organic species, ethene and propene, which emit 5.2 Tg(C)/yr, the total carbon natural emissions in TOMCAT are increased by 13.4%.

It is well established that the heterogeneous uptake of N_2O_5 by aerosols is a major atmospheric sink of NO_x in the troposphere (Ravishankara, 1997; Jacob, 2000; Tie et al., 2001). This reaction is significant at night when there is no sunlight for the photolysis of NO_3 making it possible for it to react with NO_2 to form N_2O_5. This reaction is therefore particularly significant in the polar regions during the long dark winter period, causing very low concentrations of NO_x (Tie et al., 2003). Modelling has shown that the inclusion of this reaction in a global 3D CTM can reduce NO_x and O_3 burdens by up to 50% and 9%, respectively (Dentener and Crutzen, 1993), showing that this reaction has important implications for tropospheric composition. As the focus of this thesis is on Arctic composition, the TOMCAT model has been developed to include the hydrolysis of N_2O_5 to simulate O_3 and NO_x in this region more accurately.

As part of this thesis, these two updates have been developed and tested. The impact of these updates on simulated tracer burdens and distributions are discussed in Section 4.3. Global mean OH is assessed as an indicator of the model's oxidising capacity in Section 4.4. The model is then compared to observations to see whether the developments have improved the simulation of trace gases. The ability of the model to simulate CO is discussed in Section 4.5 with the aid of retrievals of CO from the satellite instrument MOPITT and also in comparison to surface station observations. Ozone and some reactive nitrogen and NMHC species are then also compared in Sections 4.6-4.8. The overall findings from this chapter are then summarised in Section 4.9

4.2 Model setup

Three simulations were performed to assess the impact of the new extended organic chemistry and the uptake of N_2O_5 by aerosol. These are summarised in Table 4.1. The CTRL simulation was performed using the basic setup of the 'standard' version of the TOMCAT model as described in Chapter 3, without the new organic and heterogeneous chemistry, but with updated emissions. The NEWC simulation uses the same set-up as the CTRL simulation but includes the new organic chemistry (see Section 3.3.2). The HETC simulation includes both the new organic chemistry and the heterogeneous uptake of N_2O_5 by aerosol. A more detailed description of the treatment of N_2O_5 hydrolysis in TOMCAT is given in Section 3.3.3. For each simulation, TOMCAT was spun-up for 1 year and then run for the whole of 2008 using ECMWF ERA-40 winds. The IPCC AR5 anthropogenic emissions, POET natural emissions and GFED v2 monthly mean biomass burning emissions for 2008 were used for these simulations as they offered an improved surface flux estimate compared to what was previously used in the standard version of the model. These

Table 4.1 Summary of model simulations

Simulation ID	Description	Emissions
CTRL	Control simulation	AR5 anthropogenic emissions, POET natural emissions, GFED v2 2008 biomass burning emissions.
NEWC	Additional hydrocarbon and monoterpene emissions and chemistry.	AR5 anthropogenic emissions, POET natural emissions, GFED v2 2008 biomass burning emissions.
HETC	Same as NEWC but with heterogeneous uptake of N_2O_5 on black carbon, organic carbon, dust, sulphate and seasalt. (dust $\gamma = 0.02$).	AR5 anthropogenic emissions, POET natural emissions, GFED v2 2008 biomass burning emissions.

emissions were updated for the purpose of this thesis and are described in more detail in Section 3.4. For the year 2008, model output was saved every 3.75 days, giving output at 00:00, 06:00, 12:00 and 18:00 UTC from which monthly means were calculated.

4.3 Impact of extended hydrocarbon chemistry and uptake of N_2O_5 by aerosol

4.3.1 Changes in global mean burdens

The global monthly mass burdens from each of the simulations have been calculated for CO, O_3, HO_x, HNO_3, PAN, NO_y and NO_x and are shown in Figure 4.1. The percentage difference for these species between NEWC and CTRL and HETC and NEWC are shown in Figure 4.2. Considering the difference between NEWC and CTRL isolates the impact of the addition of new organic chemistry. CO is increased by 4-5% (14-18 Tg) from the CTRL to the NEWC simulation due enhanced secondary production of CO from the oxidation of additional hydrocarbons in NEWC. The biggest increase is observed in NH summer/autumn due to the higher rates of photochemistry. Ultimately, the additional NMHC and CO lead to more O_3 production and therefore the total mass burden is increased by 2-4% (8-11 Tg). The total mass burden of OH does not seem to be largely affected by the increased burden of NMHC. By considering the percentage difference in Figure 4.2, it can be seen that OH is not affected in January and February. This is because the majority of the anthropogenic emissions occur in the NH, where OH concentrations are already very low at this time of the year with reduced rates of oxidation of NMHC. As the concentrations of OH in the

Figure 4.1 Monthly mean total tropospheric mass burdens (Tg) of CO, O_3, OH, HO_2, HNO_3, PAN, NO_y, NO and NO_2 from the CTRL, NEWC and HETC simulations.

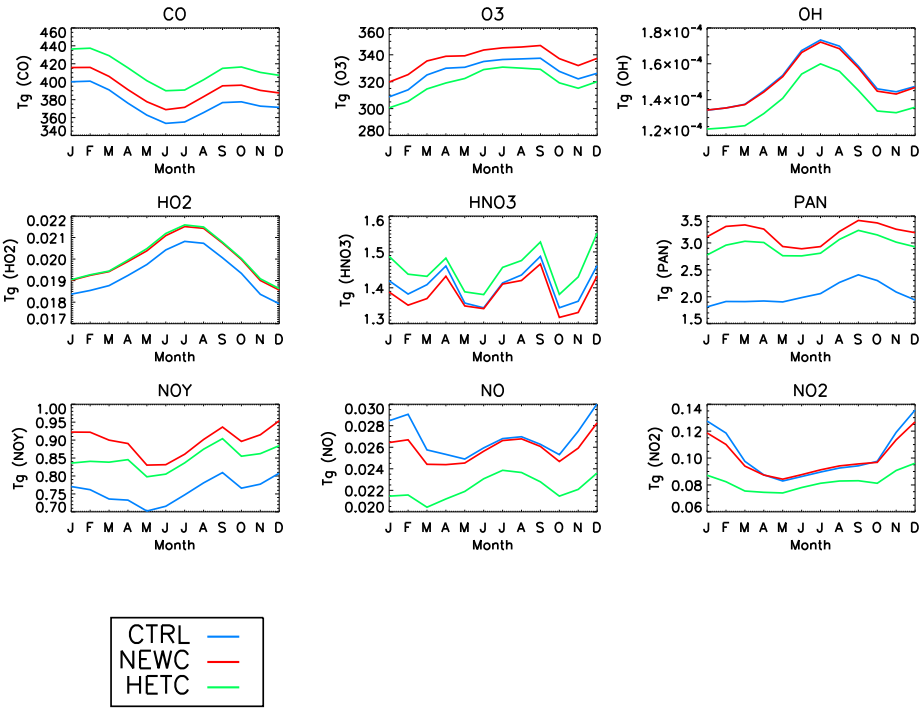

Figure 4.2 Percentage difference in monthly mean total tropospheric mass burdens of CO, O_3, OH, HO_2, HNO_3, PAN, NO_y, NO and NO_2 from NEWC-CTRL and HETC simulations.

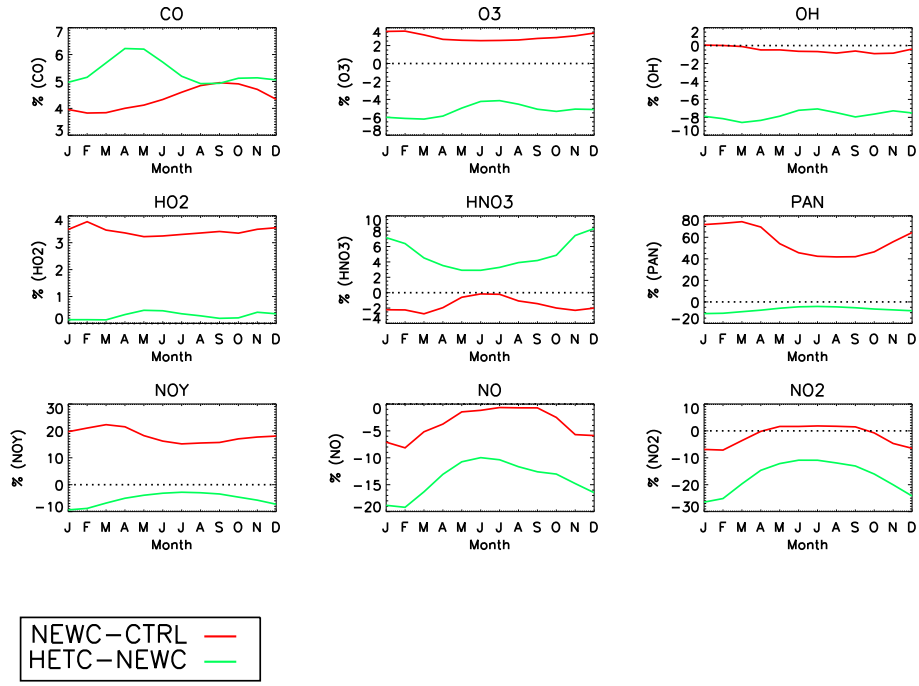

NH increase towards summer, OH is reduced by up to 1% in NEWC due to reaction with the additional hydrocarbons and CO. Conversely, HO_2 is increased by 3-4% due to the oxidation pathways of the additional hydrocarbons resulting in more formaldehyde and HO_2 production (see Section 2.4). Formaldehyde can also go on to yield another HO_2 molecule (Jacob, 1999a), boosting the oxidising capacity of the atmosphere by an overall increase in HO_x (see Section 4.3.2). One of the most significant impacts of the organic chemistry is upon the formation of PAN. The total mass burden of PAN is increased by 40-75% with the biggest increase occurring during the NH winter when the thermal decomposition of PAN is slower due to the lower temperatures. The total PAN is more sensitive to the NH winter because of larger concentrations of NO_x in the NH. This large increase in PAN occurs because the new organic chemistry scheme includes many more pathways which lead to the production of CH_3CO_3 which reacts with NO_2 to form PAN. Due to the oxides of nitrogen, NO and NO_2, being locked up in this reservoir species, HNO_3, NO and NO_2 are all reduced by up to 3%, 8% and 7%, respectively. HNO_3 is efficiently wet deposited due its high solubility and therefore acts as a sink of reactive nitrogen from the atmosphere. As more NO_x forms PAN instead of HNO_3, the total global burden of total reactive nitrogen, NO_y, is increased by 11-17%. In the NH summer, NO_2 increases by up to 2% relative to the CTRL simulation due to the breakdown of PAN which releases NO_2. This increase in NO_2 could also contribute to the extra formation of O_3 that is modelled.

Figures 4.1 and 4.2 also show the impacts of the heterogeneous uptake of N_2O_5 by aerosol by comparing HETC and NEWC. As expected, NO_x is affected quite significantly, with NO and NO_2 being reduced by 10-20% and 10-27%, respectively. In agreement with previous studies (Dentener and Crutzen, 1993; Tie et al., 2003), the biggest reductions occur in January and February where the total NO_x burden is reduced by up to 46%. The smallest difference occurs in June when NO_x is reduced by 20%. This is because the conversion of NO_x to HNO_3 by reaction 2.7-2.9 is important during darkness and at low temperatures making this efficient in the NH winter where there are also high concentrations of NO_x. Due to this new pathway, the global burden of HNO_3 increases by 3-8%, with the biggest increases occurring in winter. As more NO_x is being converted to HNO_3, PAN shows a reduction of 4-11%, also with the biggest reduction in winter. As the formation of HNO_3 acts as a sink of NO_x from the atmosphere, overall, NO_y is reduced by up to 10% in winter. As NO_x controls the production of O_3 in the troposphere, the total burden of O_3 is also reduced by 4-6%. The maximum reduction occurs in March and the minimum in July, similar to the findings of Tie et al. (2003). The biggest reduction of O_3 does not coincide with the biggest reduction in NO_x. In the NH in January and February the lack of sunlight would slow O_3 production and therefore the impact on O_3 through NO_x would not be seen until spring (Tie et al., 2003). As OH is formed from the photolysis of O_3, the burden of OH is also lowered by 7-8%. Due to a smaller global OH burden, CO has a longer lifetime increasing the global burden by 5-6%. Overall, the N_2O_5 hydrolysis results in the annual mean burdens of NO_x, O_3 and OH being reduced by 30%, 6% and

8%. The response in NO_x and O_3 are slightly smaller compared with Dentener and Crutzen (1993) who found a 50% and 9% reduction in NO_x and O_3 respectively, however, a similar reduction of OH of 9% was observed. The percentage differences of burdens calculated by different models are likely to be sensitive to the treatment of other processes and initial burdens of the aforementioned species therefore the different percentage difference may reflect this. In general, the TOMCAT model captures the response of NO_x, O_3 and OH in agreement with previous studies (Dentener and Crutzen, 1993; Jacob, 2000; Tie et al., 2001, 2003).

4.3.2 Changes in the distributions of species

The seasonal zonal mean volume mixing ratio of CO from the CTRL simulation for DJF, MAM, JJA and SON are shown in Figure 4.3. There is a clear inter-hemispheric difference due to larger emissions in the NH. The CO concentrations also decrease with increasing altitude as the distance from the surface fluxes increases. In the NH, the seasonal maximum and minimum of CO occur in DJF and JJA, when OH concentrations are at their lowest and highest, respectively. The seasonal cycle is not as distinct in the SH as it is in the NH, but it is still visible, with a maximum in JJA and a minimum in DJF. The absolute and percentage difference in CO from NEWC compared to CTRL are also shown in Figure 4.3. Including the additional hydrocarbon emissions and chemistry increases the background CO by 1-5 ppbv (2-5%) in the SH and up to 5-9 ppbv (2-10%) in the NH. There is a larger impact on CO in the NH due to the location of the source regions. The largest seasonal difference occurs during SON, in agreement with Figure 4.2, due to an increase in secondary production of CO from the oxidation of hydrocarbons. In late summer and early autumn biogenic emissions peak, driving the seasonal maximum response in CO. The absolute and percentage difference between the HETC and the NEWC simulations are also shown in Figure 4.3. Similar to the NEWC simulation, the largest increases occur in the NH.

Figure 4.4 shows the seasonal zonal mean concentrations of O_3 from the CTRL simulation. As with CO, there is a gradient between the two hemispheres due to more NMHC and NO_x emissions in the NH which are precursors of O_3. Unlike CO, the mixing ratio of O_3 increases with altitude. As emissions are transported away from the surface they begin to produce O_3. Also, near the tropopause, the influence of stratospheric-tropospheric exchange (STE) can be seen. The seasonal maximum of O_3 occurs in MAM in the NH, thought to be due to an increase in photochemical production (Monks, 2000; Atlas et al., 2003). The absolute and percentage difference in O_3 from NEWC compared to CTRL are also shown in Figure 4.4. As seen in Section 4.3.1, O_3 is increased by 1-4 ppbv (3-9%) in the NH troposphere. The SH is not largely affected (less than 1 ppbv difference) by the increase in NMHC due to lower anthropogenic emissions. The absolute and percentage difference between the HETC and the NEWC simulations are also shown in the third and bottom panel of Figure 4.4. As found in Section 4.3.1 ozone is decreased by the inclusion

Figure 4.3 Zonal mean seasonal CO absolute concentrations (ppbv) from the CTRL simulation (top row), absolute differences from NEWC-CTRL (ppbv) (second row), absolute differences from HETC-NEWC (ppbv) (third row), percentage differences from NEWC-CTRL (%) (fourth panel down) and percentage differences from HETC-NEWC (%) (bottom row).

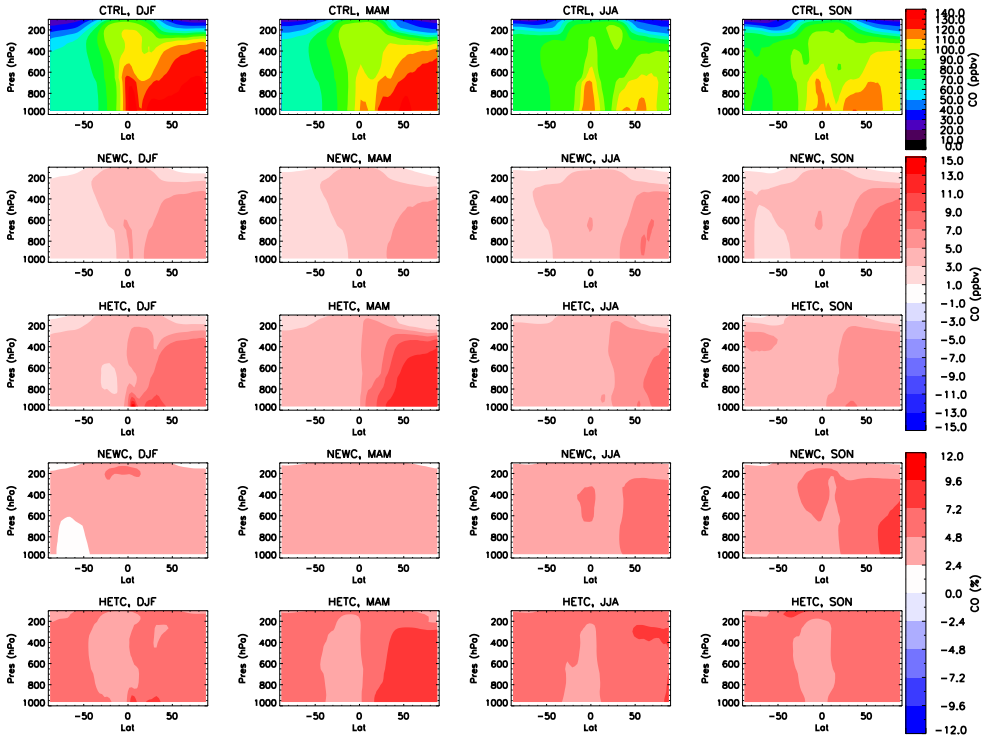

Figure 4.4 As Figure 4.3 but for O_3 (ppbv).

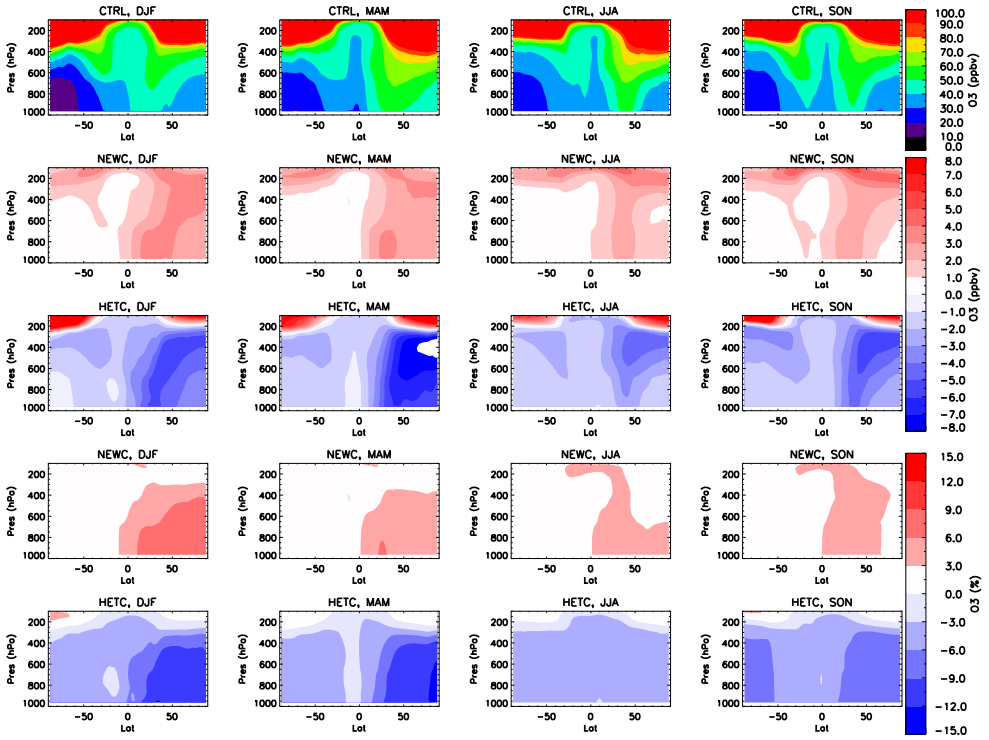

of the hydrolysis of N_2O_5 which reduces NO_x and therefore O_3 production. The biggest impact is in the NH in MAM due to the higher concentrations of NO_x in this region. However, the SH also shows a reduction in O_3 throughout the year due to the presence of aerosols, with a maximum reduction in SON during the biomass burning season.

Figure 4.5 shows the seasonal zonal mean concentrations of NO_x (NO + NO_2) from the CTRL simulation. The largest concentrations of NO_x are seen in the NH lower troposphere near large anthropogenic emission regions. The SH has very low background concentrations with larger concentrations occurring in JJA and SON during biomass burning seasons. As the lifetime of NO_x is shorter than CO, it is much less well-mixed, leading to strong concentration gradients. The stratosphere also has very high concentrations of NO_x, which acts as a source to the upper troposphere. The absolute and percentage difference in NO_x from NEWC compared to CTRL are also shown in Figure 4.5. The addition of new NMHC emissions result in a decrease in NO_x by up to 90 pptv, with the maximum effect occurring in the NH during winter. As mentioned in Section 4.3.1 this is because of the increased formation of PAN which is more stable in winter. These reductions are confined to the regions of maximum concentrations of NO_x near the surface in the NH. The percentage difference shows a different pattern to the absolute changes, with a maximum winter reduction in NO_x of 40% at 400 hPa instead of the surface. This is due to much lower background concentrations in this region, meaning a smaller absolute change can result in a larger percentage difference.

Figure 4.5 also shows the absolute and percentage difference in HETC compared to NEWC. N_2O_5 uptake reduces NO_x by more than 150 pptv near the major emission regions with the biggest impact occurring in DJF. The smallest impact occurs in JJA where a maximum of 70 pptv is lost at the surface in the NH. As with the NEWC simulation, the maximum percentage differences occur at higher altitudes due to the low concentrations, with NO_x being $>$70% lower than in NEWC. HETC shows that N_2O_5 uptake also occurs in the SH and explains the loss of O_3 in HETC in the same region which was seen in Figure 4.4. The maximum impact occurs in MAM with up to 60% of NO_x being lost. Again, the percentage and absolute difference show different patterns.

The seasonal zonal mean HO_x (OH + HO_2) from the CTRL simulation is shown in Figure 4.6. The distribution of HO_x is related to the amount of incoming solar radiation. Therefore the tropics have the highest concentrations and the maximum is centred either south or north of the equator depending on the season. The maximum concentrations occur in the NH in JJA due to the larger concentrations of O_3 in this region which is the main source of OH. The absolute and percentage difference in HO_x in NEWC compared to CTRL are also shown in Figure 4.6. The addition of NMHC increases HO_x by up to 0.4 pptv mostly between 50°S and 70°N. In JJA, the increase in HO_x is shifted to between 30°S and 90°N when photochemistry is more active in the NH. From Figure 4.2 it is known that this increase in HO_x is mostly due to an increase in HO_2 from the

Figure 4.5 Zonal mean seasonal NO_x absolute concentrations (pptv) from the CTRL simulation (top row), absolute differences from NEWC-CTRL (pptv) (second row), absolute differences from HETC-NEWC (pptv) (third row), percentage differences from NEWC-CTRL (%) (fourth row) and percentage differences from HETC-NEWC (%) (bottom panel).

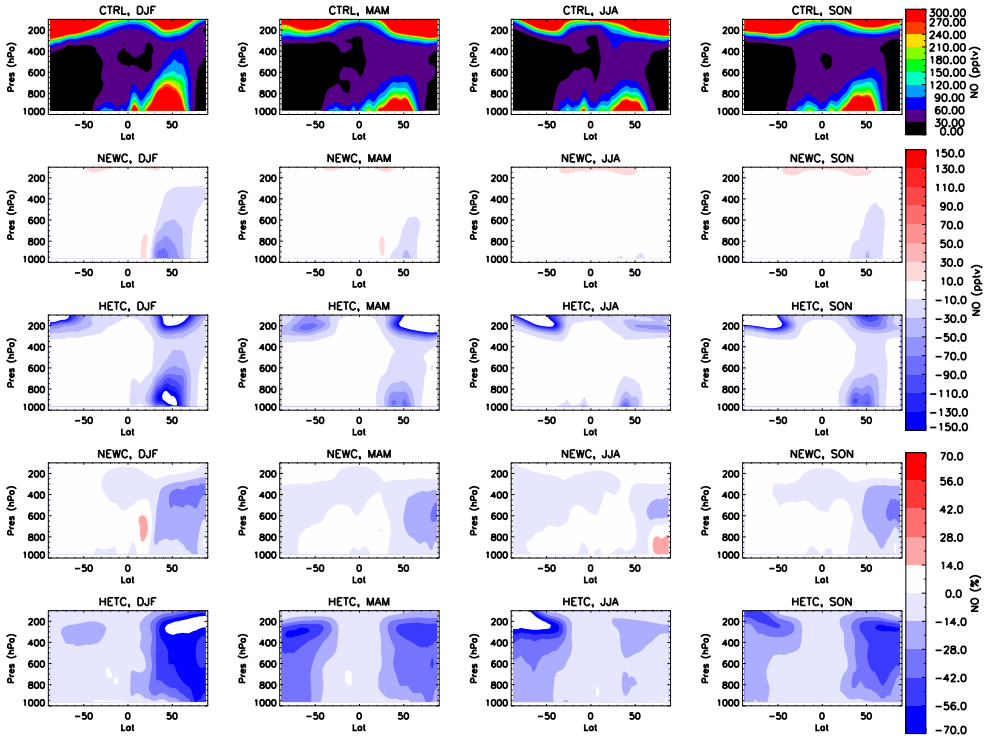

Figure 4.6 As Figure 4.3 but for HO_x (pptv).

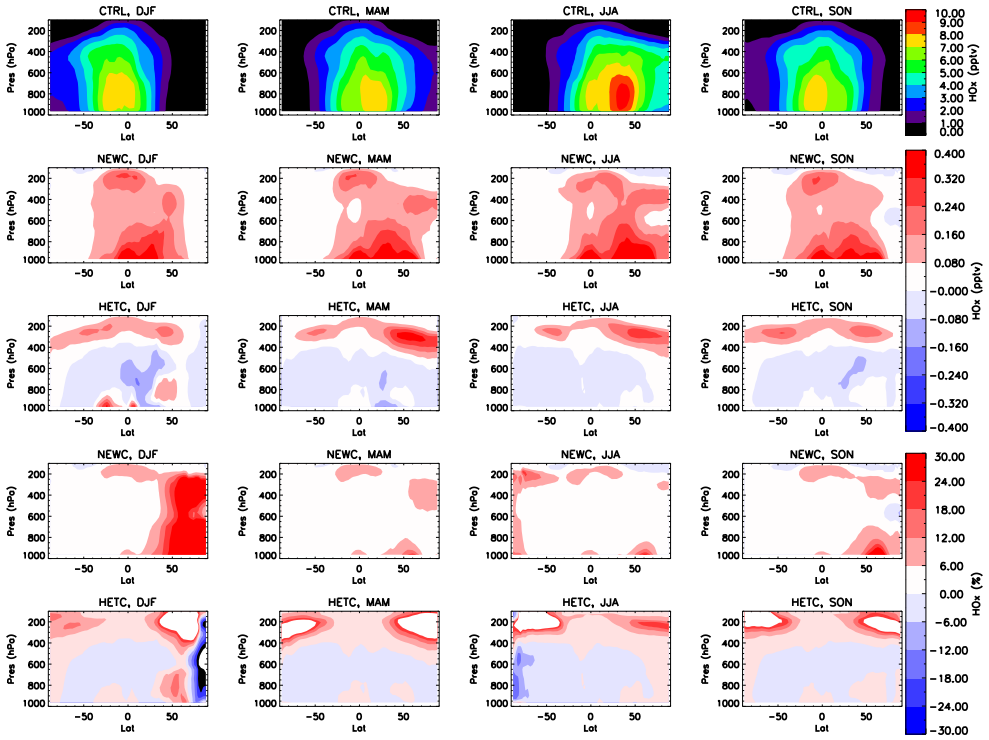

oxidation of NHMC and CO. As with NO_x, the biggest percentage difference occurs in a different location to the maximum absolute difference due to the low background concentrations. For HO_x, NEWC shows the largest percentage difference in the high northern latitudes during winter where concentrations are increased by up to 30%. The absolute and percentage difference in HO_x in HETC compared to NEWC are also shown in Figure 4.6. N_2O_5 hydrolysis has a more spatially complicated affect on HO_x. In DJF, regions between 50°S and 50°N show different responses in HO_x because OH is decreased, due to less O_3, whilst HO_2 is increased (not shown). The total HO_x response therefore depends on the magnitude of changes in the OH and HO_2 concentrations. In other seasons, the overall affect of N_2O_5 uptake by aerosol is to lower HO_x by up to 0.16 pptv.

Overall, the addition of the NMHC and N_2O_5 hydrolysis has been shown to have substantial impacts on the troposphere. However, as yet it is unknown whether these changes discussed here actually improve the simulated tracers. For this reason, it is now important to compare these three simulations to observations.

4.4 Evaluation of simulated hydroxyl radical

The hydroxyl radical (OH) is the primary oxidant in the troposphere and therefore it is a useful measure of the oxidising capacity of chemical transport models. Due to its very short lifetime, OH is very difficult to measure (Heard and Pilling, 2003). However, it can be inferred from gases whose primary loss channel is through reaction with OH if the sources are well understood. In this section OH simulated by TOMCAT is compared to global OH estimated by this method.

4.4.1 Calculation of global mean OH

As recommended by Lawrence et al. (2001), the tropospheric global mean OH concentration has been calculated, weighted by airmass ($[OH]_M$) and the methane reaction rate ($[OH]_{CH_4}$), for CTRL, NEWC and HETC. $[OH]_M$ is generally considered as an indicator of the oxidising capacity of the atmosphere for a uniformly distributed gas whose reaction with OH is not dependent on temperature and pressure (Lawrence et al., 2001). The $[OH]_{CH_4}$ considers the distribution of OH, giving more weight to areas of high temperatures due to the temperature dependence of the reaction rate. These different measures can be found in the literature for comparison to other models.

Firstly, the airmass-weighted OH concentration was calculated from:

$$[OH]_M = \frac{\sum(M \cdot [OH])}{\sum M}, \tag{4.1}$$

where M is the mass of each grid box and the sum is over the whole of the troposphere. Secondly, the global mean methane-reaction-weighted OH concentration was calculated by:

$$[OH]_{CH_4} = \frac{\sum(k \cdot M \cdot [CH_4] \cdot [OH])}{\sum(k \cdot M \cdot [CH_4])}, \tag{4.2}$$

where, k=1.85$\times 10^{-12}$exp$^{(-1690/T)}$, which is the reaction rate of methane with OH used by the TOMCAT model taken from IUPAC[1]. The monthly mean temperature from the model was used to calculate k. The lifetime of methane (τ_{CH_4}) is inversely proportional to methane-reaction-weighted OH concentration (Lawrence et al., 2001) and is therefore equal to:

$$\tau_{CH_4} = \frac{\sum(M \cdot [CH_4])}{\sum(k \cdot M \cdot [CH_4] \cdot [OH])}. \tag{4.3}$$

For these calculations, the tropopause was defined in two ways. The first method used the TOMCAT potential vorticity (PV) and potential temperature (θ) to find grid boxes located within the troposphere which was defined as the region where PV is between -2 and 2 pvu and θ is less than 380 K following the method of Arnold et al. (2005). The second method used a climatological tropopause as recommended by Lawrence et al. (2001) which was calculated as follows:

$$\rho_{cli} = 300 - 215(cos(\phi))^2, \tag{4.4}$$

where ϕ is the latitude and ρ is the pressure.

4.4.2 Comparisons of global mean OH with previous studies

The annual mean values of [OH]$_M$, [OH]$_{CH_4}$ and τ_{CH_4} have been calculated for simulations CTRL, NEWC and HETC and are shown in Table 4.2. Using the climatological tropopause yields a lower [OH]$_M$ compared to using the PV and θ model fields to define the tropopause, however, there is little difference in the [OH]$_{CH_4}$. This is because the [OH]$_{CH_4}$ is more sensitive to OH concentrations in the lower troposphere in the tropics as this is where the majority of methane is oxidised (Lawrence et al., 2001; Bloss et al., 2005), making the tropopause height less important. This is also the case with the methane lifetime as this is derived from [OH]$_{CH_4}$.

Studies by Krol et al. (1998) and Prinn et al. (2001) used observed concentrations of methyl chloroform (CH_3CCl_3), whose main sink is reaction with OH, to infer global mean OH. Krol et al. (1998) estimated OH to be in the range of 0.9 - 1.16$\times 10^6$ molecules/cm^3 and Prinn et al. (2001)

[1] http://www.iupac-kinetic.ch.cam.ac.uk/

estimated an airmass-weighted mean of 0.94 x 10^6 molecules/cm^3. Spivakovsky et al. (2000) derived a global mean airmass-weighted OH of 1.16 x 10^6 molecules/cm^3 using a photochemical box model which used observed concentrations of O_3, H_2O, NO_y, CO, hydrocarbons, temperature and cloud optical depth. The global mean $[OH]_M$ from CTRL and NEWC of 0.93 x 10^6 and 0.92 x 10^6 molecules/cm^3, respectively (see Table 4.2), are both within the range of these studies. The significant decrease of OH in HETC, due to the loss of NO_x (see Section 4.3), reduces the global mean $[OH]_M$ to 0.85 x 10^6 molecules/cm^3 (see Table 4.2), which is lower than any of these estimates. The global mean $[OH]_{CH_4}$ for the CTRL and the NEWC simulation are similar with 1.16 x 10^6 molecules/cm^3 suggesting the distribution of OH does not vary greatly between these two simulations which is in agreement with what was found in Section 4.3.1. Again, the global mean $[OH]_{CH_4}$ of 1.08 $\times$ 10^6 molecules/cm^3, calculated from HETC, is smaller than the values from CTRL and NEWC. The corresponding lifetime of methane is 8.55, 8.55 and 9.18 years from the CTRL, NEWC and HETC simulations, respectively (see Table 4.2). From Krol et al. (1998) and Prinn et al. (2001) the lifetime of CH_4 is estimated to be within the range of 8.6–10.12 years. The τ_{CH_4} calculated from the HETC simulation gives a better estimation of the methane lifetime even though the $[OH]_M$ is out of the estimated range. This is because τ_{CH_4} is dependent on the distribution of OH due to the temperature dependence of the reaction of CH_4 with OH, meaning HETC may have a more reasonable distribution of OH in regions dominating CH_4 oxidation compared to CTRL and NEWC, even though the global mean OH is lower.

To evaluate the global OH distribution, the tropospheric OH has been divided up into 12 separate domains, extending from the surface up to 250 hPa, as recommended by Lawrence et al. (2001). Figure 4.7 shows annual zonal means of OH separated into these domains calculated from the TOMCAT CTRL, NEWC and HETC simulations. In general, the NEWC and CTRL simulations show very similar distributions of OH with NEWC having slightly smaller concentrations in the upper troposphere and slightly higher concentrations in the lower troposphere. HETC showed the largest difference in the global mean OH concentration compared to CTRL (see Table 4.2) and therefore, as expected, the distribution of OH does vary from NEWC and CTRL, with concentrations in all domains becoming lower.

Table 4.2 TOMCAT global annual mean OH concentrations ($\times 10^6$ molec/cm^3) weighted by mass, weighted by reaction with CH_4 and the lifetime of CH_4 (yrs) from CTRL, NEWC and HETC.

	TOMCAT Trop.			Climatological Trop.		
Model Simulation	**[OH]**$_M$	**[OH]**$_{CH_4}$	τ_{CH_4}	**[OH]**$_M$	**[OH]**$_{CH_4}$	τ_{CH_4}
CTRL	0.9310	1.1647	8.55	0.9064	1.1551	8.96
NEWC	0.9276	1.1640	8.55	0.9035	1.1545	8.96
HETC	0.8579	1.0841	9.18	0.8352	1.0751	9.62

Figure 4.7 Annual zonal mean of OH (in molecules/cm^3) separated into 12 sub domains as suggested by Lawrence et al. (2001) from the TOMCAT simulations (CTRL, NEWC and HETC) compared to the climatology from Lawrence et al. (2001), based on the estimates of Spivakovsky et al. (2000) (referred to as Lawrence 2001), and from another CTM, MOZART v4 from Emmons et al. (2010) (referred to as Emmons 2010). The climatological tropopause (calculated by equation 4.4) has been used to remove any stratospheric OH denoted by the smooth black line at the top of the domains.

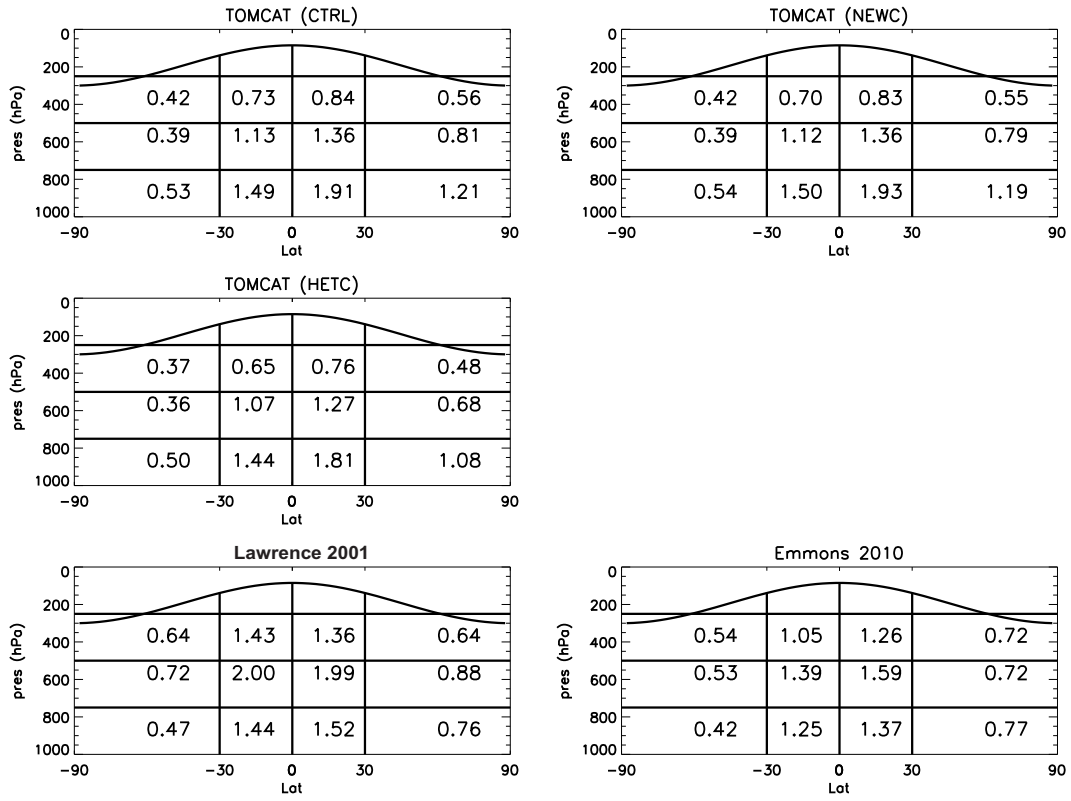

For comparison, a climatology published in Lawrence et al. (2001) and Emmons et al. (2010) (referred to as Lawrence 2001 and Emmons 2010) are also shown Figure 4.7. The Lawrence 2001 climatology is based on model calculations of Spivakovsky et al. (2000) as already described and are therefore constrained by observations. The Emmons 2010 climatology was calculated by the latest version (version 4) of the MOZART CTM (Emmons et al., 2010). By comparison to the Lawrence 2001 climatology, all three TOMCAT simulations generally underestimate OH in the two highest altitude domains at all latitudes and overestimates OH in the lowest altitude domains. HETC shows the best agreement with Lawrence 2001 in the domains between the surface and 750 hPa and CTRL shows the best agreement in the two higher domains of 750-500 hPa and 500-250 hPa. The simulated OH fields from TOMCAT show the best agreement in the two domains situated between the surface and 750 hPa and 30°S and 30°N.

For more detail the percent difference between the Lawrence 2001 climatology and TOMCAT have been calculated. For the two surface domains in the tropics the percentage difference is 3 and

25% for CTRL, 4 and 27% for NEWC, and 0 and 20% for HETC. The larger bias occurs in the in the NH extra-tropics region. As mentioned previously, the tropical lower troposphere is where a large fraction of CH_4 is oxidised by OH. The lower concentrations of OH in this region in HETC explains why it produces a longer, more reasonable methane lifetime compared to NEWC and CTRL. In the lowest domain in the region of 30°- 90°N, the model simulations show differences of 59%, 56% and 42% for CTRL, NEWC and HETC compared to Lawrence 2001, showing that the updates improve OH in this region. However, HETC still exhibits a large overestimate which will likely have important implications on the lifetime of gases in the NH at the surface. In the region of 30°S - 90°S, HETC differs from Lawrence 2001 by 6%-15%. This shows that the simulated OH has a much lower bias in the SH than in the NH compared to Lawrence 2001 .In the upper troposphere, all three simulations show very large percentage differences between 90°S - 30°N. CTRL generally shows the lowest differences, however, there are clearly systematic differences in the TOMCAT model which are not resolved by the updates included in NEWC and HETC. In the mid to high latitudes in the SH, the model shows biases of -46% and -34% in CTRL and NEWC and -42% and -50% in HETC, in the domains between 750-500 hPa and 500-250 hPa, respectively, with the biggest difference being in the lower domain. The model shows the largest disagreement compared to Lawrence 2001 in the tropics with differences of -32 – -49%, -32 – -51% and -36 – -54%, in CTRL, NEWC and HETC.

Overall, the biggest differences are found in the highest altitude domain and the model generally captures the OH in the lowest altitude domains. This suggests that there is a large missing source of OH in the upper troposphere. Photolysis of acetone (CH_3COCH_3) has been found to be a major source of OH is the upper troposphere (Jaeglé et al., 1997; Müller and Brasseur, 1999) and therefore it would be useful to compare the model to aircraft observations of acetone in the future. Another possibility is that the model overestimates OH at the surface in the NH due to underestimated convection. Convection has been shown to be underestimated in TOMCAT in the tropics (Feng et al., 2011; Hoyle et al., 2011) which would act to rapidly transport short-lived species into the upper troposphere. Convection has been shown to be an important process and has been observed to be an important process in controlling upper tropospheric HO_x concentrations (Jaeglé et al., 1997).

4.5 Evaluation of simulated carbon monoxide

CO has been estimated to have an average annual global burden of 360-370 Tg(CO) (Ehhalt et al., 2001). This is similar to the mean annual global burden of 375.25 Tg of CO calculated from the CTRL simulation. With the extended organic chemistry in NEWC this is increased to 391.61 Tg. The uptake of N_2O_5 on aerosol further increases this to 412.58 Tg in HETC. These are both higher than previous estimates. Here, a more detailed assessment of the distribution of simulated

CO in comparison to observations is given to assess the performance of the model with a regional perspective.

4.5.1 Comparisons with MOPITT

Simulated CO from all three simulations has been compared on a global scale to CO, retrieved from the satellite instrument, MOPITT (Measurements Of Pollution In The Troposphere). MOPITT is on board the NASA Terra satellite and infers global concentrations of CO from thermal infrared radiances in the CO absorption band. Version 4 of MOPITT has been processed in such a way that the data is available as both night-time and daytime retrievals. This data has been validated against other observations and shown to measure CO to within a few ppbv of in-situ estimates, with the largest bias occurring at 400 hPa Deeter et al. (2010). For comparison with TOMCAT, the daytime retrievals have been used due to increased sensitivity over land (Louisa Emmons, personal communication, 2011). Level 3, monthly mean data was used[2] and is available on a 1°x 1° grid as a profile or as a total column. MOPITT CO is retrieved on 10 levels extending from the surface up to 100 hPa. The monthly mean simulated CO from TOMCAT was interpolated vertically to the 10 retrieval levels and horizontally to the 1°x 1° MOPITT grid. Any missing data from the satellite were also removed from the TOMCAT output.

MOPITT is a nadir-viewing instrument and is therefore more sensitive to certain altitudes. For this reason, averaging kernels, a matrix holding information about the instrument's varying sensitivities at different altitudes, are supplied with the retrieval data. These are used along with the a priori to transform simulated CO profiles from a model, applying a similar sensitivity to the same altitudes as the satellite. This allows a more accurate comparison between the two. The total column of a gas, X, is calculated by integrating the concentration of the gas (in molecules/cm^3) over the total height, h, of the atmosphere as follows:

$$column = \int_{z=0}^{h} X dz. \tag{4.5}$$

The column a priori $Xapc$ is not supplied but it can be calculated from the a priori profile (Xap) following Deeter (2009):

$$Xapc = K \sum_i (\triangle p_i \cdot Xap_i), \tag{4.6}$$

where $\triangle p_i$ is the pressure level thickness of the ith MOPITT retrieval level in hPa (instead of height) and K=2.12$\times 10^{13}$ (mol/cm^3)(hPa ppb), which converts ppbv to molecules/cm^2 (Deeter,

[2] Available from http://www.acd.ucar.edu/mopitt/

Figure 4.8 TOMCAT and MOPITT total column CO for January 2008. Top row: TOMCAT total column CO from CTRL, NEWC and HETC (left-right) interpolated to MOPITT levels and grid with averaging kernels applied, second row: retrieved MOPITT CO total column, bottom row: Absolute difference between TOMCAT and MOPITT total column.

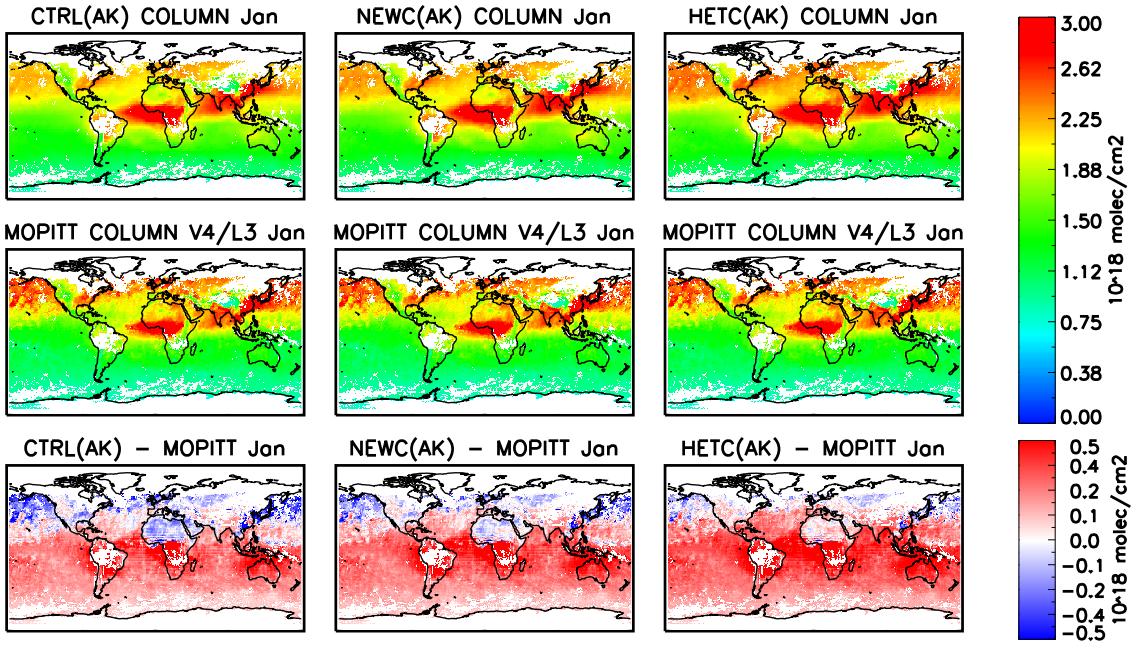

2009). The averaging kernels for the total column (*akc*) also need to be calculated from the profile averaging kernels (*ak*) as described by Deeter (2009):

$$akc = (K/log_{10}(e)) \sum_i \triangle p_i \cdot Xrtv_i \cdot ak_i, \tag{4.7}$$

where $Xrtv_i$ is the retrieved MOPITT profile at each level, i. The calculated column a priori and averaging kernels were then applied to the TOMCAT simulated profile (X_T) and a priori profile (Xap) to calculate the TOMCAT total column (X_{Tc}) according to Deeter (2009):

$$X_{Tc} = Xapc + akc(X_T - Xap). \tag{4.8}$$

Figure 4.8 and 4.9 show the January and July 2008 monthly mean CO total column from CTRL, NEWC and HETC (calculated using equation 4.8) along with the MOPITT retrieved total column and the absolute difference between the modelled and retrieved CO. In January, MOPITT shows that TOMCAT captures the large-scale features and distribution of CO, with a clear inter-hemispheric gradient and higher concentrations of CO in the NH compared to the SH. A region of high CO is located over north and central Africa from biomass burning. The easterly transport of these emissions towards South America is also visible. Other regions of high CO can also be seen

over India and South East Asia and above-background concentrations of CO are located over the anthropogenic emissions regions of eastern North America and western and central Europe. Westerly outflow regions from the anthropogenic emission regions over the North Atlantic and North Pacific are also visible. Even so, the model simulates higher concentrations than observed by MOPITT in the SH. The biomass burning emission region in South Africa extends further south in TOMCAT, than observed by MOPITT, with emissions occurring over a wider region. This results in a larger outflow of CO in TOMCAT to the west. This could suggest errors in the GFED v2 fire emissions which could be contributing to an overestimate in background CO. The latest version of GFED emissions (GFED v3) has lower estimates of area burned in SE Asia, equatorial Asia, Africa, South America and Central America (Giglio et al., 2010) and would therefore reduce this bias. In addition to this, both GFED v2 and v3 have higher burned area estimates in Africa than other databases (Giglio et al., 2010).

In the NH, the model shows a much better agreement with the observed CO column but some regions show a low bias. The CTRL model underestimates CO in comparison to MOPITT most notably over the Pacific Ocean. As this is the main outflow region of Asian emission, this suggests a possible underestimate in emissions in Asia. For this simulation, AR5 emissions estimates for the year 2000 were used. Due to the rapid expansion of Asia, emissions have increased markedly since 1980 (Ohara et al., 2007), therefore, the AR5 emissions may not capture the magnitude of emissions in 2008. Simulated CO over regions of North Africa, Europe and North America are also less than observed by MOPITT. As shown in Section 4.3, the concentration of CO is increased in NEWC and in HETC. With this increase in CO, TOMCAT shows much better agreement with MOPITT in regions of North Africa, Europe, North America and the Pacific and Atlantic Oceans. The HETC simulation shows the best agreement with MOPITT in the NH, but due to the increase in CO in the SH, the positive bias in the model in this region is also increased. This overestimate in CO in the SH is the reason why the total mean mass burden of 412.58 Tg(CO) calculated from HETC is greater than previous estimates of 360-370 Tg(CO).

The clear CO inter-hemispheric gradient in January, seen by MOPITT and captured by TOMCAT, is now less visible in July (see Figure 4.9). This is because of the shorter lifetime of CO in the NH summer compared to winter, and longer lifetime in the SH winter compared to summer, resulting in more similar concentrations in both hemispheres. In TOMCAT, the gradient is hardly visible due to higher than observed concentrations in the SH. However, as seen in January, TOMCAT and MOPITT show comparable dominant features in the distribution of CO. It is clear that CO is underestimated throughout the whole NH in the all three simulations, most notably over land near sources suggesting emissions of CO may be too low. Model inversions have found emissions of CO in Asia to be underestimated by up to 40% (Kopacz et al., 2010) due to anthropogenic emissions (Hooghiemstra et al., 2011). This would lead to an underestimate of CO near Asia, but also give a lower background CO in other regions. In the NH summer, MOPITT shows retrieved

Figure 4.9 As Figure 4.8 but for July 2008.

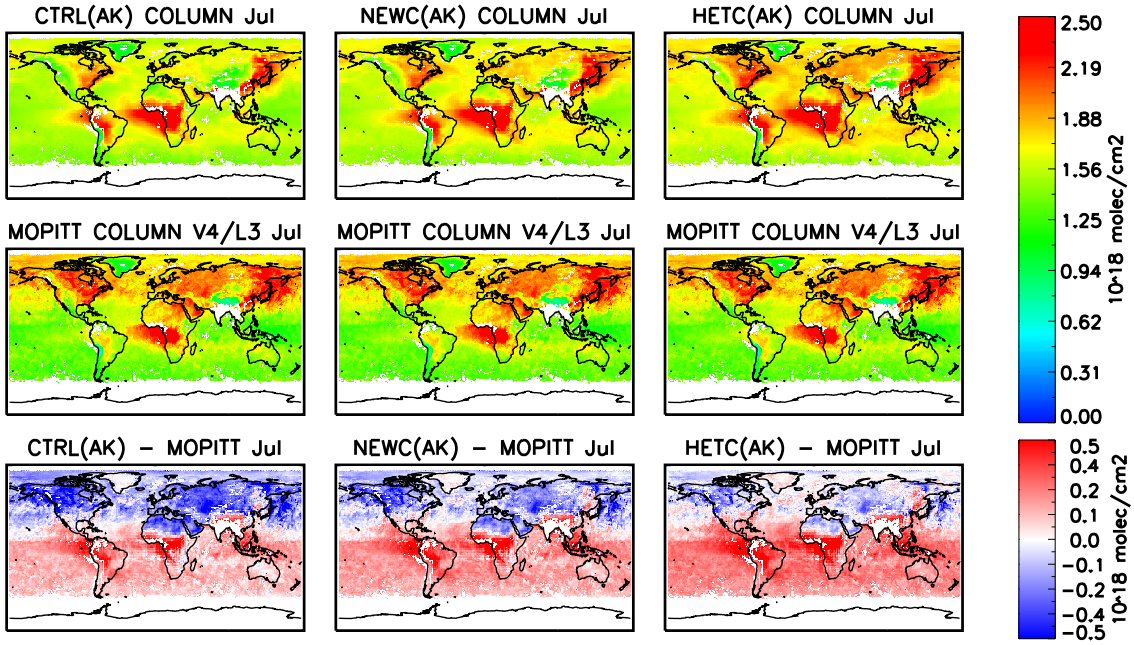

CO in the Arctic with the use of day profiles. Here it can be seen that the model shows better agreement with the satellite than near the source regions in the NH. The HETC simulation also offers a much improved comparison to the satellite than CTRL or NEWC in this region.

In the SH, CO is overestimated in July, as seen in January, but the bias is smaller. Over Africa, regions of high CO are observed by both, however, in the MOPITT retrievals, it covers a smaller region than simulated by TOMCAT. This is similar to what was seen in January. At this time of year fires also occur in South America, where TOMCAT and MOPITT show an even larger discrepancy. Due to the shorter lifetime of CO in the NH summer compared to winter, the gas is less well-mixed giving more distinct concentration gradients close to source regions. MOPITT observes high CO around the anthropogenic regions of North America, Europe and Asia. July is also the peak biomass burning season in the mid/high northern latitudes, therefore regions of Alaska, Canada and Siberia also have higher concentrations of CO compared to the background. The CTRL TOMCAT simulation has high CO concentrations near North America and Asia, but regions of Europe, Canada, Siberia and Asia are underestimated. The increased background concentration in NEWC improves the model in regions of Europe and Canada but there are still regions where the model underestimates CO. HETC shows the best agreement with MOPITT in the NH due to the longer lifetime of CO giving even higher concentrations of CO, reducing the bias quite substantially.

To understand the differences between TOMCAT and MOPITT in more detail, the retrieved profiles have been used for comparisons at different altitudes over specific regions. Eight different

Figure 4.10 Monthly mean anthropogenic, natural and biomass burning emissions (Tg/month) for 2008 used by TOMCAT for the CTRL, NEWC and HETC simulations from anthropogenic, natural and biomass burning sources in the regions defined in Table 4.3.

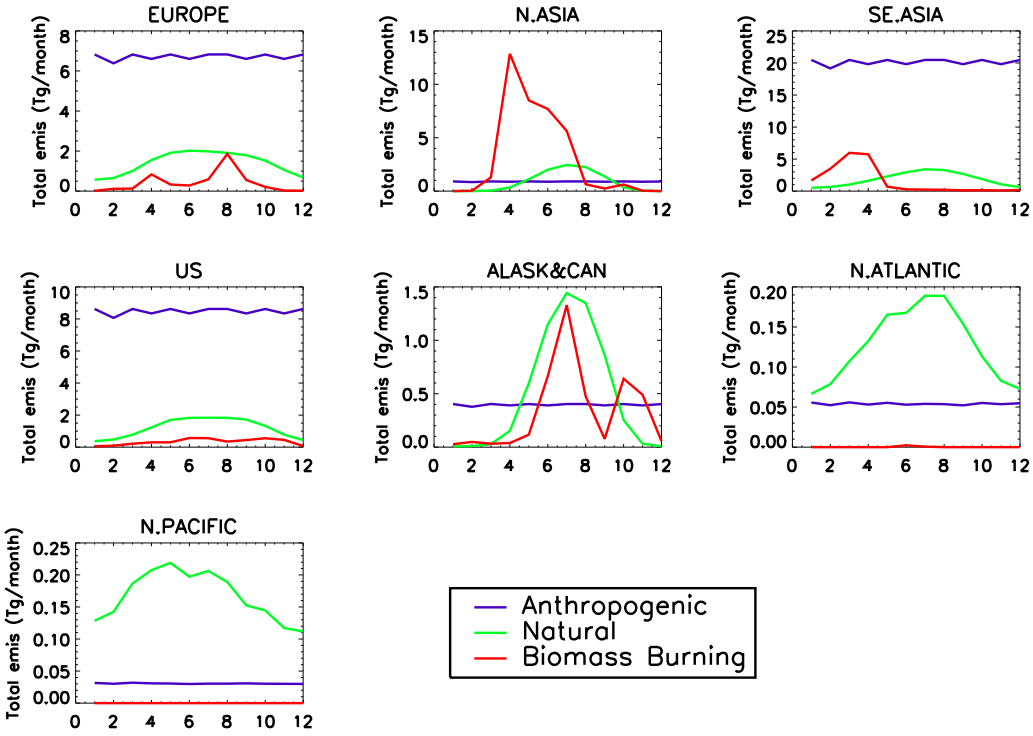

Table 4.3 Regions used for the MOPITT CO comparisons shown in Figure 4.11.

Region	Longitude and Latitude ranges
>70N	70-90N, 0-360E
EUROPE	30-70N, 350-60E
N.ASIA	45-70N, 60-150E
SE.ASIA	10-45N, 60-125E
US	25-50N, 235-300E
ALASK&CAN	50-70N, 235-300E
N.ATLANTIC	20-60N, 300-348E
N.PACIFIC	20-50N, 150-230E

regions have been chosen to represent the major sources and outflow regions in the NH. The longitudes and latitudes of these regions are listed in Table 4.3. The monthly mean anthropogenic, biomass burning (BB) and natural/biogenic emissions are shown in Figure 4.10. Europe, US and S.E Asia have been chosen as they have the highest anthropogenic emissions, with S.E. Asia having the highest overall. The N. Asia and Alaska and Canada regions have been chosen as they have much lower anthropogenic sources but experience large emissions from BB. Alaska and Canada also experience high natural emissions which are of a similar magnitude to the BB emissions. The

Figure 4.11 Correlation plots between TOMCAT HETC CO (in ppbv) profiles (interpolated to MOPITT levels with averaging kernals applied) and MOPITT CO (in ppbv) profiles for DJF, MAM, JJA and SON (left to right) for the regions defined in Table 4.3. Each symbol in the scatter plots represents a concentration of CO in one box of the 1°x 1°grid, at one the 10 levels and has been coloured by the pressure of that level. E is Root Mean Square Error (RMSE) in ppbv and r is the correlation.

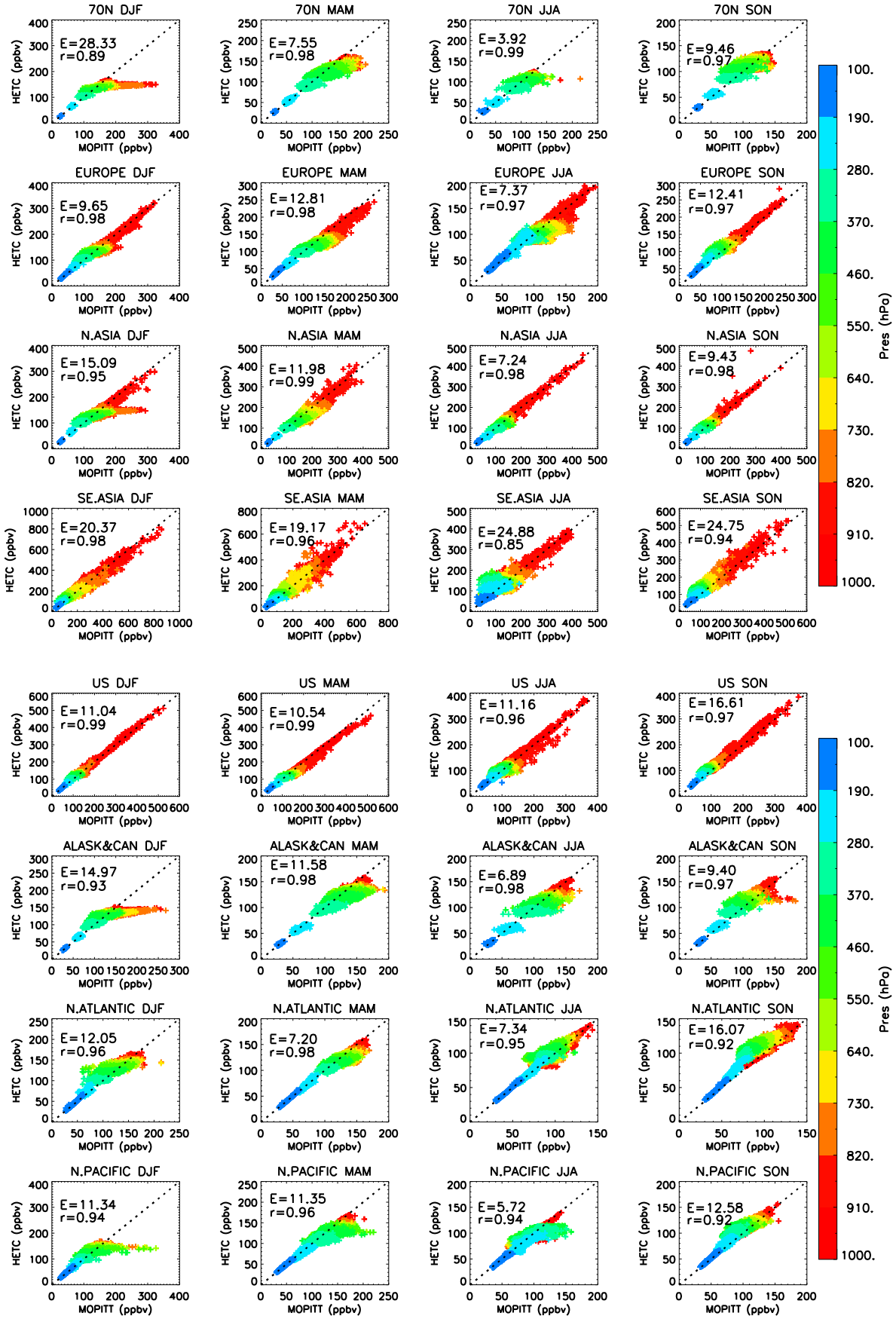

Atlantic and Pacific regions mostly experience natural emissions from the oceans. The boxes that were chosen contain a small area of land and therefore small anthropogenic emissions can be seen in Figure 4.10.

Figure 4.11 shows scatter plots of MOPITT against TOMCAT (HETC) CO. This analysis is only shown for HETC as it was shown to perform the best in comparison to MOPITT total column in the NH. The Pearson correlation (r) and the root mean square error (RMSE) between MOPITT and TOMCAT have been calculated for each region. The mean-square error is defined as:

$$RMSE = \sqrt{\frac{1}{n}\sum_{1}^{n}(X_{mod} - X_{obs})^2}, \tag{4.9}$$

where n is the number of observations in each region defined by the longitudes and latitudes listed in Table 4.3, and X_{mod} and X_{obs} are the simulated and retrieved CO volume mixing ratio. The correlation represents how similar the variations in the model and observations are in time and the RMSE represents the mean absolute difference between the model and observations.

In general, the model has high correlations of 0.85-0.99 with MOPITT suggesting that model is able to resolve variations in CO observed by MOPITT due to transport. Also, in all regions at altitudes greater than 200 hPa, the model and satellite show very similar concentrations. This is because MOPITT has very little sensitivity at this altitude and therefore the satellite and model concentrations are primarily influenced by the a priori.

Europe, US and S.E. Asia, which are dominated by anthropogenic emissions, show high concentrations of CO, with the highest concentrations being observed and simulated over S.E. Asia and the lowest over Europe, in line with the emission totals (see Figure 4.10). Over Europe the lowest RMSE is in JJA and the largest in MAM and SON. The simulated concentrations show a negative bias from the surface up to $\sim$400 hPa for all seasons apart from SON, which has a positive bias throughout the whole troposphere. Over the US, the model exhibits the highest error in SON (RMSE=16.61 ppbv). the model show the same seasonal biases as seen over Europe. Over South-East Asia, the model underestimates CO near the surface, below 700 hPa, in DJF. In winter most emissions come from anthropogenic sources and therefore support the believed underestimate in Asian emissions. In MAM, the model does, however, overestimate CO near the surface in some grid boxes. As seen in Figure 4.10, this is the peak BB season. Emissions in GFED v2 are thought to be too high in this region which would offset the underestimate in the anthropogenic emissions (Giglio et al., 2010). The largest errors occur in JJA and SON as with the other regions. Higher emission occur during the summer in Europe and US and in spring in S.E. Asia increasing the atmospheric burden of CO. In Section 4.4 it has been shown that TOMCAT has very low OH in the mid-upper troposphere, where the biggest biases are seen to increase in SON. This could suggest that this overestimation of CO in autumn is due to inefficient loss by OH in the NH.

N. Asia and Alaska and Canada are dominated by natural emissions (both biogenic and BB). Both these regions have the lowest error in JJA and the highest error in DJF. The model underestimates CO in DJF and MAM and overestimates CO in SON, as seen in the anthropogenic regions. The highest error in DJF is due to a region near the surface where the model does not capture high concentrations of CO that are observed by MOPITT. As part of this thesis, TOMCAT simulations were performed for a study by Sodemann et al. (2011), which compared the output to CO simulated by a Lagrangian model, FLEXPART, and CO from the satellite instrument, IASI. The study showed that TOMCAT was more diffusive (as expected for a Eulerian model) than FLEXPART, therefore, unable to retain filaments of very high CO observed by IASI being transported over the North Pole for two biomass burning cases. In the winter, these two regions do not have any large local emissions (see Figure 4.10) and therefore any high CO observed by MOPITT would have been transported from the lower latitudes. The diffusion of this CO in TOMCAT would lead to lower than observed CO as seen in Figure 4.11. The region of $>$70°N in DJF also shows a similar occurrence, where concentrations of MOPITT CO reach up to 300 ppbv and TOMCAT only shows a maximum of $\sim$150 ppbv at altitudes below 700 hPa. Again, the model overestimates CO in SON throughout the troposphere. As elsewhere, the model underestimates CO in MAM. JJA has the lowest RMSE as seen elsewhere .

The N. Atlantic and N. Pacific are both subjected to outflow from North America and Asia, respectively. The model overestimates CO in DJF, JJA and SON and underestimates CO in MAM. As CO from North America is generally exported over the Atlantic with passing frontal systems, the CO is lifted to higher altitudes where OH is thought to be too low which would result in more CO than observed. Over the Pacific, the model underestimates CO in DJF and MAM as in Asia and overestimates CO in SON. As with over the Atlantic, the underestimate in CO occurs at higher altitudes due to frontal lifting.

4.5.2 Comparisons with surface site measurements

Observed CO from the stations listed in Table 4.4 and shown in Figure 4.12 has been compared to simulated monthly mean CO from the TOMCAT simulations, CTRL, NEWC and HETC. All of the data has been downloaded from the World Data Centre for Greenhouse Gases (WDCGG)[3]. Figure 4.13 shows observed CO at these stations for 2008 with simulated CO interpolated both horizontally and vertically to the station location. The first five stations, ALT, ZEP, BRW, STM and ICE, are all located above 60°N. All of these stations are located in remote regions far from the mid-latitude sources. Therefore, concentrations of CO mostly reflect background CO resulting in similar concentrations at all stations. The observations show a winter/spring maximum of 150-180 ppbv in February-April and a summer minimum of 90-100 ppbv in July-August. Overall,

[3]http://gaw.kishou.go.jp/wdcgg/

Figure 4.12 Surface site locations used for CO comparisons with TOMCAT (top, left), O_3 (top, right) and NMHC/NO_y species (bottom). The locations are also listed in Figure 4.4

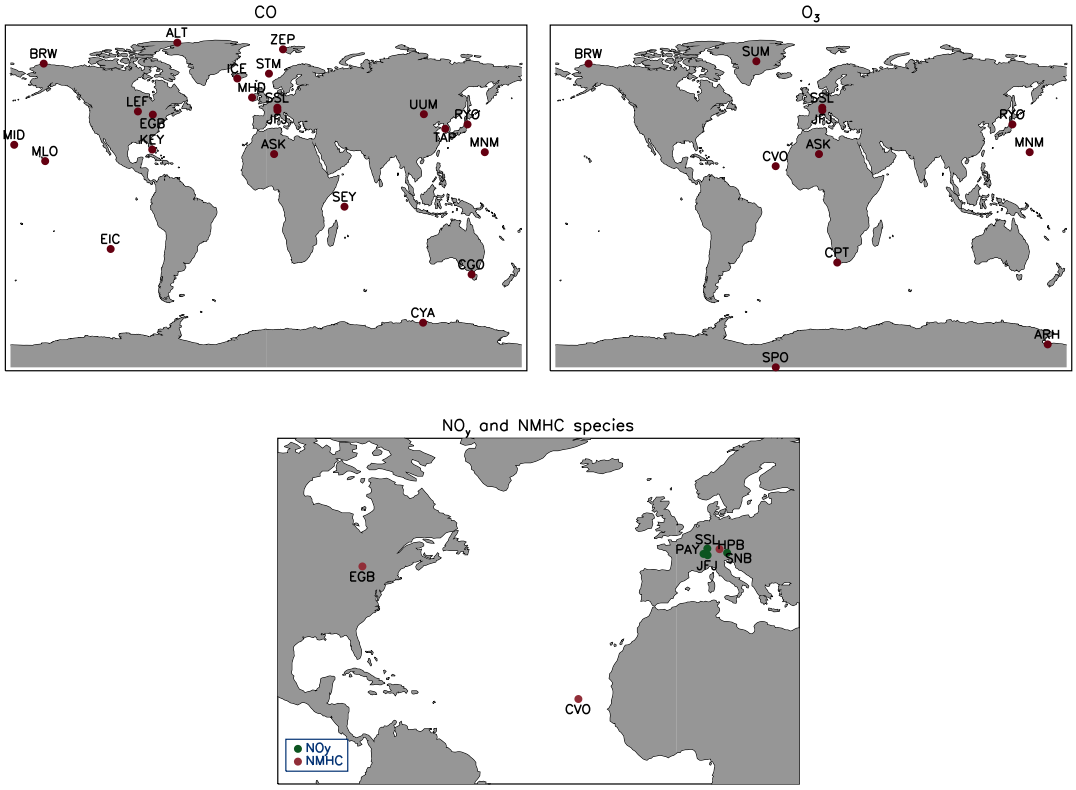

the model captures the seasonal cycle, however the amplitude of the cycle is underestimated in TOMCAT (a modelled range of ∼30-50 ppbv compared to the observed range of ∼70-80 ppbv). This is due to underestimated CO in winter and overestimated CO in summer in the model.

Including the additional hydrocarbon chemistry (NEWC) and the N_2O_5 uptake by aerosols (HETC) increases CO at the surface throughout the year at all of these stations. HETC shows the best agreement with the observations with improved correlations of between 0.82 and 0.94 and reduced RMSE of between 16.5 and 22.2 ppbv. This is at the lower end of the 17-40 ppbv range of RMSEs found in a model intercomparison study by Shindell et al. (2008) focusing on the Arctic at the surface (at ALT and BRW). Table 4.5 shows the mean bias (MB), correlations and RMSE summarised for the Arctic stations. In agreement with the results shown in Section 4.5.1, the model underestimates CO in winter and spring in the Arctic. The negative bias in the model is reduced in HETC both in winter and spring in comparison to the other simulations in the Arctic. Due to lower CO concentrations in CTRL and NEWC, they have smaller biases during this season. As seen in Figure 4.11, the model performs best during the summer.

There are eight mid-latitude stations located between 30°N - 60°N shown in Figure 4.13. MHD is located in the marine boundary layer sampling mostly air from the Atlantic, RYO, EGB and

Figure 4.13 Surface comparisons of observed and simulated CO from TOMCAT (CTRL, NEWC and HETC) in 2008. The grey shading shows the standard deviation of the monthly mean observations where available. The stations are shown in order of latitude from north to south and the correlations (r) and RMSE are also shown.

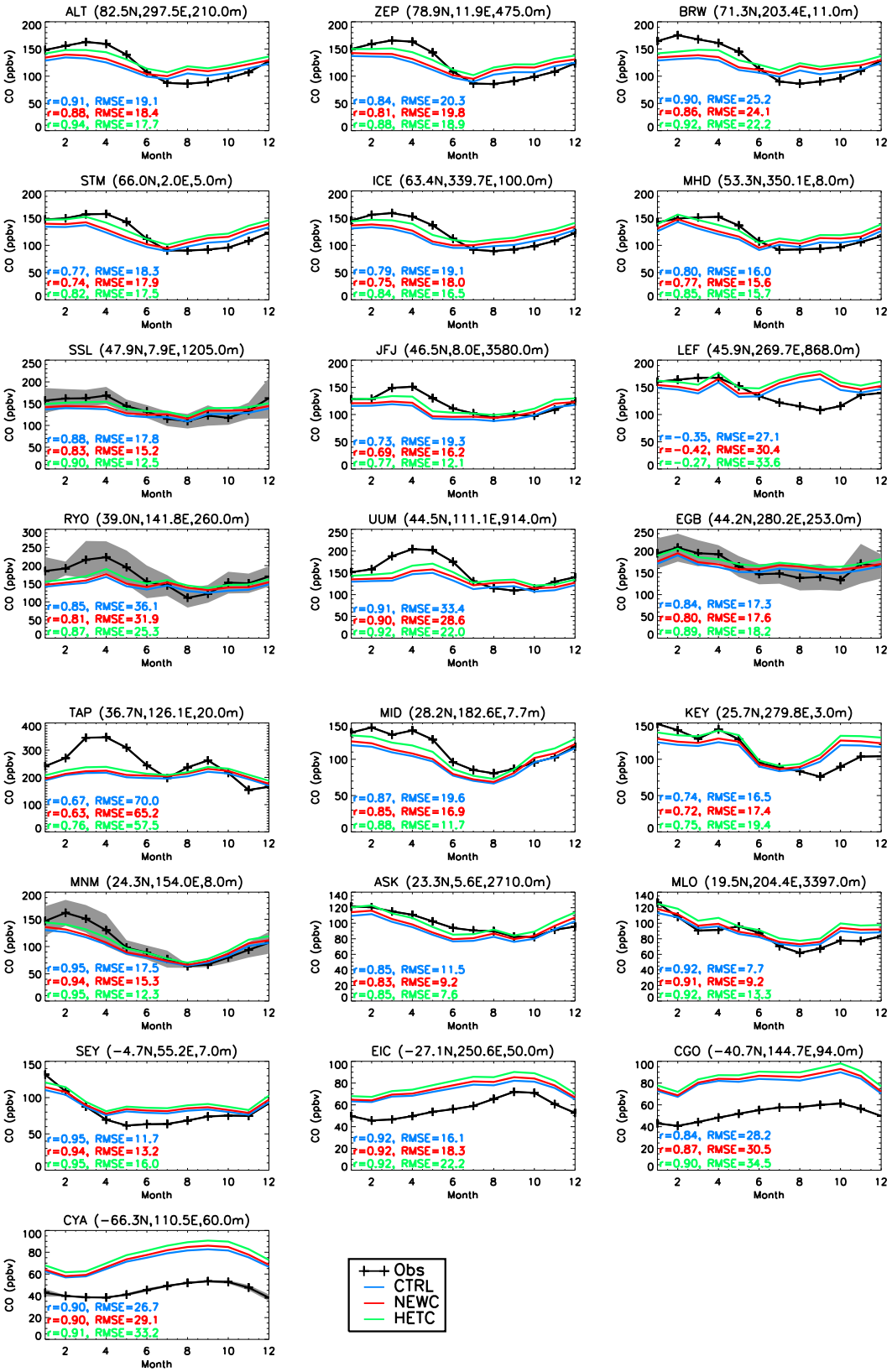

Table 4.4 List of surface station locations and species measured used for comparisons with TOMCAT. The locations are also shown in Figure 4.12.

ID	Station Name	Lon	Lat	Alt (m)	Species measured
ALT	Alert, Canada	297.48	82.45	210	CO
ARH	Arrival Heights, Antarctica	166.67	-77.80	184	O_3
ASK	Assekrem, Algeria	5.63	23.27	2710	CO, O_3
BRW	Barrow, Alaska	203.40	71.32	11	CO, O_3, NMHC
CGO	Cape Grim, Australia	144.68	-40.68	94	CO
CPT	Cape Point, South Africa	18.48	-34.35	230	O_3
CVO	Cape Verde, Central Atlantic	335.13	16.85	10	O_3 , NMHC
CYA	Casey Station, Antarctica	110.53	-66.28	60	CO
EGB	Egbert, Canada	280.22	44.23	253	CO
EIC	Easter Island,	250.55	-27.13	50	CO
HPB	Hohenpeissenberg, Germany	11.02	47.80	985	NMHC
ICE	Heimaey, Iceland	339.72	63.40	100	CO
JFJ	Jungfraujoch, Switzerland	7.99	46.55	3580	CO, O_3, NO_y
KEY	Key Biscayne, US	279.80	25.67	3	CO
LEF	Park Falls, US	269.73	45.92	868	CO
MHD	Mace Head, Ireland	350.10	53.33	8	CO
MID	Sand Island, Hawaii	182.63	28.20	7.70	CO
MLO	Mauna Loa, Hawaii	204.42	19.54	3397.00	CO
MNM	Minamitorishima, NW Pacific	153.98	24.28	8	CO, O_3
PAY	Payerne, Switzerland	6.95	46.82	490	NO, NO_2
RYO	Ryori, Japan	141.82	39.03	260	CO, O_3
SEY	Mahe Island, Seychelles	55.17	-4.67	7	CO
SNB	Sonnblick, Austria	12.95	47.05	3106	NO_y
SPO	South Pole, Antarctica	335.20	-89.98	2810	O_3
SSL	Schauinsland, Germany	7.92	47.92	1205	CO, O_3, NO, NO_2, PAN
STM	Ocean Station ‘M’, N. Atlantic	2.00	66	5.00	CO
SUM	Summit, Greenland	321.52	72.58	3238	O_3
TAP	Tae-ahn Peninsula, Korea	126.12	36.72	20	CO
UUM	Ulaan Uul, Mongolia	111.08	44.45	914	CO
ZEP	Zeppelinfjellet, Spitsbergen	11.88	78.90	475	CO

TAP are low altitude sites near polluted local sources, and JFJ, SSL, LEF and UUM are high altitude sites that are remote from local surface sources. As expected, RYO, EGB and TAP experience higher concentrations of CO compared with the remote stations, MHD, SSL, JFJ, LEF and UUM. This is due to the location of RYO, EGB and TAP being closer to the surface and therefore emissions. In general, HETC shows the best agreement in this latitudinal range, with the highest correlations and lowest RMSE error at all of the stations apart from LEF and EGB. The higher RMSE at LEF and EGB is due to the summer/autumn CO concentrations being already overestimated by the model and therefore the higher background of CO in HETC increases this bias. The model reproduces the observed seasonal cycle at 7 out of the 8 stations (MHD, SSL, JFJ, RYO, UUM, EGB and TAP) with correlations of between 0.76 and 0.92 for the HETC simulation. At

LEF, the model simulates a seasonal maximum in September and not spring, giving this station very low correlations for all three simulations. As with the high latitude stations, the model generally underestimates CO in the spring at all stations and overestimates CO in the autumn at MHD, EGB, RYO, UUM and TAP. RYO and TAP, which are located near the source region of Asia, both show particularly large underestimates of CO in the winter, again, supporting the case that emissions in Asia are underestimated.

In the region between 30°N and 30°S, there are seven stations in Figure 4.13 shown for comparison against the model simulations. MID, MNM and MLO are located in remote marine regions in the NH far from sources. However, MNM and MID are located in regions which are likely to be influenced by outflow from Asia over the Pacific. For this reason, MNM and MID underestimate CO in the winter due to low background CO with underestimated Asian emissions. KEY is located at the surface, near North American sources. Unlike other stations, the model captures the winter concentrations, however, the autumn concentrations are overestimated similar to other NH stations. ASK is a mountain site which is remote from local sources and is mostly influenced by air from the Atlantic. Here, the model has the lowest RMSE of 7.6 out of all the stations at any latitude, shown in Figure 4.13. In the SH, the model is compared to SEY and EIC, which are both located in remote marine environments. EIC shows the largest RMSE out of these two stations due to CO being overestimated throughout the year. In general, HETC shows the highest correlations with all stations in the extra-tropics and the lowest RMSE at MID, MNM, ASK. CTRL shows the lowest RMSE at KEY, MLO, SEY and EIC due to the lower CO in the SH.

Figure 4.13 also shows two stations which are located at 40°S and 66°S (CGO, CYA). As expected from the results seen so far, CO is overestimated throughout the whole of the year due to their location in the SH. All simulations captured the seasonal cycle, the highest correlations of 0.92 and 0.91 are gained from the HETC simulation.

Table 4.5 Seasonal mean bias (MB), total root mean square error (RMSE) (in ppbv) and correlations (r) between observed and simulated CO for 2008 at Arctic stations.

Station	Lon	Lat	Simulation	Seasonal MB				RMSE	r
				DJF	MAM	JJA	SON		
ALT	297.48	82.45	CTRL	-15.21	-30.30	6.02	9.25	19.11	0.91
			NEWC	-9.46	-24.58	11.93	17.31	18.43	0.88
			HETC	-1.85	-12.93	19.40	23.15	17.73	0.94
ZEP	11.88	78.90	CTRL	-11.54	-33.47	3.07	11.57	20.35	0.84
			NEWC	-5.89	-27.70	8.94	19.90	19.83	0.81
			HETC	1.75	-15.93	16.36	25.76	18.87	0.88
BRW	203.40	71.32	CTRL	-28.22	-33.36	8.79	9.24	25.17	0.90
			NEWC	-22.52	-27.82	14.84	17.49	24.09	0.86
			HETC	-14.83	-16.00	22.22	23.38	22.19	0.92
STM	2.00	66.00	CTRL	-6.58	-29.28	-2.99	12.75	18.27	0.77
			NEWC	-0.99	-23.77	2.91	20.57	17.88	0.74
			HETC	6.72	-12.26	10.16	26.60	17.55	0.82
ICE	339.72	63.40	CTRL	-10.52	-31.68	-1.55	8.44	19.09	0.79
			NEWC	-4.93	-26.41	4.00	16.20	18.04	0.75
			HETC	2.73	-14.75	11.20	22.22	16.49	0.84

4.6 Evaluation of simulated ozone

Simulated concentrations of ozone have also been compared to surface observations from the WDCGG at locations shown in Figure 4.12 for the year 2008 and are shown in Figure 4.14. SUM and BRW are both located in the Arctic. At SUM, the model reproduces the observed O_3 seasonal cycle, with a maximum in spring, therefore yielding correlations of 0.93 to 0.94 for all three simulations. The RMSE is 5.6 ppbv for HETC, 3.3 ppbv for NEWC and 4.6 ppbv in CTRL. In HETC, lower O_3 concentrations (due to loss of NO_x) increases the model's RMSE compared to the NEWC simulation. As seen in the results shown in Section 4.3, HETC shows the biggest reduction in O_3 in spring. At BRW, TOMCAT does not capture the seasonal cycle, yielding correlations of only 0.23-0.25 for the different simulations. The model predicts a similar seasonal cycle at BRW and SUM with a spring maximum. However, the observations show very low concentrations of O_3 in spring. BRW is located near the Beaufort Sea and regularly witnesses rapid O_3 depletion events (ODEs) during spring due to catalytic destruction of O_3 by halogens (Barrie et al., 1988; Simpson et al., 2007; Helmig et al., 2007). The chemistry scheme used in TOMCAT does not include halogen chemistry, therefore the model is unable to simulate ODEs. As mentioned in

Figure 4.14 Surface comparisons of observed and simulated O_3 (in ppbv) from CTRL, NEWC and HETC simulations for 2008. Shading represents standard deviation of monthly mean observed concentrations where available. The correlations (r) and RMSE are also shown.

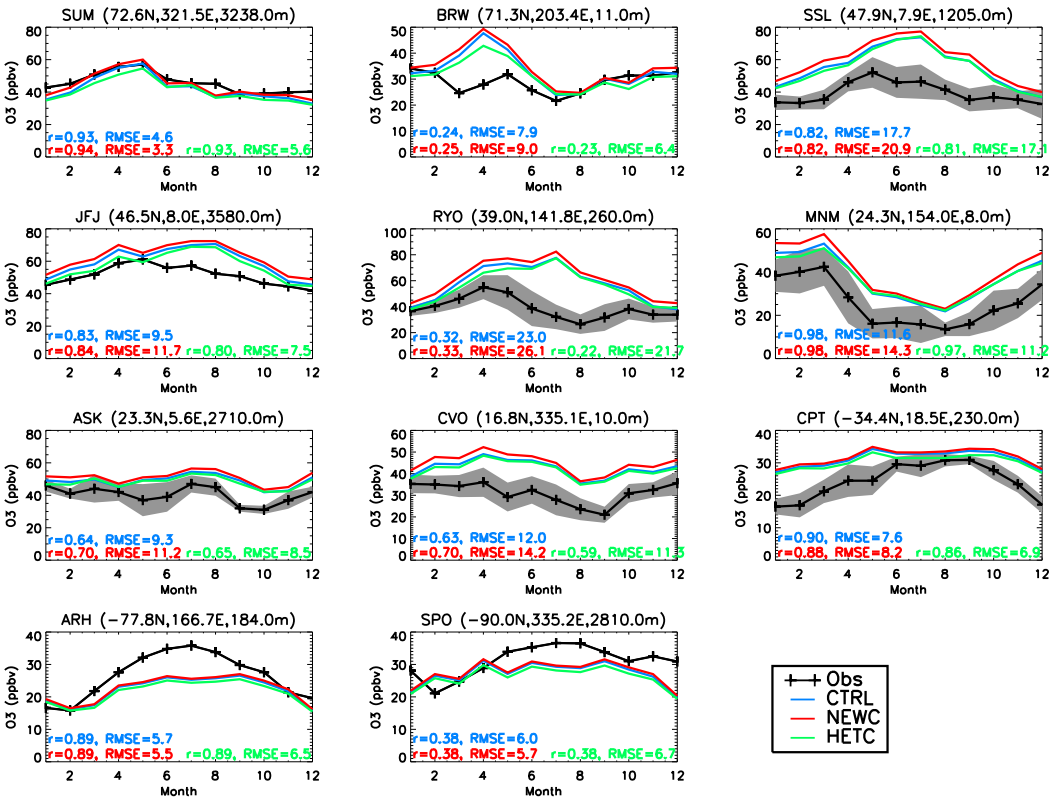

Section 2.7.6 ODES can cover large areas and will not be confined to area immediately around the BRW station, TOMCAT has recently been developed to include bromine chemistry (Breider, 2010) and future simulations to investigate the impact of halogens on the Arctic as a whole could be done using this version of the model. During the other seasons, the model does reproduce the observed concentrations of O_3. Table 4.6 shows the seasonal MB at these two Arctic stations for the CTRL, NEWC and HETC simulations. At SUM, all three simulations show the largest biases in the winter months. The lowest biases are found in autumn (similar to CO) in NEWC and HETC. Conversely, CTRL shows the lowest bias in spring. At BRW, all three simulations show the largest bias in spring due to the lack halogen chemistry as already discussed. Apart from spring, the biases at BRW are smaller than they are at SUM.

In the mid latitudes the model has been compared to observations at SSL, JFJ and RYO. The model overestimates O_3 to some extent throughout the year at all three sites but the summer months show the largest bias with simulated concentrations being up to 100% higher than observed. Overall, the model shows RMSE values that are higher than in the Arctic and HETC shows the best agreement with the lowest RMSE values of 7.5 to 21.7 ppbv. JFJ shows good agreement with the model in the winter and spring when JFJ is thought to be mostly influenced by high altitude sources (Kaiser et al., 2007). In the summer, JFJ has been shown to be mostly subjected to O_3 transported from the Mediterranean (Kaiser et al., 2007). During the summer months, RYO is subjected to easterly winds bringing air masses from over the ocean which are low in O_3 (JMA, 2009), these low concentrations are not captured by the model, possibly indicating inefficient destruction of O_3 in remote marine regions.

MNM, ASK, CVO and CPT are all located close to the tropics in remote marine environments (see Figure 4.12). As with RYO, the model overestimates O_3 at all of these stations. HETC which shows the best agreement compared to the other simulations with a RMSE of between 6.9 to 11.3. Destruction of O_3 by halogens is believed not only to be important in the Arctic. It has also been found to be important in tropical oceanic sites such as CVO (von Glasow, 2008; Read et al., 2008). This could be contributing to the model's overestimate of O_3 at all remote marine sites. Breider (2010) found an increase in O_3 destruction at CVO when bromine chemistry was included in the TOMCAT model which would reduce the concentrations of O_3, however, the model was still biased high. Remote oceans are also typically characterised by destruction of O_3 due to low concentrations of NO_x (Lee et al., 2009) and therefore the results also suggest that the model is not capturing the destruction of O_3 in these regions. This bias in the model is relatively consistent throughout the year meaning the model does manage to capture the seasonal cycle giving correlations of between 0.63 to 0.98 for CTRL, 0.7 to 0.98 for NEWC and 0.59 to 0.97 for HETC.

Table 4.6 Seasonal mean bias (MB), total root mean square error (RMSE) (in ppbv) and correlations (r) between observed and simulated O_3 for 2008 at Arctic stations.

Station	Lon	Lat	Simulation	Seasonal MB				RMSE	r
				DJF	MAM	JJA	SON		
SUM	321.52	72.58	CTRL	-6.75	-0.62	-4.84	-1.64	4.58	0.93
			NEWC	-4.11	1.78	-3.19	-0.32	3.33	0.94
			HETC	-7.57	-4.14	-4.88	-3.37	5.56	0.93
BRW	203.40	71.32	CTRL	-0.54	14.56	2.52	-0.42	7.87	0.24
			NEWC	1.72	16.54	3.64	0.25	8.97	0.25
			HETC	-1.66	11.22	2.56	-2.24	6.36	0.23

ARH and SPO are both located in Antarctica. The observations at both stations show a seasonal maximum in the austral winter and minimum in summer. The maximum in the winter is due to the lack of photochemical destruction of O_3 with constant darkness. The model captures the seasonal cycle at ARH with correlations of 0.89 for all simulations but does not capture it as well at SPO with correlations of 0.38. At SPO there is an increase in O_3 later in the calender year, this has been shown to be due to photochemical production of O_3 from NO_x released from the snow in the summer (Helmig et al., 2007) which is not captured by the model. The model shows a similar RMSE at both stations of $\sim$6 ppbv for all simulations, however the model shows a large negative bias during the austral winter.

4.7 Evaluation of simulated NO_y

Figure 4.15 shows the model compared to observations of some species of NO_y at surface sites in Europe (see Figure 4.12). NO and NO_2 are compared to the model at the stations SSL and PAY (second and third panel down). The concentrations of observed NO and NO_2 are much lower at SSL compared with PAY suggesting that observations at PAY are more influenced by local emissions of NO_x. All three of the simulations reproduce NO at SSL within 1 standard deviation of the mean (shown by the grey shaded area). However none of the simulations capture all of the observed seasonal variability, yielding correlations of between -0.08 and 0.15. It is particularly difficult for models to capture such short lived species in continental regions due to relatively large grid size. Due to the longer lifetime of NO_2, the model is more capable of capturing the seasonal variability at SSL with correlations of 0.77 to 0.9 for the different simulations, however, the model underestimates NO_2 during the summer. At PAY, the model captures the variability of NO and NO_2 better than at SSL (as indicated by the correlations), however, the model clearly does not capture the high concentrations of NO_x at this site. SSL also has observations of PAN (top panel).

Figure 4.15 Surface comparisons of observed NO_y species to TOMCAT simulations CTRL, NEWC and HETC in 2008.

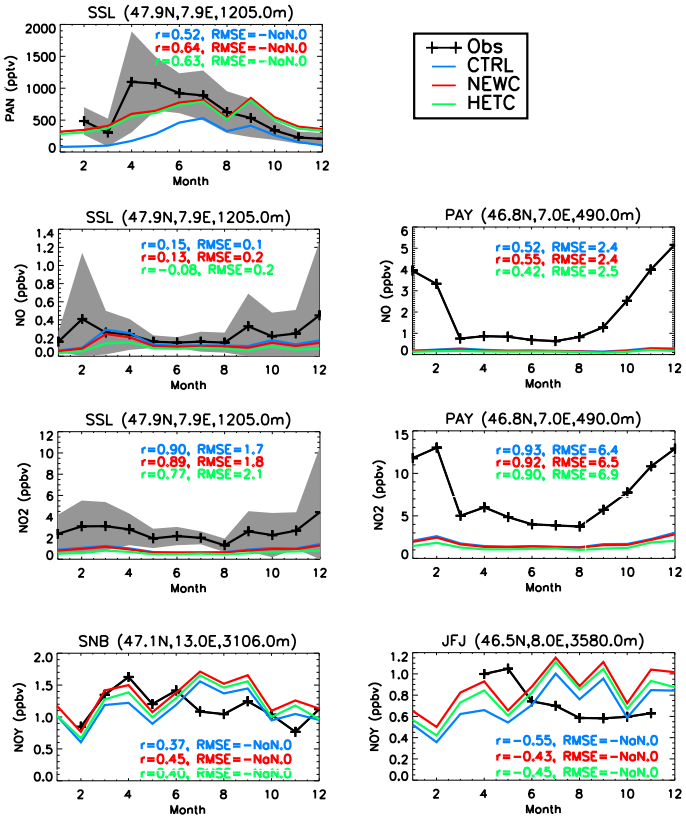

Including the additional hydrocarbon chemistry in NEWC and HETC produces much higher concentrations of PAN, as seen in Section 4.3. NEWC and HETC now simulate concentrations of PAN to within 1 standard deviation of the observed mean all year round apart from November and December where PAN is now overestimated slightly. Total reactive nitrogen (NO_y) is shown in the bottom panel of Figure 4.15 at SNB and JFJ which are both remote high altitude sites. At SNB, the model reproduces the seasonal variations very well in all three simulations apart from in the summer where NO_y is overestimated. The seasonal cycle of NO_y in the model is dominated by HNO_3 (see Figure 4.1) and may suggest inefficient loss of HNO_3. At JFJ, the model follows a similar pattern, with NO_y being overestimated in the summer.

4.7.1 Comparisons of simulated NO_x and O_3 with TOPSE aircraft.

As this work focuses on the Arctic, it is important to evaluate the model with regards to the addition of the uptake of N_2O_5 by aerosol in HETC due the importance of this reaction in dark and cold conditions. The TOPSE (Tropospheric Ozone Production about the Spring Equinox) aircraft

Table 4.7 Monthly mean NO_x and O_3 concentrations for March from the TOMCAT model (for simulations CTRL, NEWC, HETC) averaged over 60°- 85°N, 60°-105°W. Observations from an average of all flights during March 2000 as part of the TOPSE aircraft campaign.

	Surface-600 hPa		**600-350 hPa**	
	NO_x	**O_3**	**NO_x**	**O_3**
CTRL	24.0	44.2	35.9	91.4
NEWC	14.8	46.8	26.8	94.5
HETC	6.5	41.1	7.4	87.3
Obs.	8.5	50.3	25.0	63.1
MOZART	5.8	47.9	9.9	60.4

campaign took place in the year 2000, sampling concentrations of trace gases between February and May, from North America to the high latitudes (Atlas et al., 2003). TOMCAT monthly mean concentrations of O_3 and NO_x from CTRL, NEWC and HETC have been averaged over the region 60°- 85°N, 60°-105°W which covers the area of high latitude flights, giving an estimation of the average background concentrations of NO_x and O_3 in TOMCAT. Average concentrations observed from TOPSE flights in March within this region are shown in Table 4.7 along with MOZART simulated concentrations interpolated to the flights from the study Tie et al. (2003). Between the surface and 600 hPa, the CTRL and NEWC simulations estimate concentrations of NO_x which are almost a factor of 3 and 2 higher than observations. N_2O_5 hydrolysis reduces NO_x by 56% in this region (comparing NEWC to HETC) bringing the simulated concentrations of 6.5 ppbv into much better agreement with the observed average of 8.5 ppbv. TOMCAT and MOZART also show better agreement when the uptake of N_2O_5 onto aerosol is considered. The response in O_3 is much smaller between the model simulations with O_3 concentrations increasing by 5% from CTRL and NEWC and decreasing by 12% from NEWC to HETC in line with the results shown in Section 4.3. The HETC O_3 concentrations are 18% lower than observed and 14% lower than simulated by MOZART. At higher altitudes, HETC does not do as well, with NO_x being 70% lower than observed (7.4 ppbv compared to 25 ppbv) and O_3 being 38% higher than observed (87.3 ppbv compared to 63.1 ppbv). The NO_x from HETC is similar to MOZART suggesting that both models underestimate sources of NO_x in the upper troposphere at high latitudes. MOZART does capture the observed concentrations of O_3 however suggesting that TOMCAT overestimates O_3 in the upper troposphere. This is most likely due to an overestimation of stratospheric O_3 being mixed into the troposphere due to a relatively low vertical resolution around the tropopause.

4.8 Evaluation of simulated hydrocarbons

Figure 4.16 shows simulated and observed concentrations of acetone (Me_2CO), ethene (C_2H_4), ethane (C_2H_4), propene (C_3H_6), propane (C_3H_8), butane (C_4H_{10}) and toluene (C_7H_8). CTRL only

Figure 4.16 Surface comparisons of observed and simulated hydrocarbons from CTRL, NEWC and HETC. From top to bottom: acetone (Me_2CO), ethene (C_2H_4), propene (C_3H_6), propane (C_3H_8), butane (C_4H_{10}) and toluene (C_7H_8).

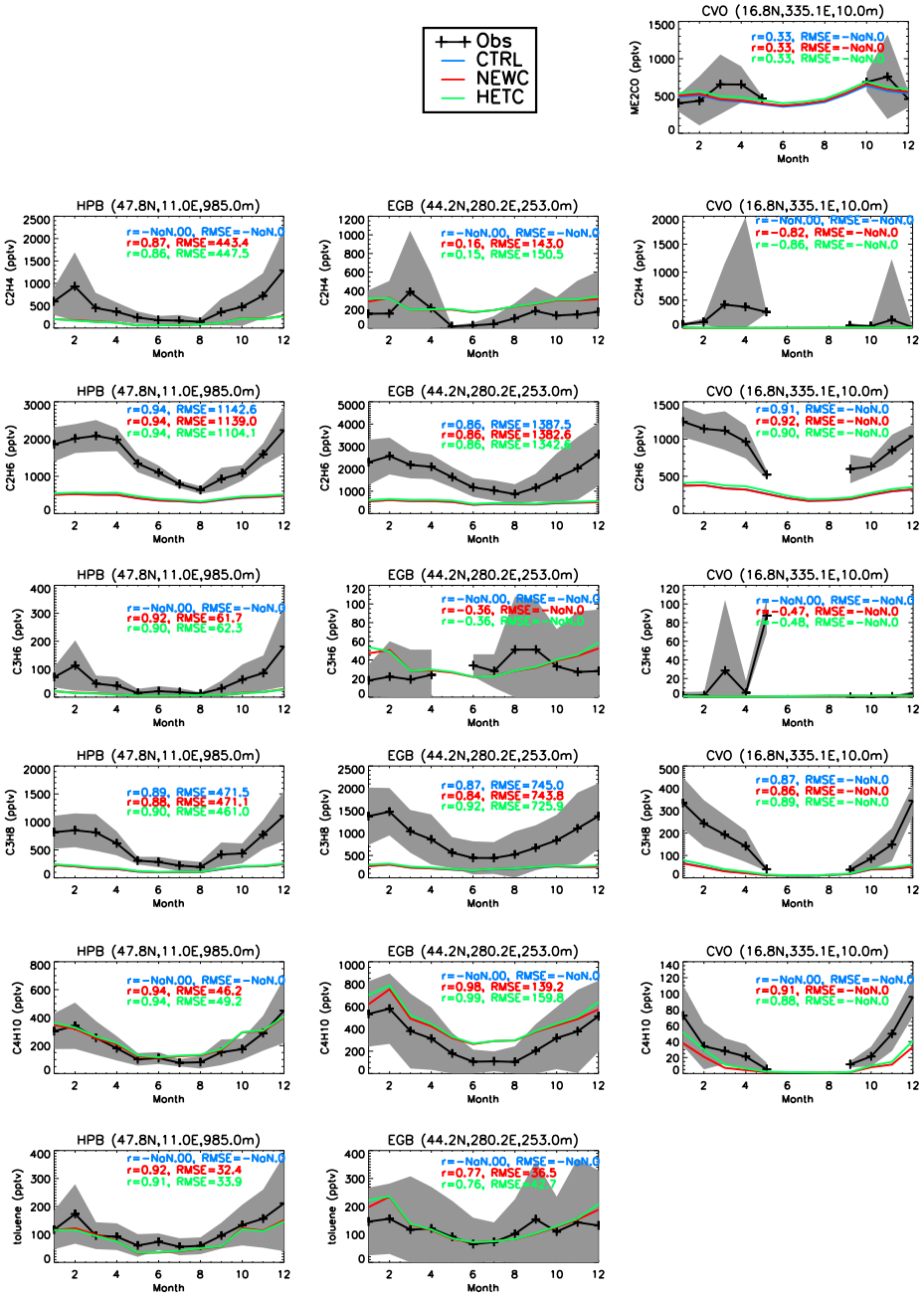

has output for the trace gases acetone, ethane and propane because the other species are not included in the standard chemistry scheme. Primary loss for these NMHC are by reaction with OH and since anthropogenic emissions are not monthly-varying, the seasonal cycle follows a pattern that reflects the minimum and maximum OH concentrations, similar to CO. HPB and EGB are located near industrialised regions in Europe and North America (see Figure 4.12) therefore high concentrations of NMHC are observed. EGB shows higher concentrations of ethane and propane

and HPB shows higher concentrations of ethene and propene. Ethane and propane have similar sources as do ethene and propene, explaining this pattern. At HPB the model captures the seasonal cycle of each NMHC with correlations of between 0.86 and 0.94 for all three simulations. However, in the cases of ethene and propene, the model does not capture the amplitude of seasonal cycle in these gases due to a winter underestimate. Ethane and propane are underestimated throughout the year suggesting the emissions of these gases are too low in the model. The model has the largest RMSE for ethane out of all the trace gases shown in Figure 4.16. HETC shows the lowest RMSE out of the three simulations due to the lower OH concentrations (see Table 4.2). Conversely, the model reproduces observed butane and toluene to within 1 standard deviation throughout the year suggesting that the sources of these two gases have been well estimated in the AR5 emissions estimates. AT EGB, the model also underestimates ethane and propane, however, due to the higher concentrations at EGB compared to HPB, the RMSE is higher (1342.6 pptv compared to 1104.1 pptv for ethane and 725.9 pptv compared to 461.0 pptv for propane for HETC). Due to the lower concentrations of ethene and propene, the model does not underestimate the concentrations in the winter. This suggests that the regional difference in ratios of NMHC emissions are not represented in the AR5 emissions estimates and therefore by extension, the model is unlikely to capture the observed concentrations. Again, toluene and butane show good agreement between the model and observed values.

4.9 Summary

Two new developments have been implemented into the TOMCAT model. The first being the extension of the organic chemistry scheme by the addition of NMHC emissions and chemistry. The second being the heterogeneous uptake of N_2O_5 by aerosol. The impacts of these two new updates have been discussed and then the model has been evaluated against surface observations and satellite retrievals. The oxidation of the additional NMHC leads to a 4-5% increase in total atmospheric CO, with the biggest impact occurring during spring due to the onset of photochemistry. O_3 was also increased by 2-4% and there was an overall increase in the burden of HO_x due to a 3-4% increase in HO_2. One of the biggest impacts was seen in the burden of PAN which was increased by 40-75%, with the largest impact during the NH winter. As more NO_x formed PAN rather than HNO_3, less NO_y was lost through wet deposition. Due to the fact that the majority of the additional hydrocarbon emissions occurred in the NH, these impacts were seen most clearly in the NH.

In agreement with previous studies, the addition of N_2O_5 uptake led to a substantial decrease of between 20-47% in the NO_x burden. The biggest impact was seen during the winter in the NH due to the long hours of darkness and low temperatures making this an efficient loss route. Lower concentrations of NO_x led to a reduction in the O_3 burden of 4-6%. The biggest impact was seen

during spring when photochemistry becomes more active in the NH. Due to the loss of O_3, OH was also reduced by 7-8%. Aerosols are present in both hemispheres and therefore these impacts were seen globally, however, as more NO_x is emitted in the NH, the impacts in this region were greater than in the SH.

An evaluation of the simulated annual global mean concentrations of OH showed that the model concentrations were within estimates inferred from observations, however, there was a missing source of OH in the upper troposphere. The model with both new updates was shown to improve OH concentrations at the surface in the NH due to reduction of OH from the loss of NO_x by N_2O_5 uptake.

Simulated CO was compared to retrievals from the MOPITT for the year 2008. Total column CO revealed the standard version of the model (CTRL) to underestimate CO in the NH and overestimate CO in the SH. When both of the updates were put into TOMCAT, the model showed a much better agreement with MOPITT CO in the NH due to the increase in CO throughout the NH. CO was also increased, to a lesser extent, in the SH which further increased the already existing positive bias. A regional analysis of the model with MOPITT in the NH and at surface stations revealed that even with the improved version of the model (HETC), TOMCAT still underestimated CO in winter and spring and overestimated CO in the autumn. In general, the model showed the best agreement in the summer. The model showed the largest winter/spring biases at stations close to Asia, suggesting Asian emissions are underestimated in the IPCC AR5 anthropogenic emissions.

Comparisons of simulated O_3 with measurements made at surface stations within the Arctic showed very good agreement. The main failing of the model was due to the lack of halogen chemistry which meant the model was unable to capture the very low concentrations of O_3 observed at BRW during spring. O_3 was found to be overestimated in remote marine regions at surface stations thought to be due to inefficient destruction of O_3. Using aircraft observations from the TOPSE campaign from 2000 which took measurements in the Arctic showed that the addition of N_2O_5 uptake in the model greatly improved simulated NO_x and O_3 during the spring at high latitudes. However, the model was found to overestimate O_3 in the upper troposphere, which is believed to be due to an overestimation of stratospheric O_3 due to low vertical resolution.

Surface observations of NHMC showed that ethane and propane are consistently underestimated throughout the year and ethene and propene are underestimated in the winter due to the emissions. Acetone and the newly included butane and propane were found to agree to within 1 standard deviation of the mean of the observations. The additional production of PAN from the oxidation of the new hydrocarbons led to much better agreement with the observations. Total NO_y was found to be overestimated during the summer and needs to be investigated further.

Chapter 5

Source contributions to Arctic CO and O_3

5.1 Introduction

It was first realised that the Arctic is a major receptor of atmospheric traces gases and aerosols in the 1950s, however, little was known about the sources (Shaw, 1995). By the mid-1980s it was discovered that the high concentrations of pollutants observed in the Arctic in winter and spring were due to long-range transport of emissions from Eurasia and North America (Rahn, 1985). Since then, there have been a number of source attribution studies aiming to quantify the burden of different species transported to the Arctic from lower latitudes (e.g., Koch and Hansen (2005); Stohl (2006); Bourgeois and Bey (2011)). The results from these studies show conflicting evidence for which region is the dominant source of Arctic trace pollutants. Some of these studies consider different species and therefore results are expected to vary, as the lifetime of a gas is related to the quantity that reaches the Arctic (Eckhardt et al., 2003). However, those considering the same species also draw different conclusions. For example, Shindell et al. (2008) and Fisher et al. (2010) both considered the anthropogenic sources of CO. Shindell et al. (2008) found that when CO is averaged annually, European emissions dominate in the lower troposphere and East Asian emissions dominate in the upper troposphere. Conversely, Fisher et al. (2010), who only considered April 2008, found North American emissions to dominate throughout the troposphere. For these studies, differences between definitions of the source region boundaries, emission totals and the season being considered are all likely to contribute to differences in the interpretation of results. It is therefore important to differentiate between which regions have the highest transport efficiency and which regions contribute the highest absolute burdens due to a combination of efficient transport and high emissions. This will help us to understand which regions contribute

the biggest absolute burdens and which regions will offer the biggest reductions in Arctic burdens if emissions are reduced by a certain fraction.

In this chapter a fixed lifetime tracer, which has been implemented into the TOMCAT model, is used to compare the transport efficiency from different anthropogenic source regions to the Arctic throughout the year. This removes any impact of OH variability on the Arctic burden, which would affect trace gases such as CO, and reveals the seasonality in transport only. It has been observed that anthropogenic emissions are not the only source of pollutants in the Arctic, with fires contributing large fractions to the budgets of species such as CO during the spring and summer (Stohl, 2006; Stohl et al., 2007; Warneke et al., 2010). For this reason, CO is used to consider the impact of anthropogenic, natural and fire emissions on the burden of CO. Realistic CO tracers decayed by monthly varying OH are used to capture both the transport efficiency and seasonality in OH. Due to the lifetime of CO being 1-6 months it can undergo long-range transport making it a useful tracer of such emissions. This work is the first to calculate the different contributions to Arctic CO from different types of fires (e.g., agricultural and forest fires) and compare them to anthropogenic sources throughout the year.

There is a need to understand the sources of O_3 because of its potential contribution to warming in the Arctic. Shindell et al. (2008) investigated the sensitivity of Arctic O_3 to a 20% reduction in NO_x emissions from the different anthropogenic regions of North America, Europe and Asia. They found North America to be the dominant source of O_3 in the Arctic which differed from those of CO in their study. This shows that the complex chemistry which governs O_3 production results in different regional sensitivities compared to other gases. Therefore, the newly developed full-chemistry version of the model is also used in this chapter to compare the source contributions to Arctic O_3 from fires and anthropogenic emissions.

The model set-up for the fixed lifetime tracers, the realistic CO tracers decayed by OH and the full chemistry simulations are described in Section 5.2. Transport efficiency from different anthropogenic regions in the model is discussed and compared to previous studies in Section 5.3. The CO tracer and CO from the full chemistry simulation is compared to observations in Section 5.4. Then the major source contributions to the CO budget are shown in Section 5.5. Finally, the results from the full chemistry simulations comparing the contributions to O_3 from fires and anthropogenic sources are discussed in Section 5.6.

Figure 5.1 Regions used for the anthropogenic regional tracers.

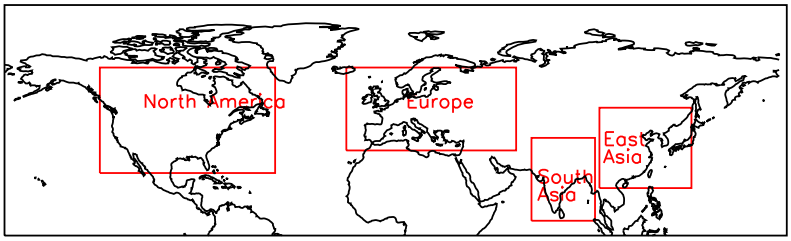

5.2 Model set-up and methodology

5.2.1 Fixed lifetime tracer simulation

Five anthropogenic tracers with fixed lifetimes of 30 days were implemented into the TOMCAT model. These have been summarised in Table 5.1. CO emissions from the IPCC AR5 dataset for the year 2000 (described in Section 3.4.1.1) were used to define the major anthropogenic source regions. These emissions contain no seasonal variability and therefore the only source of variation in the Arctic burdens will be that of transport. The first tracer (CO30_AN) includes all global sources of CO anthropogenic emissions. The other four tracers include CO emissions from one of the regions shown in Figure 5.1. These regions were chosen as they represent the locations of major anthropogenic CO emissions in Europe, North America, East Asia and South Asia. The simulation was spun-up for 1 year from January to the end of December 1989. It was then run for 20 years from January 1990 to December 2009 using ECMWF ERA-Interim meteorological fields. This meteorological data is available for the whole period from 1989-1990 and was chosen to avoid any inconsistencies which may be caused by switching between reanalysis versions.

5.2.2 Realistic CO tracer simulation

The realistic CO tracer simulation was set-up to include 16 CO tracers which are summarised in Table 5.2. Each tracer was decayed by reaction with OH only, using the CO + OH reaction rate from the full chemistry version of TOMCAT (see Appendix A). The model was provided with monthly mean OH concentration fields which vary monthly, but contain no interannual variability. These fields were created for the model inter-comparison project, TRANSCOM (Patra et al., 2011), and are based on the estimates by Spivakovsky et al. (2000).

Each tracer included CO emissions from one or all of the anthropogenic, natural or fire sources. These were created from the IPCC AR5 anthropogenic emission estimates for the year 2000, POET natural emissions and GFED v3.1 biomass burning emissions (for more details see Section 3.4).

Table 5.1 List of fixed 30-day lifetime CO tracers used to evaluate the efficiency of transport to the Arctic.

Simulation ID	Description
CO30_AN	30-day lifetime tracer of all anthropogenic CO emissions.
CO30_NA	30-day lifetime tracer of North American anthropogenic CO emissions in the region 230-310 E and 24-66 N only (see Figure 5.1).
CO30_EU	30-day lifetime tracer of European anthropogenic CO emissions in the region 342.5-60 E and 33-66 N only (see Figure 5.1).
CO30_EA	30-day lifetime tracer of East Asian anthropogenic CO emissions in the region 98-140 E and 18-50 N only (see Figure 5.1).
CO30_SA	30-day lifetime tracer of South Asian anthropogenic CO emissions in the region 67-96 E and 5-38 N only (see Figure 5.1).

Figure 5.2 Annual total CO emissions for all main sources tracers, all anthropogenic tracers and all fire tracers (averaged over 1997-2009). Left) Emissions for CO_TOT, CO_AN, CO_TF, CO_NAT, and CO_ISOP. Middle) Emissions for total anthropogenic and regional tracers tracers: CO_AN, CO_NA, CO_EA and CO_SA (note that regional tracers do not add up to total anthropogenic emissions). Right) Emissions for total climatological biomass burning emissions and for each fire type: CO_TF, CO_AGR, CO_DEF, CO_FOR, CO_PEA, CO_SAV and CO_WOO. These emissions are used for the realistic lifetime tracers and the anthropogenic 30-day fixed lifetime tracer. Note different y-axis.

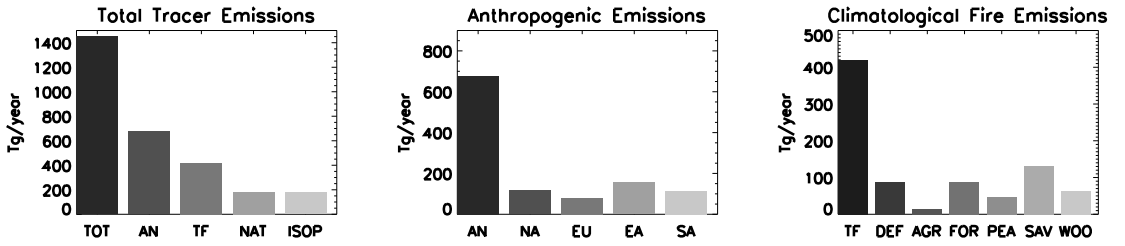

The use of the newly available GFED v3.1 emission dataset allowed contributions from different types of fires to be separated into agricultural, deforestation, forest, woodland, peat and savannah fires. These and total fire emissions are available for 1997 to 2009, allowing a long simulation to be done which accounts for the inter-annual variability in fire emissions. Secondary production of CO from hydrocarbons was accounted for by increasing all of the direct anthropogenic and biomass burning emissions by 18.5% and 11%, respectively following the estimates of Duncan et al. (2007). As with the fixed lifetime tracer (see Section 5.2.1), four different tracers were used to represent the major anthropogenic emission regions of North America, Europe, East Asia and South Asia (see Figure 5.1). As well as direct natural emissions, CO production from the biogenic

Table 5.2 Description and emissions of all realistic lifetime CO tracers used for analysing the burden of CO in the Arctic.

Tracer ID	Tracer name	Sources and emissions
CO_TOT	Total CO tracer	Direct emissions from anthropogenic, natural and biomass burning sources. Secondary production of CO from the oxidation of methane, isoprene and NMHC.
CO_AN	Total anthropogenic CO tracer	Direct anthropogenic emissions and secondary production of CO from the oxidation of anthropogenic NMHC.
CO_TF	Total biomass burning CO tracer	Direct biomass burning emissions and secondary production of CO from the oxidation of NMHC.
CO_NAT	Natural CO tracer	Direct biogenic and oceanic CO emissions.
CO_ISOP	Isoprene oxidation tracer	Secondary production of CO from the oxidation of isoprene.
CO_CH4	Methane oxidation tracer	Secondary production of CO from the oxidation of methane.
CO_AGR	Agricultural fire CO tracer	Direct emissions from agricultural fires and secondary production of CO from the oxidation of NMHC.
CO_DEF	Deforestation fire CO tracer	Direct emissions from deforestation fires and secondary production of CO from the oxidation of NMHC.
CO_FOR	Forest fire CO tracer	Direct emissions from forest fires and secondary production of CO from the oxidation of NMHC..
CO_PEA	Peat fire CO tracer	Direct emissions from peat burning and secondary production of CO from the oxidation of NMHC.
CO_SAV	Savannah fire CO tracer	Direct emissions from savannah fires and secondary production of CO from the oxidation of NMHC.
CO_WOO	Woodland fire CO tracer	Direct emissions from woodland fires and secondary production of CO from the oxidation of NMHC.
CO_NA	North American anthropogenic CO tracer	Anthropogenic emissions from the region 230-310 E and 24-66 N only (see Figure 5.1).
CO_EU	Europe anthropogenic CO tracer	Anthropogenic emissions from the region 342.5-60 E and 33-66 N only (see Figure 5.1).
CO_EA	East Asian anthropogenic CO tracer	Anthropogenic emissions from the region 98-140 E and 18-50 N only (see Figure 5.1).
CO_SA	North American anthropogenic CO tracer	Anthropogenic emissions from the region 67-96 E and 5-38 N only (see Figure 5.1).

emission of isoprene was also accounted for. Isoprene emissions were assumed to be oxidised immediately to CO, similar to the treatment of Duncan et al. (2007), and therefore were calculated by scaling the TOMCAT isoprene emissions from 568 Tg(C_5H_8)/year to yield 127 Tg(CO)/year. The total emission for each tracer is shown in Figure 5.2 showing that on average anthropogenic emissions are the dominant emission of CO in the atmosphere (when compared to an average of all fire emissions between 1997-2009).

One tracer also represented the production of CO from the oxidation of CH_4 by OH. Instead of a direct emission, the production of CO from CH_4 needed to be estimated. This was done using monthly mean CH_4 fields from a previous standard full-chemistry TOMCAT simulation for 2008 and the TRANSCOM monthly mean OH field. Using the TOMCAT reaction rate for CH_4 with OH, the rate of production of CO was estimated by assuming that for each molecule of CH_4 oxidised, one molecule of CO is formed. The simulation was spun-up for 1 year and then run for a period of 12 years from 1998 - 2009 using off-line ECMWF ERA-Interim winds.

5.2.3 Full-chemistry model set-up

The general set-up for the full-chemistry version of the model is described in detail in Chapter 3. Six different simulations were performed using the updated version of the model (evaluated in Chapter 4). One control simulation was performed with all emissions included and then a further five were performed with emissions removed from different regions. These simulations are summarised in Table 5.3. The difference between fc_tot and the other simulations were used to calculate the contributions from each of the sources considered. These contributions will be referred to as TF (for fc_tot - fc_tf), BF (for fc_tot - fc_bf), NA (for fc_tot - fc_na), EU (for fc_tot - fc_eu) and AS (for fc_tot - fc_as), representing total fires, boreal fires (all fires $>$50°N), North American anthropogenic, European anthropogenic, Asian anthropogenic sources. The non-linearity of O_3 production with different concentrations of NO_x means that the contributions are unlikely to add up linearly to O_3 simulated in fc_tot, however, this method has been used by other studies previously (e.g., Shindell et al. (2008)).

All emissions were created from the IPCC AR5 anthropogenic emission estimates for the year 2000, POET natural emissions and GFED biomass burning emissions. CO and NO_x fire emissions were taken from GFED v3.1 dataset and other species which were not available were created from the GFED v2 dataset. As the interest was in the average impact of the sources instead of the impact during one individual year, an average of the GFED fire emissions from 1997-2008 were used instead of any individual year. Each simulation was spun-up for 1-year and then run for the year 2000 using ECMWF ERA-Interim winds.

Table 5.3 List of full chemistry simulations performed for Arctic O_3 source contribution analysis.

Simulation ID	**Description**	**Emissions**	
		Tg(CO)/year	Tg(NO_2)/year
fc_tot	Control simulation with emissions of all species from all sources.	1151.08	146.51
fc_tf	As control simulation but with all fire emissions removed.	789.17	131.16
fc_bf	As control simulation but with all fire emissions removed above 50°N.	1110.76	144.54
fc_na	As control simulation but with all anthropogenic emissions removed in the North America region shown in Figure 5.1.	1045.84	122.37
fc_eu	As control simulation but with all anthropogenic emissions removed in the Europe region shown in Figure 5.1.	1080.07	123.47
fc_as	As control simulation but with all anthropogenic emissions removed in both East and South Asia regions shown in Figure 5.1.	907.60	122.36

5.3 Transport efficiency from the major anthropogenic emission regions

Figure 5.3 shows the seasonal cycle of the total and regional 30-day fixed lifetime anthropogenic tracers, at five different surface stations north of 60°N. The monthly mean absolute concentrations, which have been interpolated to the station location, have been divided by the monthly total emissions. This removes any regional difference in emissions and gives the contribution of each region in ppbv of tracer at each station per Tg emitted per month due to transport alone (this will be referred to as the transport efficiency). Firstly, by considering the total anthropogenic emissions tracer (CO30_AN), it can be seen that the stations located at lower latitudes (STM and ICE) experience higher transport efficiencies. These stations are both located in Atlantic and are therefore more likely to experience more frequent transport from the mid-latitude emission regions due to being closer to the Atlantic storm track. Even so, all stations show similar seasonality in the transport, with a peak in transport efficiency in winter and spring and a minimum in summer/autumn. This is as expected due to faster and more efficient poleward transport during the cold winter months compared to the summer months (Raatz and Shaw, 1984).

By considering the regional tracers in Figure 5.3, the efficiency of the different transport pathways, which emissions from Europe, North America, East Asia and South Asia undergo, can be compared. It is clear that European emissions experience much more efficient transport to all of the surface stations during winter and spring, apart from at ICE which is equally sensitive to North American emissions. ICE is located in the Atlantic which is particularly sensitive to the easterly flow of North American air (Barrie, 1986). During summer and autumn, the transport efficiency from Europe is reduced due to weaker winds resulting in Europe's transport efficiency becoming comparable to North America's. Again, due to the location of ICE, it is more sensitive to emissions from North America rather than Europe during the summer. BRW is unique in the fact that it has comparable transport efficiencies from Europe, North America and East Asia in the summer, even though transport from low latitude regions of Asia is thought to be less efficient than the other regions (Klonecki et al., 2003; Stohl, 2006). This is due to BRW being located in Alaska which is particularly sensitive to the typical NE Asian outflow (Barrie, 1986). In general, East Asia shows the third largest transport efficiency and South Asia shows the smallest. in contrast to Europe, East Asia shows a peak in transport efficiency in the summer and a minimum in the winter. In the Arctic, the winter is characterised by surface cooling and no daylight which results in very cold temperatures. As poleward transport tends to follows lines of constant potential temperature (Klonecki et al., 2003), the cold Arctic air acts as a barrier to air which has originated from warmer regions, such as Asia and North America. This is termed the polar dome and can extend down to regions of 40°N in the winter covering parts of Europe and Siberia (Bottenheim et al., 2004). This explains why Europe has a much higher transport efficiency in the winter compared to the other

Figure 5.3 Monthly mean 30-day lifetime anthropogenic total tracer CO30_AN (left) and North American, European, East Asian and South Asian anthropogenic regional tracers (CO30_NA, CO30_EU, CO30_EA, CO30_SA) (right) averaged over the period 1990 - 2009 at Arctic stations. The model concentrations have been interpolated to the station location and divided by total monthly CO emissions used in the model (units of ppbv/Tg (emitted)/month).

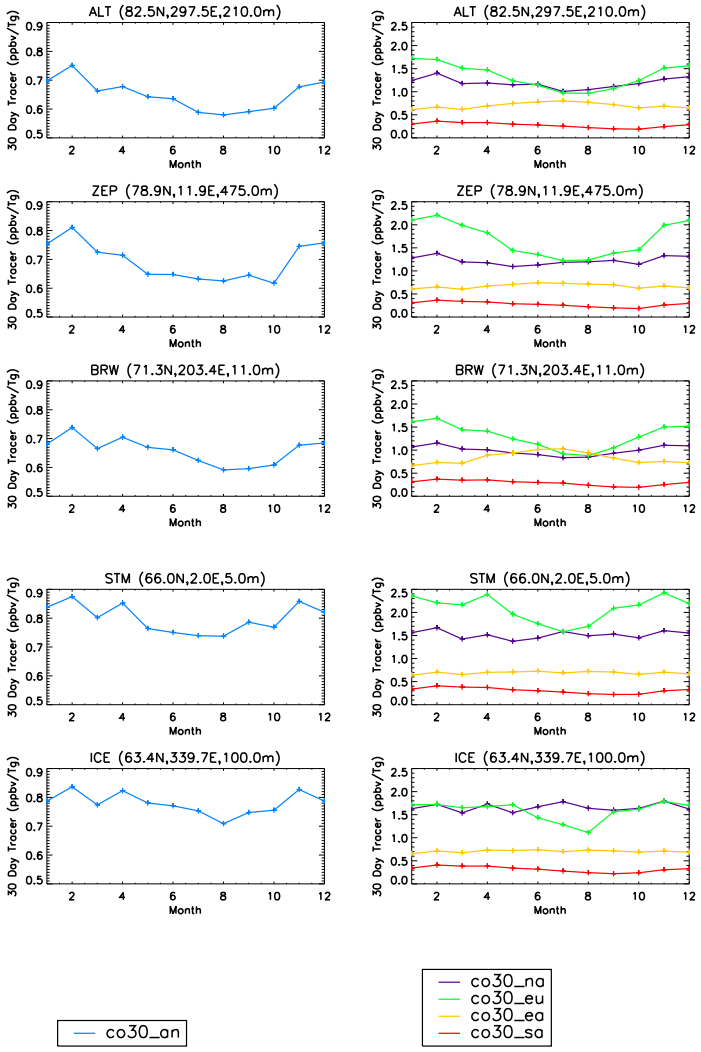

regions. During the summer, temperatures increase, reducing the effect of the polar dome allowing air from East Asia to be mixed down to the surface more effectively which is seen by the increase in the transport efficiency at these surface stations.

So far, the impact of the efficiency of transport has only be considered at surface stations. Figure 5.4 shows the seasonal zonal mean transport efficiency throughout the troposphere (in ppbv/Tg(emitted)/season) calculated from the 30-day lifetime tracers averaged over 1990-2009. There are clear differences between the regional tracers showing that emissions undergo different transport pathways depending on the source regions. In general, North American, East Asian and South

Figure 5.4 Seasonal zonal mean concentrations for the 30-day regional anthropogenic tracers (in ppbv/Tg(emitted)/season).

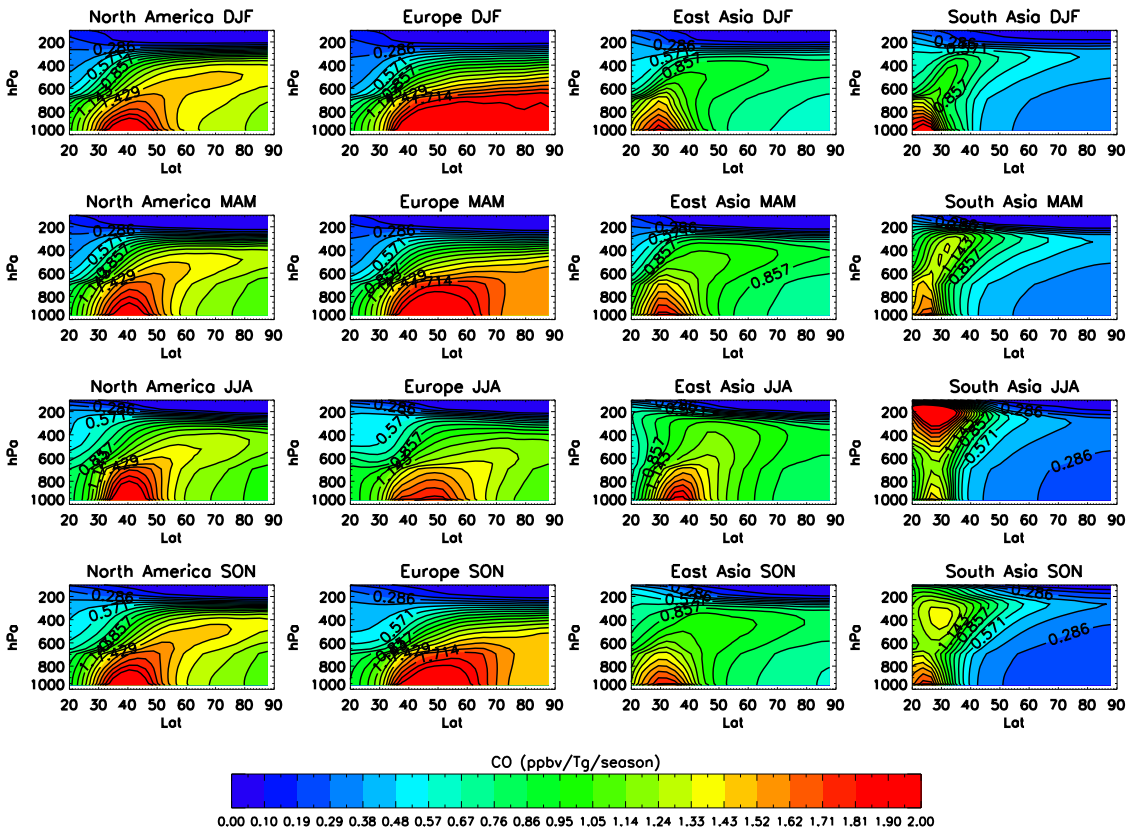

Asian emission transport pathways are characterised by lofting of emissions from the surface to higher altitudes, then poleward transport. European emissions however are mostly transported at much lower levels. This is because emissions from Asia and North America are typically lifted by warm conveyor belts to the mid to upper troposphere (Stohl and Eckhardt, 2004). Similar pathways have been identified in CTMs and Lagrangian models previously (Klonecki et al., 2003; Stohl, 2006). Due to these pathways the largest contributions to the Arctic from North America, East Asia and South Asia occur at higher altitudes where North American emissions dominate in the winter followed by East Asia. South Asian air is subject to much stronger uplifting due to deep moist convection near the tropics. This is particularly strong in the summer (JJA) during the monsoon season. Therefore, emissions from South Asia are transported at higher altitudes compared to East Asia and North America. Due to this, and South Asia being located the furthest south, it has smallest overall contribution in the Arctic troposphere throughout the year. Europe dominates in the lower troposphere during winter, spring and autumn due to the polar dome, however, there is still evidence of mixing down to the lower troposphere from North American and Asian air. During the summer, Europe shows comparable contribution to North America and East Asia during summer as seen at the surface in Figure 5.3. The relative contributions found here agree with the

study of Klonecki et al. (2003) who also used a fixed lifetime tracer to look at transport during the months of January and July. This gives us confidence in the ability of TOMCAT to capture the main transport pathways to the Arctic. The results here also contribute to previous studies (Klonecki et al., 2003; Stohl, 2006) by offering a monthly climatology of the transport efficiency from the major anthropogenic regions at Arctic surface stations and throughout the troposphere for the years 1990-2009.

5.4 Comparisons of simulated CO to surface observations

Section 5.3 showed that the model captures the altitudinal differences in the transport pathways to the Arctic from the major industrialised regions in the NH. This gives confidence in using the TOMCAT model to quantify the major sources of pollution in the Arctic using both the realistic lifetime CO tracers (described in Section 5.2.2) and the full chemistry simulations (described in Section 5.2.3). Firstly, as the simplified CO tracers have not been used previously, it is useful to compare the total tracer (CO_TOT), which includes all sources of CO, to CO calculated from the full chemistry version of the model (fc_tot) to evaluate the tracer model. These are both also compared to surface observations in Figure 5.5. The stations are the same as those used to evaluate the model in Section 4.5.2 and the station locations are shown in Figure 4.12 and listed in Table 4.4. The monthly mean CO tracer, CO_TOT, has been averaged over the years 1998-2009, whereas the full chemistry CO, fc_tot, is shown for the year 2000 only. For comparison, the observations are also shown as an average of the same 12-year period and for the year 2000 only. As found in Section 4.5.2, both the tracer and the full chemistry model generally capture the seasonal cycle throughout the globe with high correlations at most sites. Also, both model versions show similar biases, as seen previously, with NH CO being underestimated in the winter and spring and overestimated in the late summer and autumn. CO in the SH is also found to be consistently overestimated as previously seen in Section 4.5.2. There are some differences between the full chemistry model and the tracer model, however most are relatively small and could be caused by differences in meteorology during the year 2000 compared to an average over 1998-2009. However, one striking difference is seen at EIC and CYA in the SH. Here the simplified CO tracer has much lower CO compared to fc_tot CO, showing much better agreement with the observed magnitude of CO and a lower RMSE. This is attributed to the TRANSCOM OH, which is based on the Spivakovsky et al. (2000) estimates, having much higher concentrations compared to TOMCAT in the SH (see Figure 4.7). At the Arctic stations (ALT, ZEP, BRW, STM and ICE), both simulations shown here have RMSE values that are towards the lower end of the range 17-40 ppbv calculated from models from the inter-model comparison of Shindell et al. (2008), as found in Section 4.5.2.

Figure 5.5 Monthly mean CO calculated by the realistic lifetime CO tracer (CO_TOT) and the full chemistry model (from fc_tot) compared to observed CO at surface sites globally. CO from the full chemistry simulation is shown for the year 2000 and CO_TOT is shown averaged over 1998-2009. Grey shading and error bars show the observed and modelled standard deviation, respectively, when averaging over the period 1998-2009. (Note the different y-axis)

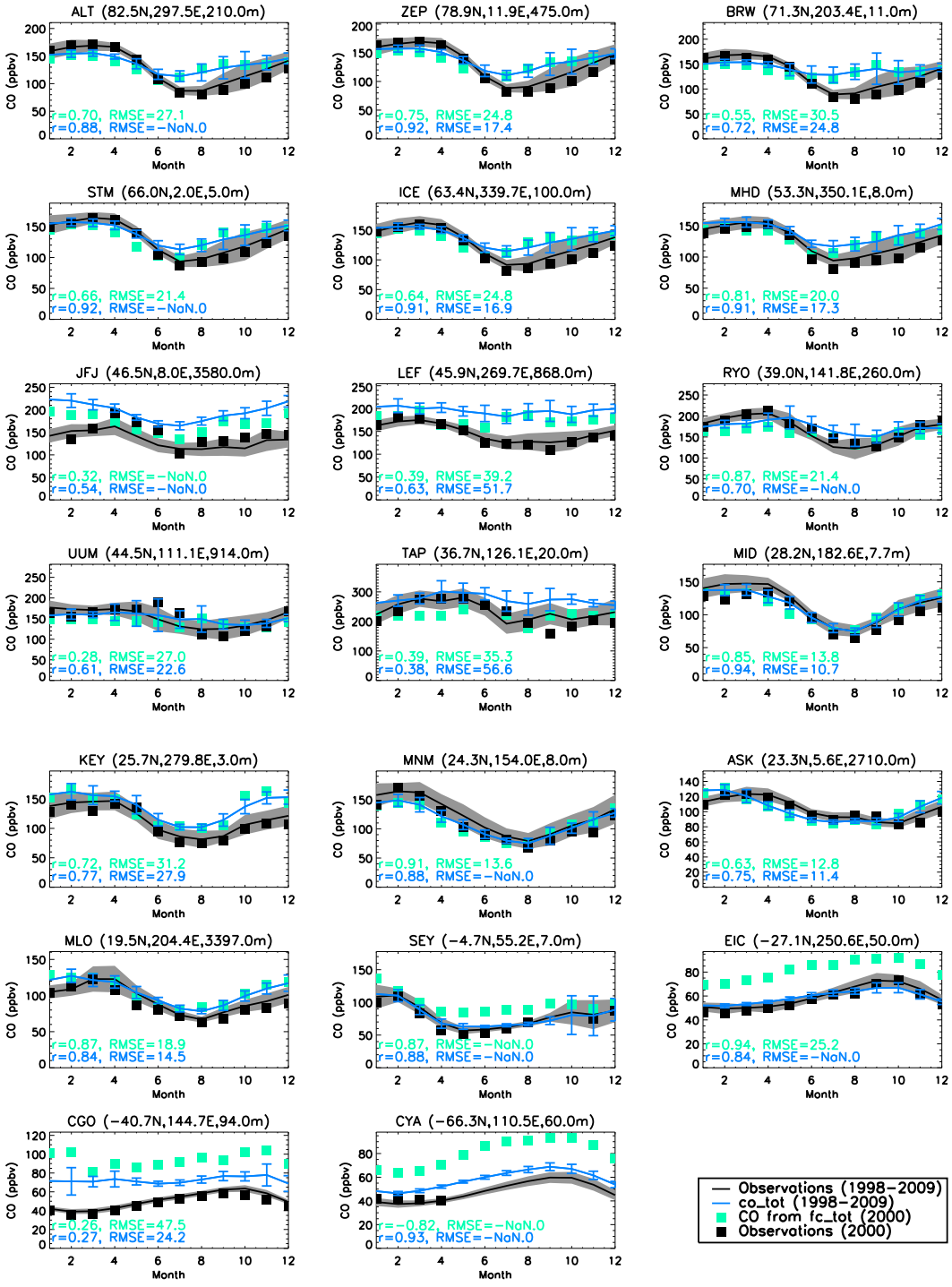

5.5 Seasonal source contributions to Arctic CO

In this section the realistic lifetime tracers described in Section 5.2.2 are used to diagnose the mean contributions to Arctic CO.

5.5.1 Contributions to Arctic total column CO.

Figure 5.6 shows the seasonal contribution from all the main source tracers as a fraction of the CO total tropospheric column averaged over 1998-2009 from the realistic CO lifetime tracer simulation. Anthropogenic emissions are the largest source of Arctic CO throughout the year, with a maximum contribution in spring (MAM) of ∼55-60% and a minimum in autumn (SON) and winter (DJF) of $<$ 40%. The second largest contribution comes from methane which shows a seasonal maximum in summer (JJA) of 30% and seasonal minimum in winter and spring of 20%. There is much more CO from methane oxidation in the tropics due to the high rate of methane destruction (Bloss et al., 2005) compared to the high latitudes. The third largest source of CO in the Arctic comes from fires with a seasonal maximum in summer of 15-25% and a minimum in winter of ∼8%. The summer maximum coincides with the biomass burning season in Alaska, Canada and Siberia where large fractions of CO is seen from boreal fires. Transport of these emissions into the Arctic is facilitated by their high latitude. Direct natural CO emissions and CO produced from the oxidation of isoprene both have a maximum contribution in autumn of 13-15% and 6% and minimum in spring of ∼7% and ∼2.5%, respectively. If we consider these two sources together, natural emissions can contribute up to 22% of CO in the autumn which is greater than the contribution from fires and almost as much as methane during this time of year.

Figure 5.7 shows the fractional seasonal contribution of the different forest fire types to the total forest fire tropospheric CO column. Due to fires exhibiting strong seasonal differences in emissions the majority of the seasonality seen in the contributions is due to emissions changes, not transport or OH monthly variations. Overall, the largest contribution to the Arctic CO fire burden comes from forest fires, with up to 80% of summer and autumn fire CO being from this source. A large fraction of forest fire emissions from the GFED v3.1 dataset occur in the boreal regions of Canada, North America and Siberia during the NH summer and autumn, making the Arctic particularly sensitive to forest fires in these regions at this time of year. Other fire tracers contribute $<$10% each to make up the rest of the budget during these season. The second largest overall contribution comes from Savannah fires which have a seasonal maximum in spring of 26-30%, where the other fire tracers contribute $<$15% each to the Arctic CO burden apart from forest fires which contribute ∼30%. A large fraction of agricultural fire CO can be seen originating from over Eurasia at quite high latitudes during Spring when agricultural fires exhibit a seasonal maximum contribution. Even though the average contribution over 1998-2009 is small compared to other

Figure 5.6 Mean seasonal fractional contribution of different sources to the total tropospheric CO column between 1998-2009 calculated from the realistic lifetime tracer simulations. Total tropospheric column from the tracers CO_AN, CO_TF, CO_NAT, CO_ISOP and CO_CH4 (top to bottom) are shown as a fraction of the CO_TOT total column for DJF, MAM, JJA and SON (left to right). (Note different colourbars).

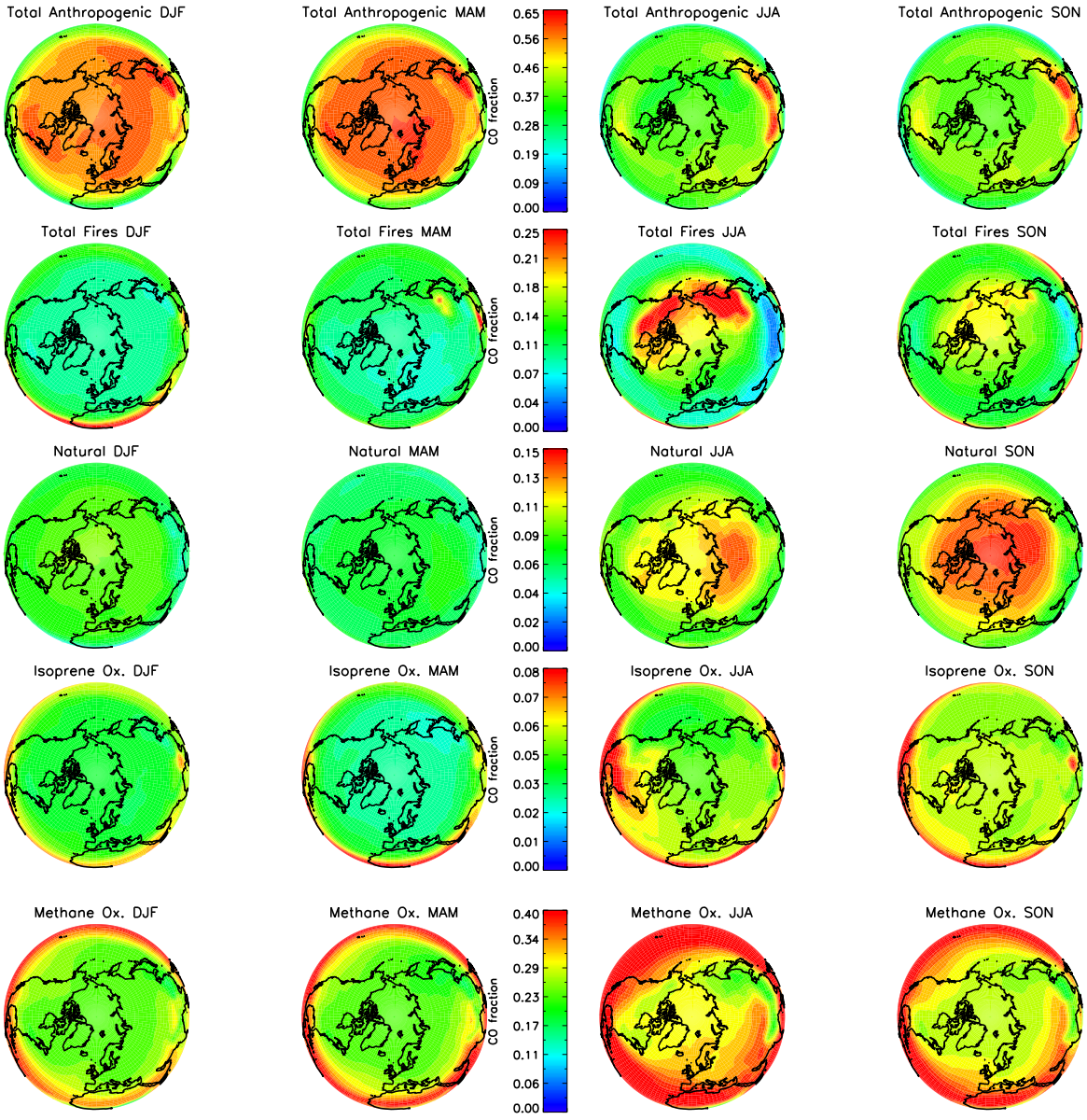

Figure 5.7 Mean seasonal fractional contribution of different fire sources to the total fire tropospheric CO column between 1998-2009 calculated from the realistic lifetime tracer simulations. Total tropospheric column from the tracers CO_AGR, CO_DEF, CO_FOR, CO_PEA, CO_SAV and CO_WOO (top to bottom) are shown as a fraction of the CO_TF total column for DJF, MAM, JJA and SON (left to right). (Note different colourbars).

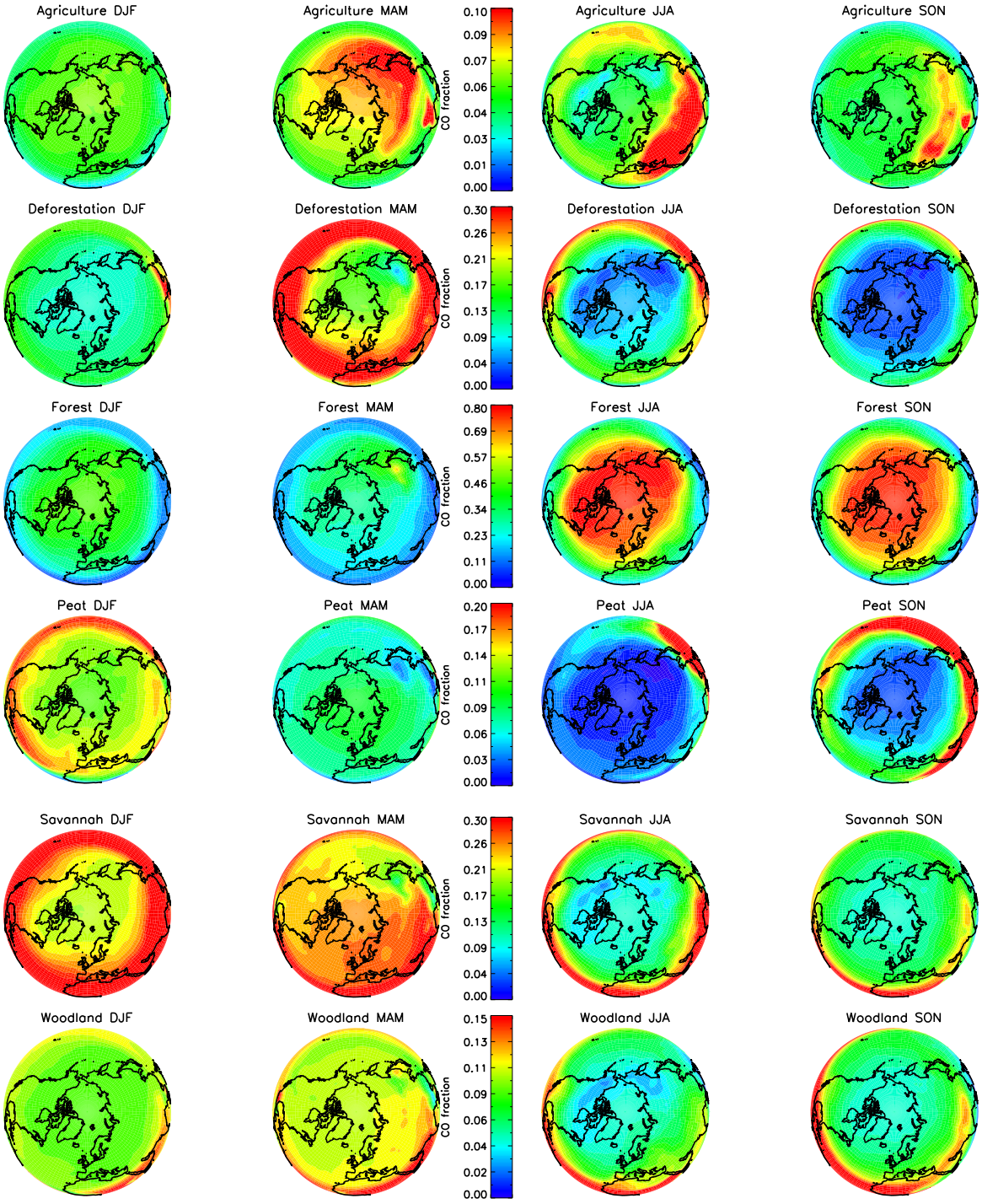

Figure 5.8 Mean seasonal fractional contribution of different anthropogenic sources to the total anthropogenic tropospheric CO column between 1998-2009 calculated from the realistic lifetime tracer simulations. Total tropospheric column from the tracers CO_NA, CO_EU, CO_EA and CO_SA (top to bottom) are shown as a fraction of the CO_AN total column for DJF, MAM, JJA and SON (left to right).

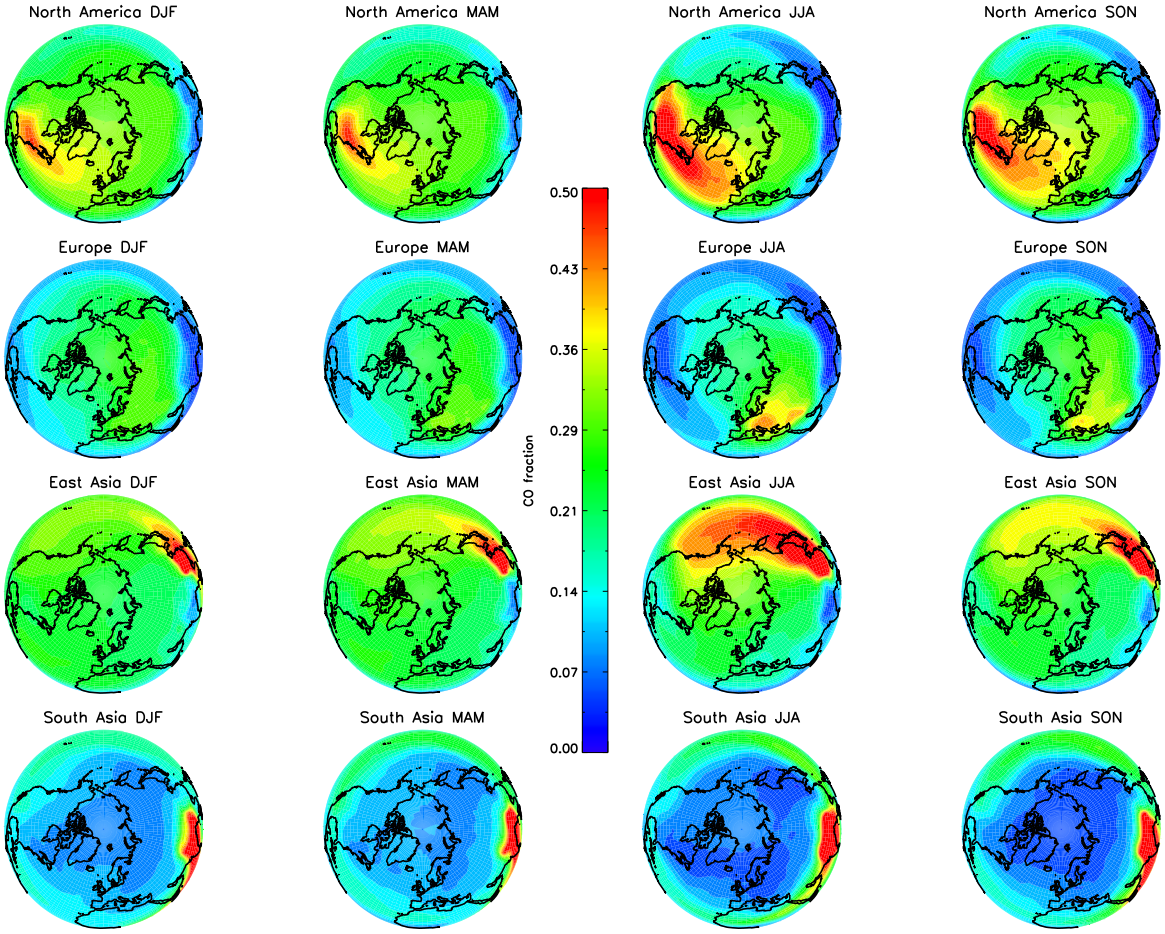

fire types, the location of these sources makes the Arctic sensitive to any increase in emissions that may occur in the future. This was seen in 2007 when unusually large agricultural fires occurred in Europe during the spring when transport is particularly efficient (see Section 5.3) and the burdens of trace gases in the Arctic were increased (Stohl et al., 2007).

Figure 5.8 shows the total column seasonal contribution of each regional anthropogenic tracer as a fraction of the total anthropogenic tracer, allowing the relative importance of emissions from each of the major Northern Hemispheric anthropogenic source regions of North America, Europe, East Asia and South Asia to be considered. Overall, South Asia contributes the smallest fraction of CO to the Arctic ($< 10\%$) throughout the year due a combination of smaller annual emissions compared to North America and East Asia (see Figure 5.2) and having the lowest transport efficiency (see Section 5.3). Europe has the second smallest contribution throughout the total troposphere

(<30%) even though it has been shown to have the highest transport efficiency in the lower and mid troposphere. This is because Europe has the smallest annual emissions (see Figure 5.2). East Asia shows the second largest contribution and North America shows the largest. In winter, the impact of East Asia is limited due to the presence of the polar dome whereas North America is still able to contribute large fractions of CO around Greenland and Svalbard. Elsewhere, North America, Europe and East Asia contribute almost equal fractions. In summer, CO is less well-mixed due to a shorter lifetime resulting in larger regional gradients. North American emissions contribute up to 40% to Arctic column CO around Greenland, and East Asian emissions contribute a similar amount close to Alaska and north-eastern Siberia.

Fisher et al. (2010) also considered anthropogenic and fire contributions to CO during April 2008. Their results show similar regional sensitivities as seen in Figure 5.8, with North American CO showing the largest impact in the area around Greenland and Asian CO having the largest impact around Alaska. However, they found anthropogenic Asian emissions to be the dominant source of Arctic CO in April 2008, with European emissions being the second largest source. They found North American emissions to be the least important anthropogenic source region of these three regions. This does not agree with the results presented here which have found North American emissions to have the largest contribution followed by East Asian, then Europe, then South Asia. However, two factors are likely to have contributed to the different results. Firstly, the interpretation of model results is likely to be sensitive to the emission totals used in each study. Fisher et al. (2010) performed a simple linear inversion based on aircraft data from April 2008 and reduced/increased the standard emissions used in their model accordingly. Compared to the emissions used for the work presented here, in April they emitted 56% less CO in their North American region (4.2 compared to 9.6 Tg(April)) and 29% more in their European region (9.1 compared 6.5 Tg(April)). As we have seen here, transport and emissions both play a role in which region dominates the Arctic CO burden and therefore this difference in emissions would explain why the results shown here disagree with those in Fisher et al. (2010). The second difference is that they also used a single Asian emission region, whereas here Asia has been separated into two regions, South and East. If these regions had been combined in this work, then the emissions would be very similar (23 compared to 21 Tg(April)) and the fractional contribution of anthropogenic Asian CO to the total burden would increase. They found the fires in April 2008 to have a very small contribution to the overall burden which agrees with results shown in Figure 5.6.

5.5.2 Contributions to Arctic surface CO.

As already discussed, the Arctic's CO burden exhibits different sensitivities to source regions at different altitudes, therefore it is useful to consider which sources are most important at surface stations which are regularly used by the scientific community. Figures 5.9 and 5.10 show the

absolute and fractional contribution to surface CO at stations which are north of 60°N. Anthropogenic emissions are the largest source of Arctic surface CO, contributing between 25 and 75% throughout the year, with the exception of BRW and ALT where fire emissions become equally important in summer. This is due to the location of these stations in Alaska and Canada which make them sensitive to fires in the summer (see Figure 5.6). Overall, methane oxidation is still the second largest source accounting for 20-25%, fires are the third largest source, contributing 10-30%, natural sources contribute around 10-15% and the smallest contribution is from isoprene oxidation accounting for $<$5%. The observed CO is also plotted in Figure 5.9 and highlights where the model under-predicts CO in the spring and over-predicts observed CO in the winter. The model was evaluated in Chapter 4 and it was suggested that an underestimation of convection in the summer/autumn near sources may contribute to an overestimation in CO at the surface. This may result in a slight bias in the absolute contributions at the surface. In the spring, the underestimation in CO is thought to be mostly caused by underestimated Asian emissions. With corrected CO emissions from Asia anthropogenic CO would contribute even larger fractions to the total CO.

Generally the North American anthropogenic tracer contributes the largest fraction 25-40% to the anthropogenic surface CO. However, at BRW, eastern Asian emissions dominate with over 25-35% coming from this region in summer. Again this is due to the location of this station. Europe shows the third highest contribution of 15-30% as seen seen in the total columns (see Figure 5.8) but accounts for larger fractions. All other anthropogenic CO (other_anth) has the fourth smallest contribution and South Asian emissions account for the smallest overall fraction.

As already noted, forest fires are the dominant source of summer fire CO. At the surface, they contribute over 80% of the summer/autumn fire CO burden which is similar to the total column fire CO (see Figure 5.7). The different seasonality in the different fire tracers can also be seen at the surface with savannah fires contributing $\sim$25% in March and April and deforestation contributing $\sim$ 20% in May. Peat, agricultural and woodland fires contribute the smallest amounts to the CO fire burden.

5.5.3 Contributions to the Arctic burden of CO at different altitudes.

As emissions from different regions undergo different transport pathways to the Arctic (see Section 5.3) it is likely that source contributions vary with altitude. Figure 5.11 shows the total tropospheric CO burden from all of the realistic CO tracers at latitudes $>$ 66 °N summed over three altitude bins, 0-2 km, 2-5 km and 5 km up to the tropopause. As seen in Figure 5.6, the anthropogenic pollution is the dominant source of Arctic CO at all altitudes, contributing between 1 and 5 Tg of CO (25-60%), depending on altitude and month. The maximum burden occurs in spring and a minimum in autumn. During autumn, fires and methane contribute a similar magnitude of CO (1-2 Tg (25-30%)) in all altitude bands apart from the highest, where fires contribute a smaller fraction

Figure 5.9 Mean monthly contribution of different tracers to total CO (CO_TOT) (left) , total anthropogenic CO (CO_AN) (middle) and total fire CO (CO_TF) (right) at 5 surface stations located $> 60°$N.

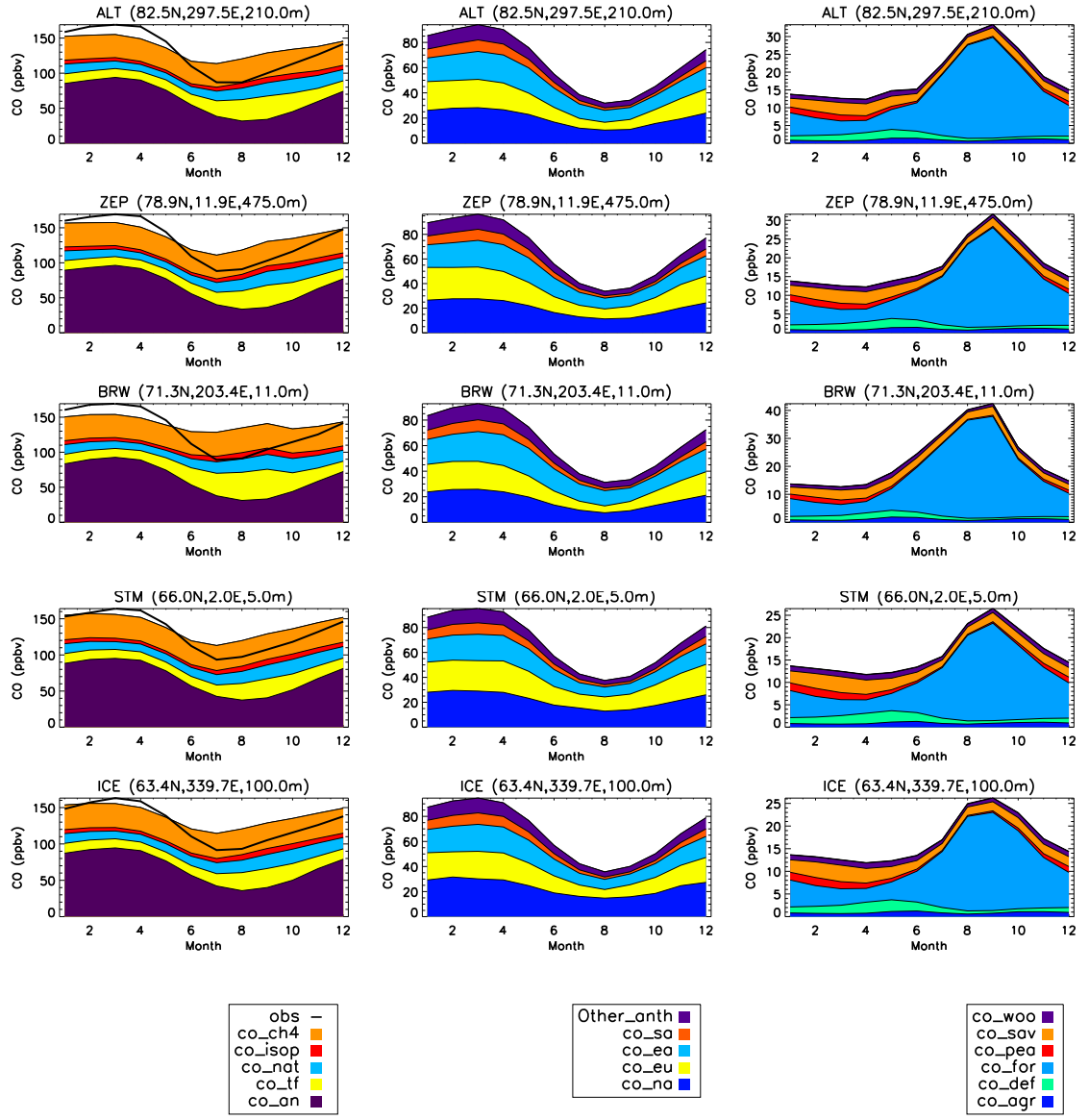

(∼18%). CO from direct natural emissions and the oxidation of isoprene exhibit very little altitude dependency.

Similar to the results shown in Figure 5.8, it can be seen that North American pollution is the dominant anthropogenic source of CO in all altitudes bands. The region contributes between 0.4 and 1.5 Tg of CO, depending on altitude and season, which is 30-35% of the total anthropogenic burden. In the highest altitude bin, East Asian emissions dominate over North American in July and August and have the second largest source in summer in the other altitudes bands. As seen in Section 5.3, this is when East Asian emissions undergo the most efficient transport to the Arctic.

Figure 5.10 Mean monthly contribution of different tracers as a fraction of total CO (CO_TOT) (left), total anthropogenic CO (CO_AN) (middle) and total fire CO (CO_TF) (right) at 5 surface stations located > 60°N.

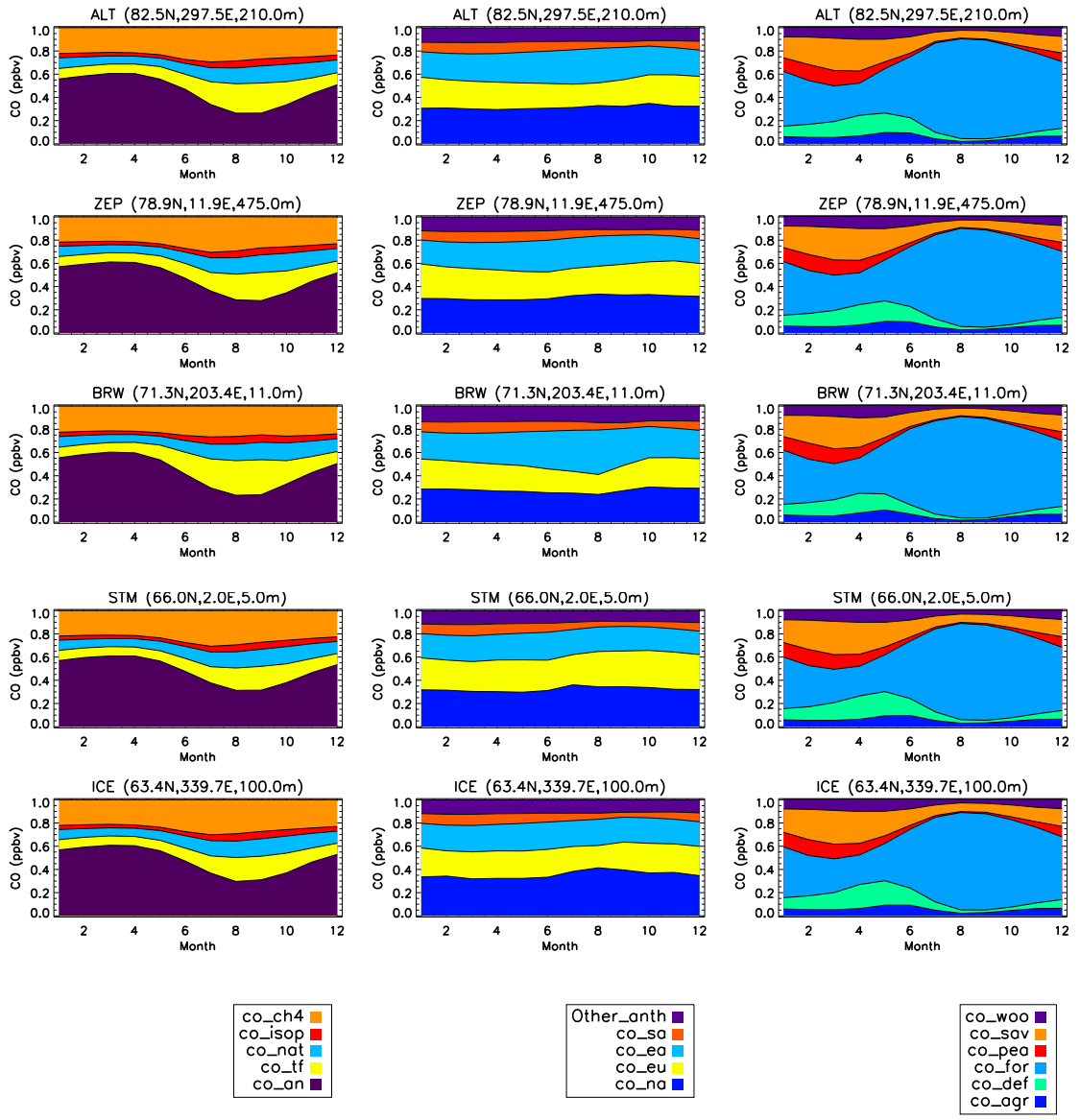

Europe has the second largest contribution in winter and spring, when air from this region is efficiently transported to the Arctic, and the third largest in summer between 0-2 km and 2-5 km. At >5 km European sources become even less important due to inefficient uplift near the emission region. This shows that even though transport of North American emissions is not the most efficient it dominates the burden due to the magnitude of emissions.

As already seen forest fires are the dominant source of fire CO contributing between 0.1 and 1.4 Tg CO to the Arctic burden, which is between 30 and 80 % of fire sourced CO. During March, Savannah fires contribute a larger fraction compared to forest fires in the highest altitude band. As

Figure 5.11 Absolute burdens and fractional contributions for realistic lifetime CO tracers calculated over latitudes > 66°N. The burdens have been calculated for three different altitude bins: 0-2 km (left), 2-5 km (middle) and 5 km up to the tropopause (right). The fractional contributions were calculated by dividing the burdens by the CO_TOT burden for the total CO burdens (2nd row), by CO_AN burden for the total anthropogenic CO burdens (4th row) and by CO_TF burden for the total fire CO burdens (6th row).

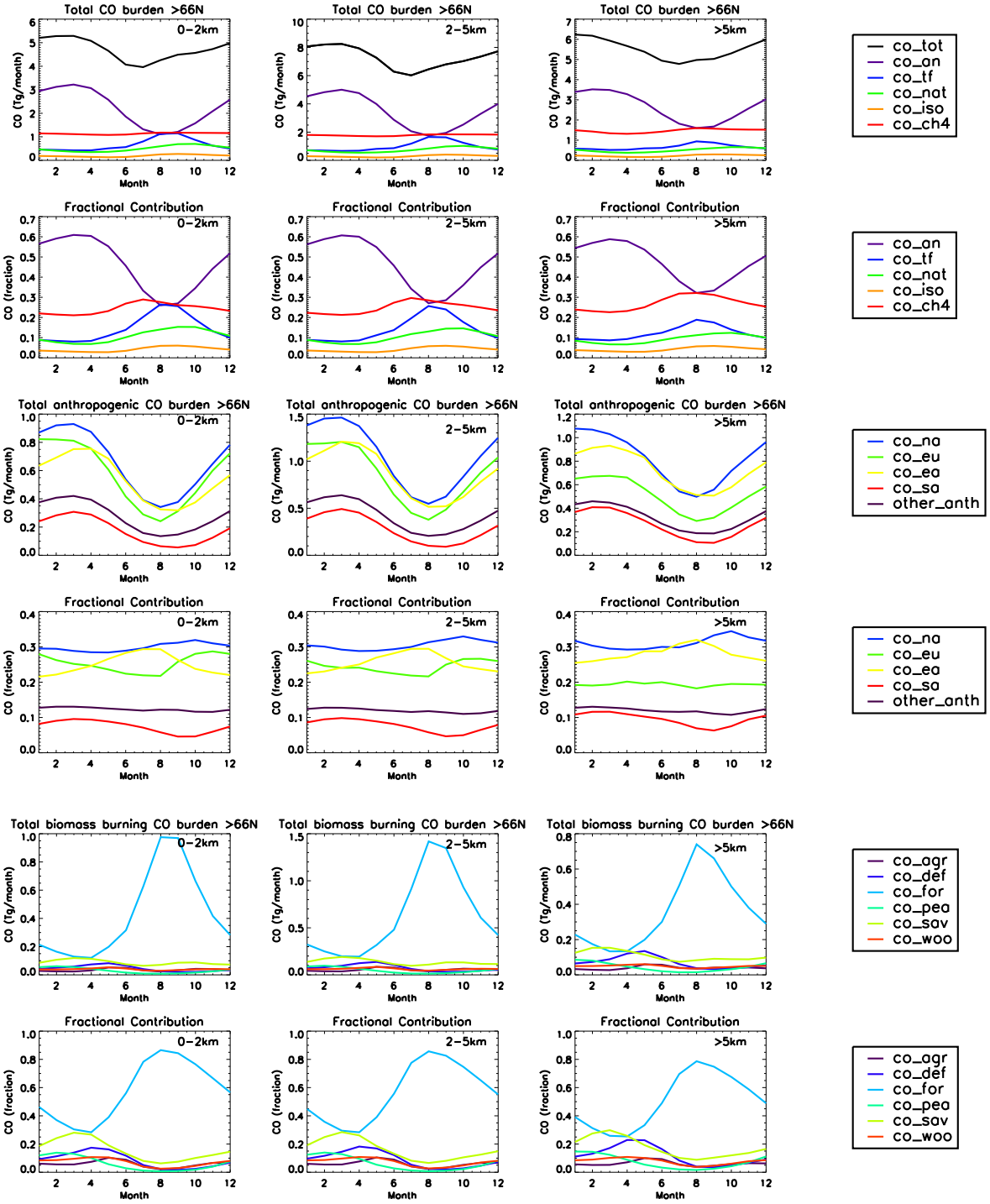

Figure 5.12 Monthly mean contributions of regional anthropogenic tracers to the Arctic CO burden between 0-2 km (left), 2-5 km (middle) and 5 km up to the tropopause (right) weighted by emission region totals from the anthropogenic tracers CO_NA, CO_EU, CO_EA and CO_SA.

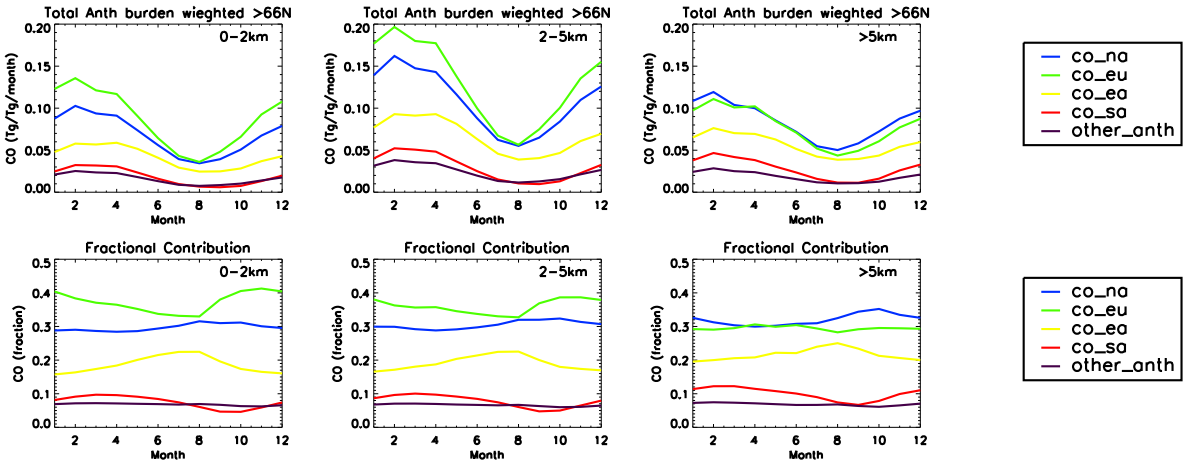

already mentioned, the seasonal minimum and maximum contribution is controlled by seasonally varying emissions. The annual mean burdens of absolute Arctic CO in all three altitude bands and the total troposphere for all of the different tracers have been summarised in Table 5.4.

As mentioned previously, model results are dependent on the emissions which are input into the model, therefore any emissions errors will result in a bias in the model results leading to different interpretations. For example, the underestimate of Asian emissions in the AR5 dataset is likely to contribute to an underestimate in the burden from the Asian sources. To overcome this, the Arctic CO burdens have been weighted by the tracer emission totals. This is done by dividing the total burden by the total emissions, giving a contribution in Tg of CO per Tg CO emitted per month. This allows the most efficient transport pathways to the Arctic in the model to be considered, as done in Section 5.3, but also accounts for the seasonal difference in OH. Even though the lifetime of CO is greater than 1-month, this is assumed to be reasonable as emissions do not vary on a monthly basis. These can be then used to estimate future burdens of Arctic CO due to any emission changes.

Figure 5.12 shows the absolute and fractional anthropogenic burden of Arctic CO weighted by emissions in the same three altitude bands. It can now be seen that the Arctic is most sensitive to European emission as seen in Section 5.3 in the two lower altitude bands. This makes the Arctic most sensitive to emissions changes in this region. European emissions become less important in the >5 km altitude bin, where North American emissions now dominate and the East Asian emission contribution increases. Overall, South Asian emissions show the smallest emission sensitivity out of these four regions and all other anthropogenic emissions (other_anth) are the least important overall. Shindell et al. (2008) also considered anthropogenic CO in a similar way to remove inter-model emission differences in an inter-comparison project. The results presented

Figure 5.13 Mean percent contributions to the total mass burden of anthropogenic CO in the Arctic (>60°N) from North America, Europe, East Asia and South Asia for the period 1998-2009 separated into altitudes bins of 0-2 km, 2-5 km, 5 km up to the tropopause. Shown as absolute burdens of CO_NA, CO_EU and CO_AS as a percentage of CO_AN (left) and absolute burdens of CO weighted by regional emissions from CO_NA, CO_EU and CO_AS (in Tg(CO)/Tg(CO)(emitted)/year), and as a percentage of CO_AN in brackets (right).

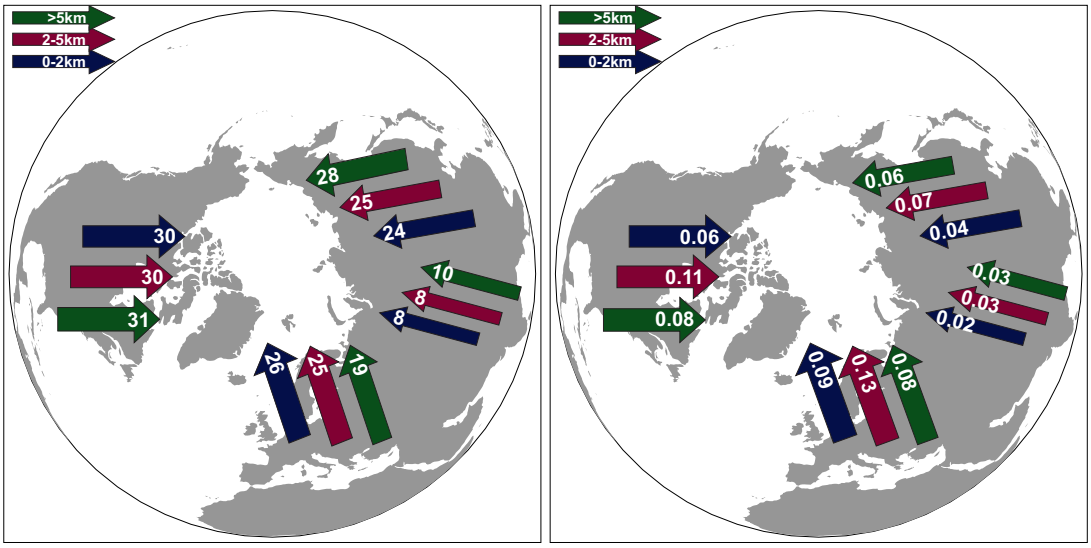

here agree with Shindell et al. (2008) who found that European emissions are the largest source of anthropogenic pollution at the surface. At 500 hPa (∼5 km) they found Europe to still dominate and North America to be the second most important contributor.

The same analysis could not be performed for the fire tracers due to large monthly gradients in emissions. However, the annual mean burdens weighted by the annual mean emissions can be calculated and have been summarised in Table 5.5 for both the anthropogenic and the fire tracers. One interesting thing to note is that when the fire type contributions are weighted by total emissions, the contribution from agricultural fires increases from 6% to 27% annually over the whole troposphere, showing that the Arctic is particularly sensitive to the agricultural practices (most likely in Eurasia due to close proximity to the Arctic (see Figure 3.4)).

The results discussed here are summarised in Figure 5.13. The numbers are taken from Tables 5.4 and 5.5. This highlights how the sensitivity of the Arctic varies with altitude, most notably for Europe where it contributes 26% to total anthropogenic CO in the lower troposphere which is greatly reduced to 19% in the upper troposphere. The overall largest contributions are clearly seen from North America with 30-31% coming from this region. When weighted by emissions, the Arctic is clearly most sensitive to Europe, making emission reductions in this region particularly effective in reducing Arctic CO.

Table 5.4 The annual total tropospheric CO burdens in the Arctic (>60°N) calculated between 0-2 km, 2-5 km, 5 km up to the tropopause and the total tropospheric column using realistic lifetime CO tracers as absolute burdens (in Tg(CO)/year). In brackets the 'All Sources' tracers are shown as a percentage of CO_TOT, the 'Anthropogenic Sources' tracers are shown as a percentage of CO_AN and the 'Fires sources' tracers are shown as a percentage of CO_TF.

CO Tracer	**0-2 km**	**2-5 km**	**>5 km**	**Tropospheric total**
All Sources				
CO_AN	2.22 (47%)	3.46 (48%)	2.64 (48%)	8.32 (48%)
CO_TF	0.66 (14%)	0.99 (14%)	0.66 (12%)	2.31 (13%)
CO_CH4	1.14 (24%)	1.79 (25%)	1.47 (27%)	4.40 (25%)
CO_NAT	0.50 (11%)	0.75 (10%)	0.52 (9%)	1.76 (10%)
CO_ISOP	0.20 (4%)	0.30 (4%)	0.23 (4%)	0.73 (4%)
CO_TOT	4.71	7.28	5.51	17.50
Anthropogenic Sources				
CO_NA	0.66 (30%)	1.05 (30%)	0.82 (31%)	2.52 (30%)
CO_EU	0.57 (26%)	0.85 (25%)	0.51 (19%)	1.93 (23%)
CO_EA	0.54 (24%)	0.87 (25%)	0.73 (28%)	2.13 (26%)
CO_SA	0.18 (8%)	0.28 (8%)	0.26(10%)	0.72 (9%)
other anth.	0.28 (12%)	0.42 (12%)	0.32 (12%)	1.02 (12%)
Fire Sources				
CO_AGR	0.03 (5%)	0.05 (6%)	0.04 (6%)	0.13 (6%)
CO_DEF	0.05 (7%)	0.07 (7%)	0.07 (11%)	0.19 (8%)
CO_FOR	0.42 (64%)	0.61 (62%)	0.35 (54%)	1.39 (60%)
CO_PEA	0.03 (5%)	0.05 (5%)	0.04 (7%)	0.12 (5%)
CO_SAV	0.09 (13%)	0.14 (14%)	0.11 (16%)	0.33 (14%)
CO_WOO	0.01 (1%)	0.01 (1%)	0.01 (1%)	0.03 (1%)

Table 5.5 The annual total tropospheric CO burdens in the Arctic (>60°N) calculated between 0-2 km, 2-5 km, 5 km up to the tropopause and the total tropospheric column weighted by annual mean emissions (in $Tg(O_3)/Tg(NO_x)$ emitted/year). In brackets the 'Anthropogenic Sources' tracers are shown as a percentage of CO_AN and the 'Fires sources' tracers are shown as a percentage of CO_TF.

CO Tracer	**0-2 km**	**2-5 km**	**>5 km**	**Tropospheric total**
Anthropogenic Sources				
CO_NA	0.07 (29%)	0.11 (30%)	0.08 (32%)	0.26 (30%)
CO_EU	0.09 (38%)	0.13 (36%)	0.08 (30%)	0.29 (35%)
CO_EA	0.04 (18%)	0.07 (19%)	0.06 (21%)	0.16 (19%)
CO_SA	0.02 (8%)	0.03 (8%)	0.03 (10%)	0.08 (9%)
other anth.	0.02 (7%)	0.02 (7%)	0.02 (7%)	0.06 (7%)
Fire Sources				
CO_AGR	0.03 (25%)	0.05 (26%)	0.03 (28%)	0.11 (27%)
CO_DEF	0.01 (5%)	0.01 (6%)	0.01 (8%)	0.03 (6%)
CO_FOR	0.07 (55%)	0.10 (53%)	0.06 (45%)	0.22 (51%)
CO_PEA	0.01 (7%)	0.01 (7%)	0.01 (9%)	0.03 (7%)
CO_SAV	0.01 (7%)	0.01 (7%)	0.01 (8%)	0.03 (7%)
CO_WOO	0.001 (1%)	0.002 (1%)	0.002 (1%)	0.01 (1%)

5.6 Seasonal source contributions to Arctic O_3

It has been shown that anthropogenic and fire emissions can contribute large amounts to the Arctic CO burden (see Section 5.5) and are therefore likely to be large sources of other trace pollutants. Here the contribution of forest fires and anthropogenic emissions to the burden of O_3, a greenhouse gas, will be considered. O_3 is not emitted and the main sources in the troposphere are photochemical production from NMHC, CO, CH_4 in the presence of NO_x and transport from the stratosphere. Precursor gases (such as NO_x and NMHC) are emitted at the surface with large amounts from anthropogenic and biomass burning sources. Using the simulations described in Section 5.2.3 and Table 5.3, the contributions to Arctic O_3 from these two sources are considered.

Figure 5.14 Seasonal mean anthropogenic and biomass burning contributions to total tropospheric O_3 column from fires <50°N (TF-BF), fires >50°N (BF), North American anthropogenic O_3 (NA), European anthropogenic emissions (EU) and Asian anthropogenic emissions (AS).

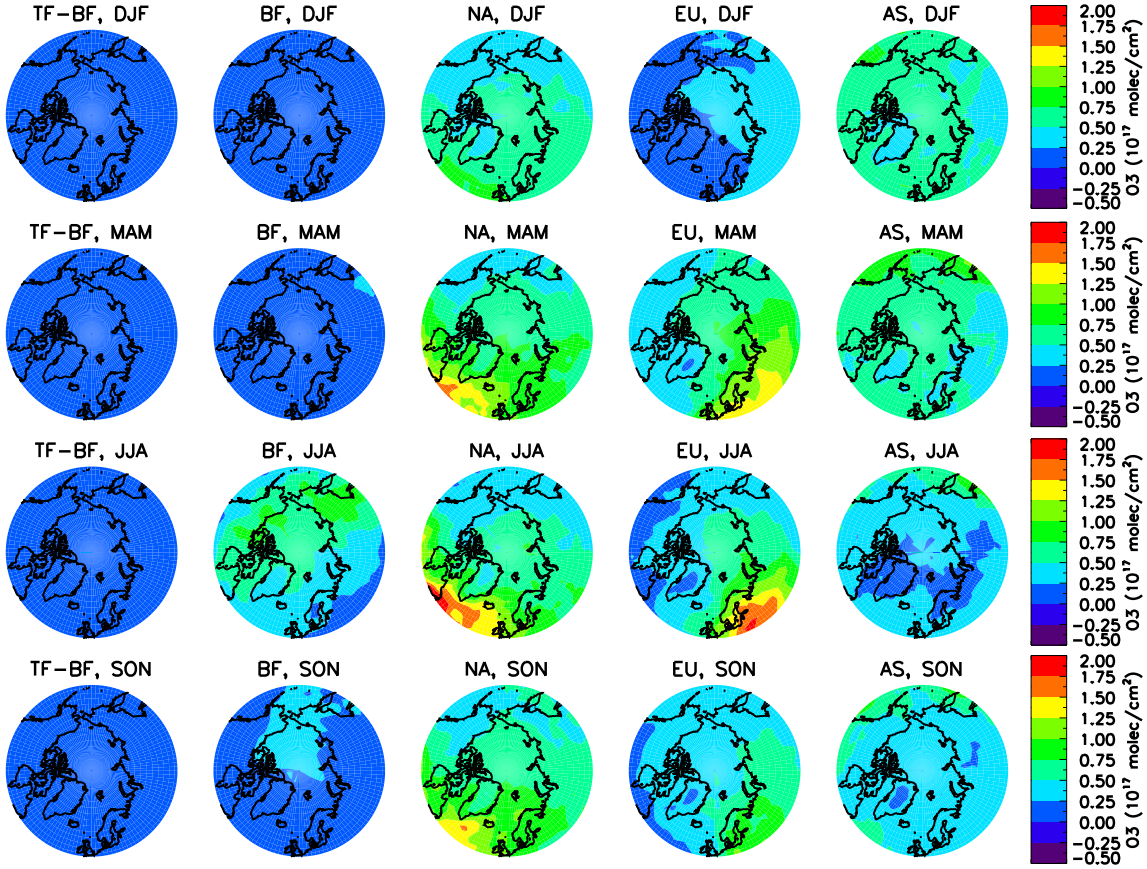

5.6.1 Contributions to total tropospheric Arctic O_3.

Figure 5.14 shows the total column of O_3 integrated over the troposphere. It can be seen that fires at latitudes lower that 50°N contribute very little to O_3 in the Arctic. Most of the O_3 formed from fire emissions originates from the boreal regions north of 50°N during the summer peak fire season. It is clear that North America contributes the largest amount of O_3 to the Arctic total column followed by Europe and then Asia. Asia exhibits a seasonal maximum in winter and spring whereas North America and Europe has a maximum contribution in spring. Both Asia and North America still contribute a large fraction of O_3 in winter which must be transported to the Arctic due to the lack of sunlight for ozone production. There are regional gradients in the emission sensitivities, with O_3 from North America being most important near the Canadian Arctic and Greenland and Europe being most important near Scandinavia and Siberia.

5.6.2 Contributions to Arctic surface O_3.

Figure 5.15 shows the contributions to surface O_3 at Arctic surface stations from fires south of 50°N (TF-BF), fires north of 50°N (BF), North American anthropogenic emissions (NA), European anthropogenic emissions (EU) and Asian anthropogenic emissions (AS). The O_3 calculated from the fc_tot simulation which is not accounted for by these sources is shown by the lined region. It is clear that a large fraction of modelled surface O_3 in the Arctic is not from fires and anthropogenic emissions from North America, Europe and Asia. Other sources of O_3 which are not considered here are transport from the stratosphere and production from NO_x emitted by lightning, biogenic and soil sources, ships, and anthropogenic emissions outside of the three main anthropogenic emission regions used in this work. Out of the sources considered, differences in contributions from North America, Europe and boreal fires (BF) are visible between the stations. However, fires at latitudes $<$50°N consistently contribute the smallest amount to O_3 with only a few ppbv being produced. O_3 produced from fires north of 50°N contribute very little to O_3 during winter and spring (due to low fire emissions at this time of year) but at some stations in summer they have the largest contribution compared to the other sources considered. Due to the location of ALT, ZEP and BRW near the boreal fire regions they are more sensitive to O_3 formed from boreal fire emissions. This is also visible in the total column O_3 (See Figure 5.14). As with CO, this seasonal maximum in O_3 coincides with the burn season. Out of anthropogenic regions, Asian O_3 contributes the smallest overall amount at the surface at all stations. Europe has the largest contribution at STM and ZEP and North America has the second largest. However, at ICE and ALT, North American O_3 is greater than European. At BRW, they both contribute a similar magnitude to the O_3 burden. This regional difference is again due to the location of the stations being situated near different dominant transport pathways from these regions (see Figure 5.14).

Figure 5.15 Monthly mean contributions to O_3 at surface stations in the Arctic from all fires <50°N (TF-BF), all fires >50°N (BF), North American anthropogenic O_3 (NA), European anthropogenic emissions (EU) and Asian anthropogenic emissions (AS). 'Other sources' represents the residual O_3 in the fc_tot simulation which is not accounted for by TF-BF, BF, NA, EU and AS. Shown in both ppbv (left) and as a fraction of fc_tot O_3 (right).

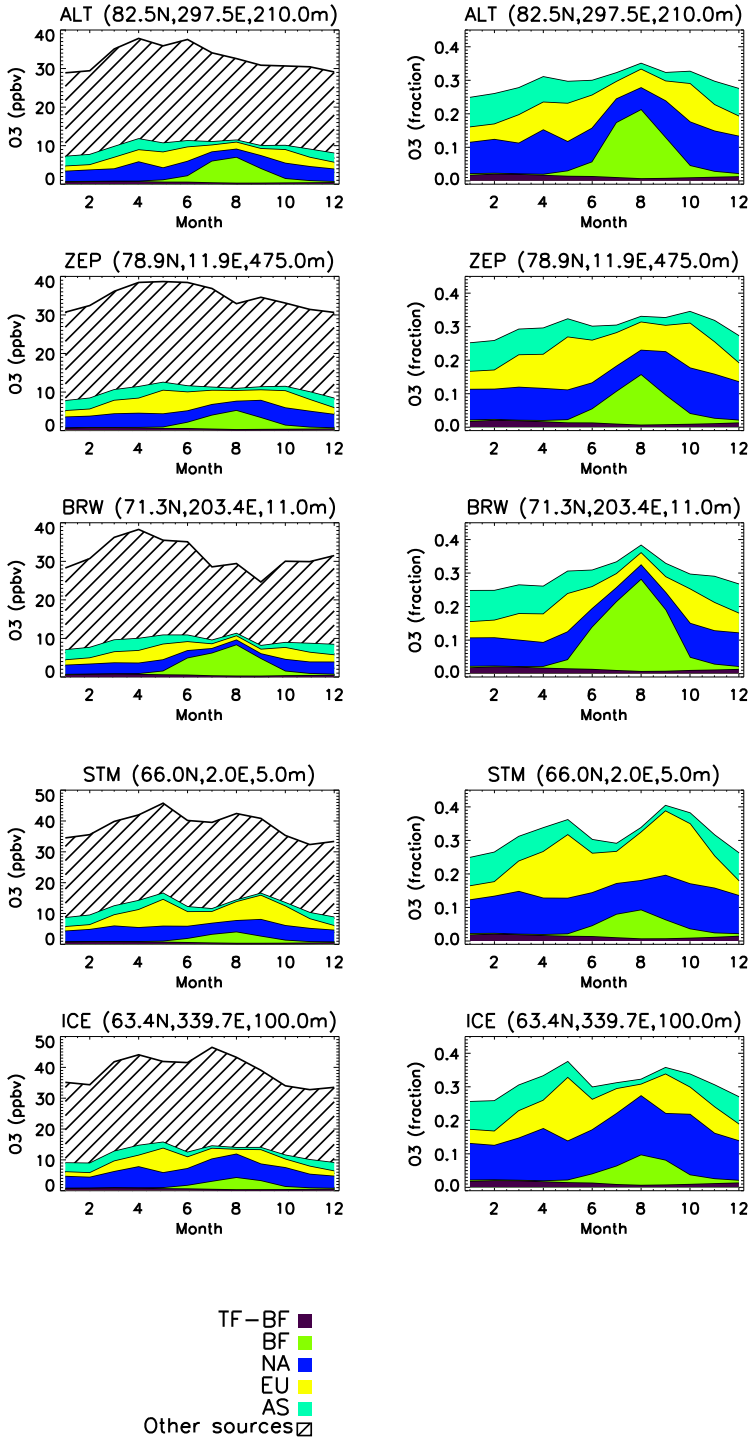

5.6.3 Contributions to the Arctic burden of O_3 and NO_y at different altitudes

The monthly mean absolute burdens of O_3, CO, NO_x and its reservoir species (NO_y, PAN and HNO_3) in three altitude bins (0-2 km, 2-5 km and $>$5 km) are shown in Figure 5.16. In the lowest altitude bin the burden of O_3 is dominated by North American and Asian O_3 in the winter, by European O_3 in spring, by boreal fire O_3 in summer and North American O_3 in the autumn demonstrating that the Arctic sensitivity to O_3 sourced from different regions has a strong seasonal dependency. Overall, O_3 from total fires is largely dominated by boreal fires.

The seasonal cycle of O_3 from the three anthropogenic regions vary, with O_3 from North America and Europe exhibiting double peaks, one in late spring/early summer and another in autumn. Conversely, Asia shows a similar seasonal cycle as CO, with a peak in spring. This demonstrates that the processes controlling O_3 in the Arctic from these three regions are different. The seasonal peak in O_3 due to fires is due to the timing of emissions, as seen in CO in Section 5.5.

Boreal and total fire emissions become less important with increasing altitude whereas the burdens of North America and Asia become more important. Europe has the smallest overall impact in the highest altitude bands. This altitude dependency exhibits similar patterns as the transport efficiencies seen in Section 5.3. For the boreal fires, more NO_y is located in the highest altitude band, which is where the lowest O_3 contribution is. A large amount of this NO_y is in the form of PAN, where it will be stable due to cold temperatures. Near the surface there is more NO_x compared to the upper troposphere in the summer, which can lead to the formation of O_3 due to the presence of sunlight.

European NO_x peaks in May in the two lowest altitude bands and is higher than NO_x from the other regions. This coincides with the peak in O_3 suggesting that this NO_x is driving O_3 formation from European sources at this time of year. North American NO_y is higher in the upper troposphere compared to the other sources considered. This is also where North American O_3 is the highest. European NO_y in the Arctic is much higher compared to the other anthropogenic regions between 0-2 km and 2-5 km, due to large PAN, HNO_3 and NO_x concentrations. The most notable difference occurs in the burden of HNO_3. Asian and North American export of pollution is generally characterised by higher rates of precipitation due to rapid uplift in warm conveyor belts (Stohl, 2006). HNO_3 is therefore efficiently scavenged from the atmosphere through wet deposition before reaching the Arctic. Conversely, European air is generally transported poleward at much lower levels (see Section 5.3) with lower levels of precipitation (Stohl, 2006).

Differences in NO_y:CO ratios between the burdens from the different anthropogenic regions can be used as a proxy for different wet deposition rates that occur along the different transport pathways. NO_y has been calculated in the model and accounts for all reservoir nitrogen species and therefore

Figure 5.16 Monthly mean absolute burdens of CO, O_3, NO_y, PAN, HNO_3 and NO_x, (top to bottom) in three altitude bins (0-2 km, 2-5 km and >5 km) (left to right) due to emissions from the three anthropogenic regions,North America (NA), Europe (EU) and Asia (AS) and total fires (TF) and boreal fires (BF). Units are in Tg(N)/month or for CO, Tg(CO)/yr.

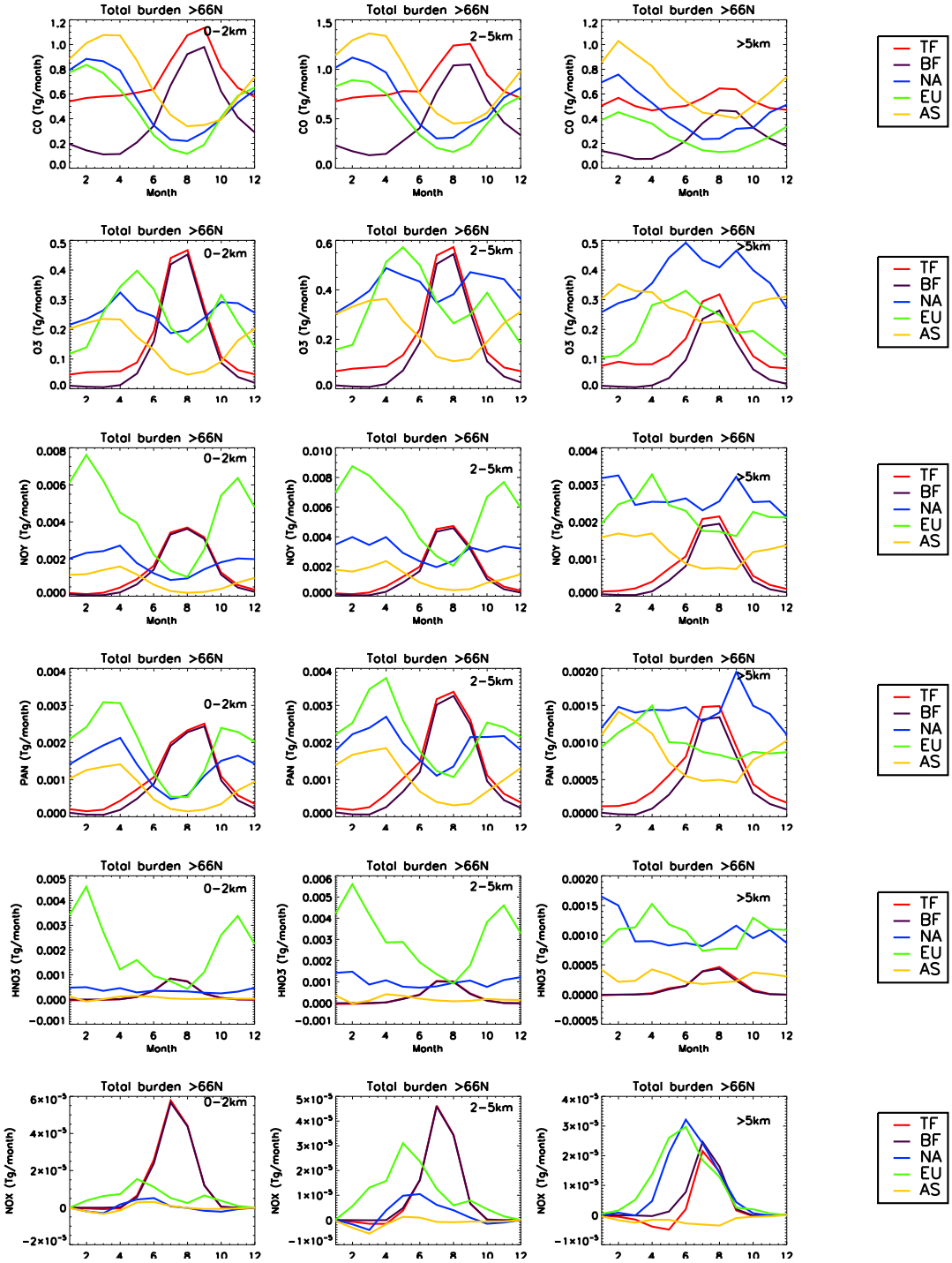

Figure 5.17 Monthly mean NO_y:CO ratios in three altitude bins (0-2 km, 2-5 km and >5 km) (left to right) calculated from burdens sourced from the three anthropogenic regions,North America (NA), Europe (EU) and Asia (AS). The burden has been normalised to 1 by dividing the NO_y:CO ratio by the NO_y:CO emission ratio from the different emission regions to remove any regional differences in initial ratios.

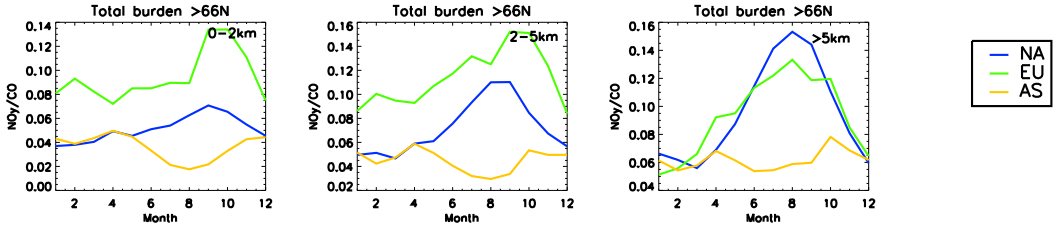

chemistry will not affect NO_y concentrations. Mixing with background air will reduce the concentrations of both gases equally, therefore this will not affect the ratio either. Therefore the major process which will affect the ratio of NO_y:CO is assumed to be loss of HNO_3 by wet deposition, which will reduce the NO_y concentration. Initial differences in the NO_x:CO emission ratio needed to be accounted for, therefore, the ratio has been normalised by the following equation:

$$dpe = \frac{B_{NO_y}}{B_{CO}} \times \frac{E_{CO}}{E_{NO_x}}, \tag{5.1}$$

where, B_{NO_y} and B_{CO} are the burdens of NO_y and CO in the Arctic, E_{CO} and E_{NO_x} are the emissions totalled over the emission regions and dpe is the 'deposition efficiency', which represents the different rates of deposition that the regional pathways experience. If no chemical loss and no deposition occurs, then the ratio would be 1.

Figure 5.17 shows the NO_y:CO ratio for Europe, North America and Asia normalised by emissions. As expected, Asia has much lower ratios throughout the year compared to Europe and North America, indicating high rates of wet deposition. Europe has the highest ratios in the two lowest altitude bins due to low level transport and the rates of precipitation. North America has reasonably high NO_y:CO ratios in the the upper troposphere. This could indicate more efficient PAN formation compared to Asia.

The annual mean O_3 burdens in the altitude bins and for the total tropospheric column have been calculated and are shown in Table 5.6 showing that when averaged over the year North America contributes the largest amount (9%) to the total tropospheric O_3 burden in the Arctic, followed by Europe (7%) and then Asia (6%). Boreal fires contribute 3% and other fires (BF-TF) contriubte just a further 1%. There is 73% of the O_3 burden which is not accounted for by these sources.

As discussed in Section 5.5, the different magnitude of emissions from the different source regions will result in different Arctic sensitivities. According to the AR5 emissions, NO_x emissions do not

Figure 5.18 Annual mean contributions to the total mass burden of anthropogenic O_3 in the Arctic (>60°N) from North America, Europe and Asia for the period 1998-2009 separated into altitudes bins of 0-2 km, 2-5 km, 5 km up to the tropopause. Percentages calculated using absolute burdens from NA, EU and AS (left) and absolute burdens weighted by regional emissions from NA, EU and AS (in $Tg(O_3)/Tg(N)$ emitted)/year (right).

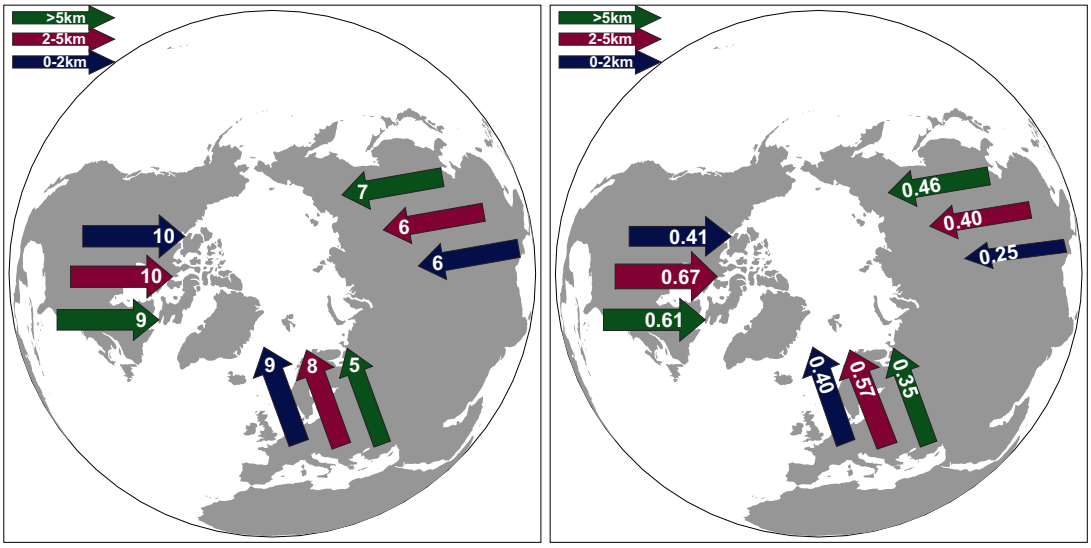

vary largely between North America, Europe and Asia and therefore weighting the emissions does not result in different interpretations of results. However, to show how much O_3 is formed from every Tg of NO_x emitted, the annual mean O_3 burdens have been weighted by NO_x emissions and are shown in Table 5.7. This shows that for every Tg of NO_x emitted in North America, Europe and Asia, there is 1.68 Tg, 1.33 Tg, and 1.11 Tg of O_3 formed in or transported to the Arctic troposphere, respectively. For every Tg emitted from boreal fires 7.18 Tg of O_3 is formed in or transported to the Arctic. Other fires have the lowest Arctic O_3 impact with only 0.43 Tg of O_3 resulting from 1 Tg of NO_x emissions. This shows that the Arctic is much more sensitive to emissions from boreal fires than from the other anthropogenic emissions regions. These results for the anthropogenic emissions are summarised in Figure 5.18.

Table 5.6 The annual total tropospheric O_3 burdens in the Arctic (>60°N) calculated between 0-2 km, 2-5 km, 5 km up to the tropopause and the total tropospheric column (in Tg(O_3)/year). In brackets show these burdens as a percentage of O_3 from fc_tot.

Full chem Sim.	**0-2 km**	**2-5 km**	**>5 km**	**Tropospheric total**
Anthropogenic Sources				
NA	0.25 (10%)	0.41 (10%)	0.37 (9%)	1.03 (9%)
EU	0.24 (9%)	0.34 (8%)	0.20 (5%)	0.78 (7%)
AS	0.15 (6%)	0.25 (6%)	0.28 (7%)	0.68 (6%)
Fire Sources				
BF	0.13 (5%)	0.15 (4%)	0.08 (2%)	0.36 (3%)
TF-BF	0.03 (1%)	0.05 (1%)	0.06 (1%)	0.14 (1%)
Other Sources				
	1.84 (70%)	2.86 (71%)	3.32 (77%)	8.01 (73%)

Table 5.7 The annual total tropospheric O_3 burdens in the Arctic (>60°N) calculated between 0-2 km, 2-5 km, 5 km up to the tropopause and the total tropospheric column (in Tg(O_3)/Tg(N) emitted/year) weighted by emissions.

Full chem Sim.	**0-2 km**	**2-5 km**	**>5 km**	**Tropospheric total**
Anthropogenic Sources				
NA	0.41	0.67	0.61	1.68
EU	0.40	0.57	0.35	1.33
AS	0.25	0.40	0.46	1.11
Fire Sources				
BF	2.54	3.09	1.55	7.18
TF-BF	0.09	0.15	0.18	0.43

5.7 Summary

Using a combination of 30-day fixed lifetime CO tracers, realistic lifetime CO tracers and simulations with full interactive chemistry, the transport efficiency and contributions to CO and O_3 in the Arctic troposphere from major sources have been investigated.

The fixed lifetime tracers were used to examine the efficiency of transport from the regions of North America, Europe, East Asia and South Asia. North America, East Asia and South Asia emissions undergo strong lifting and poleward transport, whereas Europe was characterised by low-level transport in the lower to mid troposphere in agreement with previous studies. European emissions experienced the most efficient transport to the surface and clearly dominated over other anthropogenic regions in the winter and spring due to the presence of the polar dome. In the summer, North American and East Asian emissions showed similar transport efficiencies in the lower troposphere as found for Europe, and dominated the upper troposphere.

Anthropogenic CO was found to be the largest source of Arctic CO, followed by oxidation of methane, then fires. Direct natural emissions and CO from the oxidation of isoprene had the smallest overall contribution. Out of the anthropogenic emission regions, North American emissions dominated the anthropogenic CO burden, accounting for 30-35% of the anthropogenic CO burden. This was due to efficient transport in the upper troposphere plus relatively high total emissions. East Asian emissions showed the second highest anthropogenic contribution with 24-28% of the burden being from emissions in this region. Europe showed the third largest contribution (19-26%) even though it had the highest transport efficiency due to small total emissions. South Asia had the smallest contribution (8-10%) due to inefficient transport and small emissions.

Model interpretation of source contributions to receptor regions is largely dependent on absolute emissions used in the model. Therefore, source contributions were also weighted by emissions to remove this affect giving contributions in units of Tg(CO) in the Arctic per Tg(CO) emitted per year. This showed that the Arctic is most sensitive to emissions changes in Europe, then North America and then Asia. This demonstrates that emissions reductions in some regions will be more effective in reducing pollution in the Arctic. The Arctic was shown to be highly sensitive to emissions from naturally occurring boreal forest fires, however, when weighted by emissions, the annual mean burden of fire CO is also sensitive to agricultural burning practices in the spring.

Using the newly developed full chemistry version of the TOMCAT model, the anthropogenic and fire contributions to O_3 have been quantified. The Arctic sensitivity to O_3 from emissions at lower latitudes shows a seasonal and altitude dependency. Overall North America has the largest contribution to the O_3 burden (9%) out of the anthropogenic regions considered, followed by Europe (7%) and then Asia (6%) (both South Asia and East Asia combined). This is different to the results of Arctic CO suggesting that different transport pathways experience different rates of

O_3 production. Fires contribute a total of 4% to O_3 throughout the year (3% of that from fires north of 50°N). According to the model a further 73% of O_3 found in the Arctic is from other sources, such as production from lightning and transport from the stratosphere. The different pathways that emissions undergo result in very different NO_y burdens. Asia has the smallest overall burden of NO_y and Europe has the highest. This is due to higher rates of wet deposition that are experienced by Asian emissions during transport to the Arctic. Europe also has higher PAN and NO_x burdens in the lowest two altitude bins. North America has the highest amount of NO_y in the upper troposphere due to higher concentrations of NO_x and PAN.

This study is the first time that the impact of emissions from different types of fires on the Arctic have been quantified and compared to the anthropogenic contribution. This study has also highlighted that it is important to consider both the transport efficiency and the absolute emission totals in order to understand how the Arctic will respond to emissions reduction policies. This study is also the first to consider both the anthropogenic and fire emissions contribution to the Arctic O_3 burden throughout the year and has demonstrated that the sensitivity of Arctic O_3 to different regions is not simple due to the complex chemistry involved. Therefore, future studies of different production efficiencies of O_3 during the different transport pathways would be useful.

Chapter 6

Interannual variability of carbon monoxide in the Arctic

6.1 Introduction

In the previous chapter it was shown that Arctic burdens of CO and O_3 throughout the year are sensitive to both transport patterns and absolute emissions at lower latitudes. This chapter investigates the extent of their influence on the interannual variability (IAV) of observed Arctic pollution with the aim of provide a context for understanding how future changes in both could affect Arctic composition. This is done using CO as a tracer of mid-latitude emissions, which undergoes long-range transport, making its distribution sensitive to changes in atmospheric circulation, whilst still capturing changes in emissions. One previous modelling study, by Szopa et al. (2007), considered the IAV of surface CO between 1997 and 2001 in the Arctic as part of a larger global study. They found surface CO at some Arctic stations to be almost equally affected by changes in biomass burning emissions and meteorology. However, that study only considered a five-year period, which contained an anomalously high El Niño[1] event and did not remove OH variability as a source of CO IAV. This chapter builds on their work by studying a longer period of time (13 years) and removing the effect of OH variability.

Natural climate variability can result in circulation changes and therefore affect long-range transport of trace gases. In particular, circulation changes caused by the North Atlantic Oscillation (NAO) in the NH have been found to affect Arctic composition. Eckhardt et al. (2003) showed evidence of enhanced poleward transport of anthropogenic CO and NO_2 during positive phases of the NAO. A deepening of the Icelandic low, which is associated with a positive NAO, has been

[1] El Niño - Southern Oscillation (ENSO) is a coupled mode of natural atmospheric and oceanic climate variability in the tropical Pacific causing global temperature and precipitation anomalies.

shown to be correlated with a weakening of the Aleutian low in the Pacific (Honda et al., 2001). The Pacific-North American (PNA) index describes the gradient between the Aleutian low and a persistent high pressure system over North America. The PNA has also been found to be linked to poleward transport by correlating with growth rates of observed CO_2 at Barrow and Alert (Murayama et al., 2004). Another modelling study by Fisher et al. (2010) suggested that a weakening of the Aleutian low in April 2008 hindered poleward transport causing anomalously low CO over Alaska, was associated with a La Niña event. They therefore suggested that El Niño events may result in increased poleward transport. However, their study was not conclusive and it is still unknown whether circulation changes, due to El Niño conditions, have any impact on the burdens of trace species in the Arctic. It is important to understand how these process affect Arctic composition so any future shifts in climate modes and what this means for the Arctic can be understood.

CO is emitted directly from anthropogenic, natural and biomass burning sources, produced from the oxidation of methane and NMHC, and lost from the atmosphere through reaction with OH and deposition. These different sources and sinks cause the atmospheric burden of CO to be sensitive to changes in a variety of sources and to the oxidising capacity of the atmosphere (Khalil and Rasmussen, 1984a, 1994; Novelli et al., 1998; Duncan and Logan, 2008). Biomass burning is a large source of CO to the troposphere (Wotawa et al., 2001; Duncan et al., 2007) and exhibits a high interannual variability (IAV) (van de Werf et al., 2006). For this reason, both models and observations have shown global atmospheric CO IAV to be sensitive to changes in biomass burning emissions (Duncan and Logan, 2008; Yurganov et al., 2010). The frequency and intensity of biomass burning have been found to be influenced by the coupled El Niño - Southern Oscillation (ENSO). Increased fire activity and emissions during El Niño events have been shown to affect tropospheric composition in some regions (van de Werf et al., 2004; Logan et al., 2008; Chandra et al., 2009; Nassar et al., 2009). El Niño can also affect tropospheric composition through dynamical changes in convection and circulation. For example, regional photochemistry has been shown to be influenced by the eastward shift of tropical convection during El Niño conditions, which displaces lightning and its associated NO_x emissions (Chandra et al., 1998; Staudt et al., 2001; Doherty et al., 2006; Chandra et al., 2009). Tropospheric concentrations of OH and O_3 have also been shown to be affected by increased stratospheric-tropospheric exchange (STE) during El Niño events (Zeng and Pyle, 2005; Voulgarakis et al., 2011).

This chapter focuses on answering the open question of what are the roles of atmospheric circulation and emissions in controlling the IAV of Arctic pollution. This also leads onto the question of what controls the variability in transport and emissions. For this, the influence of the NAO, PNA and El Niño are considered. These climate modes are described in more detail in Section 6.2. The simplified TOMCAT model with realistic lifetime CO tracers, used in Chapter 5, is used here as it allows other possible sources of CO IAV to be removed from the model (i.e., OH). The model simulations used in this chapter are described in Section 6.3. The contributions of transport and

emissions to the IAV of CO are discussed in Section 6.4 both at the surface and throughout the depth of the troposphere. TOMCAT is then used to investigate the influences of the PNA, NAO and ENSO on the transport of CO to the Arctic in Section 6.5. Then links between Arctic CO IAV and fire variability, with particular focus on El Niño, are discussed in Section 6.6 with analysis of regional fire climate drivers which are affected by El Niño. The results are then summarised in Section 6.7

6.2 Low frequency variability climate modes

El Niño - Southern Oscillation, the North Atlantic Oscillation and the Pacific-North American pattern are three modes of climate variability which are known to have an impact on the atmosphere by affecting the atmospheric circulation. These climate modes and global consequences are now described in more detail.

6.2.1 El Niño - Southern Oscillation

In normal conditions, high pressure off the coast of South America and low pressure in the Equatorial Pacific result in strong south-easterly trade winds across the South Pacific. These winds lead to the movement of warm surface waters from the western coast of South America towards the eastern coast of Australia. This results in cold water up-welling off the coast of Peru and Ecuador and a deepening of the thermocline (a region of warmer surface waters where temperature reduces rapidly with depth) off the coast of Australia. The warm waters in the western equatorial Pacific result in unstable atmospheric conditions leading to substantial atmospheric convection and large

Figure 6.1 Schematic showing normal (left) and El Niño (right) conditions over the Pacific. (Taken from http://www.pmel.noaa.gov/tao/elnino/nino-home.html).

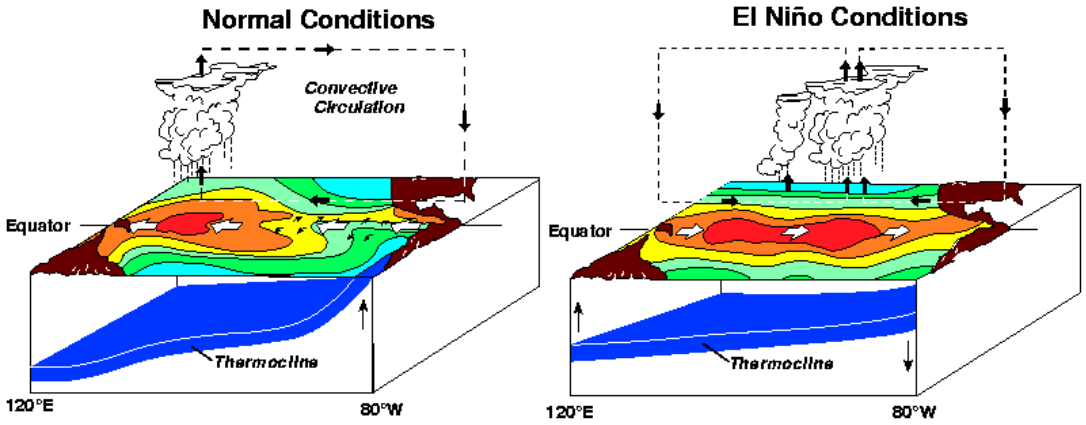

Figure 6.2 Precipitation and temperature anomalies during ENSO warm phases in DJF (top) and JJA (bottom). Taken from http://www.cpc.ncep.noaa.gov/products/analysis_monitoring/impacts.

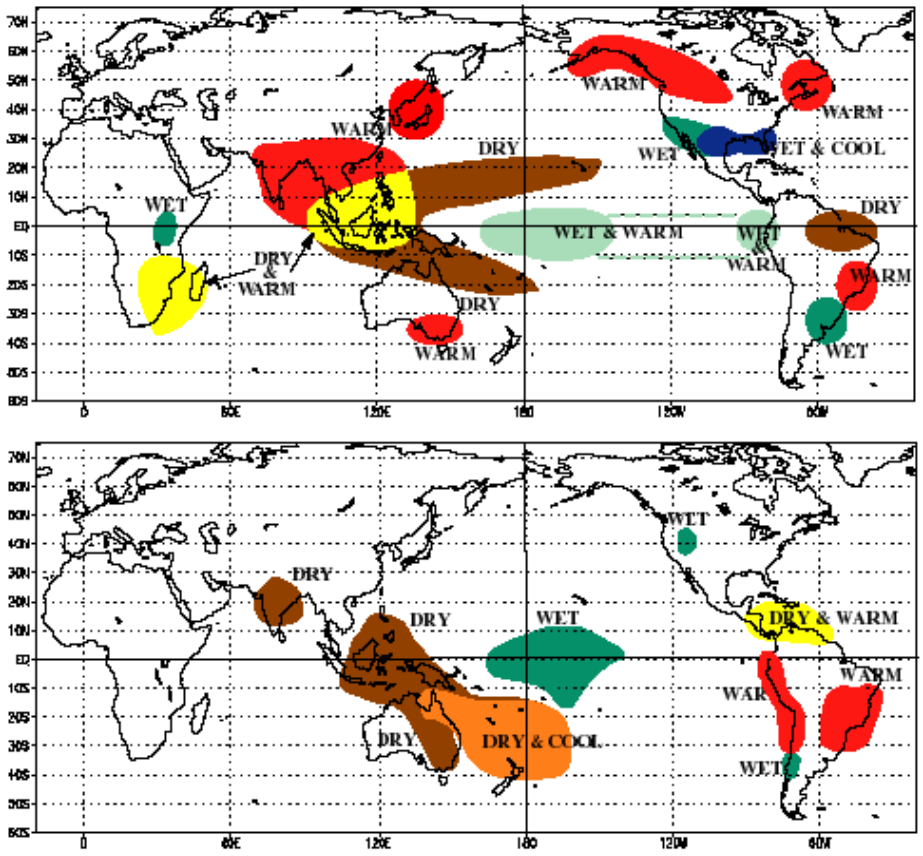

amounts of rainfall in this region. The uplifted air then moves eastward and there is a region of subsidence over South America (see Figure 6.1). This atmospheric circulation cell is known as the Walker circulation and results in tropical regions of Australia and Indonesia being characterised by large amounts of rainfall and Peru and Ecuador being more arid due to more stable atmospheric conditions.

Towards the end of the calender year, pressure over the eastern Pacific decreases and the pressure over the equatorial Pacific increases. The reduction in the pressure gradient between these two regions weakens the trade winds and therefore weakens the oceanic circulation. This leads to an increase in the depth of the thermocline in the eastern Pacific and reduction in the thermocline in the western equatorial Pacific, causing the cold waters off the coast of Peru to warm. In some years, this warming and change in pressure is more dramatic than average. It is this phenomenon which is known as the coupled El Niño-Southern Oscillation (ENSO), where El Niño refers to the ocean component and Southern Oscillation (SO) to the atmospheric component. During El Niño conditions, warm waters migrate eastward, relocating the area of convective uplift (see Figure

6.1). This shift in the atmospheric circulation leads to more rainfall in Peru and Ecuador and often droughts in Australia and Indonesia.

The changes in the atmospheric and oceanic circulation during ENSO events affect not only temperature and precipitation patterns in the equatorial Pacific but can also have global influences (Ropelewski and Halpert, 1986; Halpert and Ropelewski, 1992). Figure 6.2 shows the climatological anomalies in precipitation and temperature during ENSO warm phases (when there is an El Niño) which are linked to changes in the global circulation. Changes in the Walker circulation leads to changes in upper tropospheric circulation which can influence the subtropical jet streams and thus the location and intensity of cyclonic activity (Julian and Chervin, 1978; Arkin, 1982; Landsea, 2000).

In this work, the El Niño 3.4 index from the NOAA Climate Prediction Centre[2] (CPC) is used to define phases of ENSO. The index is the anomaly from the average sea-surface temperature from 1950-2000 calculated in the region 5°N - 5°S, 120°-170°W. This index has been chosen as it is believed to be the best representative index for the coupled impacts of both El Niño and the Southern Oscillation (Trenberth, 1997).

6.2.2 North Atlantic Oscillation

The mean state of the atmosphere in the Northern Hemisphere in winter is characterised by strong high pressure centred over Siberia and low pressure over the North Atlantic and Pacific oceans (Reynolds, 2004). In summer, the most dominant low pressure system becomes centred over south-east Asia and high pressure systems cover large parts of the Pacific and Atlantic oceans. These pressure systems lead to prevailing westerly winds across the mid-latitudes which extend up through the troposphere, reaching wind speeds of about 40 ms^{-1} in the jet-steam at around 200 hPa (Hurrell et al., 2003) (see Figure 6.3). The intensity of the westerly flow is controlled by the gradient between the pressure systems. As shown in Figure 6.3, the winds in summer are much weaker than in winter resulting in much slower zonal transport.

The North Atlantic Oscillation (NAO) is a major mode of atmospheric variability over the Northern Atlantic and affects the mean state of the atmospheric flow in the Northern Hemisphere. It describes the correlated variance in the strength of the Icelandic Low and Azores High pressure systems. During positive phases of the NAO a lower-than-normal wintertime Icelandic Low and a higher-than-normal Azores High occur. The intense low pressure system over Iceland leads to enhanced north-easterly flow to Greenland and the Labrador Ocean from the high latitudes and therefore cooler temperatures in this region and enhanced south-westerly flow of mild air over north-western Europe (Van Loon and Rogers, 1978; Wallace and Gutzler, 1981). Plots of the

[2] http://www.cpc.ncep.noaa.gov/data/indices/nino34.mth.ascii.txt

Figure 6.3 Mean wind vectors over 1958-2001 for NH winter (DJF) (top) and summer (JJA) (bottom) at 1000 hPa (left) and 200 hPa (right). (Taken from Hurrell et al. (2003)).

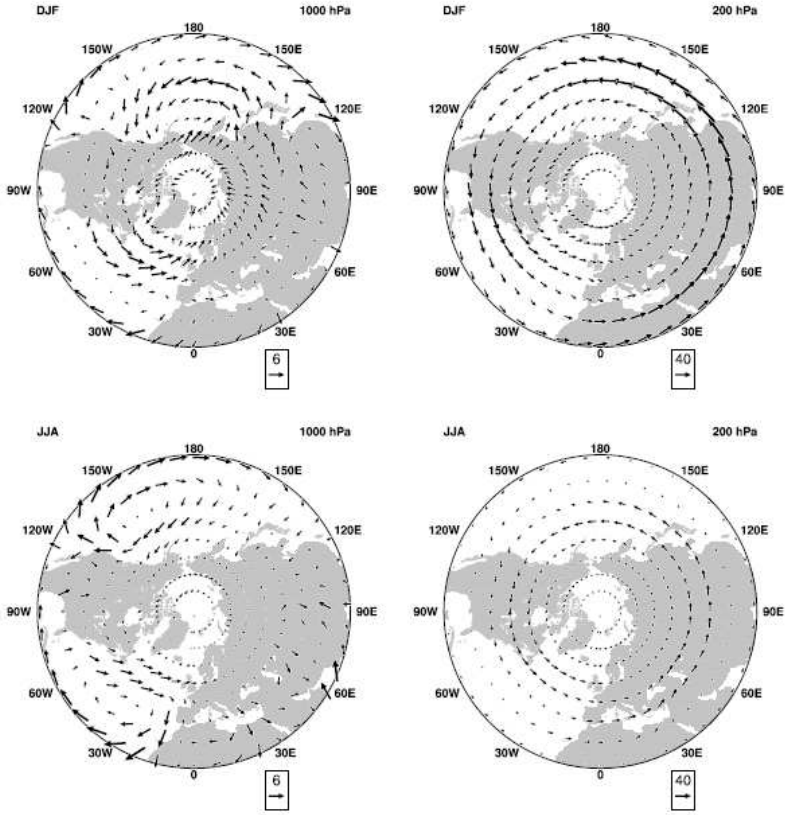

mean seasonal location of the pressure anomalies are shown in Figure 6.4. The NAO is the leading cause of atmospheric variability in the NH in winter accounting for 37% of sea-level pressure (SLP) variability and even in summer, when at its weakest, it still accounts for 22% of SLP variability (see Figure 6.4). This means teleconnections are evident throughout the year (Barnston and Livezey, 1987; Folland et al., 2009; Zveryaev and Allan, 2010). The pressure changes associated with positive NAO phases strengthen the tropospheric subtropical and polar jet streams (Ambaum et al., 2001), where the stronger-than-normal westerlies lead to stronger north-easterly trade winds (Rogers and Van Loon, 1979). These enhanced transport patterns lead to more efficient long-range transport in the upper troposphere. McCabe et al. (2001) showed that there was a poleward shift of cyclonic activity in the Northern Hemisphere during the the late 1980s until the early 1990s, when the NAO remained mostly in the positive phase. Negative phases of the NAO are representative of a weakening in the gradient in these two pressure systems and therefore it has the opposite effects.

There is no universally accepted index to describe the NAO, therefore two different indices which are generated from different techniques have been used in this work. The first (referred to as NAO

Figure 6.4 Seasonal pressure anomalies caused by the NAO (dotted lines - negative anomalies, solid lines - positive anomalies). Numbers represent % of total variability caused by the NAO. Taken from Hurrell et al. (2003).

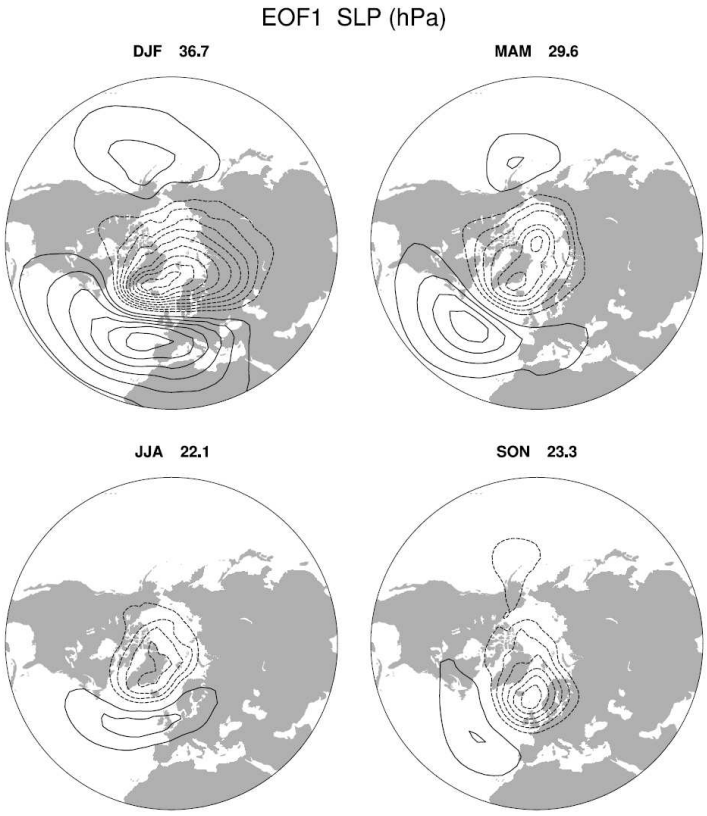

(CPC)) has been calculated by the NOAA CPC[3]. This index has been derived from rotated principal component analysis of the 500 hPa height anomalies from the NCEP/NCAR reanalysis model. This method extracts teleconnections which describe large-scale changes in the atmospheric circulation patterns due to recurring climate variability such as the NAO. These teleconnections can influence temperature, precipitation and jet stream location and intensity over vast areas. The second NAO index[4] (referred to as NAO (HUR)) is the mean winter (December through March) index of the NAO and has been calculated based on the difference of normalized sea level pressure (SLP) between Lisbon in Portugal and Reykjavik in Iceland since 1864. The SLP anomalies at each station are normalized by division of each seasonal mean pressure by the long-term mean (1864-1983) standard deviation to avoid the series being dominated by the greater variability of the northern station (Hurrell and Deser, 2010). A disadvantage of station-based indices is that they are fixed in space therefore only adequately capture NAO variability for parts of the year due to its seasonal evolution (see Figure 6.4) and are also affected by small-scale, short-term meteorological events which are not related to the NAO (Hurrell and Deser, 2010).

[3] ftp://ftp.cpc.ncep.noaa.gov/wd52dg/data/indices
[4] downloaded from: http://www.cgd.ucar.edu/cas/jhurrell/indices.html

6.2.3 Pacific North American Oscillation

The Pacific-North American (PNA) oscillation is another prominent mode of variability in the Northern Hemisphere. The positive phase of the PNA is associated with above average pressure over North America and below average pressure south of the Aleutian Islands and over south-eastern United States (Barnston and Livezey, 1987). The PNA affects the atmospheric circulation in the Northern Hemisphere and influences the strength and location of the Pacific storm track (Honda et al., 2001). The positive phase is linked with an enhancement of the East Asian jet stream and eastward shift in the jet exit region toward the western United States. The negative phase is associated with a westward retraction of that jet stream toward eastern Asia and blocking activity over the high latitudes of the North Pacific reducing transport to the Arctic. As with the NAO, these changes in atmospheric circulation lead to changes in temperature and precipitation. The positive phase of the PNA pattern is associated with above-average temperatures over western Canada and US and below average temperatures across the south-central and south-eastern US (Leathers et al., 1991). Precipitation anomalies are found in the Gulf of Alaska and north-western US with above average precipitation, and over the upper Midwestern United States with below-average rainfall (Leathers et al., 1991). The PNA signal is strongest in winter (Barnston and Livezey, 1987) but has been found to exhibit precipitation and temperature teleconnections in spring and autumn (Leathers et al., 1991). The index used in this chapter has been downloaded from the NOAA CPC and is derived by the same method as the NAO (see Section 6.2.2).

6.3 Model Set-up and methodology

The basic model set-up, used for the simulations in this chapter, has been described previously in Section 5.2.2 of Chapter 5. All runs contain the same 16 idealised tracers shown in Table 5.2 and use the same monthly varying OH fields which remain fixed for the whole 1997-2009 period. To investigate the impact of meteorology and biomass burning on the IAV of CO, four separate simulations were performed. One simulation used climatological biomass burning emissions which remain the same year-to-year and the other three used yearly varying biomass burning emissions. Each simulation was run with either interannually varying meteorology or with meteorology for one year repeated each of the 13 years. The four simulations were:

- Varying biomass burning emissions and varying meteorology (run **vgfed_vmet**).
- Climatological biomass burning emissions and varying meteorology (run **cgfed_vmet**).
- Varying biomass burning emissions and fixed meteorology for Jan 2001 - Dec 2001 (run **vgfed_met01**).

Figure 6.5 Yearly-varying CO emissions (Tg(CO)/year) from GFED v3.1 for different fire types over 1997-2009 used for the yearly-varying biomass burning emissions tracers.

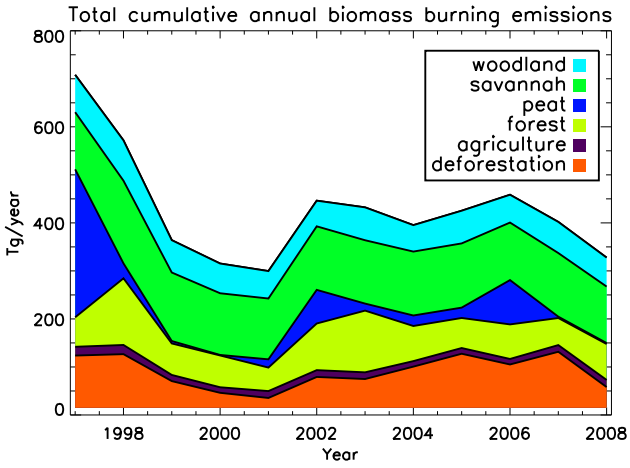

- Varying biomass burning emissions and fixed meteorology for May 1997 - April 1998 (run **vgfed_met97**).

For the fixed meteorology simulations two years were chosen, one as a 'neutral year' and one with a strong El Niño signal. The 'neutral year' was chosen by considering the mean, maximum, minimum and standard deviations for the NAO and El Niño indices. Both the NAO and El Niño indices were neither strongly positive or negative and exhibited relatively small variability in 2001, making this year the best choice for the period of study. However, it must be noted that it is impossible to choose one year alone which is representative of the mean state of atmospheric circulation due to its chaotic nature. May 1997 - April 1998 was chosen as a 'positive El Niño year' as the index remained positive for the whole period. It must also be noted that this year was a particularly strong El Niño year (Wolter and Timlin, 1998).

6.3.1 Emissions

The emissions used were described in Section 5.2.2, however, cgfed_vmet required non-yearly varying biomass burning emissions. For cgfed_vmet, monthly means were calculated from the 1997-2009 GFED v3.1 fire emissions. The fire emissions for the period 1997-2009 are shown in Figure 6.5, showing the extent of the IAV of fire emissions.

6.4 IAV of CO and the importance of meteorology and biomass burning emissions

The 2-year running mean of observed and simulated monthly mean CO at the surface are shown in Figure 6.6. This allows variations in CO to be seen with the seasonal cycle removed. In the high-mid northern latitudes (ALT, ZEP, BRW, STM, ICE and MHD (see Figure 4.12 and Table 4.4 for locations) there are two large peaks in the observed CO time series in 1998 and 2003. These peaks are captured by the three model experiments which include yearly varying biomass burning emissions (vgfed_vmet, vgfed_met97, vgfed_met01) but not the experiment with climatological emissions (cgfed_vmet). This suggests that these peaks are driven by a change in biomass burning emissions. The winters of 1997-1998 and 2002-2003 experienced El Niño events, suggesting a connection between El Niño, forest fires and global CO. The impact of El Niño on forest fires and any link with the Arctic is discussed in more detail in Section 6.6. At these stations, the simulations vgfed_vmet, vgfed_met97 and vgfed_met01 show only small differences in CO concentrations, even though they are driven with different meteorology. This suggests that even though atmospheric transport is vital for advecting emissions poleward, variability in atmospheric circulation is much less important than variability in fire emissions in terms of the Arctic CO IAV. This is important as the impact of fires on Arctic has received very little attention, however these results suggest that they have a large impact on the IAV of Arctic atmospheric composition.

One or both of the 1998 and 2003 peaks can be seen globally to some extent demonstrating the importance of biomass burning emissions as a global source of CO. Interestingly, it can be seen that meteorology becomes increasingly important at lower latitudes. For example, cgfed_vmet captures more of the observed variability at MID and KEY compared to other stations, suggesting both meteorology and fire emissions are important processes for IAV at this location. By considering the difference between the model experiments using El Niño meteorology repeatedly (vgfed_fmet97) and the simulation which uses 2001 meteorology repeatedly (vgfed_fmet01),the dynamical impact that El Niño has on CO concentrations at different locations can be deduced. At MLO, El Niño's dynamical impacts lead to an increase in CO concentrations of around 5-8 ppbv over the whole 13-year period. This indicates there circulation changes result in increased transport to the NH extra-tropics. The Arctic stations show much smaller CO enhancements of around 2 ppbv. This does suggest that there is an increase in Arctic CO during El Niño events, as hypothesised by Fisher et al. (2010). At CGO, in Australia there is less CO during El Niño, due to the weakening of the Walker circulation as shown in Figure 6.1.

CO anomalies have been calculated for each of the four simulations and observations relative to their 1997-2009 means. This allows the impact of meteorology and biomass burning emissions on the IAV of CO in the Arctic to be investigated. Figure 6.7 shows the modelled and observed CO anomaly at surface stations located north of 60°N. Values of r^2 have been calculated between the

Figure 6.6 Two year running mean of monthly mean observed CO at surface stations (for locations see Table 4.4 and Figure 4.12) compared to simulated CO from the simulations vgfed_vmet, cgfed_vmet, vgfed_met97 and vgfed_met01 calculated between 1997 and 2009. Note the different y-axis ranges.

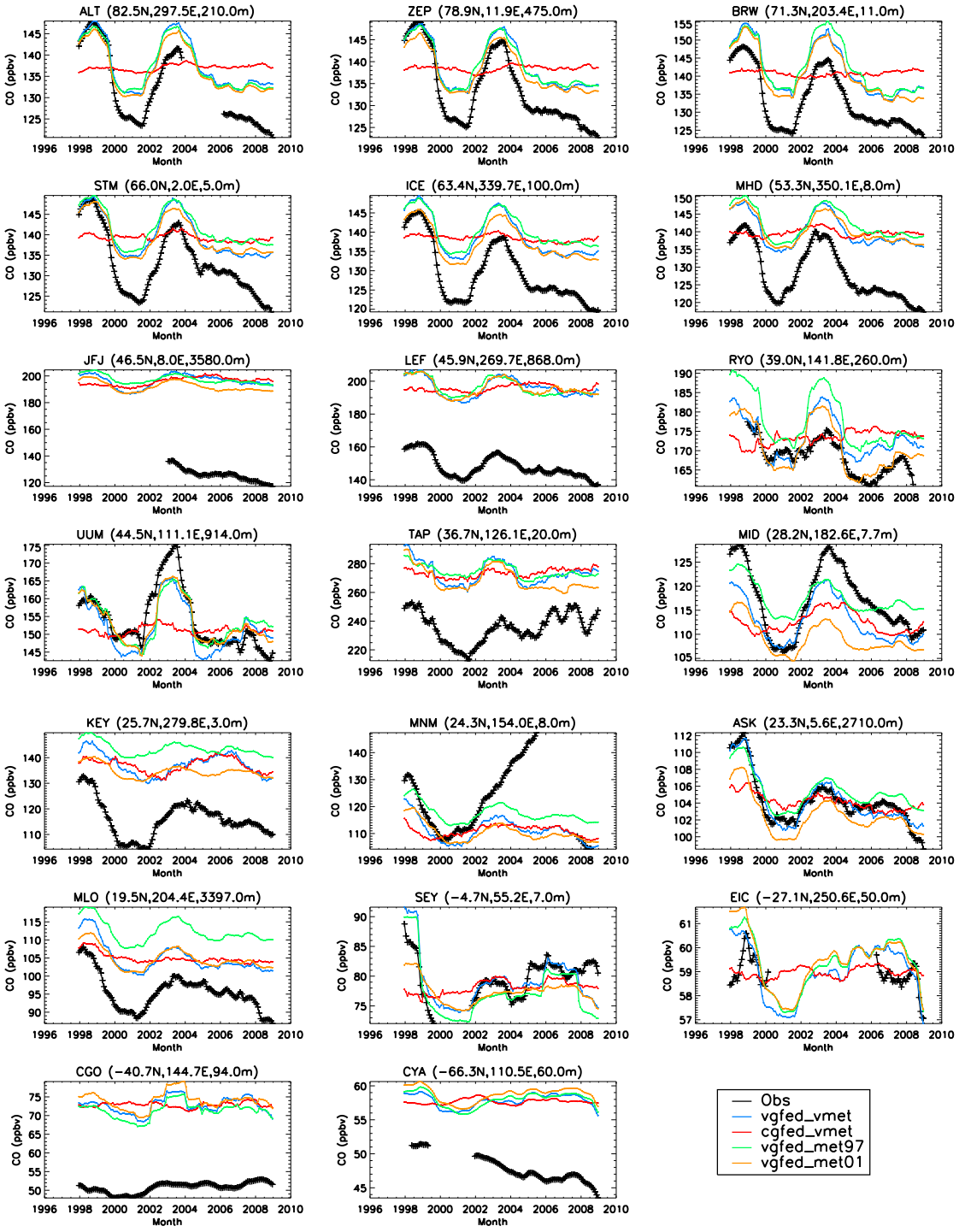

observed and simulated anomalies and are also shown in Figure 6.7. r^2 is a measure of how much each model simulation captures the observed interannual variability. The vgfed_vmet simulation, which is most realistic due to the use of correct meteorology and fire emissions each year, captures the observed anomaly very well ($r^2 > 0.86$). This gives confidence in the model's ability to capture the IAV of CO in the Arctic. Simulation cgfed_vmet, which uses climatological fire emissions and yearly varying meteorology, captures between 0 and 25% of the IAV of CO depending on the station location. The only source of variability in this simulation is the meteorology which changes according to the analyses. ICE, STM and ALT exhibit the highest values of r^2, suggesting the IAV of CO at these stations is more sensitive to changing circulation patterns compared to BRW and ZEP. When varying meteorology and biomass burning emissions are used (vgfed_vmet), TOMCAT captures 86-91% of the variability showing that biomass burning IAV is responsible for the majority of CO IAV in the Arctic. The other 9-14% of the variability which is not captured by this simulation must be due to processes which are not represented in these simplified tracer simulations or model errors. There is very little difference between the three model experiments, vgfed_vmet, vgfed_met01 and vgfed_met97, which are being forced by meteorology for different years, also showing that meteorology has only a small impact on Arctic CO IAV.

Szopa et al. (2007) concluded that meteorology and emissions played almost equal roles in regulating the IAV of CO at high northern and southern latitude stations. Specifically, they found that their model captured the range of IAV of CO more accurately at ALT and BRW when they included yearly varying biomass burning emissions. However, at STM and ICE, they found that their control simulation with only climatological biomass burning emissions already captured most of the IAV. The results shown here do suggest that ICE and STM are affected by changing circulation more than the other high latitude stations, however, biomass burning emissions still control the observed IAV. These different results could be due to differences in the model set-up and analysis of results. Szopa et al. (2007) studied a period of five-years whereas this works considers a longer period of thirteen-years. Both studies included the 1997-1998 El Niño, which is the second strongest El Niño event recorded in the 20th century (Wolter and Timlin, 1998). This was also followed by a very strong La Niña in 1999-2000. As already mentioned, these can have large impacts on tropospheric composition through biomass burning emissions, circulation changes and tropospheric chemistry (see Section 6.1). Whether regional effects of El Niño/La Niña can propagate to the Arctic is unknown. However, this time period was unusual and dominates the 1997-2001 period that Szopa et al. (2007) studied and could therefore account for some of the differences in results. One other difference which may be important is that Szopa et al. (2007) used a general circulation model (LMDZ-INCA) which was relaxed towards ECMWF ERA-40 winds whereas the work shown here used ERA-Interim winds in an offline CTM. Differences in the meteorological analyses (ERA-40 and ERA-Interim) and model differences (e.g. assimilation of data into LMDZ-INCA and forcing of TOMCAT with offline calculated winds) may also account for some

Figure 6.7 Annual mean anomalies of the El Niño, PNA and NAO indices relative to 1997-2009 (top left) and annual mean anomalies of observed and simulated CO relative to 1997-2009 at surface stations north of 60°N.

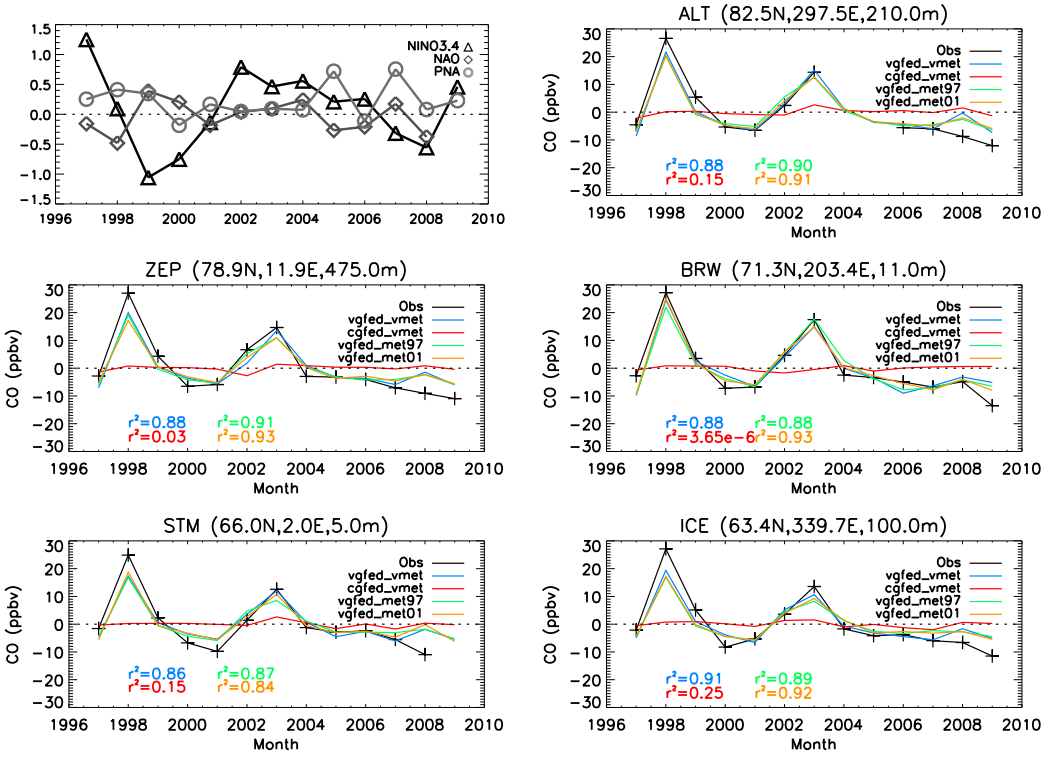

differences. Finally, Szopa et al. (2007) also used on-line calculated OH concentrations which could contribute to some of the year-to-year variability which was attributed to meteorology compared to TOMCAT which used non yearly varying OH. However the total OH variability is thought to be small (Montzka et al., 2011) and therefore is unlikely to contribute a large fraction to the IAV of CO in reality. LMDZ-INCA also yielded lower correlations with the observations (0.58-0.83) indicating that TOMCAT captures the IAV of CO at the surface in Arctic better when the model has been constrained to only account for biomass burning and meteorological variability.

To show the model-observation relationship in a global context, Figure 6.8 shows the correlations between the observed and simulated CO anomaly calculated for all four of the model simulations plotted on a map at each station location and as a function of the station's latitude. It can be seen that at high northern and southern latitudes, the use of varying biomass burning emissions results in the much higher correlations compared to cgfed_vmet, which uses climatological emissions. Towards the tropics, the difference between the correlations calculated from the observations with vgfed_vmet and with cgfed_vmet become smaller, suggesting meteorology becomes more important at lower latitudes. This is in agreement with Szopa et al. (2007) who also found meteorology to be more important in the tropics. Moreover, the correlations between vgfed_vmet and the observations decrease from the high latitudes towards the tropics suggesting that there are other sources

Figure 6.8 Global maps and zonal plots of the Pearson's correlation coefficient calculated between observed and modelled annual anomalies at the surface relative to the 1997-2009 means. CO_TOT has been used from each of the simulations vgfed_vmet (top left), cgfed_vmet (top right), vgfed_met97 (bottom left) and vgfed_met01 (bottom right). The model has been interpolated to the surface station location.

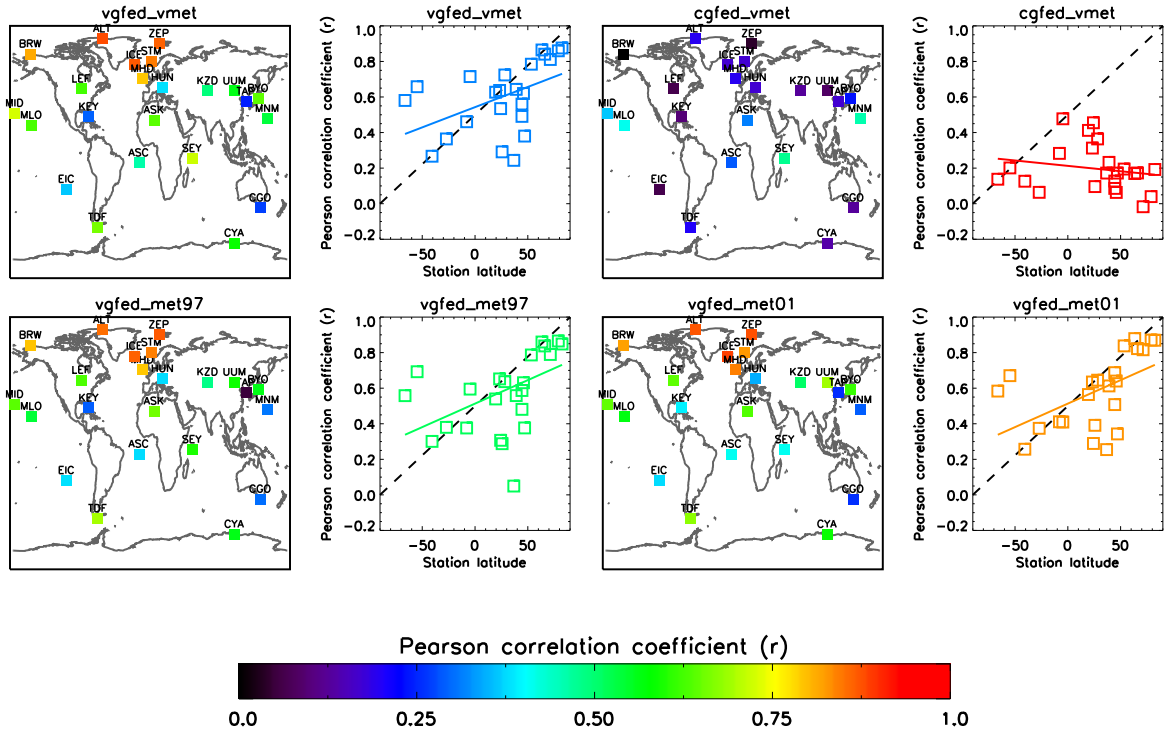

of IAV that are important in this region apart from meteorology and biomass burning emissions. One reason for this could be the tropics being more sensitive to OH concentrations due to this region being more photochemically active compared to the high latitudes. This region is therefore likely to be more sensitive to changes in the oxidising capacity of the atmosphere which will not be captured by the model experiments discussed here due to the use of fixed monthly mean OH.

Table 6.1 shows the percent contributions from different sources to the interannual variability of CO calculated from vgfed_vmet (best guess simulation). This was calculated from the standard deviation of each tracer as a fraction of the sum of all standard deviations as follows:

$$x_{ij} = \frac{\sigma_{ij}}{\sum \sigma_{ij}} \times 100, \tag{6.1}$$

where x_{ij} is the percent contribution to IAV of tracer i, at station j, and σ_{ij} is the standard deviation. The total IAV, fire IAV and anthropogenic IAV were calculated using a sum of the standard deviations of the applicable tracers. For example, for the fire IAV only the fire type tracers were

used. Also, it must be noted that the anthropogenic variability does not include variability from other anthropogenic emission regions which are outside of the regions in Figure 5.1. The percentages for the 'Total IAV' show on average fires are responsible for 85% of the total IAV at the surface in the Arctic which supports the results in Figure 6.7. This accounts for variations in both meteorology and fire emissions. Anthropogenic sources contribute a much smaller amount of 10% and direct natural, isoprene and methane sources contribute a total of 5%. As the anthropogenic and natural emissions are fixed every year, all the variations in these tracers are due to transport.

In terms of 'Fire IAV', forest fires are the largest contributor to IAV, causing 60% of IAV in the CO_TF tracer. As already shown (see Figure 5.10), forest fires are also the largest source of Arctic CO sourced from all fire types. Peat fires contribute the second largest amount to IAV of fires of 12%, followed by agricultural and savannah fires which contribute 9% each. Even though peat fires only contribute a small fraction to Arctic CO (see Figure 5.10) they exhibit a high IAV in emissions (see Figure 6.5) therefore contributing more to the IAV of Arctic CO. Conversely, savannah fires contribute a larger fraction to CO (see Figure 5.10) but do not exhibit a high IAV in emissions (see Figure 6.5). Both savannah and peat fires have fairly consistent IAV contributions at all stations whereas agricultural fires show more spatial variance with the lower latitude stations (STM and ICE) being more affected by variability in agricultural fires. This is as a result of the sources of peat and agricultural fires in GFED v3.1 being largely located in the extra-tropical regions (see Figure 3.4) and therefore emissions will be more well-mixed with background CO as they are transported polewards, however, a large fraction of agricultural fires occur in the mid-high latitudes in the NH and therefore resulting in higher concentration gradients in the CO field. Deforestation and woodland fires contribute the smallest amount to IAV of CO_TF with values of 6% and 2%.

Overall, European CO contributes the largest percentage (35%) to IAV of CO_AN, followed by North American CO (31%), then East Asian CO (19%), and the smallest contribution is from South Asian CO (15%). The contribution of different anthropogenic sources to the IAV of CO_AN show a dependence on the location of the station. European CO contributes the largest percentage (47%) to IAV at STM and ICE followed by North American CO (27-29%). East Asian and South Asian CO contribute a smaller percent of 10-15%. ALT has the largest contribution from North American CO (37%), BRW has the largest contribution from both North American and East Asian CO (27%) and ZEP has the largest contribution from North American and European CO (32-34%). BRW, ALT and ZEP have much higher contributions from Asian sources compared to STM and ICE. Again these results are similar in pattern to the transport sensitivity results shown in Section 5.3.

Until now, the IAV has only been considered at the surface. The vgfed_vmet simulation can be used as a representation of the real atmosphere to investigate how CO IAV in the free troposphere is affected by variability in biomass burning and meteorology. Figure 6.9 shows the correlations

Table 6.1 Percent contributions to the IAV of CO_TOT (Total IAV), CO_TF (Fire IAV) and CO_AN (Anthropogenic IAV) from individual tracers from the simulation vgfed_vmet at Arctic surface stations. The values have been calculated using equation 6.1.

CO Tracer	**ICE**	**STM**	**ZEP**	**BRW**	**ALT**	**Mean**
Total IAV						
CO_TF	82.5	79.5	85.1	88.9	88.3	84.7
CO_AN	12.8	14.9	9.9	5.6	7.1	10.1
CO_NAT	2.2	2.9	2.7	2.3	1.9	2.4
CO_ISO	0.9	0.7	0.8	1.7	1.1	1.0
CO_CH4	1.6	2.0	1.4	1.5	1.7	1.6
Fire IAV						
CO_AGR	12.2	14.1	9.4	5.4	6.7	9.6
CO_DEF	6.7	6.6	5.9	5.2	5.7	6.0
CO_FOR	56.5	54.9	60.4	64.8	63.7	60.1
CO_PEA	13.1	13.6	12.7	10.5	11.9	12.4
CO_SAV	8.9	8.3	8.9	11.2	9.3	9.3
CO_WOO	2.6	2.6	2.7	3.0	2.8	2.7
Anthropogenic IAV						
CO_NA	29.2	27.3	32.4	27.4	36.7	30.6
CO_EU	47.3	47.3	33.8	25.2	20.9	34.9
CO_EA	12.6	14.3	19.5	27.1	24.8	19.7
CO_SA	10.9	11.2	14.2	20.3	17.7	14.9

between the annual zonal mean CO_TOT concentrations from vgfed_vmet with CO_TOT from the other three simulations, which used either fixed meteorology or fixed fire emissions. If there is a high correlation between two model simulations, it indicates that any difference between them (either biomass burning emissions or meteorology) asserts little control on the IAV of CO at that location. Conversely, a low correlation indicates that the difference in fire emissions or meteorology results in large differences in CO and therefore the IAV. It is clear that yearly varying biomass burning emissions exert a much stronger influence on the IAV of CO than varying meteorology. The lowest correlations between cgfed_vmet and vgfed_vmet ($r<0.40$) are seen in the Arctic and extend from the surface up to around 600 hPa. This shows that model differences in biomass burning emissions are causing a large portion of the variability in the Arctic burden of CO. In the mid-upper troposphere, the correlations become larger, indicating biomass burning variability is most important in the lower troposphere. The pattern of correlations between both vgfed_met01 and vgfed_vmet, and vgfed_vmet97 and vgfed_vmet are very similar to each other. These both indicate that meteorology is not as important in the troposphere, in terms of the IAV of CO, compared with biomass burning emissions as $r>0.9$. This agrees with Duncan et al. (2007), who found the global IAV of CO to be mostly controlled by biomass burning emissions. Lower correlations

Figure 6.9 Annual zonal mean correlations between CO_TOT from vgfed_vmet and top) cgfed_vmet, middle) vgfed_met97, bottom) vgfed_met01 for the period 1997-2009.

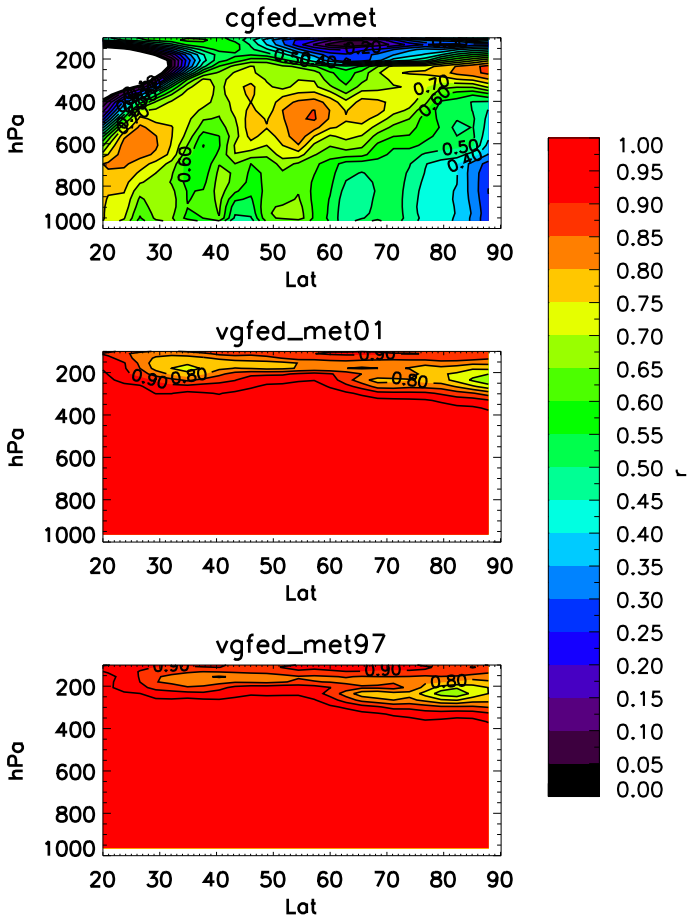

between 100-400 hPa indicates meteorology becomes more important at higher altitudes which is also where biomass burning has been shown to become less important.

6.5 Variability in transport to the Arctic

Even though Section 6.4 has shown that variability in transport plays a much smaller role compared to biomass burning emissions in determining the IAV of Arctic pollution, it is still important in terms of the sensitivity of the Arctic to emissions from mid-latitudes (see Chapter 5). Therefore, it is necessary to understand any processes that can influence poleward transport both now and in the future. There is existing evidence of a link between the North Atlantic Oscillation and winter-time observed concentrations of trace gases at the surface in the Arctic (Eckhardt et al., 2003; Sharma et al., 2006). This is of particular interest as some model predictions have suggested that increasing greenhouse gas concentrations result in a trend towards winter-time positive NAO phases (Stephenson et al., 2006; Meehl et al., 2007). If this is true, concentrations of trace gases in the Arctic may increase in the future due to increased transport. It has also been suggested that El Niño events could result in increased poleward transport (Fisher et al., 2010). Figure 6.6 showed that higher concentrations at Arctic surface stations were simulated when meteorological analyses over the 1997-1998 El Niño period were used to force TOMCAT. Any link between El Niño and transport to the Arctic has not previously been studied in detail. ENSO variability is currently thought to continue under GHG warming scenarios, however, there is evidence that teleconnnections over North America may weaken (Meehl et al., 2007). How this would affect the transport to the Arctic is not known. For these reasons, this section now investigates possible links between the NAO, PNA and El Niño with observed and simulated CO concentrations in the Arctic.

To isolate the effect of transport variability on Arctic composition, any variability due to biomass burning emissions was removed by using the cgfed_vmet simulation, which uses climatological biomass burning emissions. This also allowed the simulation to be extended back to 1990 as the length of the run was no longer constrained by the availability of yearly-varying fire emission estimates. This simulation contained the same tracers as listed in Table 5.2. For each of these tracers, two additional tracers were included which are decayed with fixed lifetimes of 30-days and 5-days rather than by reaction with OH (30-day tracers are described in Section 5.2.1). This is so the impact of transport on trace gases which have different lifetimes can seen.

Figure 6.10 shows correlations calculated for the El Niño index with observed and simulated CO at 5 surface stations north of 60°N, identifying any possible relationship between the two. Any correlation found between the index and model tracers that is not seen with the observed CO shows that El Niño does affect CO through transport but there are other processes which are more dominant (e.g. fires). Any correlation which is found between the index and observed CO which is not captured by the model suggests that this is not caused by meteorology but by El Niño affecting CO variability through other processes. The results suggest that there is a statistically significant link between variability in observed CO and El Niño in spring at ALT and BRW, and in

Figure 6.10 Pearson's correlation coefficients calculated for the El Niño index with observed and simulated CO anomalies relative to the 1990-2009 mean at surface stations located > 60°N. Symbols represent values which are significant at P<0.05 (diamonds) and P<0.01 (diamonds and crosses) levels. The monthly mean El Niño index and monthly mean CO have been separated into seasonal bins, DJF, MAM, JJA and SON (left to right). The correlations are shown for simulated tracers: CO_TOT, CO_AN, CO_NA, CO_EU, CO_EA, CO_SA (top to bottom), which are decayed by OH (prefix CO) and with fixed 30 and 5 day lifetimes (prefixes CO30 and CO5).

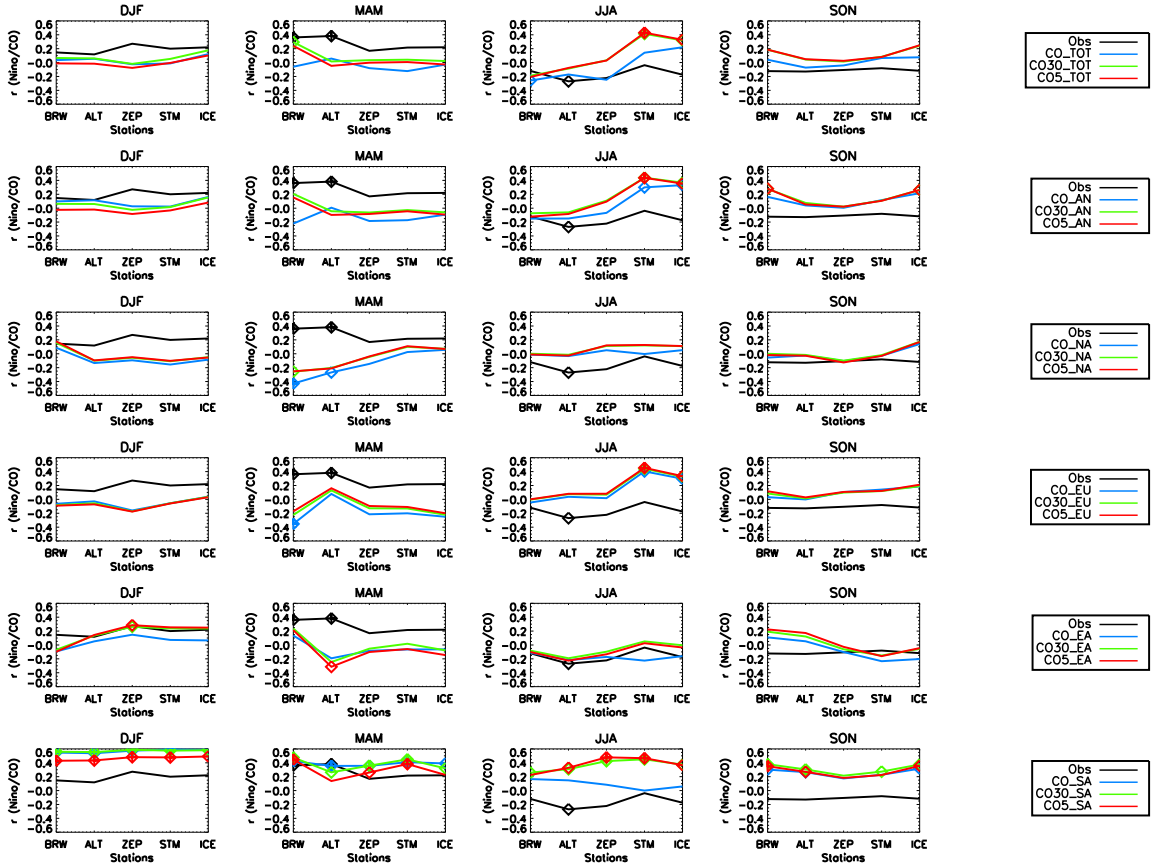

summer at ALT. Interestingly, the correlations are positive in the spring but negative in the summer. The model also shows a significant positive correlation for the CO30_TOT and CO5_TOT tracer at BRW in spring, indicating that this station is particularly sensitive to atmospheric circulation changes induced by El Niño/La Niña events, expecting increased concentrations after or during an El Niño. BRW is located in Alaska which is where Fisher et al. (2010) observed anomalously low CO during April 2008 attributing it to a La Niña, which agrees with the results shown here. Alaska is particularly sensitive to ENSO teleconnections due its Pacific coastal location, experiencing temperature and precipitation anomalies (see Figure 6.2). The regional tracers indicate that the positive correlations in the observed CO are due to increased transport from South and East Asia. The results also suggest that the transport patterns from Asia during an El Niño are especially significant for shorter lived species, enabling them to reach the Arctic. The significant correlation for observed CO at ALT in spring is not reproduced by any of the CO_TOT tracers. According to

Figure 6.11 Pearson's correlation coefficients calculated for the NAO index with observed and simulated CO anomalies relative to the 1990-2009 mean at surface stations located > 60°N. Symbols represent values which are significant at P<0.05 (diamonds) and P<0.01 (diamonds and crosses) levels. The monthly mean NAO index and monthly mean CO have been separated into seasonal bins, DJF, MAM, JJA and SON (left to right). The correlations are shown for simulated tracers: CO_TOT, CO_AN, CO_NA, CO_EU, CO_EA, CO_SA (top to bottom), which are decayed by OH (prefix CO) and with fixed 30 and 5 day lifetimes (prefixes CO30 and CO5).

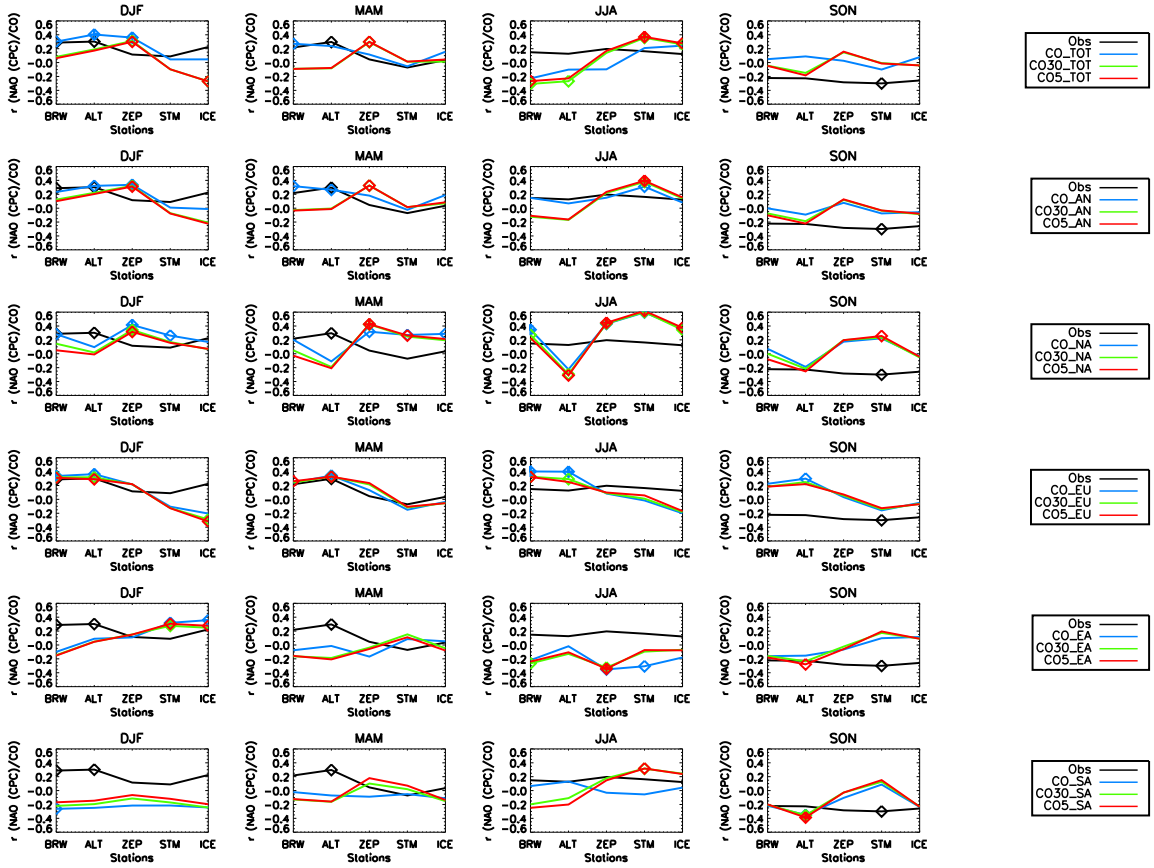

the model, the link between El Niño and CO in spring at ALT is not due to meteorology. In the summer, the regional tracers suggest that transport of emissions from East Asia is reduced during an El Niño, which could be causing the negative correlation with the observations. The tracers also show that transport to all stations from South Asia is increased and transport to STM and ICE from Europe is increased, however, this is not reflected in the observations. In winter and autumn, the only tracer which shows significant correlations is CO_SA which suggests there is a strong link between the export of South Asian emissions with El Niño. It is known that the export of South Asian emissions is mostly controlled by the monsoon (Stohl and Eckhardt, 2004) and that stronger trade winds during an El Niño have been associated with stronger monsoon seasons (Webster and Yang, 1992). However, more recently there is evidence of a weakening of this relationship possibly due to increasing atmospheric temperatures (Kumar et al., 1999; Meehl et al., 2007). This suggests

Figure 6.12 Pearson's correlation coefficients calculated for the PNA index with observed and simulated CO anomalies relative to the 1990-2009 mean at surface stations located > 60°N. Symbols represent values which are significant at P<0.05 (diamonds) and P<0.01 (diamonds and crosses) levels. The monthly mean PNA index and monthly mean CO have been separated into seasonal bins, DJF, MAM, JJA and SON (left to right). The correlations are shown for simulated tracers: CO_TOT, CO_AN, CO_NA, CO_EU, CO_EA, CO_SA (top to bottom), which are decayed by OH (prefix CO) and with fixed 30 and 5 day lifetimes (prefixes CO30 and CO5).

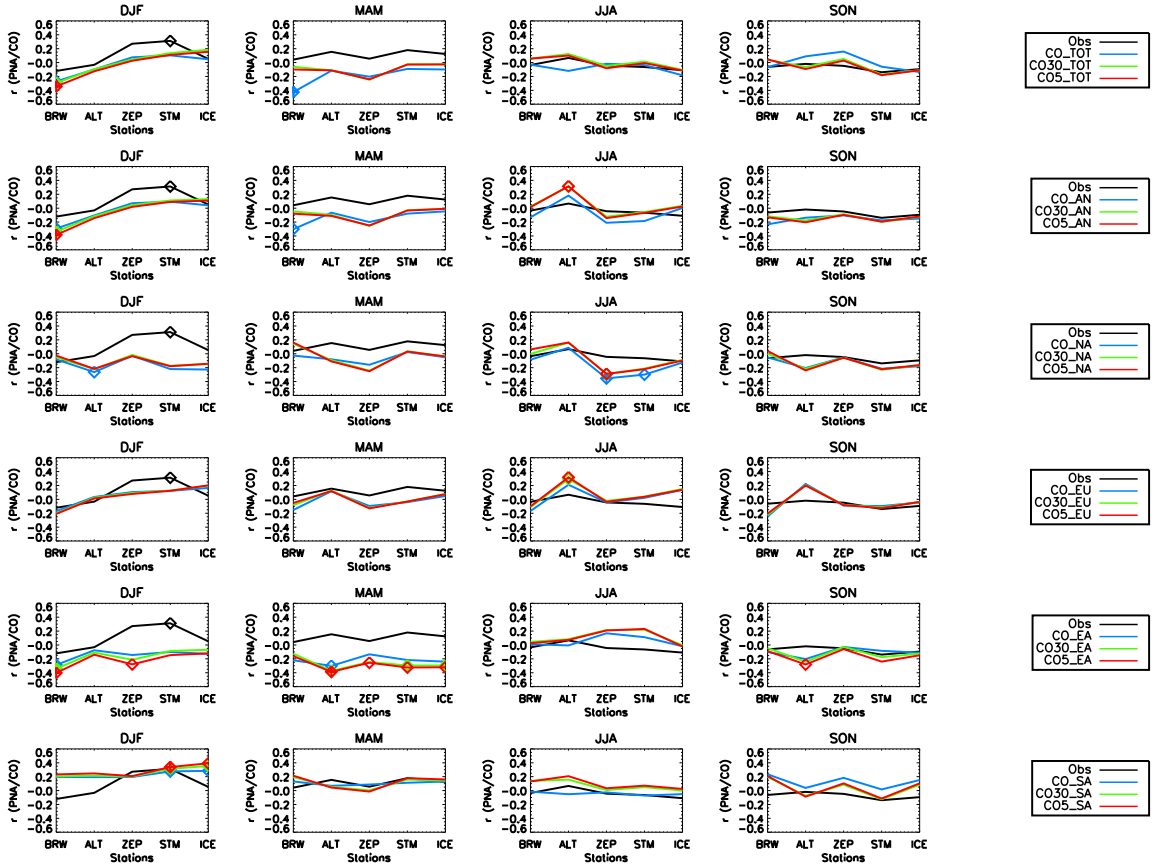

that in the future, the impact of South Asian emissions on the Arctic burden of trace gases may become even less.

Figure 6.11 is the same as Figure 6.10, but the correlations have been calculated with the NAO index. In agreement with Eckhardt et al. (2003), the winter correlations show there is a link between observed CO and the NAO index at BRW and ALT, however, the results shown here indicate that there is also a link at these stations in spring and at STM in autumn. There is a similar relationship between the NAO and CO_TOT tracers in winter and spring suggesting that variability at the surface is connected to NAO circulation changes. In winter and spring the regional tracers show that the model correlations at BRW are due to enhanced transport from North America and Europe and at ALT are due to increased transport from Europe during positive NAO years. In the

Figure 6.13 Global maps of Pearson's correlation coefficient between the El Niño 3.4 index and simulated total column CO over the 1990-2009 period averaged seasonally (left to right). Tracers CO_TOT, CO_AN, CO_NA, CO_EU, CO_SA, CO_EA (top to bottom) are from the simulation cgfed_vmet. Values which are not significant at the P<0.05 level have been removed.

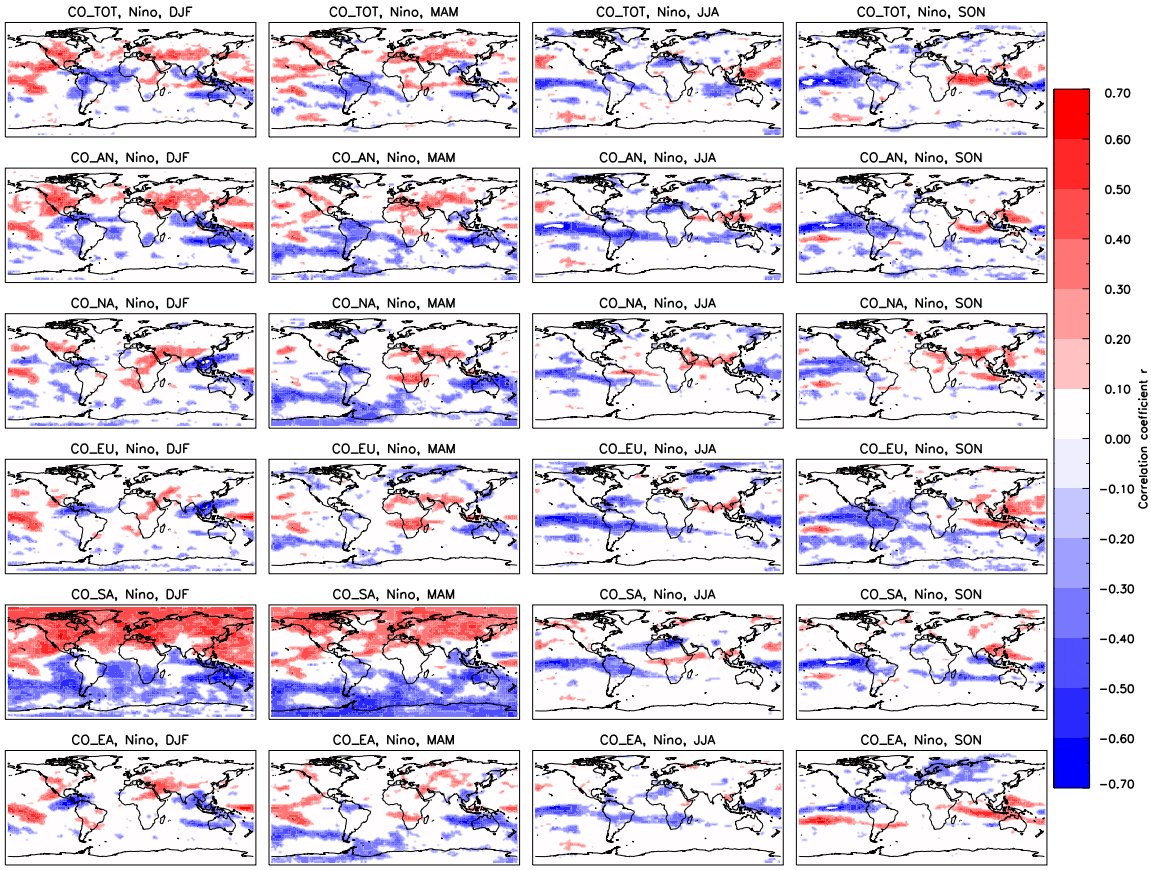

autumn, the model tracers do not reproduce the significant correlation at STM suggesting that this is caused by processes other than meteorology.

Figure 6.12 is also the same as Figure 6.10 but calculated for the PNA index. The correlations with the observations suggest that the PNA is only important in winter when at its strongest (Barnston and Livezey, 1987), with STM revealing a significant positive correlation. This suggests that in the winter a positive PNA can result in more CO being transported to the Arctic surface. This is because high latitude blocking during negative PNA phases (see Section 6.2.3) limits transport to the Arctic. The regional tracers show that this winter correlation is mostly due to increased transport from South Asia and to some extent from Europe. Even though the observations show that the PNA is only important at STM and ZEP in the winter, the model tracers show that East Asian, European and North American emissions are influenced to some extent throughout the year depending on station location.

Figures 6.13–6.15 show maps of significant correlations between the seasonally averaged climate

Figure 6.14 Global maps of Pearson's correlation coefficient between the NAO index (CPC) and simulated total column CO over the 1990-2009 period averaged seasonally (left to right). Tracers CO_TOT, CO_AN, CO_NA, CO_EU, CO_SA, CO_EA (top to bottom) are from the simulation cgfed_vmet. Values which are not significant at the P<0.05 level have been removed.

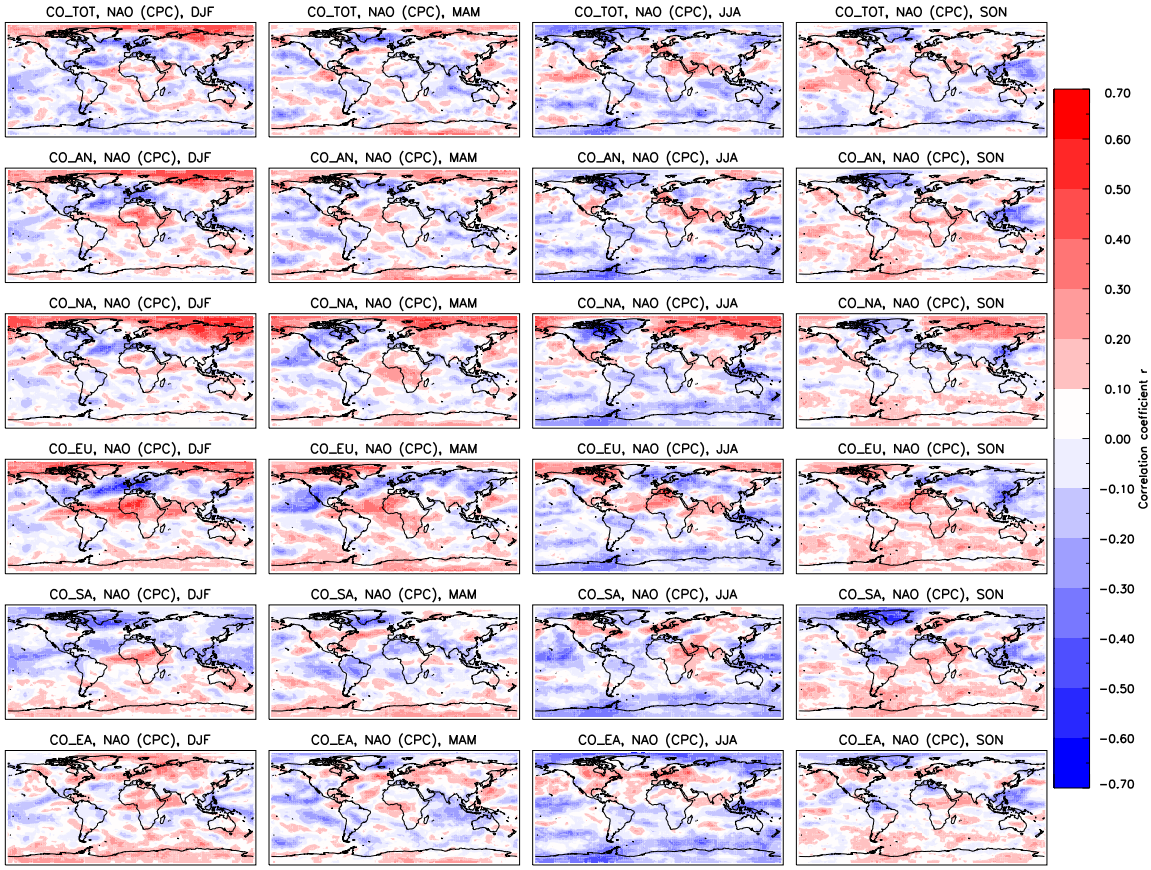

indices, El Niño, NAO and PNA, with the total tropospheric CO column calculated from five realistic lifetime tracers. As suggested by Figure 6.10, El Niño reveals limited correlations with the total Arctic CO when considering changes in circulation alone. The maps reveal the largest correlations between El Niño and the South Asian emission tracer with winter and spring showing significant positive correlations over most of the NH and the Arctic. This corresponds to what was seen in the South Asian tracer at the surface in Figure 6.10. In winter and spring, the total tracer shows statistically significant evidence of increased concentrations over parts of Alaska and Canada during El Niño events, again in agreement with the satellite observations shown in Fisher et al. (2010). In summer and autumn, there is evidence of negative correlations in the total CO tracer over parts of the Arctic ocean and Canada and Siberia. The regional tracers show that this is because of reduced concentrations of European CO in summer and East Asian CO in autumn. This suggests that the interaction of the Arctic CO burden with El Niño is complex with seasons responding in different ways.

According to the model, Figure 6.14 shows that circulation changes associated with the NAO may

Figure 6.15 Global maps of Pearson's correlation coefficient between the PNA index and simulated total column CO over the 1990-2009 period averaged seasonally (left to right). Tracers CO_TOT, CO_AN, CO_NA, CO_EU, CO_SA, CO_EA (top to bottom) are from the simulation cgfed_vmet. Values which are not significant at the P<0.05 level have been removed.

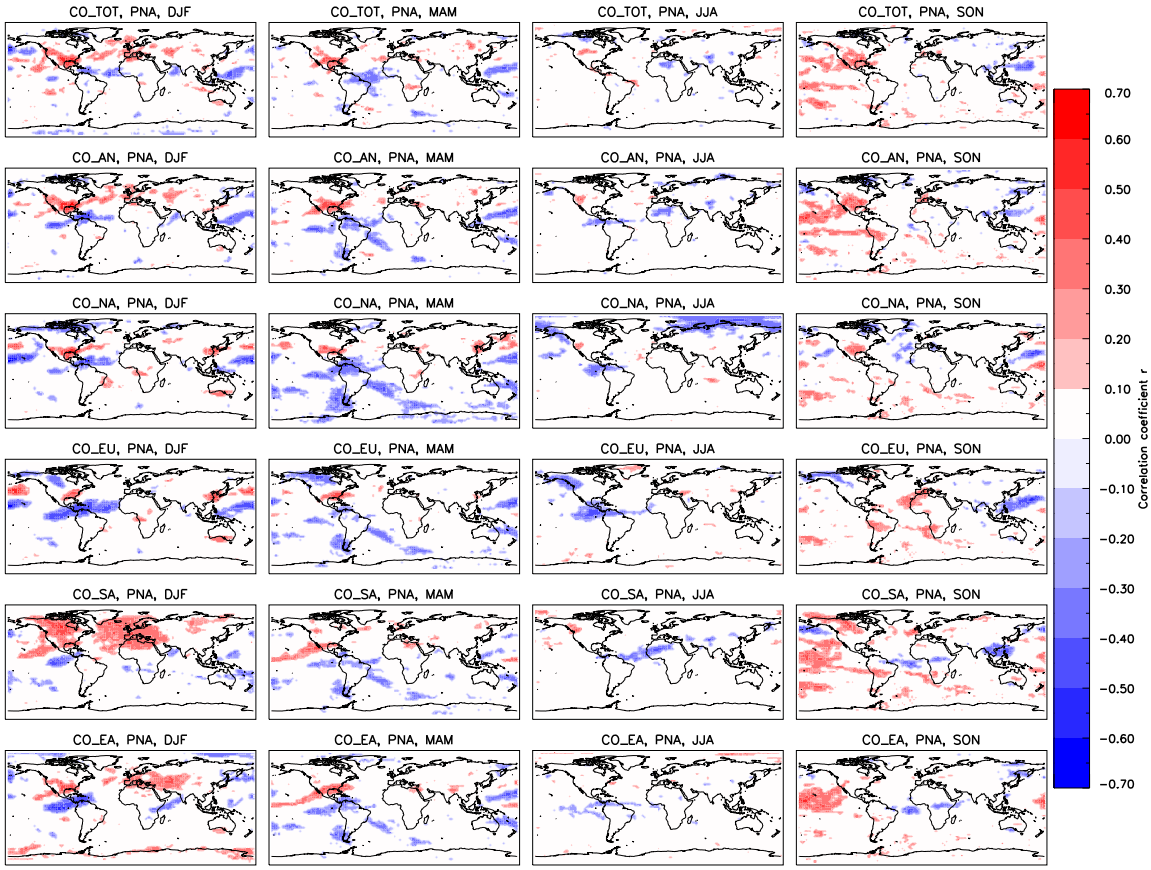

have a global impact on concentrations of CO throughout the year. For the CO_TOT tracer, the largest correlations in the Arctic occur in the winter, with clear positive correlations over the whole Arctic region, indicating total CO is increased during wintertime positive phases of the NAO. The regional tracers show that this is likely due to increased transport from Europe and North America with some indication that East Asian transport is also increased. Conversely, South Asian CO shows statistically significant negative correlations in the Arctic. North America and Europe are located either side of NAO wintertime centre, making transport pathways particularly susceptible to any strengthening/weakening of circulation over the Atlantic. The intense low pressure anomaly during positive phases also extends over parts of Asia (see Figure 6.4), drawing air polewards from East Asia. Stronger trade winds during positive NAO phases (Ambaum et al., 2001) leads to correlations that are generally positive in the SH and negative in the NH for the South Asian CO tracer. One previous study analysed the impact of the NAO on the winter-time anthropogenic export of pollution and also found increased poleward transport from North America, Europe and Asia during positive NAO phases (Eckhardt et al., 2003). As the season progresses, the influence

of the NAO on the Arctic evolves. In spring, the CO_TOT tracer shows regional differences in the correlations with the NAO in the Arctic, with negative correlations over North America and the North Atlantic spreading poleward into parts of the Canadian Arctic and over Greenland. The regional tracers show that this is because even though North American and European CO show predominately positive correlations, negative correlations are now observed in the Canadian Arctic for North American CO and in the region of Greenland for the North American, East Asian and South Asian CO. This is due to an eastward shift in the NAO centre (see Figure 6.4), which reduces the direct transport into the Arctic and draws air more over the Pacific towards North America instead of poleward. In the summer, CO_TOT shows that the overall impact on CO would be a reduction in CO during positive NAO years. East Asian CO shows significant negative correlations throughout the Arctic and North American, European, and South Asian CO show some regional negative correlations. In the summer, the Arctic becomes more sensitive to Asian emissions (see Chapter 5) and therefore the NAO influence on this region contributes more to the overall Arctic response. In summer, the centre of the NAO shifts north-eastwards (see Figure 6.4) with large parts of Europe and Scandinavia being covered in anomalously high pressure during positive phases. This draws air southwards towards North Africa where positive correlations between the NAO and CO_EU are visible with negative correlations over Scandinavia. The high pressure extends towards North America (Folland et al., 2009), drawing North American emissions towards Scandinavia where positive correlations are visible in the CO_NA tracer resulting in negative correlations over North America and Canada. Positive correlations also occur over the North America emission region suggesting air becomes more stagnant due to the associated high pressure system (Folland et al., 2009).

Figure 6.15 shows that the PNA has a limited impact on the total Arctic burden of CO. The largest correlations are seen with the South Asian tracer in winter where positive correlations occur over much of Canada and the North Atlantic and to a lesser extent during autumn. In the summer, the North American tracer shows negative correlations in the Siberian region of the Arctic suggesting that less CO from North America is found here during positive phases of the PNA.

To estimate the importance of these correlations for the absolute concentrations of CO in the Arctic, the differences between concentrations of simulated CO during seasons with strongly positive and strongly negative index values have been calculated. For each month, six years were selected, of which three were the most negative and three were the most positive over the 1990-2009 period for the El Niño, NAO and PNA indices. These months were then averaged seasonally to create CO fields to represent positive and negative index seasons (these composites will be referred to as NINO+, NINO- , NAO+, NAO-, PNA+ and PNA-). The seasonally averaged differences between the positive and negative indices varying with altitude are shown in Figure 6.16. One clear pattern, is that the indices generally have the largest impact on total Arctic CO in the mid-upper troposphere and not at the surface. Another general point is that all tracers show a significant amount of

Figure 6.16 Seasonally averaged (left to right) absolute differences in simulated CO concentrations >66°N between NINO+ and NINO- (top), NAO+ and NAO- (middle), PNA+ and PNA- (bottom) composites at different altitudes. Note the different x-axis

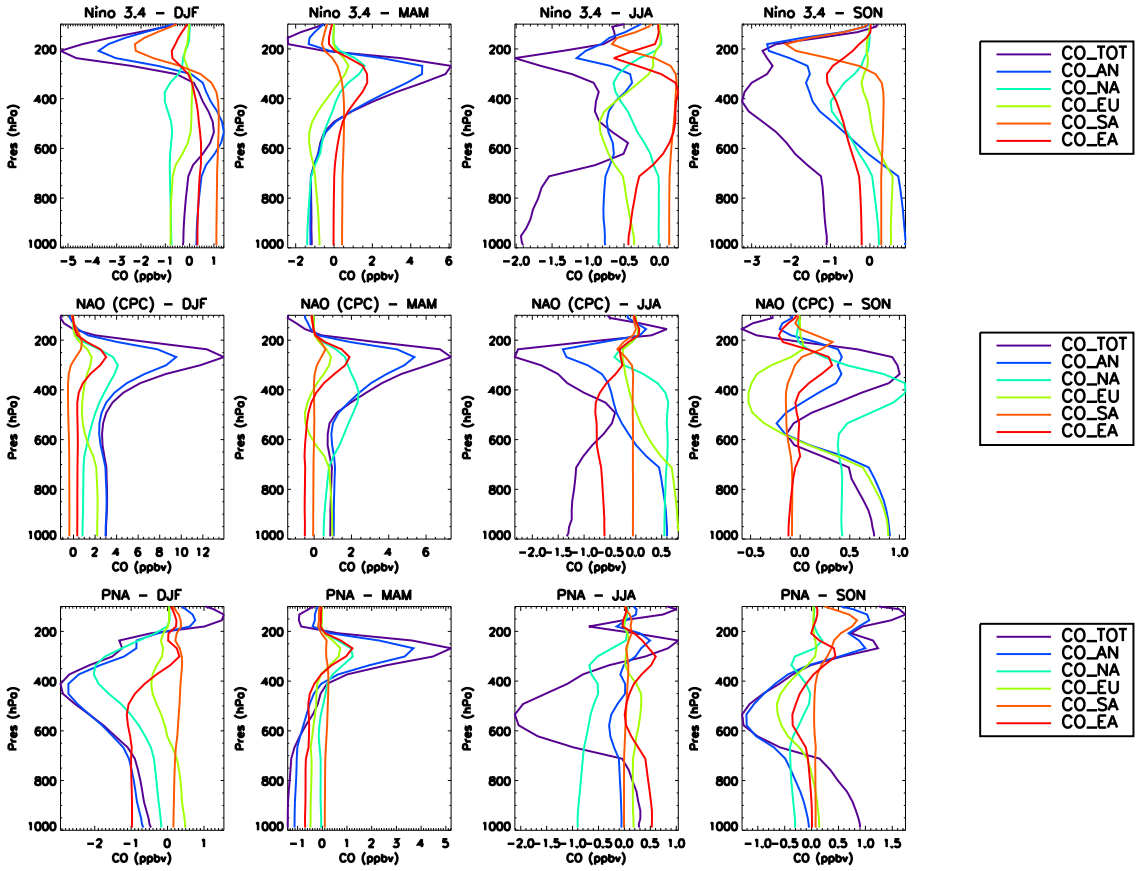

seasonal variability. Out of the indices considered, the NAO has the largest impact on total Arctic CO in the winter and spring, and the El Niño has the largest impact in autumn. In summer all three indices show similar absolute variations between the different phases.

Considering the El Niño influence alone, in winter between the surface and 300 hPa, the CO_TOT tracer shows a very small difference between NINO+ and NINO-. The regional tracers show this is because under NINO+ conditions, Arctic CO is increased by 1 ppbv from South Asia and by ∼0.4 ppbv from East Asia, however, this is countered by equivalent decreases in North American and European CO. European CO shows less difference at higher altitudes and therefore CO_TOT shows a slight increase (1 ppbv) in overall CO at around 550 hPa. The largest impact from El Niño occurs in spring where CO_TOT shows an increase of 6 ppbv at 300 hPa which supports the speculations of Fisher et al. (2010). The tracers show that 4.5 ppbv of this CO is from anthropogenic (CO_AN). All regional tracers show an increase to some extent at this altitude, however, East Asian CO shows the largest contribution of almost 2 ppbv. In the summer, the total CO responds differently and decreases by up to 2 ppbv, both at the surface and at 250 hPa. At the surface, about half

of this is due to a reduction in East Asian and European CO and the other half is due to non-anthropogenic sources, such as fires and natural emissions. In the upper troposphere, the lower CO in NINO+ is due to a reduction in East Asian, South Asian and North American sources plus other non-anthropogenic sources. In autumn, total CO is reduced by between 1 and 3 ppbv throughout the troposphere in NINO+. In the mid-upper troposphere about half of this is due to anthropogenic sources and the half is due to other sources. In the lower troposphere, anthropogenic CO shows an increase in CO due to European and to a lesser extent North American and South Asian CO, indicating that the reduction in total CO in the lower troposphere is due to less transport of emissions from fires and natural sources.

NAO+ relative to NAO- shows an increase in CO_TOT throughout the troposphere in winter and spring with up to 12 ppbv and 7 pbbv differences at 300 hPa, mostly due to increased transport of anthropogenic emissions. North American CO dominates the differences in the upper troposphere and European CO dominates the difference in the lower troposphere. East Asian and South Asian CO show slight increases in the upper troposphere at 300 hPa. Eckhardt et al. (2003) also examined the wintertime concentration response of anthropogenic fixed lifetime tracers at the surface between NAO positive and negative phases and also found a positive response in European, North American and Asian emissions. As with El Niño, the response of CO to NAO circulation changes is reversed in the summer, with CO_TOT now lower throughout the troposphere in NAO+ years relative to NAO- years. The largest impact is at 250 hPa where CO_TOT shows 1.8 ppbv difference, which is mostly due to anthropogenic emissions. At the surface CO_TOT also shows up to 1.3 ppbv less CO in NAO+ years, however, the anthropogenic tracer shows a small increase of 0.5 ppbv indicating that the NAO also influences transport from other sources such as fires and natural sources, which are more important in summer. In autumn, the CO_TOT tracer reverts back to the winter and spring response, with an increase of up to 1 ppbv from NAO- to NAO+.

The PNA generally shows smaller differences between the PNA+ and PNA- compared to the other indices. In winter, CO_TOT is up to 3 ppbv lower in PNA+ relative to PNA- at 400 hPa, this is due to anthropogenic emissions, most notably from North America and East Asia. In spring, CO_TOT shows a difference of around 1.5 ppbv from the surface up to 300 hPa, where the positive PNA increases CO by up to 5 ppbv. In summer and autumn, the PNA+ shows lower concentrations compared to PNA- as seen in winter, however, they occur lower in the troposphere, around 550 hPa. The regional tracers show that in summer, the anthropogenic CO is not solely responsible for the response in CO_TOT, even though North American CO is reduced by up to 1 ppbv, therefore transport from other sources are also reduced during PNA+. In autumn, however, a combination of less CO from East Asia and Europe are responsible for the reduced CO.

6.6 Variability in fire emissions: El Niño, biomass burning and Arctic CO.

Section 6.5 showed that CO in the Arctic can be enhanced by as much as 6 ppbv in spring and decreased by 5 ppbv in winter in the upper troposphere due to changes in meteorology during an El Niño relative to a La Niña. However, variability in biomass burning emissions has been shown to be the dominant process controlling CO IAV at latitudes greater than 60°N (see Section 6.4). Fires are intrinsically linked to temperature and the availability of water and therefore links between fire activity and natural climate oscillations have been found (Bowman et al., 2009). In particular, many studies have found regional correlations between El Niño and fire activity (Williams and Karoly, 1999; Kitzberger et al., 2001; Page et al., 2002; van de Werf et al., 2004; Westerling et al., 2006). Here, possible links between Arctic CO IAV and El Niño are investigated, through El Niño's impact on biomass burning emissions. Figure 6.7 shows the annual mean NAO, PNA and Niño 3.4 indices with the observed and simulated annual CO anomalies at the surface in the Arctic. There is a resemblance between the Niño 3.4 index and the CO anomaly time series at each Arctic station, but offset by 1 year. To investigate this relationship further, lag correlations have been calculated between the monthly mean El Niño index and the monthly mean observed and simulated CO at the same surface stations. The correlations with a lag of 1 to 12 months, calculated for the 1997-2009 time series are shown in Figure 6.17. A full observational dataset is not available at ALT and STM for this time period, therefore lag correlations are only shown for the model simulations. Significant positive correlations are found between El Niño and observed CO anomalies at ZEP, BRW and ICE, with lags of 5 to 12 months. The highest correlations ($r \approx 0.6$) occur with lags of 10 to 11 months. This shows that Arctic CO during the 1997-2009 period has increased 5-12 months after an El Niño. Significant correlations between El Niño and CO from the vgfed_met01 and vgfed_met97 simulations reveal similar correlations. The cgfed_vmet simulations, which uses climatological fire emissions, does not show any significant correlations. The model results therefore suggest that the correlation between the observations and the El Niño index is due to a link between fire emissions and El Niño, not transport.

To determine whether this link with El Niño is unique to the Arctic, lag correlations at selected surface stations south of 60°N have also been calculated and are shown in Figure 6.18. At MHD, the lag correlations show the same relationship as seen in the Arctic due to its location being relatively far North at 53°N. Interestingly, at MLO, the cgfed_vmet simulation shows some significant positive correlations suggesting that El Niño increases transport of CO to this station. The location of this station in North Pacific (see Figure 4.12) makes it particularly sensitive the atmospheric circulation changes associated with ENSO. At most stations, the observations and simulated tracers show different correlations with El Niño. This suggests that there are other processes at these latitudes that influence CO, which are not accounted for in the simplified tracer simulations used

in this chapter. As already discussed in Section 6.1, El Niño has previously been shown to shift convection in the tropics and therefore lighting emissions of NO_x, modifying budgets of O_3 and HO_x (Doherty et al., 2006). Another El Niño dynamical impact is that on STE, where increased stratospheric ozone has been found in the troposphere after an El Niño event (Zeng and Pyle, 2005). Any composition changes are likely to feed into the OH budget which will not be captured by these simulations due to the use of offline OH fields. Also, the TOMCAT model has previously been shown to underestimate convection in the tropics (Hoyle et al., 2011; Feng et al., 2011) and therefore may not accurately capture redistribution of trace gases due to convection or subsidence.

The gradual increase in correlation with increasing lag, seen in Figure 6.17, could be due to different timings and lengths of El Niño/La Niña events, timings of fires of different types being different in different regions or different transport times from different regions. The fire type tracers can be used to examine possible links between El Niño and different types of fires. The lag correlations between the El Niño index and CO anomalies from each of the simulated fire type tracers from vgfed_vmet interpolated to ZEP are shown in Figure 6.19. The model tracers show that total fire tracer (CO_TF) exhibits the same lag correlations as the total CO tracer (CO_TOT), supporting the hypothesis that the Arctic CO correlations with the El Niño index are due to interactions between El Niño and fires at lower latitudes. Most of the tracers show similar lag correlation patterns as CO_TOT and CO_TF, increasing with increasing lag until around 10 months, but with smaller correlations. The peat fire tracer (CO_PEA) and the deforestation fire tracer (CO_DEF) show lag correlations that peak earlier in the year. This is due to the burn season occurring earlier in the calender year compared to the other fire types. The agricultural fire tracer (CO_AGR) shows very little correlation with El Niño, suggesting this type of fire is not affected by the climatic teleconnections of El Niño. This is because agricultural fires are mostly controlled by humans and not the climate. The lag correlations between the index and the emissions for each of the fire tracers are also shown in Figure 6.19 which removes the impacts of El Niño on the transport of emissions in the model. The fire tracer emissions still exhibit similar relationships as seen in the model fire tracers apart from the maximum correlations occur at shorter lags. For example, the peat fire emissions have a maximum correlation with a lag of 0 months, whereas the peat fire model tracer has a maximum correlation with lag of 3 months. As the majority of peat fire emissions in GFED v3.1 occur in tropical Asia, this 3 month lag will partly be due to transport time-scales to the Arctic from the SH. As the fire emissions have been shown to exhibit similar correlations between the El Niño index and fires, these will be used in the following section to investigate the different regional fire responses to El Niño climate effects.

Figure 6.17 Monthly lag correlations at surface stations > 60°N calculated between the monthly mean El Niño 3.4 index and both monthly mean observed and simulated (from vgfed_vmet, cgfed_vmet, vgfed_vmet97 and vgfed_met01) CO anomalies for the period 1997-2009. Correlations which are significant at the level P<0.01 are denoted by symbols.

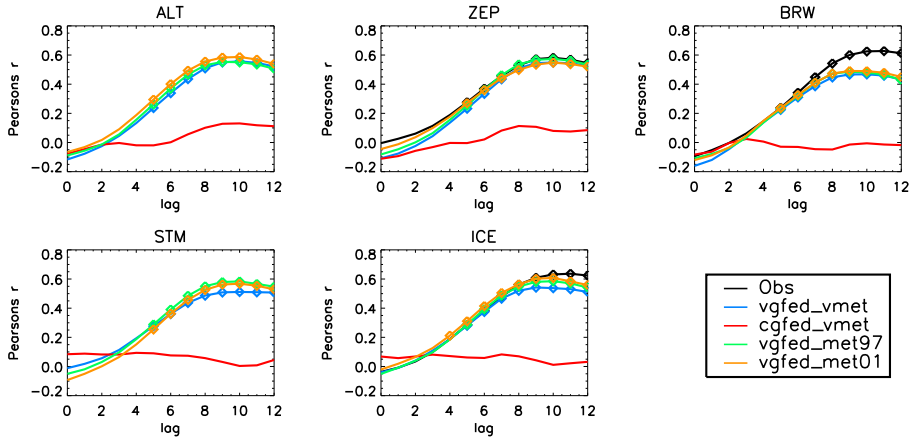

Figure 6.18 Same as Figure 6.17, but for surface stations < 60°N.

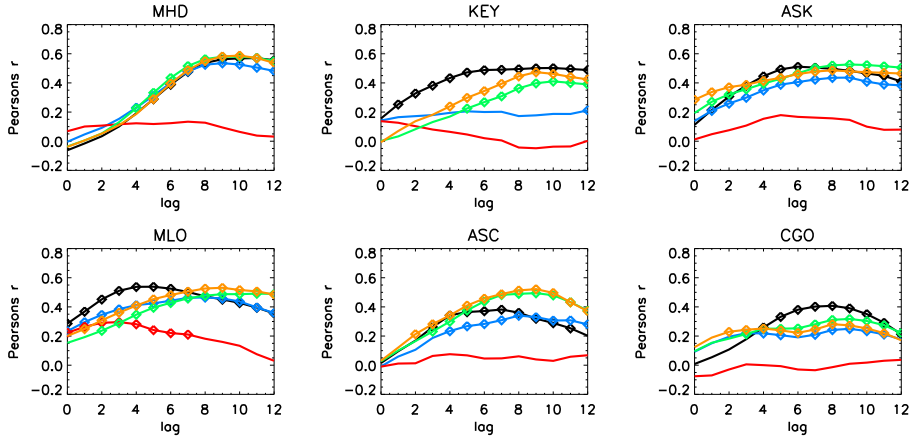

Figure 6.19 Monthly lag correlations calculated between the El Niño 3.4 index and monthly mean simulated fire type tracer CO anomalies relative to 1997-2009 mean at ZEP (left) and between the El Niño index and the monthly global fire type tracer emission anomaly relative to 1997-2009 mean (right).

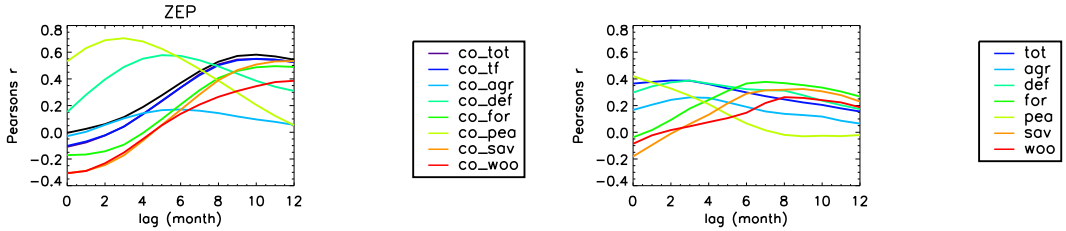

6.6.1 Climate drivers of fires and links with El Niño.

As already mentioned, there is existing evidence that fire activity can be influenced by El Niño. Arid regions of Central and South America and parts of Australia are very sensitive to increases of precipitation which lead to an increase in plant productivity providing additional fuel for fires during the dry season (Holmgren et al., 2006a). This implies that the effect of El Niño on different regions will also depend on the timing of regional burn seasons, i.e., increased precipitation before or during burn seasons could either increase fuel for fires or suppress fires by reducing the flammability of fuel. Moreover, fire activity response to El Niño also depends on the regional climatic response. For example, Peru experiences an increase in rainfall during El Niño events whereas Australia experiences a decrease (Holmgren et al., 2006b). For this reason, different regional climate drivers of fires are investigated in terms of the regional response of temperature, precipitation and relative humidity to El Niño. All previous studies have limited their focus to specific regions, here an analysis has been conducted globally.

As shown in Figure 6.2, El Niño affects both temperature and precipitation in regions other than the equatorial Pacific. These teleconnections represent the most significant, recurrent patterns which are associated with El Niño events, however, teleconnections can vary in time (McPhaden et al., 2006) and therefore certain years may not exhibit all these features. For this reason, the seasonal mean anomalies of ECMWF ERA-Interim reanalyses of temperature and precipitation were used to calculate correlations with the seasonal mean El Niño index over the 1997-2009 period and are shown as global maps in Figure 6.20. Overall, the patterns identified by these correlations during the 1997-2009 period are mostly similar to the predominant teleconnections which are shown in Figure 6.2. There is clear evidence of positive correlations in both temperature and precipitation in

Figure 6.20 Correlation coefficients between the El Niño 3.4 index and ECMWF ERA-Interim precipitation (top) and ECMWF ERA-Interim temperature (bottom) averaged over seasons (left to right) for 1997-2009. Values which are not significant at the $P<0.05$ level have been removed.

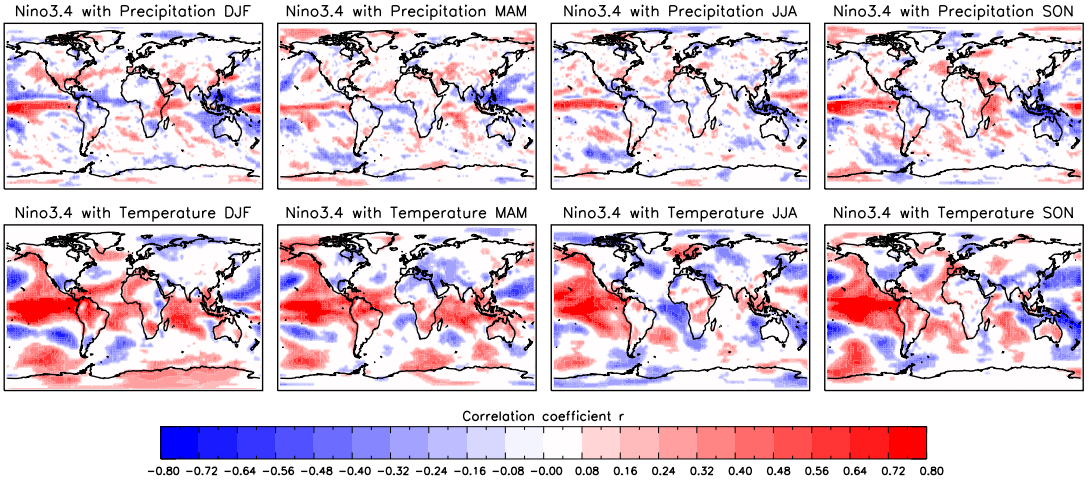

Figure 6.21 Regions used for analysing El Niño influences on fires.

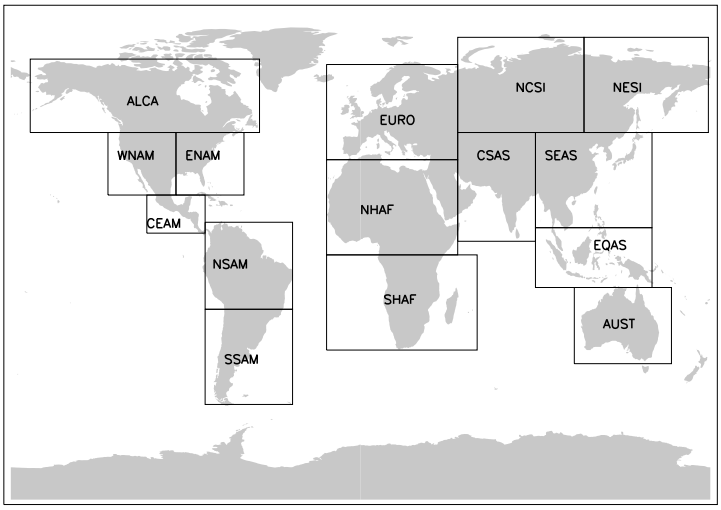

the equatorial Pacific as expected. During an El Niño, positive correlations suggest that Central and South America experience higher temperatures, and in some parts, negative correlations suggest less precipitation. Positive correlations with temperature are also seen over much of the North Pacific, up the east coast of North America and in Alaska. Conversely, southern North America shows negative correlations with temperature and positive correlations with precipitation. Negative correlations suggest Central Africa experiences wetter weather and positive correlations suggest Southern Africa experiences drier and warmer weather during El Niño events. Equatorial Asia exhibits positive correlations suggesting that it experiences drier and warmer weather during El Niños as expected. One pattern which occurred during the 1997-2009 period that is not shown in Figure 6.2, is negative correlations over the Middle East suggesting cooler and wetter weather and a region of positive correlations over Scandinavia during the summer, suggesting warmer weather under El Niño conditions. The teleconnections at mid to high latitudes are less consistent as they are affected by regional climatic noise (McPhaden et al., 2006) and may explain why these two patterns are not seen in Figure 6.2.

6.6.1.1 Climate drivers of fires

As the GFED fire emissions and the ERA-Interim reanalyses used by the TOMCAT model have been shown to capture the correlation between El Niño and Arctic surface CO and the climate teleconnections, these are now used to investigate possible driving processes of fires in different regions and links with El Niño. El Niño is generally at its strongest between November and February, therefore the index was averaged over this period to calculate correlations with the fire

emissions and the climate parameters (temperature, relative humidity and precipitation). Considering the regionally-varying climate responses to El Niño, 15 regions were defined and are shown in Figure 6.21. The monthly total emissions over the period 1997-2009 for each of these regions are shown in Figure 6.22 showing that maximum fire emissions occur during different months in different regions. For example, in the boreal regions of Alaska and Canada (ALCA), north-eastern Siberia (NESI) and central and western Siberia (NCSI), the maximum fire emissions occur during June to September, during the boreal summer. In the tropics and extra-tropics (i.e., Central America (CEAM) and south-east Asia (SEAS)), the maximum fire season occurs earlier in the year, during February to June. For this reason, a 'burn season' (BS) was defined for each region as the period with the maximum total fire emissions (also shown in Figure 6.22). There were two exceptions to this, equatorial Asia (EQAS) and western North America (WNAM). Firstly, for EQAS a smaller BS between January and March was used as it is this BS which is most easily influenced by an El Niño in the November to February period (as denoted by the significant correlations in Figure 6.22). However, it should be noted that the relationship between the later BS (August to December) and the coincident index is the same as what will be discussed here. For WNAM, the same BS as eastern North America (ENAM) was chosen because this is the peak forest fire season, which is of most interest as it was shown to be the dominant contributor to Arctic fire sourced CO (see Chapter 5). Precipitation was integrated over each region, between November (start of the El Niño period) and the start of each region's BS (referred to as pb4) and then again between the start and end of the BS (referred to as pdu). Similarly, averages of both temperature and relative humidity before (tb4 and hb4, respectively) and during (tdu and hdu, respectively) the BS were calculated over each region. The monthly mean emissions from the GFED v3.1 total fire emissions were also summed over the area of each region during the BS and will be referred to as BSem.

BSem and all of the climate parameters (pb4, tb4, hb4, pdu, tdu, hdu) were correlated with the November to February El Niño index to identify any possible regional links between El Niño and fire emissions, and El Niño and climatic fire drivers. The climate parameters were then also correlated with BSem to identify possible regional drivers of fires. These can then be used together with the El Niño correlations to understand what may be driving the fires in each region and how fires may respond under El Niño/La Niña conditions. This furthers our understanding of how global fires may respond in the future to changes in precipitation and temperature. The monthly total precipitation and monthly mean temperature for each region are shown in Figures 6.23 and 6.24 with the monthly fire emissions overlain. It can be seen that the climatic conditions which yield the maximum fire emissions differ depending on the region, suggesting that the regional response to increasing temperatures and changes in precipitation will depend on the regional fire drivers, and therefore it is important to understand what they are. For example, the boreal fire season occurs during the summer when temperatures are at their highest and total precipitation is increasing, whereas in the tropics the fire season coincides with the dry season when precipitation

Figure 6.22 Monthly mean emissions summed over the 15 selected regions. The start and end of the 'burn season' used for analysis is denoted by the blue and red dotted lines, respectively. Correlation with the monthly emissions with the El Niño 3.4 Index are also shown in by the green circles, filled circles represent values which are significant at the P>0.05 level.

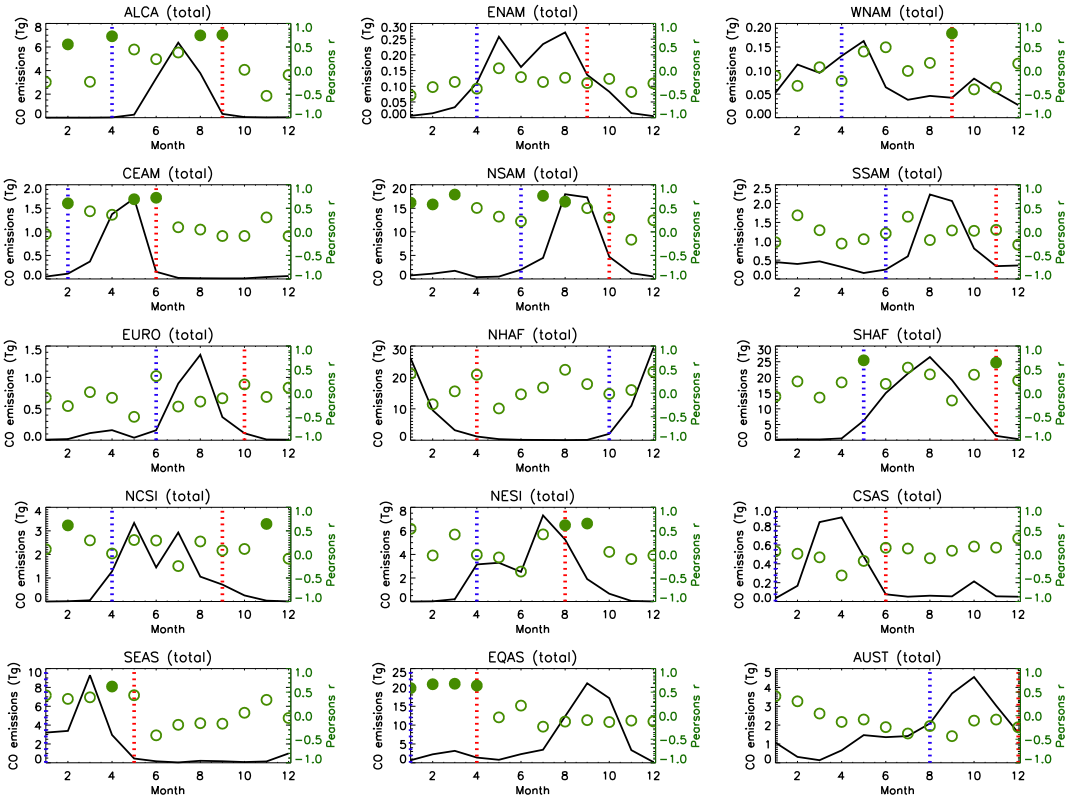

is at a minimum.

Table 6.2 shows the correlation coefficients which have been calculated between BSem with the meteorological parameters, identifying regions where these parameters appear to control or influence the intensity or frequency of fires. The climate drivers discussion has been separated into three sections below.

Boreal fires

The total precipitation prior to the BS (pb4) in Alaska and Canada (ALCA) is the only climate parameter that has a significant correlation (r=-0.61), indicating this is likely to be the dominant process which drives fires in this region out of the parameters considered. A negative correlation indicates that when there is a decrease in precipitation in this region between November to April (pb4), fire emissions tend to be greater during the BS. This is in agreement with Crevoisier et al. (2007) who found precipitation to be the most important variable in modelling burned area in Canada. Eastern Siberia (NESI), also exhibits a significant negative correlation (r=-0.74) with

Figure 6.23 Monthly total precipitation (m) over the 15 regions used for analysis (grey bars). Monthly mean GFED emissions are shown by the solid black line.

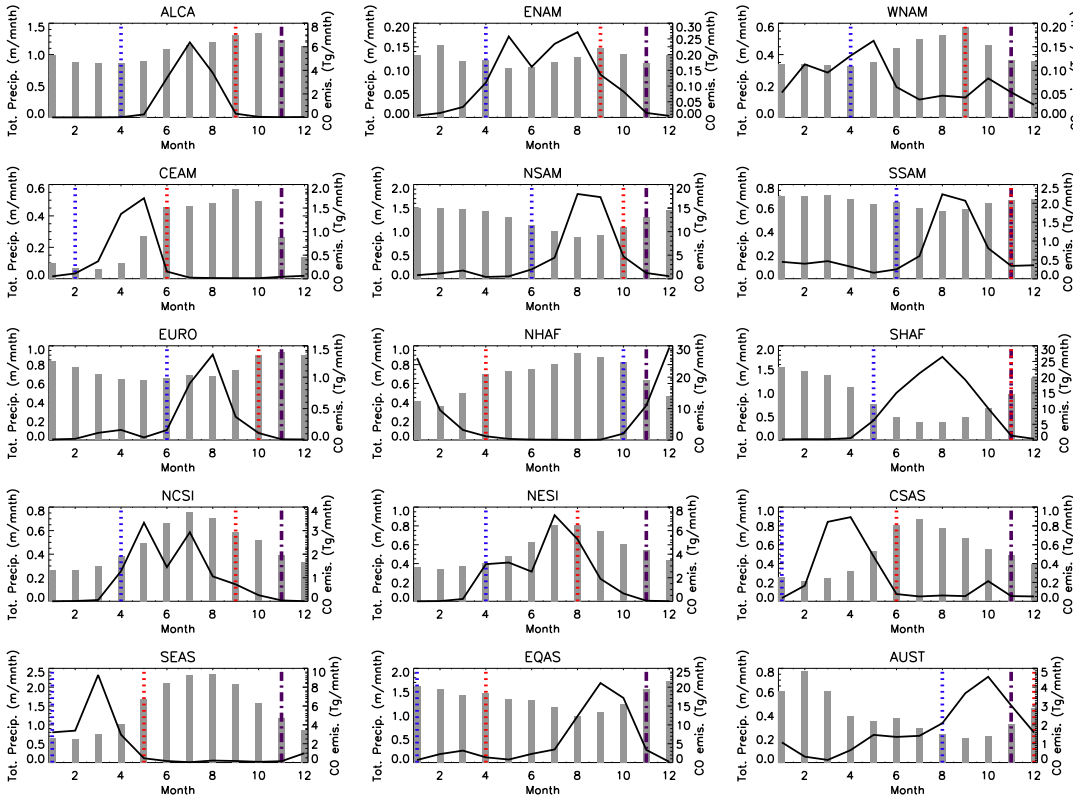

precipitation prior to the BS (pb4), showing the same climate fire driver as ALCA. The region of north central Siberia (NCSI), even though in the boreal region, does not have any significant correlations with any of the meteorological parameters. This region is dominated by agricultural fires which are driven by human activity as opposed to meteorological factors (see Figure 3.4). Model predictions suggest that the boreal regions are expected to experience an increase in precipitation (Meehl et al., 2007), which according to Table 6.2 may result in a reduction in fires. Previous fire modelling studies predict higher fire severity over parts of Canada with some regions also showing decreases (Flannigan et al., 2001). Even though overall precipitation is expected to increase, there is an expected increase in extreme events such as droughts (Meehl et al., 2007). The correlations shown here suggest that this would be expected to increase fire emissions. Model climate predictions also suggest that the boreal regions are expected to warm extensively in the future (Christensen et al., 2007). A warmer climate in Canada has been predicted to result in an increase in fires (Flannigan and Van Wagner, 1991). The correlations calculated here do show a positive relationship over Alaska and Canada, however, they are not significant for the period of study. Stocks et al. (1998) showed that Russian fires are also expected to increase with a warmer climate. In addition to temperature and precipitation, there has also been a predicted increase in lightning flashes with a doubling of CO_2 which would increase fires in the boreal regions (Price

Figure 6.24 Monthly mean temperature (K) over the 15 regions used for analysis (grey bars). Monthly mean GFED emissions are shown by the solid black line. The purple line shows the start of the period prior to BS.

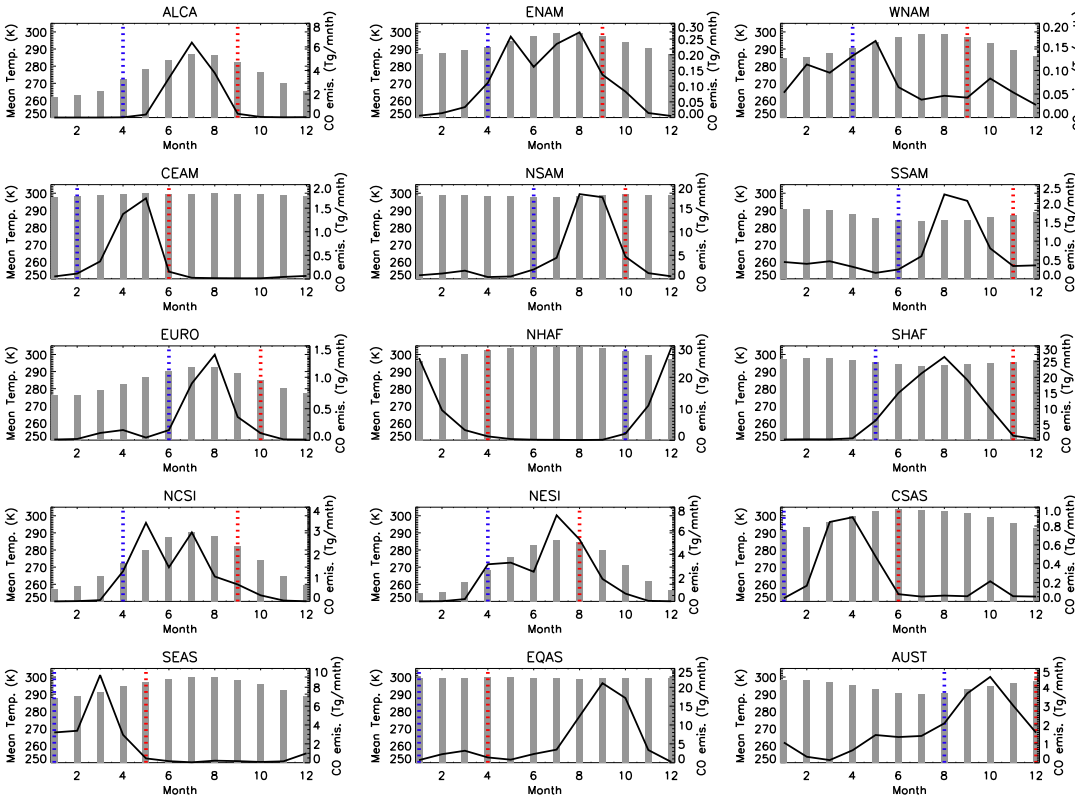

and Rind, 1994). More recently, it has also been shown that the regional fire response in Canada can be different depending on the season (Le Goff et al., 2009). Overall, the response of the boreal regions to changing climate is complex and still not fully understood and requires further investigation.

North Mid-latitudes fires

Eastern and western North America (ENAM and WNAM) exhibit different relationships with the climate variables, which could be due to the different vegetation types (see Figure 3.4). For example, fire emissions in the region WNAM have a positive correlation with pb4 (r=0.47) and ENAM has a negative correlation (r=-0.37). For WNAM, BSem correlations with tb4 (November to April) and tdu (April to September) are r=0.35 and r=0.51, suggesting fire emissions will be greater in the future warmer climate predicted by the Meehl et al. (2007). A study by Heyerdahl et al. (2008) found fires located in the Inland Northwest (located in WNAM in the work shown here) between 1652-1900 to be sensitive to spring and summer temperatures. Increased spring temperatures increased snow melt which led to dryer summer conditions, and increased summer

temperatures reduced soil moisture and increased flammability of vegetation. There is already evidence that fires in western North America have increased during a warmer climate (McKenzie et al., 2004; Gavin et al., 2007; Westerling et al., 2006) supporting the results shown here. ENAM shows a significant negative correlation with relative humidity before the BS (hb4) of r=-.57. Relative humidity modulates fires by affecting the moisture content of fuel. The negative correlation suggests that when relative humidity is low, moisture is transferred from vegetation to the atmosphere increasing its flammability. Increased future temperatures in this region will reduce relative humidity and possibly increase fire risk in the future. In Europe (EURO), a significant positive correlation was found for tb4, suggesting that increased winter or springtime temperatures would increase fires in this region. According to the IPCC model predictions of temperature (Meehl et al., 2007), the relationships shown here suggest European fire emissions will increase in the future. A study by Zumbrunnen et al. (2009) found fires in the European Alps, north of Italy, to be driven by temperature during the first half of the 20th century, in agreement with the work shown here, and then controlled by human activities for the second half. The results presented here show that temperature may still be an important fire driver for the whole of Europe. Zumbrunnen et al. (2009) also found wind to be important at high altitudes, where fires are exposed. This effect has not been considered here and may be important.

Extra-tropical, tropical and Southern Hemisphere fires

In Central America (CEAM), relative humidity, precipitation and temperature during the fire season (hdu, pdu and tdu) all reveal significant correlations with BSem of r=-0.62, r=0.59, r=-0.82, respectively. This suggests that if precipitation is increased, temperature reduced or relative humidity reduced, during February and June, then fire emissions may increase in this region. This makes fires in CEAM particularly sensitive to any future climate changes. Meehl et al. (2007) predicts future increases in temperature and decreases in precipitation in the area of CEAM, suggesting that fires will increase due to precipitation (pdu) having a negative correlation with BSem and temperature (tdu) having a positive correlation. Climate prior to the burn season (BS) is important in northern South America (NSAM) with tb4 and hb4 having significant correlations with BSem of r=0.64 and r=-0.57, respectively, again suggesting an increase in fires in this region in the future due to increased temperatures. However relative humidity during the burn season (hdu) yields the highest correlation (r=-0.74) suggesting it is the dominant climate driver for this region. Precipitation is the dominant driver of fire in the southern part of South America (SSAM), where less rainfall results in increased fires. There is a regional difference in the response of precipitation to increased concentration of greenhouse gases (Meehl et al., 2007), therefore the response of fires in this region cannot be determined from this work. Temperatures between November and December (tb4) in central and eastern South Asia (CSAS, SEAS) and between January and May

(tdu) for SEAS alone, yield positive correlations suggesting that predicted future increases in temperature in these regions (Meehl et al., 2007) will lead to increased fire emissions. Most fires in these regions are for agricultural purposes (see Figure 3.4) and therefore will mostly be controlled by human activities, however human set fires have previously grown uncontrollable due to climatic extremes (Page et al., 2002; Cochrane, 2003). Equatorial Asia (EQAS) shows pb4 and pdu yield significant correlations and may have influenced the intensity of fires during the 1997-2009 period, however temperature during the BS (tdu) shows the highest correlation. NHAF fires show a significant positive correlation with relative humidity before the BS (hb4), whereas SHAF fires show a significant positive correlation with temperature during the BS (tdu). Archibald et al. (2009) found precipitation to be important in determining area burnt in their model in Africa, which captured 68% of observed area burnt variability. They reported soil moisture to be particularly important in driving fires. They did not consider relative humidity or temperature in their model which would effect soil moisture. The correlations here suggest they are important and therefore accounting for them in future models could improve burned area estimates in the future. In Australia, precipitation during the fire season shows the highest correlation (r=-0.5) followed by temperature before the BS (r=-0.42). With the predicted reduction in rainfall over much of Australia and increase in temperature, these correlations suggest fire may be expected to increase in parts of Australia. There is already existing evidence that drought in Australia is increasing fire activity (Nicholls, 2004). Some studies have found, for some tropical and extra-tropical regions, precipitation during the burn season explains some of the variability in fires (van de Werf et al., 2003; van der Werf et al., 2008). In agreement, precipitation yields the highest correlations in equatorial Asia (EQAS) and Central America (CEAM) out of the other climate parameters, however, temperature and relative humidity also show high correlations and may need to be considered, especially in the extra-tropical regions where precipitation yields smaller correlations suggesting it to be less important.

6.6.1.2 Interactions between El Niño and climate drivers of fires

The same meteorological and emissions data has also been used to calculate correlations with the El Niño index to infer the interactions between El Niño and the climate drivers of fires in different regions. The highest correlations between BSem and the El Niño index (referred to as NINO3.4) are found for Alaska and Canada (ALCA), Central America (CEAM), northern parts of South America (NSAM), southern parts of Africa (SHAF), south-east Asia (SEAS) and equatorial Asia, where the correlations suggest El Niño conditions lead to increased emissions. However, there are some regions where the correlations of the BSem with El Niño do not yield significant correlations, but El Niño with temperature, precipitation and relative humidity do and are therefore also worth highlighting. The correlations are shown in Table 6.3 and will now be discussed in more detail. All the results from Tables 6.2 and 6.3 have been summarised in Figure 6.25.

Table 6.2 Pearson's correlation values for GFED v3.1 total emission (BSem) during the burn season (BS) with the different meteorological parameters, total precipitation, mean temperature and mean relative humidity between November leading up to the BS and during the BS. (Values significant with a P-value > 0.05 are shown in bold).

	Prior to BS			*During BS*		
Region	**Precip.**	**Temp.**	**Rel. Hum.**	**Precip.**	**Temp.**	**Rel. Hum.**
ALCA	**-0.61**	0.12	-0.23	-0.06	0.22	-0.03
NCSI	-0.20	-0.06	0.21	0.24	0.14	0.12
NESI	**-0.74**	-0.20	-0.35	-0.09	-0.13	-0.43
ENAM	-0.39	-0.08	**-0.57**	-0.13	-0.23	-0.43
WNAM	0.47	0.35	0.21	-0.37	0.51	-0.40
EURO	0.37	**0.57**	0.02	-0.30	0.25	-0.08
CEAM	-0.11	0.48	-0.33	**-0.62**	**0.59**	**-0.82**
NSAM	-0.27	**0.64**	**-0.57**	-0.21	0.26	**-0.74**
SSAM	-0.14	-0.44	-0.07	**-0.55**	-0.15	-0.27
NHAF	-0.01	-0.25	**0.60**	0.10	-0.10	0.15
SHAF	0.20	0.44	0.13	-0.34	**0.57**	-0.40
CSAS	-0.17	0.54	-0.32	-0.01	0.08	-0.25
SEAS	-0.39	0.46	0.13	-0.12	**0.64**	-0.13
EQAS	**-0.69**	-0.10	-0.35	**-0.62**	**0.73**	-0.32
AUST	0.15	-0.42	0.29	-0.50	-0.04	-0.38

Table 6.3 Pearson's correlation values for El Niño (November - February mean) with total fire emissions (BSem) during the burn season (BS) , total precipitation, mean temperature and mean relative humidity between November leading up to the BS and with total precipitation, mean temperature and mean relative humidity during the BS. (Values significant with a P-value > 0.05 are shown in bold).

	During BS	*Prior to BS*			*During BS*		
Region	**GFED emis.**	**Precip.**	**Temp.**	**Rel. Hum.**	**Precip.**	**Temp.**	**Rel. Hum.**
ALCA	**0.62**	**-0.62**	0.23	0.09	0.18	**0.60**	-0.07
NCSI	0.18	-0.00	-0.22	0.21	0.12	-0.02	0.28
NESI	0.38	-0.33	0.02	-0.13	0.34	0.04	-0.04
ENAM	-0.28	**0.69**	-0.07	**0.58**	0.15	0.17	0.16
WNAM	0.44	**0.73**	-0.18	**0.63**	0.12	0.32	0.23
EURO	-0.21	0.15	-0.09	0.25	0.21	-0.09	0.01
CEAM	**0.64**	0.25	**0.77**	-0.12	-0.37	**0.89**	-0.49
NSAM	**0.63**	**-0.59**	**0.91**	**-0.69**	-0.39	0.47	-0.45
SSAM	-0.02	**0.57**	-0.06	0.51	-0.28	0.49	0.02
NHAF	-0.04	0.19	-0.16	0.13	0.49	0.23	0.77
SHAF	**0.66**	0.26	0.51	0.23	-0.39	0.36	-0.14
CSAS	-0.36	**0.85**	**-0.61**	**0.86**	0.36	0.00	**0.79**
SEAS	**0.55**	**-0.58**	-0.09	0.51	**-0.66**	0.31	0.27
EQAS	**0.68**	**-0.83**	0.24	-0.44	**-0.74**	**0.74**	-0.48
AUST	-0.36	**-0.59**	**0.64**	-0.29	0.07	0.25	0.06

Boreal fires

In Alaska and Canada (ALCA), NINO3.4 correlates negatively with pb4 and positively with tdu. This suggests that under El Niño conditions precipitation is reduced between November and April and temperature is increased between April and September. As seen in Table 6.2, reduced rainfall prior to the BS is associated with increased emissions of CO. This is of particular importance to the Arctic, as forest fires, which are extensive in this region, are the most important source of fire sourced CO (see Chapter 5). In eastern Siberia the correlations show a similar pattern of response as ALCA with correlations between NINO3.4 and BSem equal to 0.38 and NINO3.4 with pb4 equal to -0.32. However, they are not significant for the number of samples used in this study (equal to the number of years (13) for the time series used). As this region is at higher latitudes it is likely to be influenced by other climate oscillations. Balzter et al. (2005) found some evidence of a link between burned area during 1992-2003 due to El Niño alone, however, they found the variability was best captured when they considered both El Niño and temperature or both the Arctic Oscillation and temperature in a multiple linear regression. This shows that due to the location of the boreal regions, especially Siberia, which is remote from the centre of El Niño in the tropical Pacific, several indices and local temperature and precipitation fluctuations need to be considered to best predict future forest fires and their impact on the Arctic.

North Mid-latitudes fires

In WNAM, NINO3.4 is positively correlated with pb4 and hb4. From Table 6.2, it is known that pb4 and BSem are positively correlated (r=0.47). This suggests that El Niño conditions will increase precipitation during winter/spring which will increase fires in the summer. This is in agreement Kitzberger et al. (2001) who found increased plant growth due to precipitation visible in tree rings associated with El Niño conditions, providing more fuel for the summer burn season. Interestingly, ENAM shows a response similar to WNAM in terms of climate, however, BSem show the opposite. NINO3.4 shows positive correlations with both hb4 and pb4, as in WNAM, however, Table 6.2 shows ENAM has the highest correlation with hb4 (r=-0.57). This suggests that increased relative humidity before the BS due to an El Niño will actually reduce fires due to increased fuel moisture. European fires and climate do not show any significant correlations with El Niño.

Extra-tropical, tropical and Southern Hemisphere fires

In both CEAM and SHAF, positive correlations are found between NINO3.4 and tb4, suggesting that El Niño conditions will increase temperatures prior to the burn season, which is shown in

Table 6.2 to be related to increased fire emissions. However, in CEAM temperature is found to have the highest correlation eith El Niño during the fire season (r=0.89), which is also associated with increased fires. Like CEAM, temperature in NSAM, both prior to and during the BS, is found to be highly correlated with El Niño (r=0.91 and r=0.47 respectively), although El Niño conditions is also found to correlate with both precipitation (r=-0.59) and relative humidity (r=-0.69) prior to the BS. The results in Table 6.2 suggest that increased temperature before the BS and reduced relative humidity before and during the BS may result in increased fire emissions in northern South America. This is in agreement with the positive correlation of 0.63 between NINO3.4 and BSem. Previous studies have found Peru to experience increased fires due to El Niño increasing precipitation (Holmgren et al., 2006a). The whole of NSAM in this study shows reduction in precipitation, however emissions are still increased. This is because even though parts of Peru experience increased precipitation during an El Niño, NSAM mostly experiences a decrease (see Figure 6.2) therefore differences will arise due to this work considering a much larger area and therefore regionally varying fuel type and response. EQAS and SEAS both exhibit a similar relationship with El Niño, whereby precipitation is negatively correlated both during and prior to the fire season which may increase fires (according to correlations in Table 6.2). In EQAS positive correlations suggest increased temperature during the BS due to an El Niño may also contribute to increased fire activity. Even though EQAS is dominated by deforestation fires which are set by humans, Page et al. (2002) showed that during the extreme El Niño event of 1997-1998, fires in this region burned uncontrollably, causing large perturbations to the atmospheric carbon budget. In Australia (AUST), significant correlations of NINO3.4 with pb4 and tb4 are found (r=-0.59 and r=0.64, respectively). A correlation between BSem and NINO of -0.36 is found but it is not significant at the $p<0.05$ level used for this study. Other studies found El Niño reduced precipitation prior to the burn season (in agreement with correlations found here), which reduced plant growth and therefore, fuel for fires (Holmgren et al., 2006b; Harris et al., 2008). A study by Williams and Karoly (1999) found parts of Australia to exhibit different responses to El Niño, with parts experiencing an increase in fires and parts experiencing a decrease. As the whole area of Australia has been included in the analysis done here, this may explain why there is not a high correlation for this analysis. Also, drought in Australia has already been shown have resulted in increased fires (Nicholls, 2004), which could partially offset the increase in fires from increased precipitation during an El Niño. CSAS is similar to AUST in the case that during El Niño events, less fires are expected due to a correlation of -0.36 between NINO3.4 and BSem, however, the climate drivers correlations differ. In CSAS, El Niño is negatively correlated with temperature before the BS instead of positively correlated, as found in AUST, which in turn reduces fire emissions according to the positive correlation (r=0.54) that was found between BSem and tb4 (see Table 6.2).

Figure 6.25 Correlations showing the regional response in precipitation, temperature and relative humidity and how these responses can feed back into fire emissions. For details of the correlations see Tables 6.2 and 6.3.

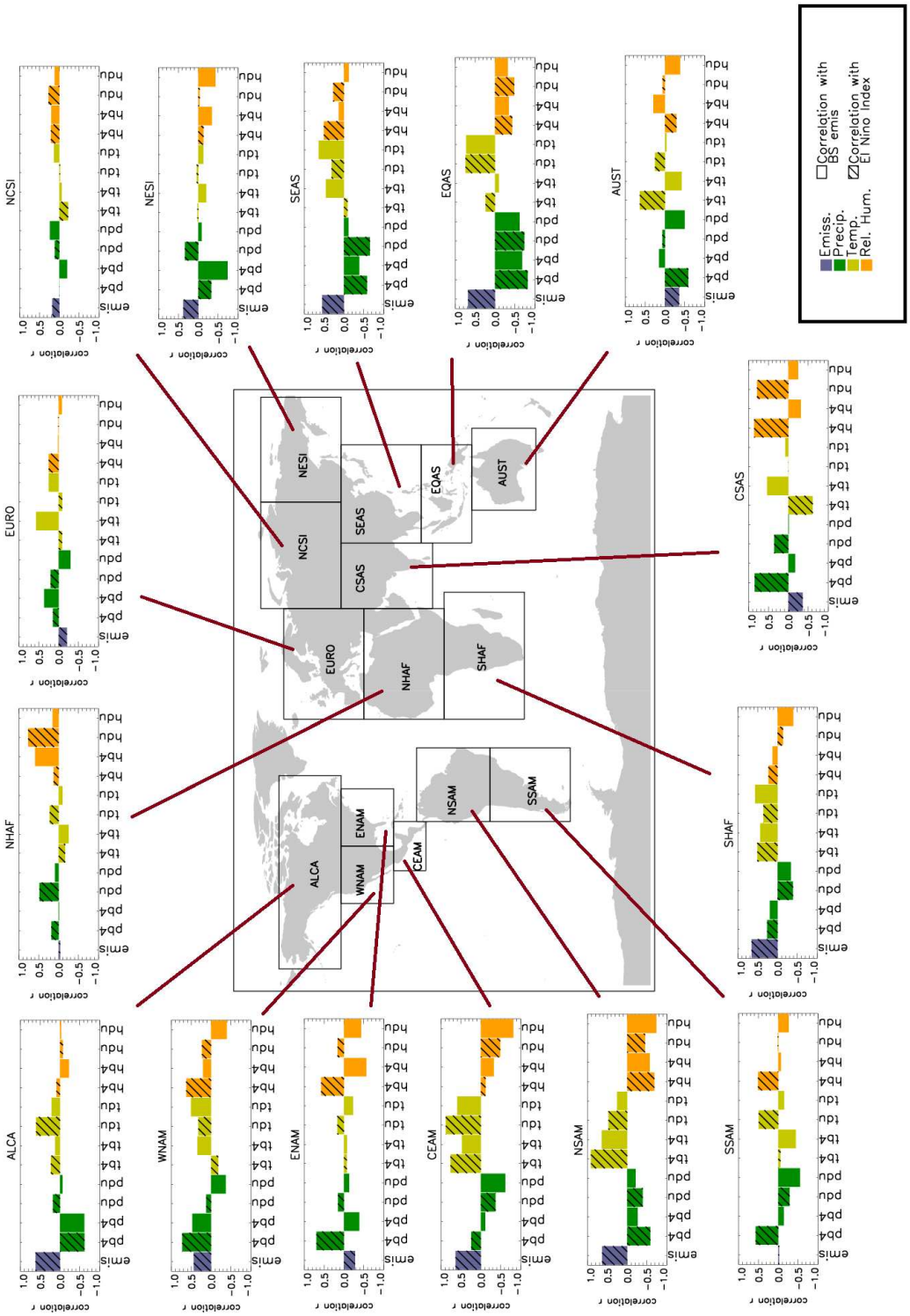

6.6.2 Arctic surface response to El Niño/La Niña events

To understand what these El Niño-fire relationships mean in terms of Arctic CO, the observed and simulated surface CO concentrations at each of the Arctic stations (STM, ICE, ALT, ZEP and BRW) have been averaged over selected years during the 1997-2009 period. Years were chosen to represent either a strong El Niño or La Niña years or years which were 'neutral'. The observed concentrations are on average 21 ppbv (16%) higher in El Niño years and 7 ppbv (5%) lower in La Niña years relative to neutral years. One possible reason for El Niño years showing a larger percent difference relative to neutral years, could be that a La Niña event generally follows an El Niño event. This has been shown in some regions to result in particularly intense fires during the La Niña (Kitzberger et al., 2001). This was due to increased plant growth from enhanced precipitation during El Niño years, followed by drying of vegetation in La Niña years, providing favourable conditions for fires (Kitzberger et al., 2001). The model estimates that there is a 18 ppbv (13%) enhancement in CO in El Niño years, which is similar to the observations, however, the model only simulates a 1.6 ppbv (0.01%) reduction in La Niña years. The reason why the model fails to capture the extent of the La Niña CO reduction is not known and would need to be investigated further, but could be related to the model overestimating background CO in the autumn in the Arctic or the fire inventory used in the model overestimating emissions in some regions.

Table 6.4 November - February El Niño 3.4 Index and CO concentrations for El Niño years (NINO3.4 > 1), La Niña years (NINO3.4 <-1) and years without a strong El Niño or La Niña (<0.5NINO3.4<0.5). The observed and modelled CO (from vgfed_vmet) concentrations are an average of annual means at the surface stations ALT, ZEP, BRW, STM and ICE.

Year	**Nino Index**	**Observed CO**	**Modelled CO**
El Nino years:			
1998.00	2.35	158.16	159.43
2003.00	1.27	146.13	152.11
Average		152.15	155.77
No strong Niño/Niña:			
1997.00	-0.34	128.85	131.80
2002.00	-0.09	135.34	142.38
2004.00	0.42	129.65	139.29
Average		131.41	137.82
La Nina years:			
2000.00	-1.55	124.79	135.20
2008.00	-1.34	123.57	137.16
Average		124.18	136.18

6.6.3 Fires and other indices.

As fire emissions are inherently linked to temperature and precipitation (see Table 6.2) which are influenced by the NAO and PNA in the NH, correlations of these indices with BSem for each region shown in Figure 6.21 have been calculated and are shown in Figure 6.26. The indices were averaged over December to March, whereas the El Niño index was averaged from November to January, representing the strongest seasons of the climate modes. The PNA exhibits similar correlations as the El Niño in each region except that they are slightly smaller in value. The PNA is thought to be modulated by ENSO and may explain this pattern (Straus and Shukla, 2002). The NAO(CPC) and NAO(HUR) indices show similar relationships at each station, but the NAO (HUR) yields higher correlations. This may be because the NAO(HUR) index is influenced by local climate noise (Hurrell and Deser, 2010) and therefore may be capturing some regional climate fluctuations which is affecting fires but is not actually due the NAO. The NAO yields significant positive correlations in western US (WNAM), northern Africa (NHAF) and central-south Asia (CSAS), which are higher than found with El Niño or the PNA, suggesting the NAO was the dominant climate mode, out of the ones considered, which affected fires in these regions between 1997-2009. Li et al. (2008) found areas of increased SST in western Northern America and parts of India, and decreased SST in Northern Africa during positive NAO phases relative to negative phases. Increased temperature in both SEAS and WNAM have both been shown to be related to increased fire emissions (see Table 6.2). In northern Africa, with decreasing temperature, relative humidity would increase (assuming all other factors remained the same) and as seen in Table 6.2, increased relative humidity was related to increased fire emissions in this region. Therefore, the teleconnections found by Li et al. (2008) could explain the positive correlations found between the NAO (both HUR and CPC) and BSem.

Figure 6.26 Correlations between the climate indices (NAO (CPC), NAO (HUR), PNA and NINO3.4) and CO emissions from GFED v3.1 during the burn season for the 15 different regions shown in Figure 6.21. The dotted lines represent the correlation value need to be significant at the P<0.05 level (r=0.55) and P<0.1 level (r=0.48).

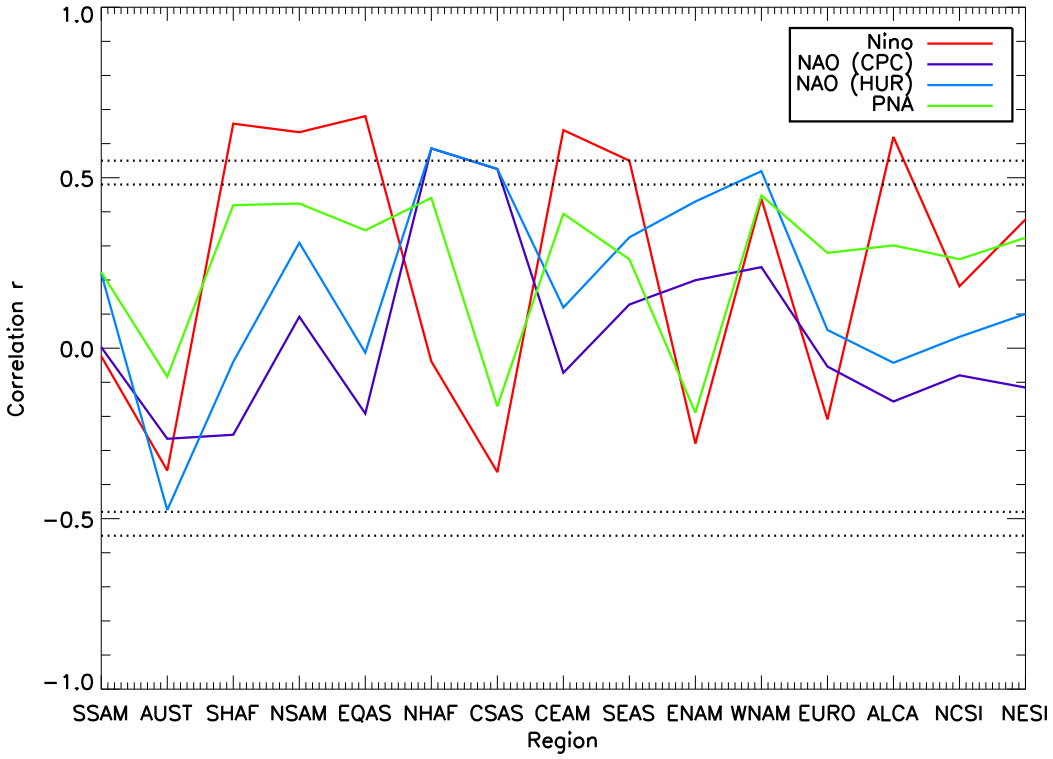

6.7 Summary

In this chapter the question of what is driving Arctic IAV has been investigated. Using CO as a tracer of lower latitude emissions, the contributions to CO IAV from varying meteorology and biomass burning emissions have been quantified. Simplified model simulations, which include yearly varying meteorology and yearly varying biomass burning emissions, captured between 86% and 91% of the total observed CO IAV at the surface in the Arctic. A simulation which accounted for variability in meteorology alone captured 0-25% of the observed IAV and simulations which accounted for variability in biomass burning emissions alone captured 84-93% of the variability. This showed that the dominant driver of observed Arctic surface CO IAV is variability in fire emissions. At the lower latitudes and higher altitudes, variability in meteorology became more important in driving CO IAV. At the surface, the model total fire tracer caused an average of 85% of the total model CO IAV, which included both meteorology and fire variability. Forest fires caused 60% of this variability, peat fires caused 12%, agricultural savannah fires both caused 9%, deforestation caused 6% and woodland fires caused 3%. Anthropogenic CO caused 10% of the total modelled CO IAV at the surface.

Correlations between the NAO, PNA and El Niño indices with total column CO anomalies taken from the model with only meteorology varying were used to investigate possible links between variability in transport and the Arctic. The results showed the NAO to yield the most significant correlations throughout the year, suggesting it to be the dominant driver of variability in transport to the Arctic out of the modes considered. In the winter, significant positive correlations are seen throughout the Arctic, due to circulation impacts on European, North American and East Asian emissions transport, and in the summer, significant negative correlations are seen throughout the Arctic, due to impacts on the transport from East and South Asia. The reversal of the correlation from positive to negative for the East Asian tracer in summer was due to the shift in the centre of the NAO, showing that the seasonal evolution of the NAO is important. Also, East Asian CO contributes more to the total Arctic CO burden in the summer, making the total Arctic response more sensitive to the regional response of East Asia. El Niño in the winter and spring showed significant positive correlations in the Arctic for the South Asian tracer causing significant correlations in the total Arctic CO in winter and spring over parts of the Canadian Arctic, Alaska and Siberia. This suggests that increased CO in these regions would occur during El Niño events due to circulation changes causing enhanced transport from South Asia. The PNA was not found to be significantly correlated with the Arctic through transport. This is the first time that the El Niño and the PNA have been considered in terms of their influence on transport of CO to the Arctic and is the first time the NAO has been considered throughout the year in the Arctic and not just in winter.

Significant positive correlations were found between the El Niño index and observed Arctic CO at the surface, which peaked at a lag of 10-11 months. The model was used to show that this

correlation was related to variability in fire emissions. GFED v3.1 CO emissions and ECMWF ERA-Interim analyses of temperature, relative humidity and precipitation were used to investigate possible regional climate drivers of fires and how these may be affected by ENSO. El Niño was found to be significantly negatively correlated with precipitation in the boreal regions suggesting reduced precipitation would increase fire emissions in Alaska and Canada and eastern Siberia during El Niño events. This is particularly important for the Arctic as forest fires in the boreal regions are a large source of CO and O_3 in the Arctic in the summer (seen in Chapter 5). In the NH middle latitudes, El Niño events were also found to be positively correlated with emissions in western North America which according to the correlations calculated here may be related to increased relative humidity and precipitation during El Niño events. Negative correlations in eastern North America suggest reduced fire emissions possibly due to increased precipitation during El Niño events. In Europe and western North America, increased temperature were found also found to be highly correlated with emissions suggesting them to be important drivers of fires. This also indicates that increased fire emissions may occur in these regions in the future due to the predicted rise in temperatures over the next century. In the tropics, extra-tropics and SH, El Niño was found to be positively correlated with emissions in Central America, northern South America and south-east and equatorial Asia suggesting emissions would be increased in these regions during El Niño events. The climate driver analysis however suggested the regional cause of the increase in emissions differs and would need to be considered in models. In contrast, El Niño events were found to be negatively correlated with fire emissions in southern Asia and Australia.

Chapter 7

Arctic tropospheric chemistry during POLARCAT Summer 2008

7.1 Introduction

Recent radiative forcing calculations in the Arctic have shown O_3 to be an important greenhouse gas, contributing to warming in this region (Shindell, 2007; Quinn et al., 2008; Shindell and Faluvegi, 2009). O_3 is formed in the troposphere from NO_x, CO and non-methane hydrocarbons (Crutzen, 1973; Fishman et al., 1979; Liu et al., 1987). In the Arctic, O_3 production has been shown to be sensitive to the concentrations of NO_x and HO_x (Emmons et al., 2003), however, little is known about the sources of these trace gases (Jacob et al., 2010). There are very few local emissions and NO_x, which has a very short lifetime ($\sim$1 day (Jacob, 1999c)) and is therefore unlikely to be transported from mid-latitude sources to the Arctic. Peroxyacetyl nitrate (PAN), a reservoir species of NO_x, has been shown to be important in redistributing NO_x throughout the troposphere acting as a source of NO_x in remote regions (Moxim et al., 1996). Therefore, PAN presents a method of transporting NO_x into the Arctic, which can lead to the production of tropospheric O_3. PAN has been observed to be the dominant NO_y species in the Arctic during spring (Bottenheim et al., 1986, 1993) and may lead to the formation of O_3 (Beine et al., 1997). There is a need to better understand the sources of Arctic tropospheric O_3, and therefore NO_x and PAN, in order to better understand current changes in O_3 concentrations and how they may vary in the future.

POLARCAT (POLar study using Aircraft, Remote Sensing, surface measurements and models of Climate, chemistry, Aerosols, and Transport) was a project proposed as part of the International Polar Year 2007-2008. It brought together scientists from around the world to investigate the impact of poleward transport of pollution on Arctic atmospheric composition and climate. A major objective of the campaign was to investigate the impact of mid-latitude emissions on the

Arctic troposphere during the summer, sampling plumes in the sub-Arctic and Arctic. This is the first major campaign to intensively sample the Arctic throughout the atmosphere during summer and therefore provides a valuable dataset to evaluate models in the Arctic during this season.

This chapter focuses on using measurements of several trace gases from participating aircraft during the summer POLARCAT campaign, to evaluate the TOMCAT model throughout the troposphere in different regions of the Arctic and sub-Arctic. The importance of PAN as a source of NO_x in the Arctic and the production of tropospheric O_3 is then considered through some sensitivity experiments. Section 7.2 describes the POLARCAT campaign and measurements used in this chapter. Section 7.3 describes the basic model set-up and methodology for the aircraft comparisons. Section 7.4 presents comparisons between the TOMCAT model and aircraft observations during June and July 2008. Then sensitivity simulations are shown, where the TOMCAT model has been used to study the importance of PAN in the Arctic as a source of O_3 (Section 7.5) and the importance of ethane transported to the Arctic as a source of PAN (Section 7.6). A summary of results is given in Section 7.7.

7.2 POLARCAT aircraft data

7.2.1 ARCTAS-B

As part of ARCTAS-B (Arctic Research of the Composition of the Troposphere from Aircraft and Satellites) the NASA DC8 aircraft was based in Cold Lake, Canada from 29th June - 10th July 2008 with a focus on sampling Canadian biomass burning and North American anthropogenic plumes before they were transported to the Arctic (Jacob et al., 2010). The flight tracks for the DC8 aircraft are shown in Figure 7.1 and covered a range of latitudes from 50°N to 87°N. Due to the large payload of the DC8, this dataset provides a valuable suite of measurements for evaluating tropospheric O_3 photochemistry, including CO, O_3, HO_x, NO_x, HNO_3, PAN and total NO_y.

7.2.2 POLARCAT-France and POLARCAT-GRACE

The POLARCAT-GRACE and POLARCAT-France projects were jointly based in Kangerlussuaq, Greenland with two aircraft, the German DLR Falcon and the French ATR-42. These projects aimed to sample plumes which had been transported to the Arctic during the summer. The POLARCAT-France project took place from 30th June - 14th July 2008, covering 50°N to 71°N (see Figure 7.1). The aircraft measured CO using an infrared absorption analyser which has an accuracy of 5 ppbv with a 30 s integration time (Nedelec et al., 2003). O_3 was measured using an ultraviolet (UV) absorption instrument with an accuracy of 2 ppbv for an integration time of 4

Figure 7.1 Flight tracks from the YAK-AEROSIB (top, left), ARCTAS-B DC8 (top, right), POLARCAT-France ATR (bottom, left) and POLARCAT-GRACE Falcon (bottom, right) during the summer June-July 2008 POLARCAT campaign.

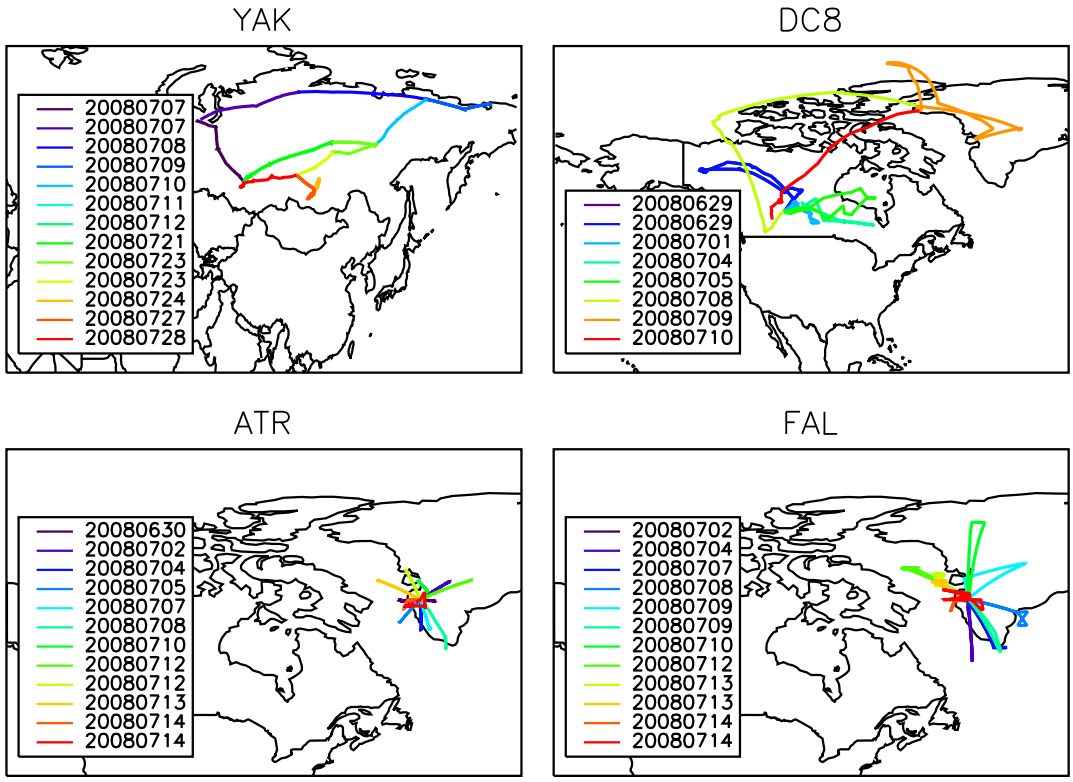

s (Ancellet et al., 2009). The Falcon aircraft had a larger range than the ATR, covering 57-79°N between the 2nd-14th July 2008 measuring CO, O_3, NO, NO_y and PAN. CO was measured using a vacuum UV fluorescence instrument (Gerbig et al., 1999) which has an accuracy of 5 ppbv and O_3 was measured using a UV absorption analyser with an accuracy of 3 ppbv (Roiger et al., 2011b). NO and NO_y (defined as NO + NO_2 + NO_3 + PAN + 2×N_2O_5 + HNO_3 + HNO_2 +HNO_3) were measured using a chemiluminescence detector with an accuracy of 10 and 15 pptv, respectively (Ziereis et al., 2000). The NO_y was converted to NO for measurement (Roiger et al., 2011b; Ziereis et al., 2000). PAN was measured using a fast response chemical ionisation - ion trap mass spectrometer with a 25 pptv accuracy (Roiger et al., 2011a).

7.2.3 YAK-AEROSIB

The Russian YAK-AEROSIB (Airborne Extensive Regional Observations in Siberia) project was performed in collaboration with the POLARCAT-France project. Scientific flights covered large areas of Siberia (see Figure 7.1), sampling Siberian biomass burning plumes and Asian and European anthropogenic plumes (Paris et al., 2009). Flights were conducted between 7th - 28th July

2008 between 52°N and 72°N. CO was measured using the same instrument as aboard the ATR-42 (an infrared absorption analyser) and O_3 was measured using an ultraviolet absorption gas analyser with a precision of 2 ppbv for an integration time of 4 s (Paris et al., 2008).

7.3 TOMCAT model simulations

A 1-year simulation for 2008 was performed using the TOMCAT model (referred to as CTRL), preceded by a 6-month spin-up. The emissions used were different from those used in previous chapters to offer a better representation of 2008. The AR5 2000 emissions were replaced by the Streets v1.2 emission dataset described in Section 3.4. These emissions were created for the INTEX-B (Intercontinental Chemical Transport Experiment- Phase B) campaign in 2006 to provide a better representation of Asian emissions, as other datasets underestimated the magnitude of emissions from this region (Zhang et al., 2009). This dataset provides an amalgamation of the latest regional and global emissions datasets. The monthly mean GFED biomass burning emissions were replaced by the daily mean biomass burning emission dataset, FINNv1, which was specifically created for the POLARCAT campaign (Wiedinmyer et al., 2011) (see Section 3.4). Due to large fire variability, models which use fire emissions with a temporal resolution greater than monthly have been shown to compare better with aircraft observations which sampled biomass burning plumes (Turquety et al., 2007). Therefore, as some of the aircraft used for the comparisons encountered biomass burning plumes (Jacob et al., 2010; Paris et al., 2009) it was deemed necessary to account for daily variability in fires in TOMCAT. The non-fire natural emissions were provided by Louisa Emmons[1] and were created by the more recent version (v2) of the MEGAN (Model of Emissions of Gases and Aerosols from Nature) model (Guenther et al., 2006) as part of the Monitoring Atmospheric Composition and Climate (MACC) project.

To evaluate the TOMCAT model against the POLARCAT data, the model output was saved every hour and then interpolated offline horizontally and vertically to the flight tracks. 60 s averaged data was used from all flights allowing the vertical interpolation to be done every minute. In general, the aircraft flight path is likely to cross over several model grid boxes in the vertical direction in one hour, therefore requiring a high frequency of vertical interpolation. The flight longitude and latitudes were averaged over hourly sections for the horizontal interpolation.

[1]National Center for Atmospheric Research, USA

7.4 POLARCAT aircraft comparisons with TOMCAT

7.4.1 Carbon monoxide

Figures 7.2 - 7.5 show CO measured over Siberia (YAK), Greenland (Falcon and ATR), Canada and the Arctic Ocean (DC8). The model reproduces the observed concentrations, with median simulated concentrations lying within the 25th and 75th percentiles of the observations. Table 7.1 shows the mean observed and simulated concentrations calculated over the vertical profiles shown in Figures 7.2 - 7.5, along with the correlation between the observed and simulated vertical distributions. The root mean square error (RMSE) has also been calculated according to equation 4.9. The RMSE error for the YAK and ATR aircraft are both 5.2 ppbv, which are similar to the instruments 5 ppbv uncertainty, showing very good overall agreement. The DC8 and Falcon however show higher RMSEs of 49 and 17 ppbv, respectively. By considering Figure 7.4 and 7.5 it

Table 7.1 Mean modelled ($\bar{M}$) and observed ($\bar{O}$) concentrations of vertical profiles of trace gases in the Arctic in June-July 2008. Correlations (r) and root mean square error (RMSE) between the modelled and observed profiles have also been calculated.

Aircraft	Trace Gas	$\bar{M}$	$\bar{O}$	r	RMSE
ATR:					
	CO (ppbv)	103.4	105.1	0.89	5.2
	O_3 (ppbv)	51.8	52.4	0.98	3.4
DC8:					
	CO (ppbv)	109.6	149.0	0.85	49.1
	O_3 (ppbv)	77.6	71.5	0.98	14.5
	PAN (pptv)	339.3	353.6	0.64	77.9
	HNO_3 (pptv)	343.7	122.6	0.87	244.0
	NO (pptv)	47.0	64.3	0.87	42.2
	NO_2 (pptv)	80.0	115.7	0.85	71.5
	NO_y (pptv)	890.0	729.5	0.83	255.6
	OH (pptv)	0.12	0.12	-0.33	0.05
	C_2H_6 (pptv)	625.4	1071.76	0.91	478.5
	C_3H_8 (pptv)	34.6	245.9	0.85	234.2
	CH_3CHO (pptv)	57.4	352.4	0.92	399.2
Falcon:					
	CO (ppbv)	96.1	97.7	0.72	17.3
	O_3 (ppbv)	90.6	92.6	0.98	29.9
	PAN (pptv)	277.1	180.6	0.87	125.3
	NO (pptv)	29.5	38.3	0.97	16.7
	NO_y (pptv)	698.5	667.2	0.92	403.2
YAK:					
	CO (ppbv)	106.4	105.1	0.62	5.2
	O_3 (ppbv)	52.6	52.3	0.97	4.9

Figure 7.2 Vertical profiles of median concentrations of CO (left) and O_3 (right) observed during the YAK-AEROSIB project over Siberia compared to simulated concentrations from the TOMCAT model interpolated to the flight tracks. The data has been binned into 50 hPa pressure bins for averaging. The error bars represent the 25th and 75th percentiles of the observed concentrations in each bin. The dates correspond to the first and the last flight of the campaign.

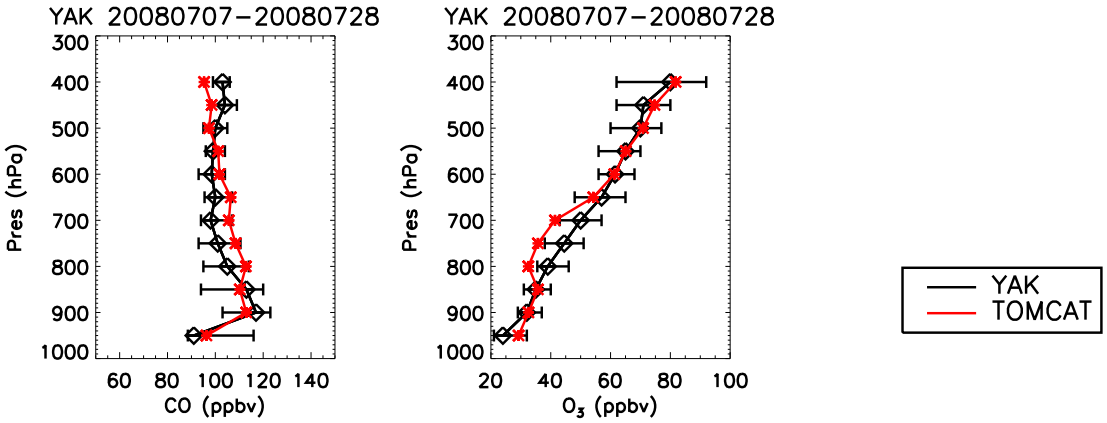

is clear that these higher RMSE values are due to an underestimate in CO in the upper troposphere (UT). At these altitudes it is likely that the model may overestimate the influence of stratospheric air due to a lower vertical resolution at these pressures, which would explain the lower simulated CO concentrations. These two aircraft flew at higher altitudes compared to the ATR and Falcon (see Table 7.3), therefore increasing the influence stratospheric air as diagnosed by the model.

7.4.2 Ozone

Figures 7.2 - 7.5 show O_3 measured over Siberia (YAK), Greenland (Falcon and ATR) and Canada and the Arctic Ocean (DC8). As with CO, the model generally does a good job at reproducing the observed concentrations of O_3. The ATR and YAK regions yield similar RMSE of 3.4 ppbv and 4.9 ppbv, respectively. The Falcon and DC8 comparison show that the model has a RMSE of 29.9 ppbv and 14.5 ppbv, respectively. As seen with CO, these aircraft flew at higher altitudes sampling more stratospheric air, which is reflected in the higher mean concentrations of O_3 in Table 7.1. For O_3 from the DC8 and Falcon flights, the model overestimates the amount of stratospheric O_3 in the UT between 500 and 300 hPa.

7.4.3 Reactive nitrogen species

The Falcon measured NO, NO_y and PAN in the region of Greenland (see Figure 7.4). The results show that TOMCAT captures the NO well, mostly lying within the 25th and 75th percentiles, but

Figure 7.3 Vertical profiles of median concentrations of CO (left) and O_3 (right) observed during the POLARCAT-France project aboard the ATR over Greenland compared to simulated concentrations from the TOMCAT model interpolated to the flight tracks. The data has been binned into 50 hPa pressure bins for averaging. The error bars represent the 25th and 75th percentiles of the observed concentrations in each bin. The dates correspond the first and the last flight of the campaign.

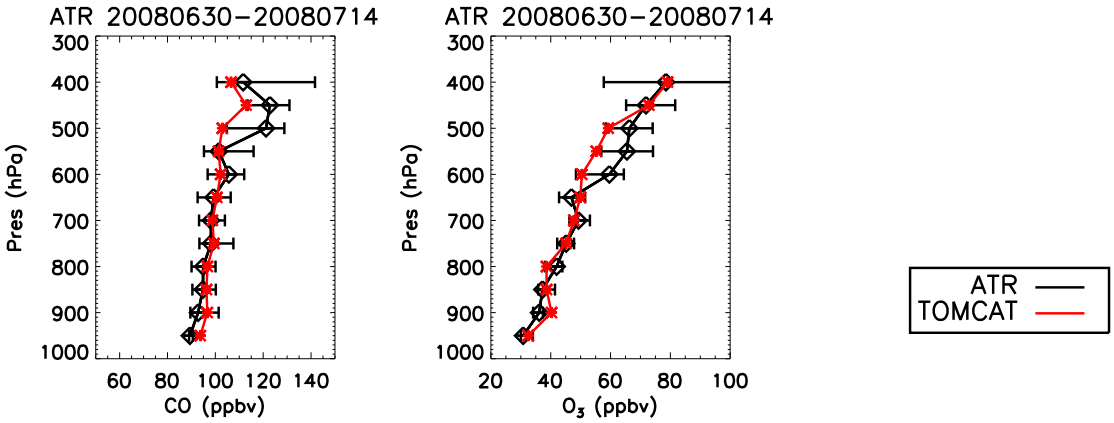

may underestimate NO in the boundary layer. PAN is overestimated by TOMCAT, simulating a mean vertical concentration of 277 pptv compared to the observed 180 pptv, giving a RMSE of 125 pptv. As discussed in Section 4.3, the addition of the more hydrocarbons in the new chemistry scheme led to increased formation of CH_3CO_3 from the oxidation of the hydrocarbons which then goes on to form PAN. This overestimate in PAN leads to the total NO_y also being overestimated.

The DC8 also measured NO, PAN and NO_y along with NO_2 and HNO_3 (see Figure 7.5). The model does a good job of reproducing NO and NO_2. In contrast to the Falcon, the model shows good agreement with PAN measured aboard the DC8. The model still overestimates total NO_y, however, this is now due to an overestimate of HNO_3. On several flights, the DC8 sampled biomass burning plumes near the source where large emissions of NO_x were converted rapidly to PAN (Alvarado et al., 2010) giving higher concentrations ($\bar{O}$=353.6 pptv) compared to the Falcon ($\bar{O}$=180 pptv) (see Table 7.1). The model shows enhanced PAN for the DC8 flights ($\bar{M}$=339 pptv) compared to the Falcon flights ($\bar{M}$=277 pptv), suggesting the model captures some of the NO_x conversion to PAN from fires, however, the model difference between the two aircraft is not as large as seen in the observations.

7.4.4 Hydroxyl radical

The DC8 was the only aircraft to measure OH. Due to its short lifetime ($\sim$1 s) and low concentrations, the hydroxyl radical proves to be a difficult gas to measure accurately, however recent

developments in instrumentation have vastly improved measurement capability (Heard and Pilling, 2003). The observed OH is compared to TOMCAT simulated OH in Figure 7.5. In general the model lies within the 25th and 75th percentiles, however there are some interesting features to note. Firstly, between 925 and 825 hPa, the measurements indicate that TOMCAT overestimates OH in the DC8 flight region. In Section 4.4, the model was compared against a published global OH climatology constrained by observation of precursor gases. This comparison also suggested that TOMCAT may overestimate NH OH in the lower troposphere. Secondly, between 725 and 575 hPa, the model predicts OH to be around the 25th percentile of the observations, which may suggest a small overall underestimate in OH at this altitude. Due to model peak in OH at 900 hPa and the subsequent decrease, the vertical distribution of the model does not capture the overall observed decrease in OH with altitude, resulting in a low correlation (r=-0.33), however the overall mean vertical OH concentration does agree (see Table 7.1).

7.4.5 Non-methane hydrocarbons

The DC8 was the only aircraft to measure hydrocarbons. Simulated and observed ethane, propane and acetaldehyde are compared in Figure 7.5. The model underestimates ethane, propane and acetaldehyde throughout the atmosphere by factors of 2, 7 and 6, respectively. Biomass burning can act as a significant source of acetaldehyde, contributing up to 15% to the total global source (Holzinger et al., 1999). As the DC8 sampled a large amount of biomass burning plumes (Alvarado et al., 2010), the measurements may be biased with high amounts of fire emissions. If this is the case, the results shown here suggest that the boreal biomass burning emission factors used to create the FINN v1 inventory may be too low for the Canadian and Californian fires sampled in 2008. Previous estimates of emissions factors of acetaldehyde have been highly variable (Andreae and Merlet, 2001; de Gouw et al., 2006) and may account for some of the bias in TOMCAT. It is also possible that the model resolution is unable to capture the high concentrations within fire plumes, however, good agreement between modelled-observed CO suggests that this is not the case. Propane and ethane emissions are dominated by anthropogenic sources, therefore the results shown here suggest that the Streets v1.2 anthropogenic emissions are underestimated. Recent studies have estimated anthropogenic emissions of ethane to be about 13 Tg/yr (Xiao et al., 2008) which is a factor of two greater than the 6 Tg/yr emitted in the Streets v1.2 anthropogenic emissions in TOMCAT. As mentioned in Section 3.4, the Streets inventory is only available as total NMHC and the partitioning was done by Louisa Emmons for the ARCTAS campaigns (Wespes et al., 2011). Therefore, this suggests that either the Streets total VOCs are underestimated for the year 2008 or the speciation of NMHC was inaccurate. This could also be causing underestimated propane due to its anthropogenic origin and contributing to the low bias in acetaldehyde in TOMCAT as this also has anthropogenic sources.

Figure 7.4 Vertical profiles of median concentrations of CO (top, left), O_3 (top, middle), NO(top, right), NO_y (bottom, left) and PAN (bottom,middle) observed during the POLARCAT-GRACE project aboard the Falcon over Greenland compared to simulated concentrations from the TOMCAT model interpolated to the flight tracks. The data has been binned into 50 hPa pressure bins for averaging. The error bars represent the 25th and 75th percentiles of the observed concentrations in each bin. The dates correspond the first and the last flight of the campaign.

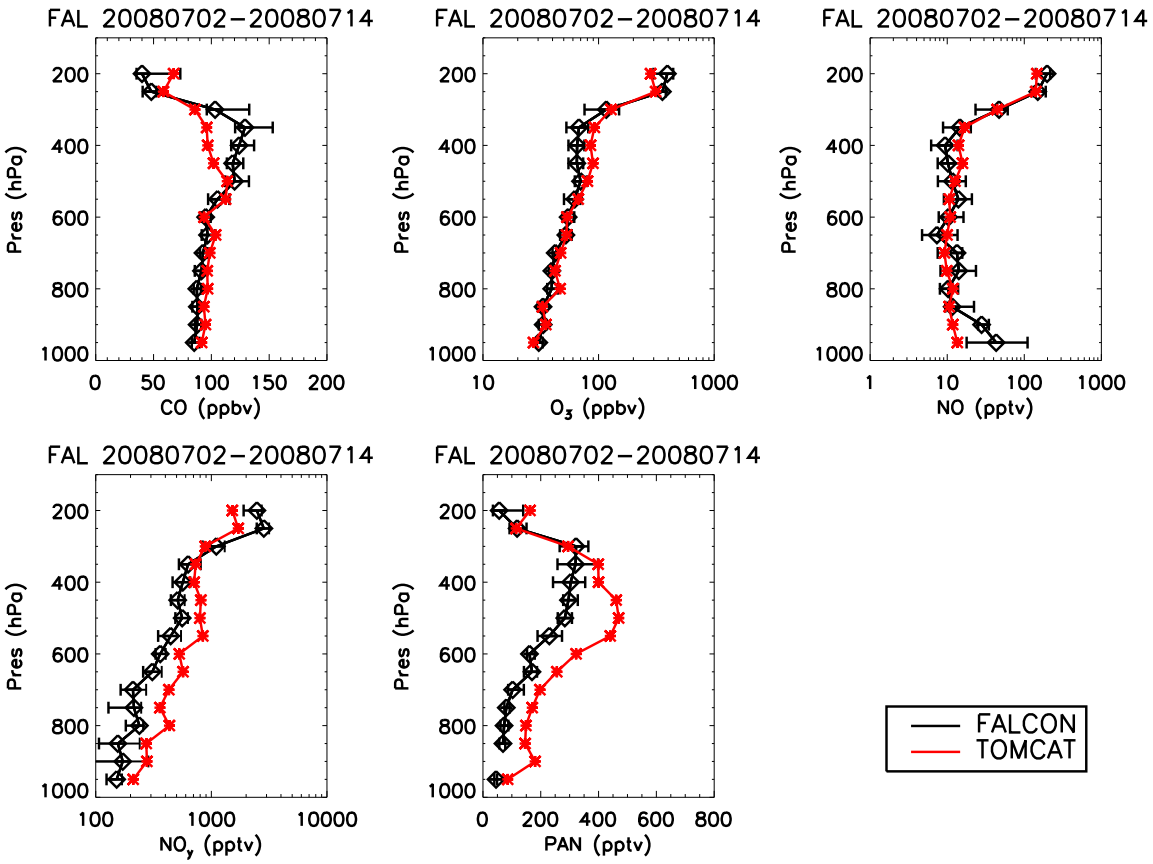

Figure 7.5 Vertical profiles of median concentrations of CO, O_3, NO, NO_2, NO_y, PAN, HNO_3, OH, C_2H_6, C_3H_8 and CH_3CHO observed during the ARCTAS-B project aboard the DC8 over Canada and the central Arctic compared to simulated concentrations from the TOMCAT model interpolated to the flight tracks. The data has been binned into 50 hPa pressure bins for averaging. The error bars represent the 25th and 75th percentiles of the observed concentrations in each bin. The dates correspond the first and the last flight of the campaign.

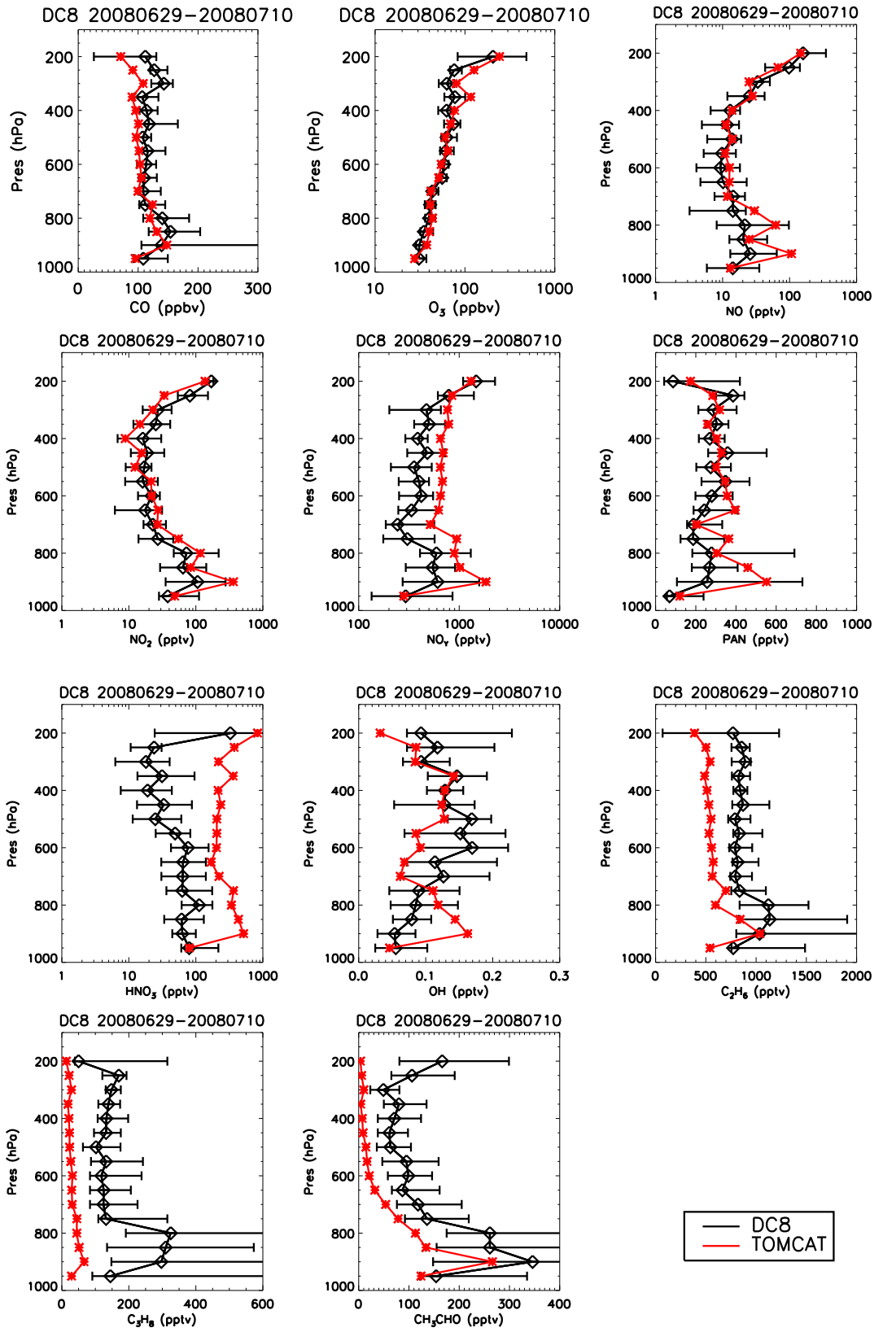

7.5 Sensitivity of O_3 to Arctic PAN

To investigate the importance of PAN, which is either transported to the Arctic or formed within the Arctic, a sensitivity simulation has been performed with all PAN above 66°N removed from the model atmosphere. The removed PAN was converted to HNO_3 and CH_3CHO, which effectively provides a sink of reactive nitrogen and roughly maintains the carbon balance. The sensitivity simulation (which will be referred to as EPAN) had the same set-up as the previously described CTRL simulation and was also run for a 1 year period over 2008 outputting every 3.75 days, after a 6-month spin-up, from which monthly means were calculated.

Figure 7.6 shows the seasonal zonal mean NO_x concentrations from the CTRL simulation in the Northern Hemisphere (NH) along with the absolute and percentage differences between the CTRL and EPAN simulations. Overall, Arctic PAN acts as a source of up to 80 to 100% of NO_x in the Arctic throughout the year with the biggest contributions seen at the surface. This demonstrates the importance of this reservoir species as a source of NO_x in this remote region. The biggest absolute contribution of PAN to NO_x is seen in the summer (June-August), with a difference of up to 8 pptv of NO_x seen between CTRL and EPAN. The smallest contribution is seen in winter (December to February), with less than 2 pptv of NO_x difference. In winter, due to the cold dark conditions, PAN is more thermally stable and therefore has a longer lifetime (Beine and Krognes, 2000), reducing its importance as a source of NO_x. Moving from winter to spring, thermal decomposition of PAN increases, releasing NO_x. PAN exhibits a spring maximum in the Arctic at the surface which is believed to be due to an increase in the photochemical source of PAN at mid-latitudes and efficient poleward transport. PAN exhibits a summer minimum, which is believed to be due to its shorter lifetime ($\sim$ 4 days at the surface in summer compared to $\sim$40 days in winter) and slower poleward transport (Penkett and Brice, 1986; Beine and Krognes, 2000). Even though slower poleward transport does occur in the summer (shown by the simulated CO tracers in Section 5.3), the summer maximum in NO_x shown here, suggests that the summer PAN minimum is most likely controlled by increased decomposition and not transport processes. However, the occurrence of the spring maximum in PAN combination with increasing rates of decomposition in summer, could mean that the summer maximum in NO_x could be due to the accumulation of PAN in spring, masking any transport effects on the PAN concentrations in summer.

The O_3 concentrations from the CTRL simulation (see Figure 7.7) show that TOMCAT has a spring maximum in O_3 which is well known to characterise the O_3 seasonal cycle in the Arctic and has received much interest over the past decade (Atlas et al., 2003; Jacob et al., 2010). It has been noted that PAN could be an important driver in the maximum of O_3 (Penkett and Brice, 1986), however, it has also been suggested that the springtime maximum in Arctic PAN occurs later than the O_3 maximum, suggesting it may not be the driving process (Beine and Krognes, 2000). The O_3 differences between CTRL and EPAN show that overall, Arctic PAN leads to a net

Figure 7.6 Zonal mean NO_x concentrations (ppbv) from CTRL (top), absolute differences between CTRL and EPAN (middle) and percentage differences between CTRL and EPAN (bottom) for DJF , MAM, JJA and SON (left to right) for 2008.

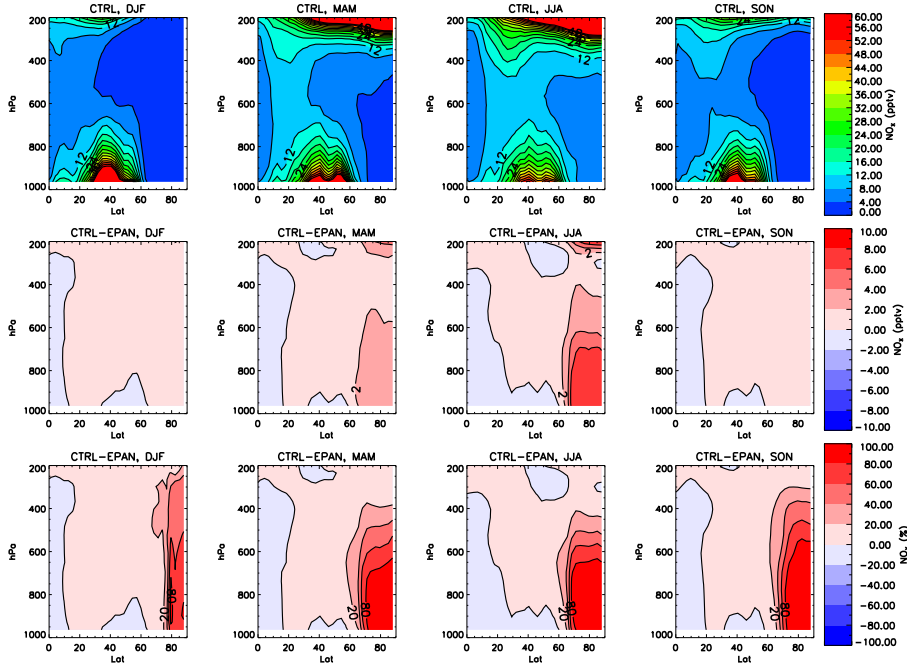

Figure 7.7 Zonal mean O_3 concentrations (ppbv) from CTRL (top), absolute differences between CTRL and EPAN (middle) and percentage differences between CTRL and EPAN (bottom) for DJF , MAM, JJA and SON (left to right) for 2008.

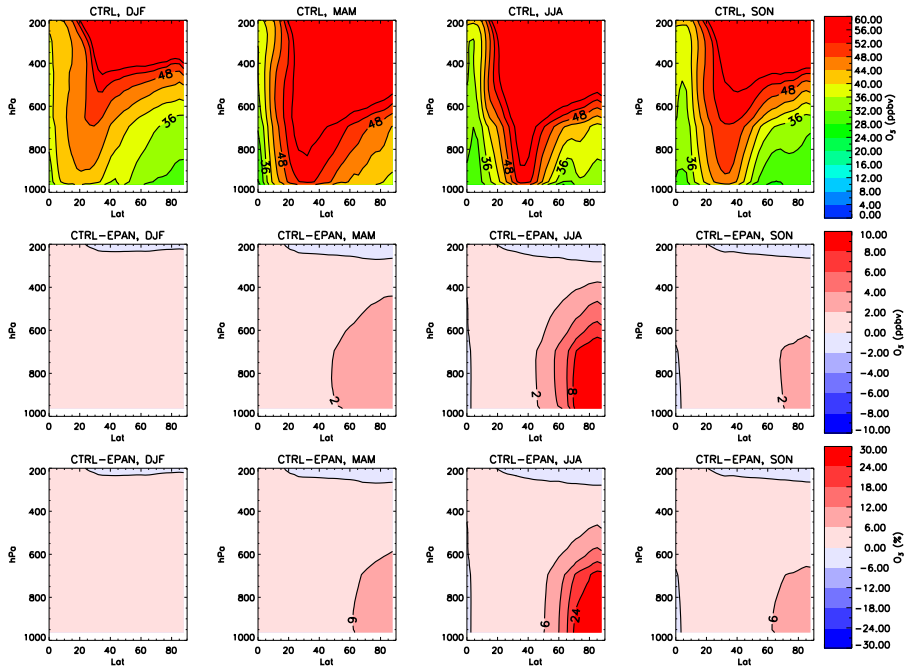

Table 7.2 TOMCAT Northern Hemisphere (NH) annual mean OH concentrations (molec/cm^3) weighted by airmass, calculated by Equation 4.4.1, for CTRL and EPAN.

Model Simulation	**NH** $[\bar{OH}]_M$
CTRL	0.9307×10^6
EPAN	0.9046×10^6
Percent Diff	-2.8%

O_3 production in the Arctic. The biggest impact is seen in the summer in the lower troposphere with >24% of O_3 in the Arctic being formed from PAN. This is in agreement with the response seen in NO_x in Figure 7.6, which also showed the biggest impact in summer. This indicates that PAN is actually more important in summer than in the spring as a source of O_3, suggesting that it is not PAN which is driving the O_3 springtime maximum. The smallest impact is seen in winter when photochemistry is slower due to the lack of daylight. Interestingly, the PAN which has been removed from the Arctic also has an impact on O_3 at lower latitudes which has also been suggested by other studies (Honrath et al., 1996).

Figure 7.8 shows total monthly burdens of O_3, OH, NO_y, PAN and NO_x, calculated at latitudes north of 66°N for three different altitude ranges. O_3 in the highest altitude bin shows very little impact difference between CTRL and EPAN due to a larger influence from stratospheric O_3. As seen in Figure 7.7, the biggest impact on O_3 is seen lower in the troposphere, between 0-2 km. In response to this, OH also shows the biggest impact between 0-2 km with up to 50% of OH in summer coming from O_3 which has been produced from NO_x released from PAN. Overall, NO_y is decreased throughout the year. This is because even though PAN has been converted to HNO_3 in the model, HNO_3 is efficiently lost from the atmosphere by wet deposition, reducing the total burden of reactive nitrogen (NO_y). Between 0-2 km, most of the NO_x comes from PAN decomposition in the Arctic. Between 2-5 km about 50 % of NO_x comes from PAN decomposition. Above 5 km, there is a much smaller difference in the NO_x from the different simulations suggesting other sources of NO_x are more important at higher altitudes. Large concentrations of NO_x and HNO_3 are found in the stratosphere and can therefore be transported to the UT during stratospheric-tropospheric exchange (STE) and are a major source at these altitudes (Wespes et al., 2011). A large amount of NO_x in the upper troposphere is also formed from lightning especially in summer (Levy et al., 1996; Tie et al., 2002).

Table 7.2 shows the airmass-weighted mean tropospheric OH concentration for the NH. The NH OH concentrations are approximately 2.8% lower in the EPAN simulation due to lower O_3 concentrations. As PAN is converted to HNO_3, more NO_y is lost by wet deposition. This suggests that PAN is more important than HNO_3 in contributing to the oxidising capacity of the atmosphere, through the formation of O_3. Any future changes between the partitioning of NO_y may lower

Table 7.3 Minimum and maximum longitudes and latitudes and maximum altitudes (in hPa) reached by the POLARCAT-France ATR, ARCTAS-B DC8, POLARCAT-GRACE Falcon and YAK-AEROSIB aircraft during the POLARCAT summer June-July 2008 campaign.

Aircraft	Min. Lon.	Max. Lon.	Min. Lat.	Max Lat.	Min. Pres (hpa)
ATR:	300.0	320.2	59.4	71.6	379.6
DC8:	224.0	322.1	50.0	87.1	187.3
Falcon:	294.7	322.0	57.5	79.1	213.8
YAK:	66.2	170.7	52.0	72.1	391.2

concentrations of OH. Due to the temperature dependence of PAN, increasing temperatures may shorten its tropospheric lifetime, making more NO_x available to form HNO_3. Lower concentrations of OH, due to increased HNO_3 formation and therefore loss, will increase the lifetimes of greenhouse gases, such as CH_4, which will have important consequences for the radiative budget of the atmosphere, increasing temperatures further. Further investigation into this possible chemical feedback would be needed to understand whether this could be important.

To understand the importance of PAN for O_3 formation during the POLARCAT campaign, simulated O_3 and NO for July 2008 from CTRL and EPAN have been averaged over regions defined by the maximum and minimum longitudes and latitudes and between the surface and the maximum altitudes for each of the campaigns (see Table 7.3). The model is not expected to capture the variability of the observations, as it has not been interpolated to the flight tracks. Figure 7.9 shows that between 0-10 ppbv (0-33%) of O_3 is produced from NO_x released from PAN. Therefore there is still a significant source of O_3 which is not from PAN decomposition. Wespes et al. (2011) showed that during ARCTAS-B a large fraction of O_3 came from lightning production of NO_x and direct transport of O_3 from the stratospheric in the UT. In Figure 7.10, one interesting feature is that over the DC8 region, approximately 50% of TOMCAT NO in the lower troposphere comes from PAN decomposition, whereas for the Falcon region, the majority of the TOMCAT NO comes from PAN. The DC8 was mostly located in the sub-Arctic, closer to fresh emissions of NO_x. In contrast, the Falcon, covering regions close to Greenland which is more remote from emission sources, PAN is more important as a source of NO_x.

Figure 7.8 Monthly mean burdens of O_3 ($Tg(O_3)$/month), OH (Tg(OH)/month), NO_y (Tg(N)/month), PAN (Tg(N)/month), NO_x (Tg(N)/month) calculated at latitudes >66°N in three altitude bins: 0-2 km (left), 2-5 km (middle) and 5 km-tropopause (right).

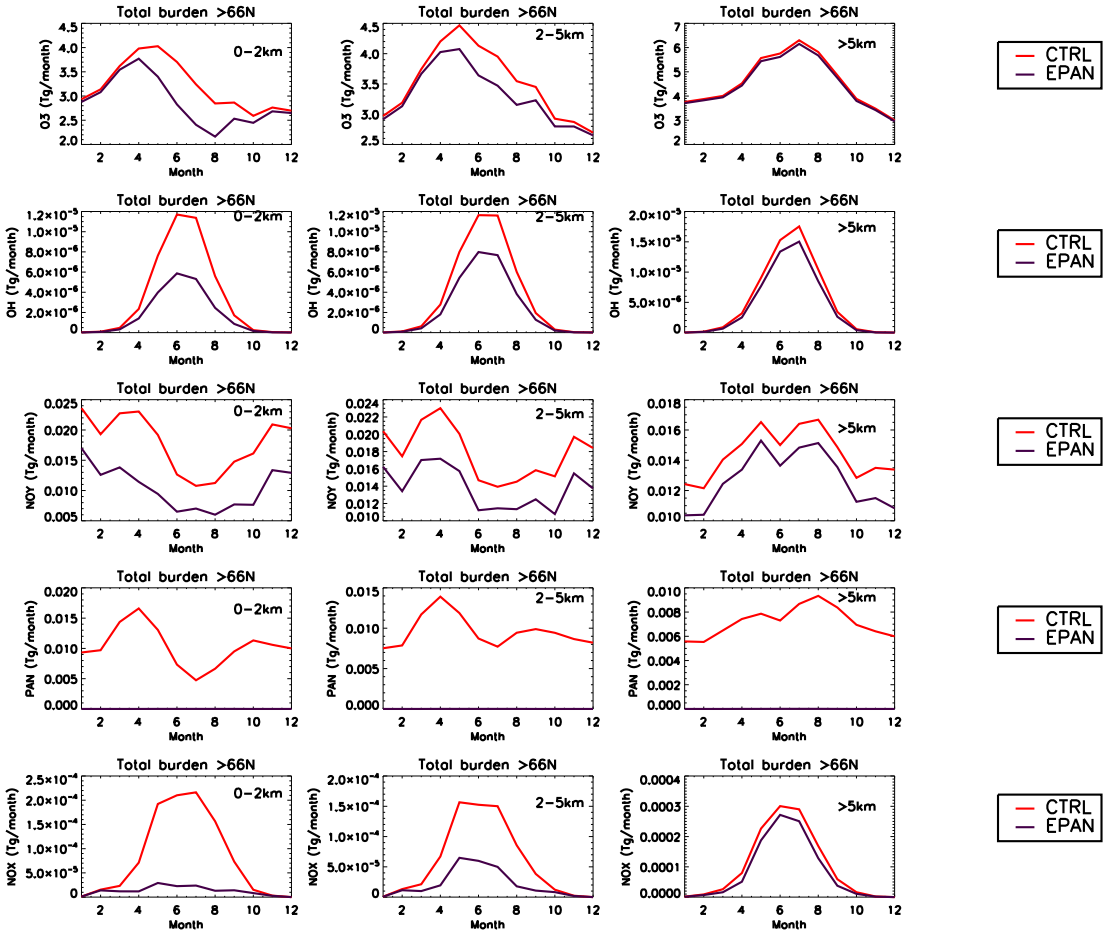

Figure 7.9 Campaign-averaged vertical profiles of O_3 observed by aircraft during the YAK-Aerosib (top, left), POLARCAT-France (ATR) (top, right), POLARCAT-Grace (Falcon) (bottom, left) and ARCTAS-B (DC8) (bottom, right) projects compared to the July 2008 monthly mean simulated O_3 profiles from the CTRL and EPAN simulations averaged over the flight regions given in Table 7.3.

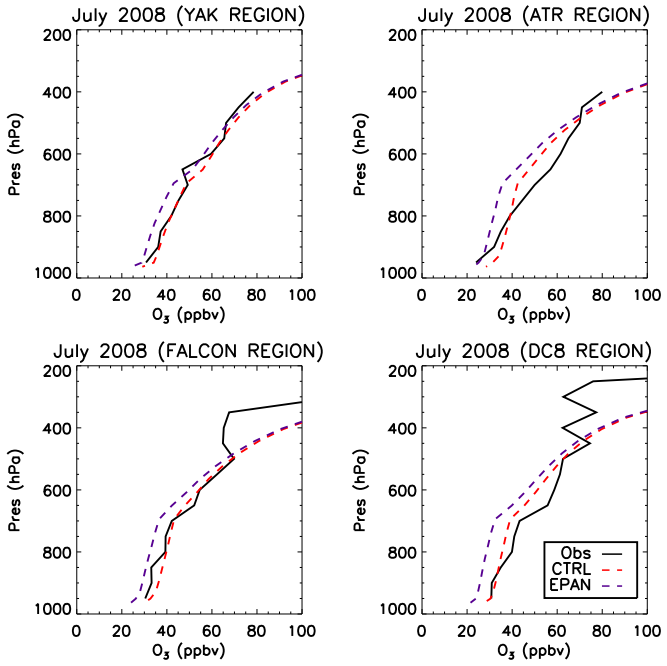

Figure 7.10 Campaign-averaged vertical profiles of NO observed by aircraft during the YAK-Aerosib (top, left), POLARCAT-France (ATR) (top, right), POLARCAT-Grace (Falcon) (bottom, left) and ARCTAS-B (DC8) (bottom, right) projects compared to the July 2008 monthly mean simulated NO profiles from the CTRL and EPAN simulations averaged over the flight regions given in Table 7.3.

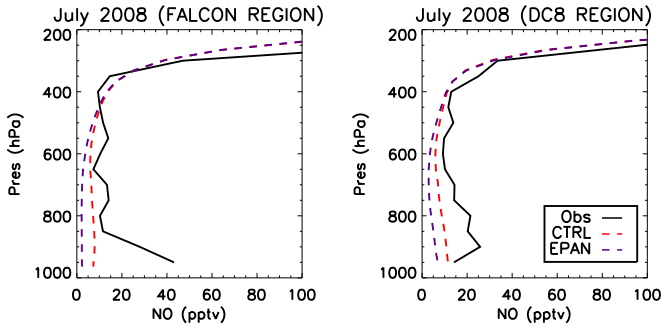

7.6 Sensitivity of O_3 to Arctic C_2H_6

A recent study by Liang et al. (2011) has suggested that in-situ production may be an important source of PAN in the Arctic in the UT. The study analysed observations of PAN during the ARCTAS-B campaign and showed that approximately 120 pptv (∼37%) of observed PAN in mixed stratospheric and tropospheric air could not be explained by mixing of the two airmasses alone. They hypothesised that this PAN could have come from insitu production. In the atmosphere PAN can be formed from species such as acetaldehyde as described in Section 2.4.4. Acetaldehyde (CH_3CHO) is oxidised to form the acetyl radical (CH_3CO) which reacts very quickly to form the peroxyacetyl radical (CH_3CO_3), which can then react with NO_2 to form PAN. Liang et al. (2011) argued that stratospheric air, high in NO_2, mixed with tropospheric air containing acetyl radicals, leading to the formation of PAN. They hypothesised that the acetaldehyde required to form the acetyl radical could only have come from ethane (C_2H_6), due to it being the only hydrocarbon to have a long enough lifetime to reach the Arctic in sufficient quantities.

To test the sensitivity of total PAN concentrations to production from C_2H_6 in the Arctic, a simulation has been performed using the TOMCAT model, where all C_2H_6 was removed above 66°N. This simulation was set-up in the same way as the CTRL simulation and will be referred to as EC2H6. Figure 7.11 shows zonal mean concentrations of PAN from CTRL and the absolute and percentage difference between CTRL and EC2H6. The biggest absolute difference is seen in spring in the lower and mid troposphere but the biggest percentage difference is seen in summer (due to the much smaller concentrations of PAN), also in the lower and mid troposphere. Overall, C_2H_6 contributes between 0-30 pptv (0-8%) to PAN in the Arctic which is much lower then estimated by Liang et al. (2011) from the aircraft data. However, Liang et al. (2011) was considering background airmasses only and in TOMCAT different types of airmasses were not differentiated between and they are likely to be more mixed in the model due to the size of the grid-boxes. The production of PAN from C_2H_6 in the Arctic also contributes up to 10 pptv (4%) of PAN at lower latitudes. In order to understand the impact of this PAN on the formation of O_3, Figure 7.12 shows the zonal mean O_3 concentrations. Overall, C_2H_6 has very little impact on O_3, causing a difference of less than 0.04 ppbv. However, if the acetyl radicals were not present to form PAN, then the stratospheric NO_2 could be photolysed to form O_3 without forming PAN first, therefore reducing any impact on O_3.

Figure 7.13 shows the monthly mean burdens of O_3, PAN, CH_3CHO, C_2H_6 and NO_x, at latitudes north of 66°N. Considering the differences between CTRL and EC2H6, approximately 10-35% of CH_3CHO is produced from C_2H_6 in the Arctic in spring and summer, with the biggest percentage contribution in summer. In winter and autumn, when CH_3CHO concentrations are much higher, C_2H_6 contributes a smaller percent to the total CH_3CHO concentrations. Most of this acetaldehyde is likely to be transported to the Arctic in these seasons from lower latitudes when transport is more

efficient (see Section 5.3) and photochemistry in the Arctic is slower due to less incoming solar radiation. Some of the acetaldehyde produced from C_2H_6 then goes onto to produce PAN, however it has a much smaller impact on the total PAN ($<$10%). Again the biggest response is seen in June. June-July is when Liang et al. (2011) hypothesised approximately 37% of PAN in the UT in STE airmasses came from in-situ production. The TOMCAT burden of O_3 shows hardly any response to the change in C_2H_6.

Figure 7.14 shows the PAN and O_3 concentrations averaged over the flight regions of the DC8 during ARCTAS-B to limit the area of study to the region where the PAN measurements were made that were analysed by Liang et al. (2011). The PAN and O_3 concentrations are also shown for the Falcon during POLARCAT-GRACE campaign for comparison. As seen in the burdens, C_2H_6 in the Arctic does result in PAN formation. For the DC8 region, the impact is larger towards to the UT, which is where Liang et al. (2011) believed the production to be occurring. The TOMCAT model does not simulate the 120 pptv difference which was estimated to be from this source. For the Falcon region the impact on PAN is similar throughout the troposphere. The TOMCAT O_3 profiles show hardly any change between CTRL and EPAN.

According to the TOMCAT model, the majority of PAN found in the Arctic, which results in the formation of O_3 (seen in Section 7.5), is not formed insitu from C_2H_6. This suggests that the source of PAN discussed in Liang et al. (2011) does not play a large role in the budget of O_3 or PAN. It must be noted however, that C_2H_6 in the TOMCAT model is underestimated by 50% (see Section 7.4) and therefore the contribution to PAN is likely to be higher than shown here, but it is still unlikely to make a significant contribution to O_3. It is also important to note that the source of PAN hypothesised by Liang et al. (2011) did not account for 37% of total PAN in the UT, but 37% in STE airmasses therefore accounting for background PAN concentrations only. Polluted airmasses are likely to contain larger concentrations of PAN and therefore the overall contribution to the total Arctic PAN budget is likely to be smaller than Liang et al. (2011) estimated.

Figure 7.11 Zonal mean PAN concentrations (pptv) from CTRL (top), absolute differences between CTRL and EC2H6 (middle) and percentage differences between CTRL and EC2H6 (bottom) for DJF , MAM, JJA and SON (left-right) for 2008.

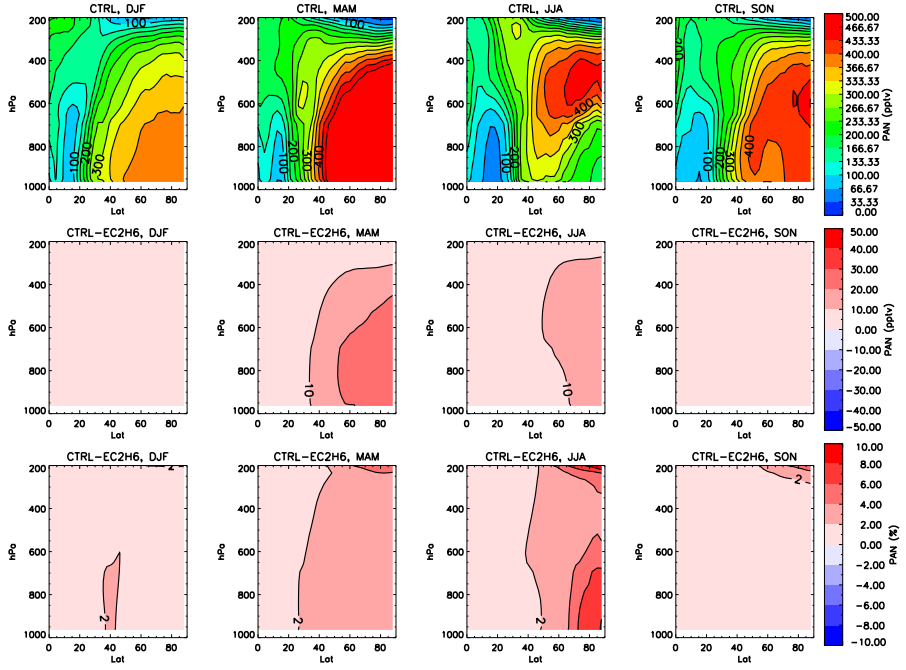

Figure 7.12 Zonal mean O_3 concentrations (ppbv) from CTRL (top), absolute differences between CTRL and EC2H6 (middle) and percentage differences between CTRL and EC2H6 (bottom) for DJF , MAM, JJA and SON (left-right) for 2008.

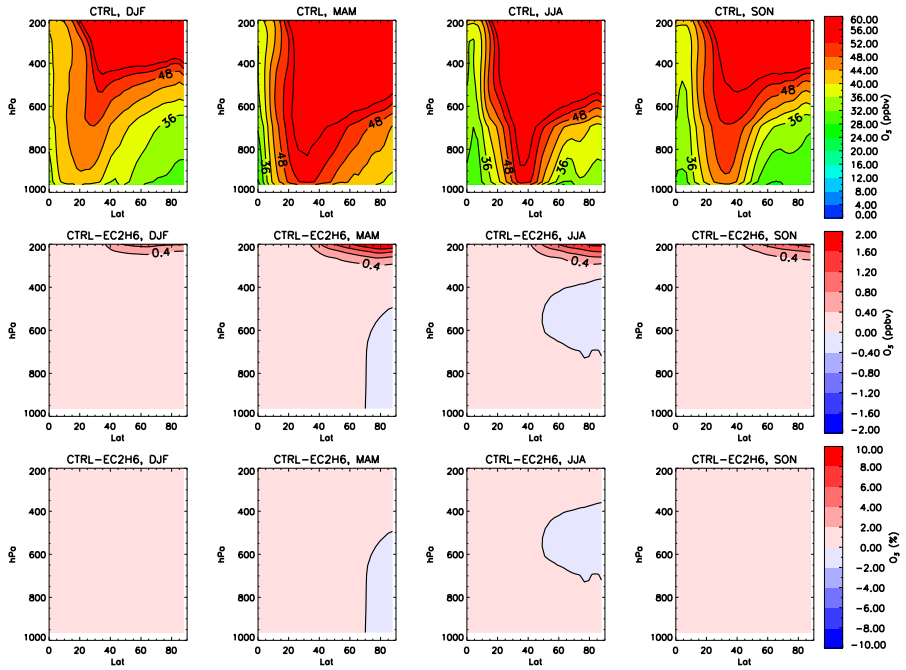

Figure 7.13 Monthly mean burdens of O_3 ($Tg(O_3)$/month), PAN (Tg(N)/month), CH_3CHO (Tg(C)/month), C_2H_6 (Tg(C)/month), NO_x (Tg(N)/month) calculated at latitudes >66°N in three altitude bins: 0-2 km (left), 2-5 km(middle) and 5 km-tropopause (right).

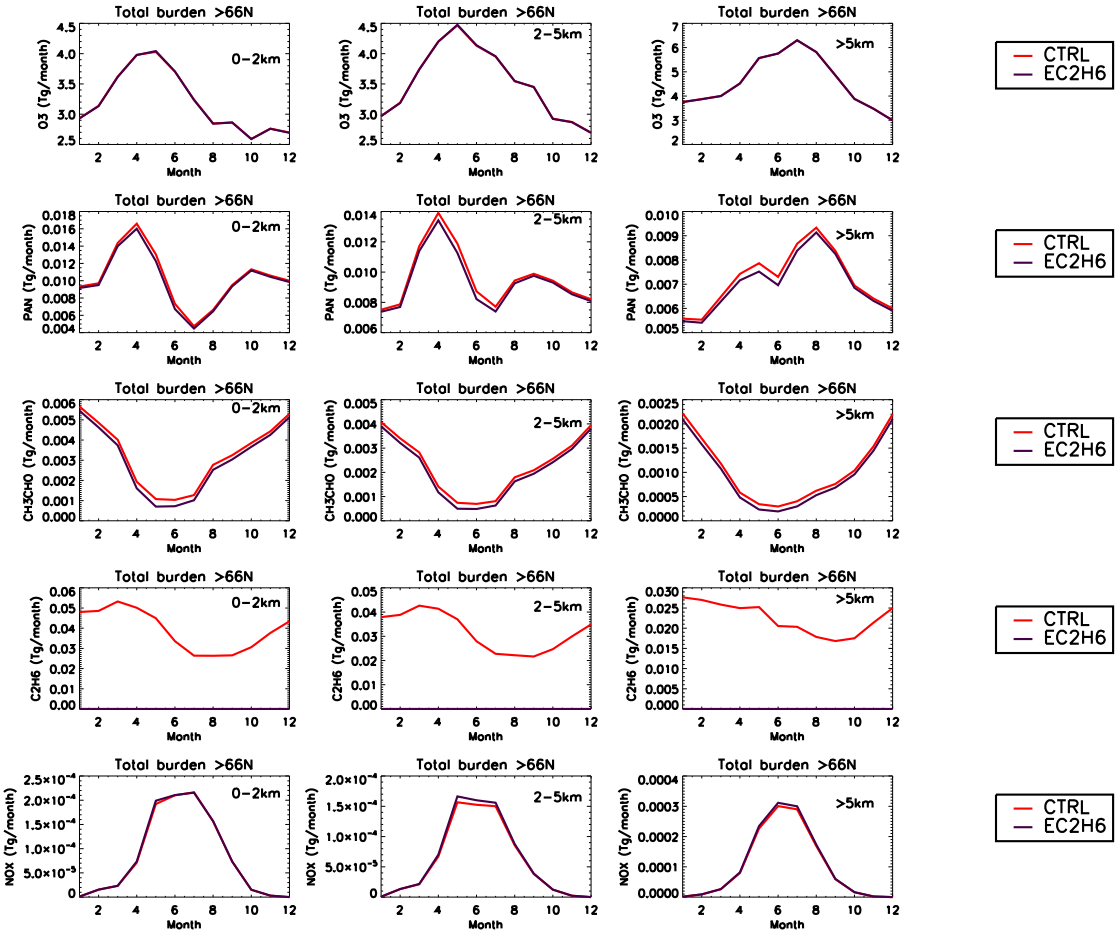

Figure 7.14 Campaign-averaged vertical profiles of O_3 (top) and PAN (bottom) observed by aircraft during the POLARCAT-GRACE (Falcon) (left) and ARCTAS-B (DC8) (right) projects compared to the July 2008 monthly mean simulated O_3 and PAN profiles from the CTRL and EC2H6 simulations averaged over the flights regions given in Table 7.3.

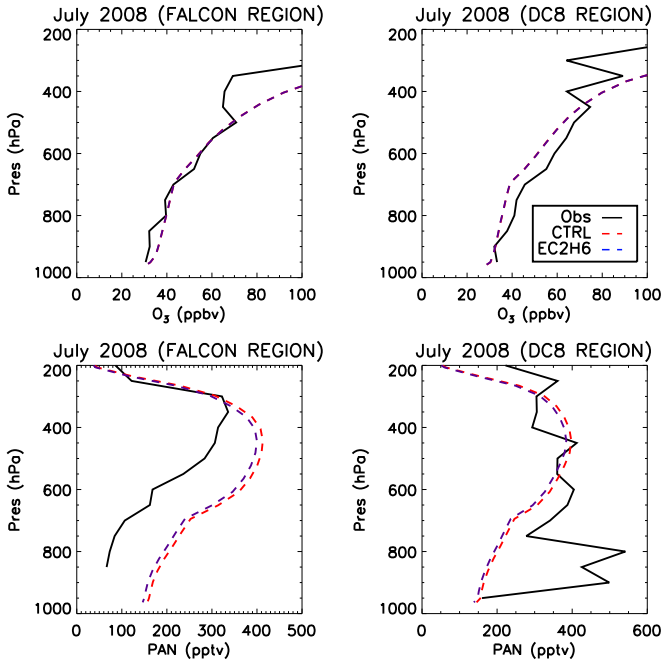

7.7 Summary

In this chapter the TOMCAT model has been further evaluated against newly available aircraft measurements from the POLARCAT campaign. Data collected as part of ARCTAS-B, POLARCAT-France, POLARCAT-GRACE and YAK-AEROSIB, sub-projects of the POLARCAT-summer campaign, offered an important opportunity to evaluate the ability of numerical models to simulate Arctic composition during summer. A combination of measurements from these projects provided measurements of several trace gases between June and July 2008 in regions of Siberia, Canada, Greenland and the Arctic Ocean.

Comparisons with the measured vertical profiles of CO and O_3 showed that TOMCAT was able to capture the vertical distribution and mean concentrations well. In the upper troposphere, there was some evidence that the model overestimated the influence of stratospheric air, seen by an overestimate of observed O_3 and an underestimate of CO. This is most likely due to the reduced vertical resolution of the model near the tropopause. NO_x was also reproduced well by the model both in the Arctic and over Canada. Total NO_y however was found to be overestimated in the Arctic against the POLARCAT-GRACE data which also showed PAN to be overestimated in the model. In contrast, modelled PAN matched the ARCTAS-B observed PAN well. The DC8 measurements were made in more polluted air with fresh emissions from fires where NO_x has been shown in other studies to be rapidly converted to PAN. In this region, the modelled NO_y was also overestimated along with HNO_3. Ethane, propane and acetaldehyde were all underestimated by TOMCAT which is likely to be due to an underestimate of emissions.

A simulation was performed to estimate the importance of Arctic PAN for the tropospheric O_3 burden. PAN was shown to be the dominant source of NO_x in the lower troposphere where it resulted in the formation of up to 30% of O_3 in the summer. This showed Arctic PAN to be an important source of O_3. Another simulation was performed to estimate the importance of Arctic C_2H_6 for the formation of PAN. C_2H_6 oxidation was shown to contribute a large fraction (30%) to the acetaldehyde burden, however concentrations of PAN only increased by up to 8%. According to the TOMCAT model, the production of PAN from from C_2H_6 and stratospheric NO_x proposed by Liang et al. (2011) does not contribute a large fraction to the PAN burden in the Arctic.

Chapter 8

Conclusions

In this thesis, the TOMCAT chemical transport model has been used to investigate the processes which control the concentrations of CO, O_3 and its precursors in the Arctic troposphere. The main results are discussed with reference to the research aims that were presented in Chapter 1 and possible future work is also discussed.

8.1 Synthesis of main results

Aim 1: Evaluate the ability of a chemical transport model to simulate Arctic tropospheric composition

Chapter 4 presented the first results from a new version of the TOMCAT chemical transport model, which included an extension of the standard hydrocarbon chemistry scheme and a treatment of heterogeneous uptake of N_2O_5. Chapter 7 also compared the new version of the model to newly available data from the POLARCAT-summer 2008 aircraft campaign which took place in the Arctic and sub-Arctic.

The oxidation of the additional NMHC led to a 4-5% increase in the global tropospheric burden of CO, a 2-4% increase in the burden of O_3 and a 3-4% increase in the burden of HO_2. Total reactive nitrogen was also increased due to a 40-75% increase in the PAN burden. This demonstrates the importance of the oxidation of NMHC as a source of CO in the troposphere, but also its effect on O_3, HO_x and NO_y. Model intercomparisons have previously shown large variability between simulated budgets of tropospheric CO, both in the Arctic and throughout the globe (Shindell et al., 2006b, 2008). It is believed that this may have been caused by different levels of complexity in their chemical schemes (i.e., hydrocarbons) leading to different NMHC emissions and treatment (Shindell et al., 2006b). The results presented in this thesis also show that different levels of

complexity in chemical schemes may also contribute to previously observed model differences in simulated tropospheric O_3 in the troposphere (Wild, 2007). The large sensitivity of PAN to additional NMHC may have a significant impact on modelled regional O_3 budgets due to it acting as a source of NO_x in remote regions (Moxim et al., 1996). This may be particularly important in the Arctic, as PAN was shown to be the dominant source of NO_x in the Arctic lower troposphere in Chapter 7, where it resulted in the formation of up to 30% of O_3 in the summer. This demonstrates that PAN is an important source of Arctic O_3. In addition to this, comparisons to the POLARCAT aircraft data also showed the TOMCAT model to overestimate total NO_y. Measurements from two different aircraft showed that this was due to an overestimate of HNO_3 and possibly also due to PAN. This has also been observed in other studies along with model-observation differences in other species such HO_x (Stroud et al., 2003; Law and Stohl, 2007; Mao et al., 2010). Mao et al. (2010) argued that high biases of modelled HO_2 could be explained by including the heterogeneous uptake of H_2O_2, a reservoir species of HO_2, providing an additional loss route for HO_x. This suggests that there is still considerable uncertainty in model predictions of NO_y and HO_x budgets in the Arctic and warrants further investigation. In addition to this, the low bias of ethane and propane found in TOMCAT suggest the need for better global emission inventories for these species.

In agreement with previous studies (Dentener and Crutzen, 1993; Tie et al., 2003), the addition of N_2O_5 uptake led to substantial decreases of 20-47% in the global tropospheric NO_x burden, 4-6% in the O_3 burden and 7-8% in the OH burden. An evaluation of simulated OH against the Lawrence et al. (2001) climatology showed that the new version of the model (with both heterogeneous and extended hydrocarbon chemistry) offered improved OH concentrations in the Northern Hemisphere (NH) lower troposphere (due to lower OH concentrations), however it also suggested that the model was missing a source of OH in the upper troposphere in the tropics. Comparisons with TOPSE aircraft data in the Arctic showed that lower concentrations of NO_x simulated by TOMCAT were in much better agreement in winter and spring due to this additional NO_x loss route. One criticism of this work would be the use of offline aerosol fields. The lack of co-located plumes of trace gases and aerosols is likely to result in errors in simulated fields in polluted plumes, however, the model is assumed to capture the overall monthly mean loss of NO_x. In the future, it would be advisable to switch to using the coupled TOMCAT-GLOMAP model developed by Breider (2010) for a more complex treatment of interactions between aerosol and gases.

Overall, simulated CO from the new version of the model was in much better agreement with observed CO in the NH due to increased CO production from the additional NHMC and more accurate lower OH concentrations at the surface in the NH. This improved simulated CO in winter and spring and accounting for additional NMHC may reduce the low biases found in simulated CO in the NH by Shindell et al. (2006b)

Aim 2: Quantify the main sources of trace gases within the Arctic

As discussed in Chapters 1 and 2 it has been suggested that reducing emissions of gases which lead to the formation of O_3 may reduce warming in the Arctic (Quinn et al., 2008). It is therefore important to understand the sources of Arctic O_3 to ascertain whether regional emission reduction policies will be effective. Chapter 5 investigated the transport efficiency and contributions to CO (a tracer of natural and anthropogenic combustion processes) and O_3 in the Arctic troposphere from major sources. This chapter contained the first ever source contribution analysis to consider the impacts of fire emissions and different fire types throughout the year in comparison to anthropogenic sources.

The Arctic sensitivity to emissions at lower latitudes showed a strong seasonal and altitude dependency in agreement with previous studies (Klonecki et al., 2003; Stohl, 2006). Overall, anthropogenic emissions were found to be the largest source of Arctic CO (48%), followed by oxidation of methane (25%), then fires (13%). Natural emissions (10% direct emissions and 4% from isoprene oxidation) had the smallest contributions. In summer, fire and anthropogenic sourced CO had equal contributions in the Arctic between the surface and the mid-troposphere, demonstrating the importance of this as a source of pollution during this season. The majority of the fire-sourced CO came from naturally occurring forest fires (60%), however the annual mean burden of fire CO was also shown to be sensitive to agricultural burning practices in the spring if weighted by total emissions (27%). Boreal fires were also shown to be the dominant sources of O_3 and NO_y species in the lower and mid troposphere during the summer compared to anthropogenic emissions from North America, Europe and Asia. This has important implications for the Arctic as fires in the boreal regions are expected to increase due to increased temperatures releasing more emissions of CO and O_3 precursors (Soja et al., 2007). Also, if human agricultural fires are increased then they can impact the Arctic quite substantially during spring. Spring is of particular concern as it is when snow-albedo feedbacks are most important due to warming affecting the timing of the spring melt (Hall and Qu, 2006) and has been shown to be the season where the Arctic exhibits the largest temperature response to O_3 (Quinn et al., 2008).

Out of the anthropogenic emission regions North America contributed the largest amount (30%) to the total anthropogenic CO burden. This was due to efficient transport in the upper troposphere plus relatively high total emissions. East Asian emissions showed the second highest anthropogenic contribution (26%) due to high total emissions. Europe showed the third largest contribution (23%) even though this region had the highest transport efficiency. This was due to small total emissions compared to the other regions. South Asia had the smallest overall contribution (9%) due to inefficient transport and small emissions. This is in disagreement with Fisher et al. (2010), who found Asia to be the dominate source of CO in the Arctic in April 2008. However, model

interpretation of source contributions was shown to be largely dependent on the absolute emissions used in different studies, making results sensitive to errors in inventories. For this reason, the emission region contributions were weighted by total emissions to give the Arctic sensitivity to CO emissions (in units of Tg(CO) per Tg(CO) emitted per year). This showed that the Arctic is most sensitive to emissions changes in Europe, then North America and then Asia in agreement with Shindell et al. (2008). This demonstrates that emissions reductions in some regions will be more effective in reducing pollution in the Arctic due to their location and the transport pathways that emissions undergo to the Arctic.

For the total Arctic O_3 burden, North America had the largest contribution (9%) out of the anthropogenic regions considered, followed by Europe (7%) and then Asia (6%) (both South and East Asia combined). In contrast to CO, O_3 in the Arctic is most sensitive to emissions from North America and not Europe, demonstrating that the different transport pathways to the Arctic must experience different O_3 production efficiencies. The different pathways that emissions undergo result in very different NO_y burdens. Europe has the largest burden of NO_y in the Arctic, then North America and then Asia. This was mostly due to different concentrations of HNO_3. The smaller concentrations were believed to be related to the different rates of precipitation along the pathways to the Arctic from the different regions (Barrie, 1986; Stohl, 2006). Europe emissions had the largest contribution to PAN and NO_x below 5 km, whereas North America dominated the NO_x and PAN burdens above 5 km. The amount of NO_x required for net O_3 production in the springtime Arctic has been shown to vary with altitude, with lower concentrations of NO_x being required in the upper troposphere (UT) compared to the lower troposphere (Stroud et al., 2004). This, along with the larger abundance of NO_x and PAN in the UT, could partially explain why North America contributes a larger fraction to O_3 compared to Europe even though transport is less efficient. Also, more O_3 could be produced en route to the Arctic from North America as it is at a lower latitude band compared to Europe (see Figure 5.1), and therefore has warmer temperatures and more incoming radiation resulting in more O_3 and less PAN. The PAN from Europe may remain as PAN whilst in the Arctic and could then be transported back to mid-latitudes, where it could form O_3. PAN export from the Arctic has previously been hypothesised by Honrath et al. (1996).

Aim 3: Investigate the processes which control observed inter-annual variability in the Arctic.

An important part of understanding future changes in the burdens of atmospheric trace gases in the Arctic is knowledge of the current processes which lead to recent observed variability. In Chapter 6 the drivers of Arctic CO interannual variability (IAV) were investigated considering the contributions from meteorology and biomass burning.

Model simulations showed that 0-25% and 84-93% of observed CO variability at different Arctic surface stations was caused by variability in meteorology and variability in fires, respectively. This showed that fires are the dominant driver of CO IAV in the Arctic. Most of the variability in fires was caused by variability in forest fires (60%). This is particularly interesting as it has been suggested that future changes in Arctic concentrations may result from a shift in the North Atlantic Oscillation (NAO) towards the positive phase associated with greenhouse gases (Law and Stohl, 2007), however, the results shown here suggest that changes in fire emissions dominate short-term variability over transport changes, however, for long-term trends, changes in transport may still be important.

Links between Arctic CO IAV and meteorological variability with phase changes in the NAO, PNA and ENSO were also investigated. The model showed that the NAO has the most significant effect on the Arctic throughout the year. During positive phases of the NAO in the winter, concentrations of trace gases and aerosols would be expected to be increased due to enhanced transport from Europe, North America and East Asia. This is in agreement with a previous study by Eckhardt et al. (2003). In contrast to this, summer concentrations would be expected to be lower due to reduced transport from East and South Asia in summer. The reversal of the Arctic response is due to a shift in the centre of the NAO, changing its influence on transport patterns along with the increasing importance of Asian sources in summer. The spring and autumn seasons showed a more complicated response due to them being transitional seasons between the winter and summer NAO patterns (Hurrell et al., 2003). This is the first time that the NAO's influence on transport to the Arctic has been considered throughout the year, demonstrating that the seasonal evolution of the NAO is important. It has been suggested that increased greenhouse gases may result in a shift in the NAO towards a more positive phase (Hurrell et al., 2003) and the results shown here suggest that the response of Arctic trace gas burdens will not be simple. ENSO was shown to only influence emissions from South Asia during winter and spring. Enhanced transport during El Niño events would result in enhanced concentrations over parts of the Canadian Arctic in winter and over parts of Alaska and Siberia in spring. The suggests that the anomalously low concentrations of CO observed by AIRS over Alaska during 2008 was due to the La Niña, causing reduced transport from South Asia, as speculated by Fisher et al. (2010). The export from Asia is strongly reliant on the occurrence of the seasonal monsoon (Lawrence, 2004) which has been shown to be influenced by El Niño (Webster and Yang, 1992). The results described here are the first to show a relationship with El Niño and export of South Asian emission to high northern latitudes. The PNA did not significantly affect transport to the Arctic.

Lag correlations between observed CO at surface stations in the Arctic and the El Niño 3.4 Index revealed significant positive correlations which peaked at a lag of 10-11 months. Model simulations were used to show that this relationship was caused by a link between El Niño and forest fires and not transport. It is well known that El Niño events have resulted in large forest fires perturbing

regional trace gases (Chandra et al., 1998; van de Werf et al., 2004), however, this is the first time this relationship has been identified in the Arctic. Further investigation showed that the regional fire response to an El Niño event was different depending on what drove the fires (temperature, precipitation and relative humidity) in each region and how the region responded to El Niño. El Niño was shown to be strongly associated with increased fire emissions from Alaska, Canada, western North America, Central America, northern South America, southern Africa, south-east and equatorial Asia and to a lesser extent in eastern Siberia. In the boreal regions, precipitation is reduced which results in increased fire emissions. This is particularly important for the Arctic, as the work presented here also showed that forest fires in the boreal regions are a dominant source of CO and O_3 in the Arctic during summer (therefore providing a strong link between El Niño and observed Arctic CO). In contrast, El Niño events are associated with reduced fires in eastern North America, Europe, southern Asia and Australia. Due to the predicted warming of the global climate (Meehl et al., 2007), the regions which showed strong relationships between temperature and fire emissions are of particular interest. Results shown in this thesis suggest that Europe, western North America, Central America, northern South America, southern Africa, south-east Asia and equatorial Asia will all show an increase in fire activity in the future due to a warmer climate. Fires were also shown to be sensitive to precipitation in several regions, however, the predicted future changes in precipitation show much more small-scale variability, therefore making any comments on regional fire response difficult.

Overall, this thesis has shown that fires are currently important as a source of pollutants in the Arctic, but may also drive futures changes in concentrations of trace gases and aerosols in the Arctic through expected increases in their frequency and intensity (Soja et al., 2007). Estimates of fire emissions are still poorly constrained even after much improvement with the incorporation of global burned area estimates from satellite data now being available. In particular, development of current models to include a treatment to accurately predict fire emissions would greatly improve out ability to model future global changes (Bowman et al., 2009). A better understanding of meteorological global fire drivers which could be included in models would be particularly helpful. The global study of fire drivers presented in this thesis would be useful for this purpose. Other major uncertainties still lie in estimates of emissions factors and combustion efficiencies, which need to be improved if we are to further improve our ability to accurately emissions from fires (French et al., 2004). The results presented in this thesis demonstrate this will greatly improve our ability to understand changes in the Arctic due to the importance of fires in this region.

8.2 Future work

Work performed for this thesis has highlighted areas which would benefit from further investigation, such as:

- Further research into O_3 production along the transport pathways from North America, Europe and Asia. This would help us to further understand the sensitivity of the Arctic O_3 burden to the different regions. In addition to this it would also be useful to study the regional contributions to radiative forcing in the Arctic from O_3. Europe, North America and Asia all showed different seasonal and altitudinal maxima and minima. It has previously been shown that O_3 has the biggest impact on radiative forcing at higher altitudes and during spring in the Arctic. Therefore, it is likely that the Arctic radiative budget will show different sensitivities to the different anthropogenic emission regions due to their different transport pathways, which cause European O_3 to dominate in the lower troposphere and North American and Asian O_3 to dominate in the UT. It would also be useful to consider the importance of biomass burning in terms of radiative forcing in the Arctic in comparison to anthropogenic emissions.

- During the late summer and autumn, CO was shown to be overestimated at the surface. Convection in TOMCAT has been previously shown to be underestimated (Hoyle et al., 2011) and therefore due to its importance in summer, it would be useful to perform some simulations using an improved convection scheme (using archived mass fluxes) (Feng et al., 2011) to see how this would influence CO at the surface and if it would improve future simulations.

- In Section 6.4 it was shown that fires dominate the IAV of CO in the Arctic. A previous study by Szopa et al. (2007) found that meteorology and fires both played almost equal roles in the Arctic IAV of CO. One important difference was the use of different ECMWF winds. It would be useful to perform a simulation testing the difference between ERA40 (used by Szopa et al. (2007)) and ERA-Interim (used by TOMCAT) to see how sensitive the results are to the different input files.

- In Section 6.6.1 an investigation into fire drivers was performed. The robustness of this analysis could be checked by using satellite-observed precipitation and temperature instead of ECMWF ERA-Interim reanalyses. However, it is assumed that as the ECMWF reanalyses assimilate satellite observations into their model, that the results found here would not change. A more useful re-evaluation method would be to use a range of satellite observed area burnt statistics instead of the CO emissions used from the GFED v3.1 inventory. This would allow the uncertainty in area burnt datasets to be accounted for and also the work could then be extrapolated to other gases and not just CO. Also, as correlations only show a possible link between El Niño and regional fires and their climate drivers the correlations calculated in this chapter could be further tested by incorporating precipitation, relative humidity and temperature in fire/area burned models and testing the importance of each of the parameters in different regions against observed area burned data. Climate models could

then be used to further investigate climate patterns associated with El Niño and how these would influence area burnt and fire emissions.

- Due to the importance of halogen chemistry and heterogeneous chemistry (shown in Chapter 4) in the Arctic it is suggested that future Arctic simulations be done using the coupled TOMCAT/GLOMAP model which will allow the impact of halogens on O_3 in the troposphere to be considered and the use of online aerosol fields which interact with the oxidants in the model. It would be particularly interesting to calculate the Arctic O_3 budget including ozone depletion by bromine to better understand the extent of these events on total tropospheric O_3 and OH.

Appendix A

List of Chemical Reactions in the TOMCAT Model

TABLE A.1: Chemical species in the TOMCAT CTM

	Species	Category	Family	Dry Deposited?	Wet Deposited?	Emitted?
1	$O(^3P)$	FM	Ox	N	N	N
2	$O(^1D)$	FM	Ox	N	N	N
3	O_3	FM	Ox	Y	N	N
4	NO	FM	NOx	Y	N	N
5	NO_3	FM	NOx	Y	Y	N
6	NO_2	FM	NOx	Y	N	Y
7	N_2O_5	TR		Y	Y	N
8	HO_2NO_2	TR		Y	Y	N
9	$HONO_2$	TR		Y	Y	N
10	OH	SS		N	N	N
11	HO_2	SS		N	Y	N
12	H_2O_2	TR		Y	Y	N
13	CH_4	TR		N	N	Y
14	CO	TR		Y	N	Y
15	HCHO	TR		Y	Y	Y
16	MeOO	SS		N	Y	N
17	H_2O	CF		N	N	N
18	MeOOH	TR		Y	Y	N
19	HONO	TR		Y	Y	N
20	C_2H_6	TR		N	N	Y
21	EtOO	SS		N	N	N
22	EtOOH	TR		Y	Y	N
23	MeCHO	TR		Y	N	Y
24	$MeCO_3$	SS		N	N	N
25	PAN	TR		Y	N	N
26	C_3H_8	TR		N	N	Y

Continued on next page

Table A.1 – continued from previous page

	Species	Category	Family	Dry Deposited?	Wet Deposited?	Emitted?
27	n-PrOO	SS		N	N	N
28	i-PrOO	SS		N	N	N
29	n-PrOOH	TR		Y	Y	N
30	i-PrOOH	TR		Y	Y	N
31	EtCHO	TR		Y	N	N
32	$EtCO_3$	SS		N	N	N
33	Me_2CO	TR		Y	N	Y
34	$MeCOCH_2OO$	SS		N	N	N
35	$MeCOCH_2OOH$	TR		Y	Y	N
36	PPAN	TR		Y	N	N
37	$MeONO_2$	TR		N	N	N
38	$O(^3P)S$	FM	Sx	N	N	N
39	$O(^1D)S$	FM	Sx	N	N	N
40	O_3S	FM	Sx	Y	N	N
41	NOXS	SS		Y	N	N
42	HNO_3S	SS		Y	Y	N
43	NOYS	TR		Y	Y	N
44	C_5H_8	TR		N	N	Y
45	$C_{10}H_{16}$	TR		N	N	Y
46	TERPOOH	TR		Y	Y	N
47	ISO_2	SS		N	N	N
48	ISOOH	TR		Y	Y	N
49	ISON	TR		Y	Y	N
50	MACR	TR		Y	N	N
51	$MACRO_2$	SS		N	N	N
52	MACROOH	TR		Y	Y	N
53	MPAN	TR		Y	N	N
54	HACET	TR		Y	Y	N
55	MGLY	TR		Y	Y	N
56	NALD	TR		Y	N	N
57	HCOOH	TR		Y	Y	N
58	$MeCO_3H$	TR		Y	Y	N
59	$MeCO_2H$	TR		Y	Y	N
60	MeOH	TR		Y	Y	Y
61	$TERPO_2$	SS		N	N	N
62	C_2H_4	TR		N	N	Y
63	C_2H_2	TR		N	N	Y
64	C_4H_{10}	TR		N	N	Y
65	C_3H_6	TR		N	N	Y
66	AROM	TR		N	N	Y
67	MEK	TR		N	N	N
68	MeCOCOMe	TR		Y	Y	N
69	BtOO	SS		N	N	N
70	PrpeOO	SS		N	N	N
71	$AROMO_2$	SS		N	N	N
72	MEKOO	SS		N	N	N

Continued on next page

Table A.1 – continued from previous page

	Species	Category	Family	Dry Deposited?	Wet Deposited?	Emitted?
73	BtOOH	TR		Y	Y	N
74	PrpeOOH	TR		Y	Y	N
75	AROMOOH	TR		Y	Y	N
76	MEKOOH	TR		Y	Y	N
77	ONIT	TR		N	N	N
78	$EtCO_3H$	SS		N	N	N
79	$EtCO_2H$	SS		N	N	N
80	H_2	CT		N	N	N
81	CO_2	CT		N	N	N
82	O_2	CT		N	N	N
83	N_2	CT		N	N	N

FM = Family, TR = Independent Tracer, SS = Steady State, CT = constant in space and time, CF = constant in time, spatially variant

S denotes stratospheric species

Me=CH_3, Et=C_2H_5, Pr= C_3H_7, Prpe = C_3H_7O, Bt= C_4H_9

TERP = Generic terpine compound, e.g. C_6H_{10} (monoterpine)

MACR = Lumped species consisting of methacrolein, methyl vinyl ketone and other C4 carbonyls from isoprene chemistry

HACET = Hydroxyacetone, $CH_2OHC(O)CH_3$

MGLY = Methylglyoxal, $CH_3C(O)CHO$

NALD = Nitrooxy acetaldehyde, O_2NOCH_2CHO

AROM = Generic aromatic compound, e.g. $C_6H_5CH_3$ (toluene)

MEK = Methyl ethyl ketone, $CH_3C(O)CH_2CH_3$

ONIT = Organic nitrate (from propene and butane chemistry), e.g. $CH_3CH_2CH(ONO_2)CH_3$

TABLE A.2: TOMCAT heterogeneous reactions

Reaction	Reactants	Products
1	$N_2O_5 + H_2O$	$\rightarrow HNO_3 + HNO_3$

TABLE A.3: TOMCAT gas-phase bimolecular reactions

	Reactants	Products	k_0	α	β	Reference
1	HO_2 + NO	$\rightarrow$ OH + NO_2	3.60×10^{-12}	0.00	-270.0	IUPAC [2005]
2	HO_2 + NO_3	$\rightarrow$ OH + NO_2	4.00×10^{-12}	0.00	0.0	IUPAC [2005]
3	HO_2 + O_3	$\rightarrow$ OH + O_2	2.03×10^{-16}	4.57	-693.0	IUPAC [2005]
4	HO_2 + HO_2	$\rightarrow$ H_2O_2	2.20×10^{-13}	0.00	-600.0	IUPAC [2005]
5	HO_2 + MeOO	$\rightarrow$ MeOOH	3.80×10^{-13}	0.00	-780.0	IUPAC [2005]
6	HO_2 + MeOO	$\rightarrow$ HCHO	3.80×10^{-13}	0.00	-780.0	IUPAC [2005]
7	HO_2 + EtOO	$\rightarrow$ EtOOH	3.80×10^{-13}	0.00	-900.0	IUPAC [2005]
8	HO_2 + $MeCO_3$	$\rightarrow$ $MeCO_3H$	2.08×10^{-13}	0.00	-980.0	IUPAC [2005]
9	HO_2 + $MeCO_3$	$\rightarrow$ $MeCO_2H$ + O_3	1.04×10^{-13}	0.00	-980.0	IUPAC [2005]
10	HO_2 + $MeCO_3$	$\rightarrow$ OH + MeOO	2.08×10^{-13}	0.00	-980.0	IUPAC [2005]
11	HO_2 + n-PrOO	$\rightarrow$ n-PrOOH	1.51×10^{-13}	0.00	-1300.0	MCM
12	HO_2 + i-PrOO	$\rightarrow$ i-PrOOH	1.51×10^{-13}	0.00	-1300.0	MCM
13	HO_2 + $EtCO_3$	$\rightarrow$ O_2 + $EtCO_3H$	3.05×10^{-13}	0.00	-1040.0	MCM
14	HO_2 + $EtCO_3$	$\rightarrow$ O_3 + $EtCO_2H$	1.25×10^{-13}	0.00	-1040.0	MCM
15	HO_2 + $MeCOCH_2OO$	$\rightarrow$ $MeCOCH_2OOH$	1.36×10^{-13}	0.00	-1250.0	MCM
16	MeOO + NO	$\rightarrow$ HO_2 + HCHO + NO_2	2.95×10^{-12}	0.00	-285.0	IUPAC [2005]
17	MeOO + NO	$\rightarrow$ $MeONO_2$	2.95×10^{-15}	0.00	-285.0	IUPAC [2005]
18	MeOO + NO_3	$\rightarrow$ HO_2 + HCHO + NO2	1.30×10^{-12}	0.00	0.0	IUPAC [2005]
19	MeOO + MeOO	$\rightarrow$ MeOH + HCHO	1.03×10^{-13}	0.00	-365.0	IUPAC [2005]
20	MeOO + MeOO	$\rightarrow$ HO_2 + HO_2 + HCHO + HCHO	1.03×10^{-13}	0.00	-365.0	IUPAC [2005]
21	MeOO + $MeCO_3$	$\rightarrow$ HO_2 + HCHO + MeOO	1.80×10^{-12}	0.00	-500.0	IUPAC [2005]
22	MeOO + $MeCO_3$	$\rightarrow$ $MeCO_2H$ + HCHO	2.00×10^{-13}	0.00	-500.0	IUPAC [2005]
23	EtOO + NO	$\rightarrow$ MeCHO + HO_2 + NO_2	2.60×10^{-12}	0.00	-380.0	IUPAC [2005]
24	EtOO + NO_3	$\rightarrow$ MeCHO + HO_2 + NO_2	2.30×10^{-12}	0.00	0.0	IUPAC [2005]
25	EtOO + $MeCO_3$	$\rightarrow$ MeCHO + HO_2 + MeOO	4.40×10^{-13}	0.00	-1070.0	IUPAC [2005]
26	$MeCO_3$ + NO	$\rightarrow$ MeOO + CO_2 + NO_2	7.50×10^{-12}	0.00	-290.0	IUPAC [2005]
27	$MeCO_3$ + NO_3	$\rightarrow$ MeOO + CO_2 + NO_2	4.00×10^{-12}	0.00	0.0	MCM

Continued on next page

Table A.3 – continued from previous page

	Reactants	Products	k_0	α	β	Reference
28	n-PrOO + NO	$\rightarrow$ EtCHO + HO_2 + NO_2	2.90×10^{-12}	0.00	-350.0	IUPAC [2005]
29	n-PrOO + NO_3	$\rightarrow$ EtCHO + HO_2 + NO_2	2.50×10^{-12}	0.00	0.0	MCM
30	i-PrOO + NO	$\rightarrow$ Me_2CO + HO_2 + NO_2	2.70×10^{-12}	0.00	-360.0	IUPAC [2005]
31	i-PrOO + NO_3	$\rightarrow$ Me_2CO + HO_2 + NO_2	2.50×10^{-12}	0.00	0.0	MCM
32	$EtCO_3$ + NO	$\rightarrow$ EtOO + CO_2 + NO_2	6.70×10^{-12}	0.00	-340.0	IUPAC [2005]
33	$EtCO_3$ + NO_3	$\rightarrow$ EtOO + CO_2 + NO_2	4.00×10^{-12}	0.00	0.0	MCM
34	$MeCOCH_2OO$ + NO	$\rightarrow$ $MeCO_3$ + HCHO + NO_2	2.80×10^{-12}	0.00	-300.0	Tyndall et al. [2001]
35	$MeCOCH_2OO$ + NO_3	$\rightarrow$ $MeCO_3$ + HCHO + NO_2	2.50×10^{-12}	0.00	0.0	MCM
36	NO + NO_3	$\rightarrow$ NO_2 + NO_2	1.80×10^{-11}	0.00	-110.0	IUPAC [2005]
37	NO + O_3	$\rightarrow$ NO_2	1.40×10^{-12}	0.00	1310.0	IUPAC [2005]
38	NO_2 + O_3	$\rightarrow$ NO_3	1.40×10^{-13}	0.00	2470.0	IUPAC [2005]
39	NO_3 + HCHO	$\rightarrow$ $HONO_2$ + HO_2 + CO	2.00×10^{-12}	0.00	2440.0	IUPAC [2005]
40	NO_3 + MeCHO	$\rightarrow$ $HONO_2$ + $MeCO_3$	1.40×10^{-12}	0.00	1860.0	IUPAC [2005]
41	NO_3 + EtCHO	$\rightarrow$ $HONO_2$ + $EtCO_3$	3.46×10^{-12}	0.00	1862.0	MCM
42	NO_3 + Me_2CO	$\rightarrow$ $HONO_2$ + $MeCOCH_2OO$	3.00×10^{-17}	0.00	0.0	IUPAC [2005]
43	N_2O_5 + H_2O	$\rightarrow$ $HONO_2$ + $HONO_2$	$0.00\times10^{+00}$	0.00	0.0	Set to 0.0, using het.chem
44	$O(^3P)$ + O_3	$\rightarrow$ O_2 + O_2	8.00×10^{-12}	0.00	2060.0	IUPAC [2005]
45	$O(^1D)$ + CH_4	$\rightarrow$ OH + MeOO	1.05×10^{-10}	0.00	0.0	IUPAC [2005]
46	$O(^1D)$ + CH_4	$\rightarrow$ HCHO + H_2	7.50×10^{-12}	0.00	0.0	IUPAC [2005]
47	$O(^1D)$ + CH_4	$\rightarrow$ HCHO + HO_2 + HO_2	3.45×10^{-11}	0.00	0.0	IUPAC [2005]
48	$O(^1D)$ + H_2O	$\rightarrow$ OH + OH	2.20×10^{-10}	0.00	0.0	IUPAC [2005]
49	$O(^1D)$ + N_2	$\rightarrow$ $O(^3P)$ + N_2	2.10×10^{-11}	0.00	-115.0	Ravishankara et al. [2002]
50	$O(^1D)$ + O_2	$\rightarrow$ $O(^3P)$ + O_2	3.20×10^{-11}	0.00	-67.0	IUPAC [2005]
51	OH + CH_4	$\rightarrow$ H_2O + MeOO	1.85×10^{-12}	0.00	1690.0	IUPAC [2005]
52	OH + C_2H_6	$\rightarrow$ H_2O + EtOO	6.90×10^{-12}	0.00	1000.0	IUPAC [2005]
53	OH + C_3H_8	$\rightarrow$ n-PrOO + H_2O	7.60×10^{-12}	0.00	585.0	IUPAC [2005]
54	OH + C_3H_8	$\rightarrow$ i-PrOO + H_2O	7.60×10^{-12}	0.00	585.0	IUPAC [2005]
55	OH + CO	$\rightarrow$ HO_2	1.44×10^{-13}	0.00	0.0	IUPAC [2005]

Continued on next page

Table A.3 – continued from previous page

	Reactants	Products	k_0	α	β	Reference
56	OH + EtCHO	$\rightarrow H_2O + EtCO_3$	5.10×10^{-12}	0.00	-405.0	IUPAC [2005]
57	OH + EtOOH	$\rightarrow H_2O$ + MeCHO + OH	8.01×10^{-12}	0.00	0.0	MCM
58	OH + EtOOH	$\rightarrow H_2O$ + EtOO	1.90×10^{-12}	0.00	-190.0	MCM
59	OH + H_2	$\rightarrow H_2O + HO_2$	7.70×10^{-12}	0.00	2100.0	IUPAC [2005]
60	OH + H_2O_2	$\rightarrow H_2O + HO_2$	2.90×10^{-12}	0.00	160.0	IUPAC [2005]
61	OH + HCHO	$\rightarrow H_2O + HO_2$ + CO	5.40×10^{-12}	0.00	-135.0	IUPAC [2004]
62	OH + HO_2	$\rightarrow H_2O$	4.80×10^{-11}	0.00	-250.0	IUPAC [2005]
63	OH + HO_2NO_2	$\rightarrow H_2O + NO_2$	1.90×10^{-12}	0.00	-270.0	IUPAC [2005]
64	OH + HO_2NO_2	$\rightarrow H_2O + NO_3$	1.50×10^{-13}	0.00	0.0	IUPAC [2005]
65	OH + HONO	$\rightarrow H_2O + NO_2$	2.50×10^{-12}	0.00	-260.0	IUPAC [2005]
66	OH + MeOOH	$\rightarrow H_2O$ + HCHO + OH	1.02×10^{-12}	0.00	-190.0	IUPAC [2005]
67	OH + MeOOH	$\rightarrow H_2O$ + MeOO	1.89×10^{-12}	0.00	-190.0	IUPAC [2005]
68	OH + $MeONO_2$	$\rightarrow$ HCHO + $NO_2 + H_2O$	4.00×10^{-13}	0.00	845.0	IUPAC [2005]
69	OH + Me_2CO	$\rightarrow H_2O + MeCOCH_2OO$	8.80×10^{-12}	0.00	1320.0	IUPAC [2005]
70	OH + Me_2CO	$\rightarrow H_2O + MeCOCH_2OO$	1.70×10^{-14}	0.00	-420.0	IUPAC [2005]
71	OH + $MeCOCH_2OOH$	$\rightarrow H_2O + MeCOCH_2OO$	1.90×10^{-12}	0.00	-190.0	MCM
72	OH + $MeCOCH_2OOH$	$\rightarrow$ OH + MGLY	8.39×10^{-12}	0.00	0.0	MCM
73	OH + MeCHO	$\rightarrow H_2O + MeCO_3$	4.40×10^{-12}	0.00	-365.0	IUPAC [2005]
74	OH + NO_3	$\rightarrow HO_2 + NO_2$	2.00×10^{-11}	0.00	0.0	IUPAC [2005]
75	OH + O_3	$\rightarrow HO_2 + O_2$	1.70×10^{-12}	0.00	940.0	IUPAC [2005]
76	OH + OH	$\rightarrow H_2O + O(^3P)$	6.31×10^{-14}	2.60	-945.0	IUPAC [2005]
77	OH + PAN	$\rightarrow$ HCHO + $NO_2 + H_2O$	3.00×10^{-14}	0.00	0.0	IUPAC [2005]
78	OH + PPAN	$\rightarrow$ MeCHO + $NO_2 + H_2O$	1.27×10^{-12}	0.00	0.0	MCM
79	OH + n-PrOOH	$\rightarrow$ n-PrOO + H_2O	1.90×10^{-12}	0.00	-190.0	MCM
80	OH + n-PrOOH	$\rightarrow$ EtCHO + H_2O + OH	1.10×10^{-11}	0.00	0.0	MCM
81	OH + i-PrOOH	$\rightarrow$ i-PrOO + H_2O	1.90×10^{-12}	0.00	-190.0	MCM
82	OH + i-PrOOH	$\rightarrow Me_2CO$ + OH	1.66×10^{-11}	0.00	0.0	MCM
83	$O(^3P) + NO_2$	$\rightarrow NO + O_2$	5.50×10^{-12}	0.00	-188.0	IUPAC [2005]

Continued on next page

Table A.3 – continued from previous page

	Reactants	Products	k_0	α	β	Reference
84	OH + C_5H_8	→ ISO_2	2.70×10^{-11}	0.00	-390.0	IUPAC [2005]
85	OH + C_5H_8	→ MACR + HCHO + $MACRO_2$ + $MeCO_3$	3.33×10^{-15}	0.00	1995.0	IUPAC [2005][1]
86	OH + C_5H_8	→ MeOO + HCOOH + CO + H_2O_2	3.33×10^{-15}	0.00	1995.0	IUPAC [2005][1]
87	OH + C_5H_8	→ HO_2 + OH	3.33×10^{-15}	0.00	1995.0	IUPAC [2005][1]
88	NO_3 + C_5H_8	→ ISON	3.15×10^{-12}	0.00	450.0	IUPAC [2005]
89	NO + ISO_2	→ NO_2 + MACR + HCHO + HO_2	2.43×10^{-12}	0.00	-360.0	MCM v3.1/Pöschl et al. [200]
90	NO + ISO_2	→ ISON	1.12×10^{-13}	0.00	-360.0	MCM v3.1/Pöschl et al. [200]
91	HO_2 + ISO_2	→ ISOOH	2.05×10^{-13}	0.00	-1300.0	MCM v3.1/P öschl et al. [200]
92	ISO_2 + ISO_2	→ MACR + MACR + HCHO + HO_2	2.00×10^{-12}	0.00	0.0	P öschl et al. [200]
93	OH + ISOOH	→ MACR + OH	1.00×10^{-10}	0.00	0.0	P öschl et al. [200]
94	OH + ISON	→ HACET + NALD	1.30×10^{-11}	0.00	0.0	P öschl et al. [200]
95	OH + MACR	→ $MACRO_2$	1.30×10^{-12}	0.00	-610.0	IUPAC [2005]
96	OH + MACR	→ $MACRO_2$	4.00×10^{-12}	0.00	-380.0	IUPAC [2005]
97	O_3 + MACR	→ MGLY + HCOOH + HO_2 + CO	2.13×10^{-16}	0.00	1520.0	IUPAC [2005][1]
98	O_3 + MACR	→ OH + $MeCO_3$	2.13×10^{-16}	0.00	1520.0	IUPAC [2005][1]
99	O_3 + MACR	→ MGLY + HCOOH + HO_2 + CO	3.50×10^{-16}	0.00	2100.0	IUPAC [2005][1]
100	O_3 + MACR	→ OH + $MeCO_3$	3.50×10^{-16}	0.00	2100.0	IUPAC [2005][1]
101	NO + $MACRO_2$	→ NO_2 + $MeCO_3$ + HACET + CO	1.27×10^{-12}	0.00	-360.0	MCM v3.1/P öschl et al. [200] [1]
102	NO + $MACRO_2$	→ MGLY + HCHO + HO_2	1.27×10^{-12}	0.00	-360.0	MCM v3.1/P öschl et al. [200] [1]
103	HO_2 + $MACRO_2$	→ MACROOH	1.83×10^{-13}	0.00	-1300.0	MCM v3.1/P öschl et al. [200]
104	$MACRO_2$ + $MACRO_2$	→ HACET + MGLY + HCHO + CO	1.00×10^{-12}	0.00	0.0	MCM v3.1/P öschl et al. [200] [1]
105	$MACRO_2$ + $MACRO_2$	→ HO_2	1.00×10^{-12}	0.00	0.0	MCM v3.1/P öschl et al. [200] [1]
106	OH + MPAN	→ HACET + NO_2	2.90×10^{-11}	0.00	0.0	IUPAC [2005]
107	OH + MACROOH	→ $MACRO_2$	3.00×10^{-11}	0.00	0.0	P öschl et al. [200]
108	OH + HACET	→ MGLY + HO_2	3.00×10^{-12}	0.00	0.0	IUPAC [2005]/P öschl et al. [200]
109	OH + MGLY	→ $MeCO_3$ + CO	1.50×10^{-11}	0.00	0.0	IUPAC [2005]/P öschl et al. [200]
110	NO_3 + MGLY	→ $MeCO_3$ + CO + $HONO_2$	3.46×10^{-12}	0.00	1860.0	MCM v3.1
111	OH + NALD	→ HCHO + CO + NO_2	4.40×10^{-12}	0.00	-365.0	IUPAC [2005]/P öschl et al. [200]

Continued on next page

Table A.3 – continued from previous page

	Reactants	Products	k_0	α	β	Reference
112	OH + $MeCO_3H$	→ $MeCO_3$	3.70×10^{-12}	0.00	0.0	MCM v3.1/P öschl et al. [200]
113	OH + $MeCO_2H$	→ MeOO	4.00×10^{-13}	0.00	-200.0	JPL [2003]
114	OH + HCOOH	→ HO_2	4.50×10^{-13}	0.00	0.0	IUPAC [2005]
115	MeOH + OH	→ HCHO + HO_2	2.85×10^{-12}	0.00	345.0	IUPAC [2007]
116	OH + $C_{10}H_{16}$	→ $TERPO_2$	1.20×10^{-11}	0.00	-444.0	MOZART3
117	O_3 + $C_{10}H_{16}$	→ OH + MEK + HO_2	1.00×10^{-15}	0.00	732.0	MOZART3
118	NO_3 + $C_{10}H_{16}$	→ ISON + MACR	1.20×10^{-12}	0.00	-490.0	NOTE[6]
119	NO + $TERPO_2$	→ Me_2CO + HO_2 + NO_2	2.10×10^{-12}	0.00	-180.0	MOZART3[1]
120	NO + $TERPO_2$	→ MACR + MACR	2.10×10^{-12}	0.00	-180.0	MOZART3[1]
121	HO_2 + $TERPO_2$	→ TERPOOH	7.50×10^{-13}	0.00	-700.0	MOZART3[1]
122	OH + TERPOOH	→ $TERPO_2$	3.80×10^{-12}	0.00	-200.0	MOZART3[1]
123	C_4H_{10} + OH	→ BtOO + H_2O	9.10×10^{-12}	0.00	405.0	IUPAC [2006]
124	BtOO + NO	→ NO_2 + MEK + HO_2 + EtOO	1.27×10^{-12}	0.00	-360.0	MCM v3.1[1]
125	BtOO + NO	→ ONIT + MeCHO	1.27×10^{-12}	0.00	-360.0	MCM v3.1[1]
126	BtOO + HO_2	→ BtOOH	1.82×10^{-13}	0.00	-1300.0	MCM v3.1
127	BtOO + MeOO	→ MEK + HCHO + HO_2 + MeCHO	1.25×10^{-13}	0.00	0.0	MCM v3.1[1]
128	BtOO + MeOO	→ MeOH + EtOO	1.25×10^{-13}	0.00	0.0	MCM v3.1[1]
129	BtOOH + OH	→ BtOO + MEK + OH + H_2O	1.90×10^{-12}	0.00	-190.0	MCM v3.1[1]
130	MEK + OH	→ MEKOO	1.30×10^{-12}	0.00	25.0	IUPAC [2006]
131	MEKOO + NO	→ MeCHO + $MeCO_3$ + NO_2 + ONIT	2.54×10^{-12}	0.00	-360.0	MCM v3.1
132	MEKOO + HO_2	→ MEKOOH	1.82×10^{-13}	0.00	-1300.0	MCM v3.1
133	MEKOOH + OH	→ MeCOCOMe + OH + OH	1.90×10^{-12}	0.00	-190.0	MCM v3.1
134	ONIT + OH	→ MEK + NO_2 + H_2O	1.60×10^{-12}	0.00	0.0	IUPAC [2006]/RvK01
135	C_2H_4 + O_3	→ HCHO + HO_2 + OH + CO	4.55×10^{-15}	0.00	2580.0	IUPAC [2006][1]
136	C_2H_4 + O_3	→ H_2 + CO_2 + HCOOH	4.55×10^{-15}	0.00	2580.0	IUPAC [2006][1]
137	C_3H_6 + O_3	→ HCHO + MeCHO + OH + HO_2	1.83×10^{-15}	0.00	1880.0	IUPAC [2006][1]
138	C_3H_6 + O_3	→ EtOO + MGLY + CH_4 + CO	1.83×10^{-15}	0.00	1880.0	IUPAC [2006][1]
139	C_3H_6 + O_3	→ MeOH + MeOO + HCOOH	1.83×10^{-15}	0.00	1880.0	IUPAC [2006][1]

Continued on next page

Table A.3 – continued from previous page

	Reactants	Products	k_0	α	β	Reference
140	C_3H_6 + NO_3	→ ONIT	4.60×10^{-13}	0.00	1155.0	IUPAC [2006][1]
141	PrpeOO + NO	→ MeCHO + HCHO + HO_2 + NO_2	1.27×10^{-12}	0.00	-360.0	MCM v3.1[1]
142	PrpeOO + NO	→ ONIT	1.27×10^{-12}	0.00	-360.0	MCM v3.1[1]
143	PrpeOO + HO_2	→ PrpeOOH	1.50×10^{-13}	0.00	-1300.0	MCM v3.1
144	PrpeOOH + OH	→ PrpeOO + H_2O	1.90×10^{-12}	0.00	-190.0	MCM v3.1
145	PrpeOOH + OH	→ HACET + OH	2.44×10^{-11}	0.00	0.0	MCM v3.1
146	AROM + OH	→ $AROMO_2$ + HO_2	1.81×10^{-12}	0.00	-338.0	Folberth et al. (2006)[1]
147	$AROMO_2$ + NO	→ MGLY + NO_2 + $MeCO_3$ + CO	1.35×10^{-12}	0.00	-360.0	Folberth et al. (2006)[1]
148	$AROMO_2$ + NO	→ HO_2	1.35×10^{-12}	0.00	-360.0	Folberth et al. (2006)[1]
149	$AROMO_2$ + NO_3	→ MGLY + NO_2 + $MeCO_3$ + CO	1.20×10^{-12}	0.00	0.0	Folberth et al. (2006)[1]
150	$AROMO_2$ + NO_3	→ HO_2	1.20×10^{-12}	0.00	0.0	Folberth et al. (2006)[1]
151	$AROMO_2$ + HO_2	→ AROMOOH	1.90×10^{-13}	0.00	1300.0	Folberth et al. (2006)[1]
152	$AROMO_2$ + MeOO	→ MGLY + CO + $MeCO_3$ + MeOH	1.15×10^{-13}	0.00	0.0	Folberth et al. (2006)[1]
153	$AROMO_2$ + MeOO	→ HO_2 + HCHO	1.15×10^{-13}	0.00	0.0	Folberth (2006)[1]
154	AROMOOH + OH	→ $AROMO_2$	1.90×10^{-12}	0.00	-190.0	Folberth et al. (2006)[1]
155	AROMOOH + OH	→ OH + H_2O	4.61×10^{-18}	0.00	-253.0	Folberth et al. (2006)[1]
156	AROMOOH + OH	→ $MeCO_3$ + CO + HO_2 + OH	4.19×10^{-17}	0.00	-696.0	Folberth et al. (2006)[1]
157	HO_2 + O_3S	→ HO_2 + O_2	2.03×10^{-16}	4.57	-693.0	IUPAC [2005]
158	OH + O_3S	→ OH + O_2	1.70×10^{-12}	0.00	940.0	IUPAC [2005]
159	$O(^1D)S$ + H_2O	→ H_2O	2.20×10^{-10}	0.00	0.0	IUPAC [2005]
160	$O(^1D)S$ + N_2	→ $O(^3P)S$ + N_2	2.10×10^{-11}	0.00	-115.0	Ravishankara et al. [2002]
161	$O(^1D)S$ + O_2	→ $O(^3P)S$ + O_2	3.20×10^{-11}	0.00	-67.0	IUPAC [2005]

Rate constant k = k_0 $(\frac{T}{300})^{\alpha}$ $\exp(\frac{-\beta}{T})$ where T is temperature (K)

[1] Reactions split between multiple channels in order to accommodate large number of products

TABLE A.4: TOMCAT gas-phase termolecular and thermal decomposition reactions

	Reactants	Products	f	k_1	α_1	β_1	k_2	α_2	β_2	Reference
1	$HO_2 + HO_2 + M$	$\rightarrow H_2O_2 + O_2 + M$	0.00	1.90×10^{-33}	0.00	-980.0	$0.00\times10^{+00}$	0.00	0.0[1]	IUPAC [2005]
2	$HO_2 + NO_2 + M$	$\rightarrow HO_2NO_2 + M$	0.60	1.80×10^{-31}	-3.20	0.0	4.70×10^{-12}	0.00	0.0	IUPAC [2005]
3	$HO_2NO_2 + M$	$\rightarrow HO_2 + NO_2 + M$	0.60	4.10×10^{-05}	0.00	10650.0	$4.80\times10^{+15}$	0.00	11170.0	IUPAC [2005]
4	$MeCO_3 + NO_2 + M$	$\rightarrow$ PAN + M	0.30	2.70×10^{-28}	-7.10	0.0	1.20×10^{-11}	-0.90	0.0	IUPAC [2005]
5	PAN + M	$\rightarrow MeCO_3 + NO_2 + M$	0.30	4.90×10^{-03}	0.00	12100.0	$5.40\times10^{+16}$	0.00	13830.0	IUPAC [2005]
6	$N_2O_5 + M$	$\rightarrow NO_2 + NO_3 + M$	0.35	1.30×10^{-03}	-3.50	11000.0	$9.70\times10^{+14}$	0.10	11080.0	IUPAC [2005]
7	$NO_2 + NO_3 + M$	$\rightarrow N_2O_5 + M$	0.35	3.60×10^{-30}	-4.10	0.0	1.90×10^{-12}	0.20	0.0	IUPAC [2005]
8	$O(^3P) + O_2 + M$	$\rightarrow O_3 + M$	0.00	5.70×10^{-34}	-2.60	0.0	$0.00\times10^{+00}$	0.00	0.0	IUPAC [2005]
9	OH + NO + M	$\rightarrow$ HONO + M	1420.00	7.40×10^{-31}	-2.40	0.0	3.30×10^{-11}	-0.30	0.0	IUPAC [2005]
10	$OH + NO_2 + M$	$\rightarrow HONO_2 + M$	0.40	3.30×10^{-30}	-3.00	0.0	4.10×10^{-11}	0.00	0.0	IUPAC [2005]
11	OH + OH + M	$\rightarrow H_2O_2 + M$	0.50	6.90×10^{-31}	-0.80	0.0	2.60×10^{-11}	0.00	0.0	IUPAC [2005]
12	$EtCO_3 + NO_2 + M$	$\rightarrow$ PPAN + M	0.30	2.70×10^{-28}	-7.10	0.0	1.20×10^{-11}	-0.90	0.0	MCM
13	PPAN + M	$\rightarrow EtCO_3 + NO_2 + M$	0.36	1.70×10^{-03}	0.00	11280.0	$8.30\times10^{+16}$	0.00	13940.0	IUPAC [2005]
14	$MACRO_2 + NO_2 + M$	$\rightarrow$ MPAN + M	0.30	2.70×10^{-28}	0.00	11280.0	$8.30\times10^{+16}$	0.00	13940.0	P öschl et al. [200]
15	MPAN + M	$\rightarrow MACRO_2 + NO_2 + M$	0.30	4.90×10^{-03}	0.00	12100.0	$5.40\times10^{+16}$	0.00	13830.0	P öschl et al. [200]
16	$O(^3P) + O_2 + M$	$\rightarrow O_3 + M$	0.00	5.70×10^{-34}	-2.60	0.0	$0.00\times10^{+00}$	0.00	0.0	IUPAC [2005]
17	$C_2H_4 + OH + M$	$\rightarrow$ PrpeOO + M	0.48	2.87×10^{-29}	-3.10	0.0	3.00×10^{-12}	-0.85	0.0	IUPAC [2006]
18	$C_2H_4 + OH + M$	$\rightarrow$ PrpeOO + M	0.48	2.87×10^{-29}	-3.10	0.0	3.00×10^{-12}	-0.85	0.0	IUPAC [2006]
19	$C_2H_4 + OH + M$	$\rightarrow$	0.48	2.87×10^{-29}	-3.10	0.0	3.00×10^{-12}	-0.85	0.0	IUPAC [2006]
20	$C_3H_6 + OH + M$	$\rightarrow$ PrpeOO + M	0.50	8.00×10^{-27}	-3.50	0.0	3.00×10^{-11}	-1.00	0.0	IUPAC [2006]

Rate constant k = $(\frac{k_0[M]}{1+k_0[M]/k_\infty})F_c^{(1+[log_{10}\frac{k_0[M]}{k_\infty}]^2)^{-1}}$

$k_0=k_1\ (\frac{T}{300})^{\alpha_1}\exp(\frac{-\beta_1}{T})$

$k_\infty=k_2\ (\frac{T}{300})^{\alpha_2}\exp(\frac{-\beta_2}{T})$

If f is lees than 1, then $F_c = f$. Otherwise, $F_c = \exp(-T/f)$

[1] Reaction (1), Rate k = $(2.2\text{x}10^{-13}\exp(600/T)+1.9\text{x}10^{-33}[N_2]\exp(980/T))\times(1+1.4\text{x}10^{-21})[H_2O]\exp(2200/T))$

TABLE A.5: TOMCAT photolysis reactions

Reaction	Reactants	Products	Reference
1	EtOOH + hν	$\rightarrow$ MeCHO + HO_2 + OH	JPL [1990]
2	H_2O_2 + hν	$\rightarrow$ OH + OH	JPL [1992]
3a	HCHO + hν	$\rightarrow$ HO_2 + HO_2 + CO	IUPAC
3b	HCHO + hν	$\rightarrow$ H_2 + CO	IUPAC
5	HO_2NO_2 + hν	$\rightarrow$ HO_2 + NO_2	IUPAC
6	$HONO_2$ + hν	$\rightarrow$ OH + NO_2	IUPAC
7a	MeCHO + hν	$\rightarrow$ MeOO + HO_2 + CO	Blitz et al., [2004]
7b	MeCHO + hν	$\rightarrow$ CH4 + CO	Blitz et al., [2004]
9	MeOOH + hν	$\rightarrow$ HO_2 + HCHO + OH	JPL [1990]
10	N_2O_5 + hν	$\rightarrow$ NO_3 + NO_2	IUPAC
11	NO_2 + hν	$\rightarrow$ NO + $O(^3P)$	JPL [1992]
12a	NO_3 + hν	$\rightarrow$ NO + O_2	IUPAC
12b	NO_3 + hν	$\rightarrow$ NO_2 + $O(^3P)$	IUPAC
14	O_2 + hν	$\rightarrow$ $O(^3P)$ + $O(^3P)$	IUPAC
15a	O_3 + hν	$\rightarrow$ O_2 + $O(^1D)$	IUPAC
15b	O_3 + hν	$\rightarrow$ O_2 + $O(^3P)$	IUPAC
17	PAN + hν	$\rightarrow$ $MeCO_3$ + NO_2	IUPAC [1999]
18	HONO + hν	$\rightarrow$ OH + NO	JPL [1992]
19	EtCHO + hν	$\rightarrow$ EtOO + HO_2 + CO	IUPAC [2002]
20	Me_2CO + hν	$\rightarrow$ $MeCO_3$ + MeOO	IUPAC [1999]
21	n-PrOOH + hν	$\rightarrow$ EtCHO + HO_2 + OH	JPL [1990]
22	i-PrOOH + hν	$\rightarrow$ Me_2CO + HO_2 + OH	JPL [1990]
23	$MeCOCH_2OOH$ + hν	$\rightarrow$ $MeCO_3$ + HCHO + OH	JPL [1990]
24	PPAN + hν	$\rightarrow$ $EtCO_3$ + NO_2	IUPAC
25	$MeONO_2$ + hν	$\rightarrow$ HO_2 + HCHO + NO_2	IUPAC
26a	TERPOOH + hν	$\rightarrow$ OH + HO_2 + MACR + MACR	JPL [1990]
26b	TERPOOH + hν	$\rightarrow$ TERPOOH + Me_2CO	JPL [1990]

Continued on next page

Table A.5 – continued from previous page

Reaction	Reactants	Products	Reference
28	ISOOH + hν	$\rightarrow$ OH + MACR + HCHO + HO_2	JPL [1990]
29	ISON + hν	$\rightarrow$ NO_2 + MACR + HCHO + HO_2	IUPAC [2002]
30	MACR + hν	$\rightarrow$ $MeCO_3$ + HCHO + CO + HO_2	IUPAC [2002]
31	MPAN + hν	$\rightarrow$ $MACRO_2$ + NO_2	
32a	MACROOH + hν	$\rightarrow$ OH + HO_2 + OH + HO_2	JPL [1990]
32b	MACROOH + hν	$\rightarrow$ HACET + CO + MGLY + HCHO	JPL [1990]
34	HACET + hν	$\rightarrow$ $MeCO_3$ + HCHO + HO_2	Orlando et. al., (1999)
35	MGLY + hν	$\rightarrow$ $MeCO_3$ + CO + HO_2 +	IUPAC [2002]
36	NALD + hν	$\rightarrow$ HCHO + CO + NO_2 + HO_2	Blitz et al., [2004]
37	$MeCO_3H$ + hν	$\rightarrow$ MeOO + OH	Orlando and Tyndall [2003]
38a	O_3S + hν	$\rightarrow$ O_2 + O(1D)S	IUPAC
38b	O_3S + hν	$\rightarrow$ O_2 + O(3P)S	IUPAC
40a	BtOOH + hν	$\rightarrow$ MEK + MEK + EtOO + MeCHO	JPL [1990]
40b	BtOOH + hν	$\rightarrow$ HO_2 + HO_2	JPL [1990]
40c	BtOOH + hν	$\rightarrow$ OH + OH + OH	JPL [1990]
43	MEK + hν	$\rightarrow$ $MeCO_3$ + EtOO	IUPAC
44	MeCOCOMe + hν	$\rightarrow$ $MeCO_3$ + $MeCO_3$	IUPAC
45	MEKOOH + hν	$\rightarrow$ $MeCO_3$ + MeCHO + OH	JPL [1990]
46a	ONIT + hν	$\rightarrow$ NO_2 + MEK + HO_2 + EtOO	IUPAC
46b	ONIT + hν	$\rightarrow$ MeCHO + ONIT	IUPAC
48a	AROMOOH + hν	$\rightarrow$ OH + Me_2CO + HO_2 + CO	JPL [1990]
48b	AROMOOH + hν	$\rightarrow$ $MeCO_3$ + AROMOOH	JPL [1990]

References

Folberth, G. A. and D.A Hauglustaine and J. Lathiere and F. Brocheton (2006), Interactive chemistry in the Laboratoire de Meteorologie Dynamique general circulation model: model description and impact analysis of biogenic hydrocarbons on tropospheric chemistry,*Atmos. Phys. Chem.*, 6, 2273–2319.

Evaluated Kinetic Data International Union of Pure and Applied Chemistry (IUPAC) (2006) *http://www.iupac-kineti.ch.cam.ac.uk/index.html*

Chemical Kinetics and Photochemical Data for Use in Atmospheric Studies, Jet Propulsion Laboratory (JPL), *http://jpldataeval.jpl.nasa.gov/download.html*

Master Chemical Mechanism (MCM), Leeds, UK *http://mcm.leeds.ac.uk/MCM/*

Orlando, J., G. Tyndall, J. Fracheboud, E. Estupiñan, S. Haberkorn, A. Zimmer (1999), The rate and mechanism of the gas-phase oxidation of hydroxyacetone, *Atmospheric Environment*, 33, 1621–1629.

P öschl, U., R. Von Kuhlmann, N. Poisson and P. J. Crutzen (2000), Development and Intercomparison of Condensed Isoprene Oxidation Mechanisms for Global Atmospheric Modeling, *Journal of Atmospheric Chemistry*, 37, 2952.

Orlando, J. and G. Tyndall (2003), Gas phase UV absorption spectra for peracetic acid, and for acetic acid monomers and dimers, *Journal of Photochemistry and Photobiology A: Chemistry*, 157 161–166.

Ravishankara, A. R. , E. J. Dunlea, M. A. Blitz, T. J. Dillon, D. E. Heard, M. J. Pilling, R. S. Strekowski, J. M. Nicovich, and P. H. Wine (2002), Redetermination of the rate coefficient for the reaction of O(D) with N, *Geophys Res Lett,*, 15, doi:10.1029/2002GL014850.

Tyndall, G., R. Cox, C. Granier, R. Lesclaux, G. Moortgat, M. Pilling, A. Ravishankara, and T. Wallington (2001), Atmospheric chemistry of small organic peroxy radicals, *J. Geophys. Res.*, 106, D11, doi:10.1029/2000JD900746.

Bibliography

ACIA, 2004: *ACIA, Impacts of a Warming Arctic: Arctic Climate Impact Assessment*. Cambridge University Press,.

ACIA, 2005: *Arctic Climate Impact Assessment - Scientific Report*, Cambridge University Press, New York, USA. 21–60.

Alvarado, M. J., J. A. Logan, J. Mao, E. Apel, D. Riemer, D. Blake, R. C. Cohen, K.-E. Min, A. E. Perring, E. C. Browne, P. J. Wooldridge, G. S. Diskin, G. W. Sachse, H. Fuelberg, W. R. Sessions, D. L. Harrigan, G. Huey, J. Liao, A. Case-Hanks, J. L. Jimenez, M. J. Cubison, S. A. Vay, A. J. Weinheimer, D. J. Knapp, D. D. Montzka, F. M. Flocke, I. B. Pollack, P. O. Wennberg, A. Kurten, J. Crounse, J. M. S. Clair, A. Wisthaler, T. Mikoviny, R. M. Yantosca, C. C. Carouge, and P. Le Sager, 2010: Nitrogen oxides and PAN in plumes from boreal fires during ARCTAS-B and their impact on ozone: an integrated analysis of aircraft and satellite observations. *Atmospheric Chemistry and Physics*, **10**, 9739–9760.

Ambaum, M., B. Hoskins, and D. Stephenson, 2001: Arctic Oscillation or North Atlantic Oscillation? *Journal of Climate*, **14**, 3495–3507.

Ancellet, G., J. Leclair de Bellevue, C. Mari, P. Nedelec, A. Kukui, A. Borbon, and P. Perros, 2009: Effects of regional-scale and convective transports on tropospheric ozone chemistry revealed by aircraft observations during the wet season of the AMMA campaign. *Atmospheric Chemistry and Physics*, **9**, 383–411.

Andreae, M. and P. Merlet, 2001: Emissions of trace gases and aerosols from biomass burning. *Global Biogeochemical Cycles*, **15**, 955–966.

Archibald, S., D. Roy, B. Van Wilgen, and R. Scholes, 2009: What limits fire? An examination of drivers of burnt area in Southern Africa. *Global Change Biology*, **15**, 613–630.

Arkin, P. A., 1982: The relationship between interannual variability in the 200 mb tropical wind field and the southern oscillation. *Monthly Weather Review*, **110**, 1393–1404.

Arnold, S. R., M. P. Chipperfield, and M. A. Blitz, 2005: A three-dimensional model study of the effect of new temperature-dependent quantum yields for acetone photolysis. *Journal of Geophysical Research*, **110**, D22305.

Atlas, E., R. BA, and C. CA, 2003: The tropospheric ozone production about the spring equinox (TOPSE) experiment: Introduction. *Journal of Geophysical Research*, **108**, doi:10.1029/2002JD003172.

Austin, J., 1980: The blocking of middle latitude westerly winds by planetary waves. *Quarterly Journal of the Royal Meteorological Society*, **106**, 327–350.

Balzter, H., F. F. Gerard, C. T. George, C. S. Rowland, T. E. Jupp, I. McCallum, A. Shvidenko, S. Nilsson, A. Sukhinin, A. Onuchin, and C. Schmullius, 2005: Impact of the arctic oscillation pattern on interannual forest fire variability in central siberia. *Geophys. Res. Lett.*, **32**, L14709.

Barnston, A. G. and R. E. Livezey, 1987: Classification, seasonality and persistence of low-frequency atmospheric circulation patterns. *Monthly Weather Review*, **115**, 1083–1126.

Barrie, L., J. Bottenheim, R. Schnell, P. Crutzen, and R. Rasmussen, 1988: Ozone destruction and photochemical reactions at polar sunrise in the lower arctic atmosphere. *Nature*, **334**, 138–141.

Barrie, L., M. Olson, and K. Oikawa, 1989: The flux of anthropogenic sulphur into the arctic from mid-latitudes in 1979/80. *Atmospheric Environment (1967)*, **23**, 2505 – 2512.

Barrie, L. A., 1986: Arctic air pollution: An overview of current knowledge. *Atmospheric Environment (1967)*, **20**, 643 – 663.

Beine, H. J., D. A. Jaffe, J. A. Herring, J. A. Kelley, T. Krognes, and F. Stordal, 1997: High-latitude springtime photochemistry. part I: NO_x, PAN and ozone relationships. *Journal of Atmospheric Chemistry*, **27**, 127–153.

Beine, H. J. and T. Krognes, 2000: The seasonal cycle of peroxyacetyl nitrate (PAN) in the european arctic. *Atmospheric Environment*, **34**, 933 – 940.

Bergamaschi, P., R. Hein, M. Heimann, and P. J. Crutzen, 2000: Inverse modeling of the global CO cycle 1. Inversion of CO mixing ratios. *Journal of Geophysical Research*, **105**, 1909–1927.

Berntsen, T. K., S. Karlsdttir, and D. A. Jaffe, 1999: Influence of Asian emissions on the composition of air reaching the north western United States. *Geophys. Res. Lett.*, **26**, 2171–2174.

Bethan, S. and G. Vaughan, 1998: Chemical air mass differences near fronts. *Journal of Geophysical Research*, **103**, 13413–13434.

Bindoff, N., J. Willebrand, V. Artale, C. A, J. Gregory, S. Gulev, K. Hanawa, C. L. Qur, S. Levitus, Y. Nojiri, C. Shum, L. Talley, and A. Unnikrishnan, 2007: *Observations: Oceanic Climate Change and Sea Level. In: Climate Change 2007: The Physical Science Basis. Contribution of Working Group I to the Fourth Assessment Report of the Intergovernmental Panel on Climate Change*, Cambridge University Press, Cambridge, United Kingdom and New York, NY, USA., chapter 5.

Bloss, W., M. Evans, J. Lee, R. Sommariva, D. Heard, and M. Pilling, 2005: The oxidative capacity of the troposphere: Coupling of field measurements of OH and a global chemistry transport model. *Farraday Discussions*, **130**, 425–436.

Bottenheim, J., A. Dastoor, S.-L. Gong, K. Higuchi, and Y.-F. Li, 2004: *Long Range Transport of Air Pollution to the Arctic in Intercontinental Transport of Air Pollution*, Springer-Verlag Berlin Heidelberg New York, volume 4.G of *The Handbook of Environmental Chemistry*, chapter 2. 13–39.

Bottenheim, J., A. Gallant, and K. Brice, 1986: Measurements of NO_y species and O_3 at 82°n latitude. *Geophys. Res. Let.*, **13**, 113–116.

Bottenheim, J. W., L. A. Barrie, and E. Atlas, 1993: The partitioning of nitrogen oxides in the lower Arctic troposphere during spring 1988. *Journal of Atmospheric Chemistry*, **17**, 15–27.

Bourgeois, Q. and I. Bey, 2011: Pollution transport efficiency toward the arctic: Sensitivity to aerosol scavenging and source regions. *Journal of Geophysical Research*, **116**, D08213.

Bowman, D. M. J. S., J. K. Balch, P. Artaxo, W. J. Bond, J. M. Carlson, M. A. Cochrane, C. M. DAntonio, R. S. DeFries, J. C. Doyle, S. P. Harrison, F. H. Johnston, J. E. Keeley, M. A. Krawchuk, C. A. Kull, J. B. Marston, M. A. Moritz, I. C. Prentice, C. I. Roos, A. C. Scott, T. W. Swetnam, G. R. van der Werf, and S. J. Pyne, 2009: Fire in the earth system. *Science*, **324**, 481–484.

Breider, T., 2010: *Coupled Halogen-Sulphur-Aerosol Modelling in a 3D Chemical Transport Model*. Ph.D. thesis, University of Leeds.

Browell, E. V., J. W. Hair, C. F. Butler, W. B. Grant, R. J. DeYoung, M. A. Fenn, V. G. Brackett, M. B. Clayton, L. A. Brasseur, D. B. Harper, B. A. Ridley, A. A. Klonecki, P. G. Hess, L. K. Emmons, X. Tie, E. L. Atlas, C. A. Cantrell, A. J. Wimmers, D. R. Blake, M. T. Coffey, J. W. Hannigan, J. E. Dibb, R. W. Talbot, F. Flocke, A. J. Weinheimer, A. Fried, B. Wert, J. A. Snow, and B. L. Lefer, 2003: Ozone, aerosol, potential vorticity, and trace gas trends observed at high-latitudes over north america from february to may 2000. *Journal of Geophysical Research*, **108**, doi:10.1029/2001JD001390.

Carver, G., P. Brown, and O. Wild, 1997: The asad atmospheric chemistry integration package and chemical reaction database. *Computer Physics Communications*, **105**, 197–215.

Chandra, S., J. Ziemke, W. Min, and W. Read, 1998: Effects of 1997-1998 El Nino on tropospheric ozone and water vapor. *Geophys. Res. Let.*, **25**, 3867–3870.

Chandra, S., J. R. Ziemke, B. N. Duncan, T. L. Diehl, N. J. Livesey, and L. Froidevaux, 2009: Effects of the 2006 El Nino on tropospheric ozone and carbon monoxide: implications for dynamics and biomass burning. *Atmospheric Chemistry and Physics*, **9**, 4239–4249.

Chipperfield, M. P., 2006: New version of the tomcat/slimcat off-line chemical transport model: Intercomparison of stratospheric tracer experiments. *Quarterly Journal of the Royal Meteorological Society*, **132**, 1179–1203.

Choi, Y., Y. Wang, T. Zeng, R. V. Martin, T. P. Kurosu, and K. Chance, 2005: Evidence of lightning nox and convective transport of pollutants in satellite observations over north america. *Geophys. Res. Lett.*, **32**, L02805.

Christensen, J., B. Hewitson, A. Busuioc, A. Chen, X. Gao, I. Held, R. Jones, R. Kolli, W.-T. Kwon, R. Laprise, V. M. Rueda, L. Mearns, C. Menndez, J. Risnen, A. Rinke, A. Sarr, and P. Whetton, 2007: *Regional Climate Projections. In: Climate Change 2007: The Physical Science Basis. Contribution of Working Group I to the Fourth Assessment Report of the Intergovernmental Panel on Climate Change*, Cambridge University Press, Cambridge, United Kingdom and New York, NY, USA., chapter 11.

Clark, P. U., N. G. Pisias, T. F. Stocker, and A. J. Weaver, 2002: The role of the thermohaline circulation in abrupt climate change. *Nature*, **415**, 863–869.

Cochrane, M. A., 2003: Fire science for rainforests. *Nature*, **421**, 913–919.

Conway, T. J., W. E. Raatz, and H. Richard, 1985: Airborne CO_2 measurements in the Arctic during spring 1983. *Atmospheric Environment (1967)*, **19**, 2195 – 2201.

Cook, P., H. Savage, S. Turquety, G. Carver, F. OConnor, A. Heckel, D. Stewart, L. Whalley, A. Parker, H. Schlager, H. Singh, M. Avery, G. Sachse, W. Brune, A. Richter, J. Burrows, R. Purvis, A. Lewis, C. Reeves, P. Monks, J. Levine, and J. Pyle, 2007: Forest fire plumes over the North Atlantic: p-TOMCAT model simulations with aircraft and satellite measurements from the ITOP/ICARTT campaign. *Journal of Geophysical Research*, **112**, D10S43.

Cooper, O. R., C. Forster, D. Parrish, M. Trainer, E. Dunlea, T. Ryerson, G. Hbler, F. Fehsenfeld, D. Nicks, J. Holloway, J. de Gouw, C. Warneke, J. M. Roberts, F. Flocke, and J. Moody, 2004: A case study of transpacific warm conveyor belt transport: Influence of merging airstreams on trace gas import to North America. *Journal of Geophysical Research*, **109**, D23S08.

Cooper, O. R., J. L. Moody, D. D. Parrish, M. Trainer, T. B. Ryerson, J. S. Holloway, G. Hbler, F. C. Fehsenfeld, S. J. Oltmans, and M. J. Evans, 2001: Trace gas signatures of the airstreams within North Atlantic cyclones: Case studies from the North Atlantic Regional Experiment (NARE '97) aircraft intensive. *Journal of Geophysical Research*, **106**, 5437–5456.

Crevoisier, C., E. Shevliakova, M. Gloor, C. Wirth, and S. Pacala, 2007: Drivers of fire in the boreal forests: Data constrained design of a prognostic model of burned area for use in dynamic global vegetation models. *Journal of Geophysical Research*, **112**, D24112.

Crutzen, P., 1973: A discussion of the chemistry of some minor constituents in the stratosphere and troposphere. *Pure and Applied Geophysics*, **106**, 1385–1399.

Damoah, R., N. Spichtinger, R. Servranckx, M. Fromm, E. W. Eloranta, I. A. Razenkov, P. James, M. Shulski, C. Forster, and A. Stohl, 2006: A case study of pyro-convection using transport model and remote sensing data. *Atmospheric Chemistry and Physics*, **6**, 173–185.

de Gouw, J. A., C. Warneke, H. A. Scheeren, C. van der Veen, M. Bolder, M. P. Scheele, J. Williams, S. Wong, L. Lange, H. Fischer, and J. Lelieveld, 2001: Overview of the trace gas measurements on board the citation aircraft during the intensive field phase of INDOEX. *Journal of Geophysical Research*, **106**, 28453–28467.

de Gouw, J. A., C. Warneke, A. Stohl, A. G. Wollny, C. A. Brock, O. R. Cooper, J. S. Holloway, M. Trainer, F. C. Fehsenfeld, E. L. Atlas, S. G. Donnelly, V. Stroud, and A. Lueb, 2006: Volatile organic compounds composition of merged and aged forest fire plumes from Alaska and western Canada. *Journal of Geophysical Research*, **111**, D10303.

Deeter, M., 2009: MOPITT (Measurements of Pollution in the Troposphere) validated version 4 product user's guide.

Deeter, M. N., D. P. Edwards, J. C. Gille, L. K. Emmons, G. Francis, S.-P. Ho, D. Mao, D. Masters, H. Worden, J. R. Drummond, and P. C. Novelli, 2010: The MOPITT version 4 CO product: Algorithm enhancements, validation, and long-term stability. *Journal of Geophysical Research*, **115**, D07306.

Dentener, F. J. and P. J. Crutzen, 1993: Reaction of N_2O_5 on Tropospheric Aerosols: Impact on the Global Distributions of NO*x*, O_3, and OH. *Journal of Geophysical Research*, **98**, 7149–7163.

Dibb, J. E., R. W. Talbot, E. Scheuer, G. Seid, L. DeBell, B. Lefer, and B. Ridley, 2003: Stratospheric influence on the northern North American free troposphere during TOPSE: 7Be as a stratospheric tracer. *Journal of Geophysical Research*, **108**, doi:10.1029/2001JD001347.

Dirksen, R. J., K. Folkert Boersma, J. de Laat, P. Stammes, G. R. van der Werf, M. Val Martin, and H. M. Kelder, 2009: An aerosol boomerang: Rapid around-the-world transport of smoke from the December 2006 Australian forest fires observed from space. *Journal of Geophysical Research*, **114**, D21201.

Doherty, R. M., D. S. Stevenson, C. E. Johnson, W. J. Collins, and M. G. Sanderson, 2006: Tropospheric ozone and El Nino-Southern Oscillation: Influence of atmospheric dynamics, biomass burning emissions, and future climate change. *Journal of Geophysical Researchs.*, **111**, doi:10.1029/2005JD006849.

Duncan, B., J. Logan, I. Bey, I. Megretskaia, R. Yantosca, P. Novelli, N. Jones, and C. Rinsland, 2007: Global budget of CO, 1988-1997: Source estimates and validation with a global model. *Journal of Geophysical Research*, **112**, D22301.

Duncan, B. N. and I. Bey, 2004: A modeling study of the export pathways of pollution from Europe: Seasonal and interannual variations (1987-1997). *Journal of Geophysical Research*, **109**, D08301.

Duncan, B. N. and J. A. Logan, 2008: Model analysis of the factors regulating the trends and variability of carbon monoxide between 1988 and 1997. *Atmospheric Chemistry and Physics*, **8**, 7389–7403.

Eckhardt, S., A. Stohl, S. Beirle, N. Spichtinger, P. James, C. Forster, C. Junker, T. Wagner, U. Platt, and S. Jennings, 2003: The North Atlantic Oscillation controls air pollution transport to the Arctic. *Atmospheric Chemistry and Physics*, **3**, 1769–1778.

Eckhardt, S., A. Stohl, H. Wernli, P. James, C. Forster, and N. Spichtinger, 2004: A 15-Year Climatology of Warm Conveyor Belts. *Journal of Climate*, **17**, 218–237.

Ehhalt, D., M. Prather, F. Dentener, R. Derwent, E. Dlugokencky, E. Holland, I. Isaksen, J. Katima, V. Kirchhoff, P. Matson, P. Midgley, and M. Wang, 2001: *Atmospheric Chemistry and Greenhouse Gases in Working Group I: The Scientific Basis.*, Cambridge University Press, Cambridge, United Kingdom and New York, NY, USA., chapter 4. 239.

Emmons, L., P. Hess, A. Klonecki, X. Tie, L. Horowitz, J. Lamarque, D. Kinnison, G. Brasseur, E. Atlas, E. Browell, C. Cantrell, F. Eisele, R. Mauldin, J. Merrill, B. Ridley, and R. Shetter, 2003: Budget of tropospheric ozone during TOPSE from two chemical transport models. *Journal of Geophysical Research*, **108**, doi:10.1029/2002JD002665.

Emmons, L., S.Walters, P. Hess, J.-F. Lamarque, G. Pfister, D. Fillmore, C. Granier, A. Guenther, D. Kinnison, T. Laepple, J. Orlando, X. Tie, G. Tyndall, C.Wiedinmyer, S. Baughcum, and S. Kloster, 2010: Description and evaluation of the Model for Ozone and Related chemical Tracers, version 4 (MOZART-4). *Geoscientific Model Development*, **3**, 43–67, doi:10.1029/2005GL022469.

Evans, M. and D. Jacob, 2005: Impact of new laboratory studies of N_2O_5 hydrolysis on global model budgets of tropospheric nitrogen oxides, ozone, and OH. *Geophys. Res. Let.*, **32**.

Feng, W., M. P. Chipperfield, S. Dhomse, B. M. Monge-Sanz, X. Yang, K. Zhang, and M. Ramonet, 2011: Evaluation of cloud convection and tracer transport in a three-dimensional chemical transport model. *Atmospheric Chemistry and Physics*, **11**, 5783–5803, doi:10.5194/acp-11-5783-2011.

Fischer, H., M. de Reus, M. Traub, J. Williams, J. Lelieveld, J. de Gouw, C. Warneke, H. Schlager, A. Minikin, R. Scheele, and P. Siegmund, 2003: Deep convective injection of boundary layer air into the lowermost stratosphere at midlatitudes. *Atmospheric Chemistry and Physics*, **3**, 739–745.

Fisher, J. A., D. J. Jacob, M. T. Purdy, M. Kopacz, P. Le Sager, C. Carouge, C. D. Holmes, R. M. Yantosca, R. L. Batchelor, K. Strong, G. S. Diskin, H. E. Fuelberg, J. S. Holloway, E. J. Hyer, W. W. McMillan, J. Warner, D. G. Streets, Q. Zhang, Y. Wang, and S. Wu, 2010: Source attribution and interannual variability of Arctic pollution in spring constrained by aircraft (ARCTAS, ARCPAC) and satellite (AIRS) observations of carbon monoxide. *Atmospheric Chemistry and Physics*, **10**, 977–996.

Fishman, J., V. Ramanathan, P. J. Crutzen, and S. C. Liu, 1979: Tropospheric ozone and climate. *Nature*, **282**, 818–820.

Flannigan, M., I. Campbell, M. Wotton, C. Carcaillet, P. Richard, and Y. Bergeron, 2001: Future fire in Canada's boreal forest: paleoecology results and general circulation model - regional climate model simulations. *Canadian Journal of Forest Research*, **31**, 854–864.

Flannigan, M. and C. Van Wagner, 1991: Climate change and wildfire in Canada. *Canadian Journal of Forest Research*, **21**, 66–72.

Folberth, G. A., D. Hauglustaine, J. Lathiere, and F. Brocheton, 2006: Interactive chemistry in the Laboratoire de Meteorologie Dynamique general circulation model: model description and impact analysis of biogenic hydrocarbons on tropospheric chemistry. *Atmospheric Chemistry and Physics*, **6**, 2273–2319.

Folland, C. K., J. Knight, H. W. Linderholm, D. Fereday, S. Ineson, and J. W. Hurrell, 2009: The Summer North Atlantic Oscillation: Past, Present, and Future. *Journal of Climate*, **22**, 1082–1103.

Forster, C., U. Wandinger, G. Wotawa, P. James, I. Mattis, D. Althausen, P. Simmonds, S. O'Doherty, C. Kleefield, S. Jennings, J. Schneider, T. Trickl, S. Kreipl, H. Jager, and A. Stohl, 2001: Transport of boreal forest fire emissions from Canada to Europe. *Journal of Geophysical Research*, **106**, 22887–22906.

Forster, P., V. Ramaswamy, P. Artaxo, T. Berntsen, R. Betts, D. Fahey, J. Haywood, J. Lean, D. Lowe, G. Myhre, J. Nganga, R. Prinn, G. Raga, M. Schulz, and R. V. Dorland, 2007: *Changes in Atmospheric Constituents and in Radiative Forcing. In: Climate Change 2007: The Physical Science Basis. Contribution of Working Group I to the Fourth Assessment Report of the Intergovernmental Panel on Climate Change*, Cambridge University Press, Cambridge, United Kingdom and New York, NY, USA., chapter 2.

French, N. H. F., P. Goovaerts, and E. S. Kasischke, 2004: Uncertainty in estimating carbon emissions from boreal forest fires. *Journal of Geophysical Research*, **109**, D14S08.

Fromm, M. D. and R. Servranckx, 2003: Transport of forest fire smoke above the tropopause by supercell convection. *Geophys. Res. Lett.*, **30**, doi:10.1029/2002GL016820.

Gavin, D. G., D. J. Hallett, F. S. Hu, K. P. Lertzman, S. J. Prichard, K. J. Brown, J. A. Lynch, P. Bartlein, and D. L. Peterson, 2007: Forest fire and climate change in western North America: insights from sediment charcoal records. *Frontiers in Ecology and the Environment*, **5**, 499–506.

Gerbig, C., S. Schmitgen, D. Kley, A. Volz-Thomas, K. Dewey, and D. Haaks, 1999: An improved fast-response vacuum-UV resonance fluorescence CO instrument. *Journal of Geophysical Research*, **104**, 1699–1704.

Giannakopoulos, C., M. P. Chipperfield, K. S. Law, and J. A. Pyle, 1999: Validation and intercomparison of wet and dry deposition schemes using 210Pb in a global three-dimensional off-line chemical transport model. *Journal of Geophysical Research*, **104**, 23761–23784.

Giglio, L., J. Descloitres, C. Justice, and Y. Kaufman, 2003: An enhanced contextual fire detection algorithm for MODIS. *Remote Sensing of the Environment*, **87**, 273–282.

Giglio, L., J. Randerson, G. van der Werf, P. Kasibhatla, G. Collatz, D. Morton, and R. DeFries, 2010: Assessing variability and long-term trends in burned area by merging multiple satellite fire products. *Biogeosciences*, **7**, 1171–1186.

Giglio, L., G. van der Werf, J. Randerson, G. Collatz, and P. Kasibhatla, 2006: Global estimation of burned area using MODIS active fire observations. *Atmospheric Chemistry and Physics*, **6**, 957–974.

Granier, C., J. Lamarque, A. Mieville, J. Muller, J. Olivier, J. Orlando, J. Peters, G. Petron, G. Tyndall, and S. Wallens, 2005: POET. http://www.aero.jussieu.fr/projet/ACCENT/POET.php.

Guenther, A., T. Karl, P. Harley, C. Wiedinmyer, P. Palmer, and C. Geron, 2006: Estimates of global terrestrial isoprene emissions using MEGAN (Model of Emissions of Gases and Aerosols from Nature). *Atmospheric Chemistry and Physics*, **6**, 3181–3210.

Hall, A. and X. Qu, 2006: Using the current seasonal cycle to constrain snow albedo feedback in future climate change. *Geophys. Res. Lett.*, **33**, L03502.

Halpert, M. and C. Ropelewski, 1992: Surface-temperature patterns associated with the Southern Oscillation. *Journal of Climate*, **5**, 577–593.

Hansen, J., M. Sato, and R. Ruedy, 1997: Radiative forcing and climate response. *Journal of Geophysical Research*, **102**, 6831–6864.

Harris, S., N. Tapper, D. Packham, B. Orlove, and N. Nicholls, 2008: The relationship between the monsoonal summer rain and dry-season fire activity of northern Australia. *International Journal of Wildland Fire*, **17**, 674–684.

Harriss, R. C., S. C. Wofsy, D. S. Bartlett, M. C. Shipham, D. J. Jacob, J. Hoell, J. M., R. J. Bendura, J. W. Drewry, R. J. McNeal, R. L. Navarro, R. N. Gidge, and V. E. Rabine, 1992: The Arctic Boundary Layer Expedition (ABLE 3A): July-August 1988. *Journal of Geophysical Research*, **97**, 16383–16394.

Harriss, R. C., S. C. Wofsy, J. Hoell, J. M., R. J. Bendura, J. W. Drewry, R. J. McNeal, D. Pierce, V. Rabine, and R. L. Snell, 1994: The Arctic Boundary Layer Expedition (ABLE-3B): July-August 1990. *Journal of Geophysical Research*, **99**, 1635–1643.

Hauglustaine, D. A., G. R. Brasseur, S. Walters, P. J. Rasch, J.-F. Mller, L. K. Emmons, and M. A. Carroll, 1998: MOZART, a global chemical transport model for ozone and related chemical tracers 2. Model results and evaluation. *Journal of Geophysical Research*, **103**, 28291–28335.

Heard, D. E. and M. J. Pilling, 2003: Measurement of OH and HO_2 in the troposphere. *Chemical Reviews*, **103**, 5163–5198.

Heintzenberg, J., 1989: Arctic Haze: Air Pollution in Polar Regions. *Ambio*, **18**, 50–55.

Helmig, D., S. J. Oltmans, D. Carlson, J.-F. Lamarque, A. Jones, C. Labuschagne, K. Anlauf, and K. Hayden, 2007: A review of surface ozone in the polar regions. *Atmospheric Environment*, **41**, 5138 – 5161.

Heyerdahl, E. K., P. Morgan, and J. P. Riser, 2008: Multi-season climate synchronized historical fires in dry forests (1650-1900), Northern Rockies, USA. *Ecology*, **89**, 705–716.

Holmgren, M., P. Stapp, C. R. Dickman, C. Gracia, S. Graham, J. R. Gutirrez, C. Hice, F. Jaksic, D. A. Kelt, M. Letnic, M. Lima, B. C. Lpez, P. L. Meserve, W. B. Milstead, G. A. Polis, M. A. Previtali, M. Richter, S. Sabat, and F. A. Squeo, 2006a: A synthesis of ENSO effects on drylands in Australia, North America and South America. *Advances in Geosciences*, **6**, 69–72.

Holmgren, M., P. Stapp, C. R. Dickman, C. Gracia, S. Graham, J. R. Gutirrez, C. Hice, F. Jaksic, D. A. Kelt, M. Letnic, M. Lima, B. C. Lpez, P. L. Meserve, W. B. Milstead, G. A. Polis, M. A. Previtali, M. Richter, S. Sabat, and F. A. Squeo, 2006b: Extreme climatic events shape arid and semiarid ecosystems. *Frontiers in Ecology and the Environment*, **4**, 87–95.

Holtslag, A. and B. Bolville, 1993: Local versus nonlocal boundary layer diffusion in a global climate model. *Journal of Climate*, **6**, 1825–1842.

Holzinger, R., C. Warneke, A. Hansel, A. Jordan, W. Lindinger, D. H. Scharffe, G. Schade, and P. J. Crutzen, 1999: Biomass burning as a source of formaldehyde, acetaldehyde, methanol, acetone, acetonitrile, and hydrogen cyanide. *Geophys. Res. Lett.*, **26**, 1161–1164.

Honda, M., H. Nakamura, J. Ukita, I. Kousaka, and K. Takeuchi, 2001: Interannual Seesaw between the Aleutian and Icelandic Lows. Part I: Seasonal Dependence and Life Cycle. *Journal of Climate*, **14**, 1029–1042.

Honrath, R. E., A. J. Hamlin, and J. T. Merrill, 1996: Transport of ozone precursors from the Arctic troposphere to the North Atlantic region. *Journal of Geophysical Research*, **101**, 29335–29351.

Honrath, R. E. and D. A. Jaffe, 1992: The Seasonal Cycle of Nitrogen Oxides in the Arctic Troposphere at Barrow, Alaska. *Journal of Geophysical Research*, **97**, 20615–20630.

Hooghiemstra, P. B., M. C. Krol, J. F. Meirink, P. Bergamaschi, G. R. van der Werf, P. C. Novelli, I. Aben, and T. Röckmann, 2011: Optimizing global CO emission estimates using a four-dimensional variational data assimilation system and surface network observations. *Atmospheric Chemistry and Physics*, **11**, 4705–4723.

Hough, A., 1988: The calculation of photolysis rates for use in global tropospheric modelling studies. *AERE Rep.*, **R-13259**.

Hough, A. M. and R. G. Derwent, 1990: Changes in the global concentration of tropospheric ozone due to human activities. *Nature*, **344**, 645–648.

Houghton, J., Y. Ding, D. Griggs, M. Noguer, P. van de Linden, X. Dai, K. Maskell, and C. Johnson, eds., 2001: *IPCC, Climate Change 2001: The Scientific Basis, Contribution of Working Group I to the Third Assesment Report of the Intergovernmental Panel on Climate Change*. Cambridge University Press, U.K. and New York, NY, USA.

Hov, O., S. A. Penkett, I. S. A. Isaksen, and A. Semb, 1984: Organic gases in the Norwegian Arctic. *Geophys. Res. Lett.*, **11**, 425–428.

Hoyle, C. R., V. Marécal, M. R. Russo, G. Allen, J. Arteta, C. Chemel, M. P. Chipperfield, F. D'Amato, O. Dessens, W. Feng, J. F. Hamilton, N. R. P. Harris, J. S. Hosking, A. C. Lewis, O. Morgenstern, T. Peter, J. A. Pyle, T. Reddmann, N. A. D. Richards, P. J. Telford, W. Tian, S. Viciani, A. Volz-Thomas, O. Wild, X. Yang, and G. Zeng, 2011: Representation of tropical deep convection in atmospheric models - part 2: Tracer transport. *Atmospheric Chemistry and Physics*, **11**, 8103–8131, doi:10.5194/acp-11-8103-2011.

Huntrieser, H., C. Feigl, H. Schlager, F. Schrder, C. Gerbig, P. van Velthoven, F. Flaty, C. Thry, A. Petzold, H. Hller, and U. Schumann, 2002: Airborne measurements of NO_x, tracer species, and small particles during the European Lightning Nitrogen Oxides Experiment. *Journal of Geophysical Research*, **107**, doi:10.1029/2000JD000209.

Hurrell, J., Y. Kushnir, G. Ottersen, and M. Visbeck, 2003: *Overview of the NAO in The North Atlantic Oscillation: Climate Significance and Environmental Impact*, volume 134 of *Geophysical Monograph Series*. 279 pp.

Hurrell, J. W. and C. Deser, 2010: North Atlantic climate variability: The role of the North Atlantic Oscillation. *Journal of Marine Systems*, **79**, 231 – 244.

IPCC, 2007: *IPCC, Climate Change 2007: The Physical Science Basis, Contribution of Working Group I to the Fourth Assessment Report of the IPCC*. Cambridge University Press, Cambridge, United Kingdom and New York, NY, USA.

Isaksen, I. and . Hov, 1987: Calculation of trends in the tropospheric concentration of O_3, OH, CO, CH_4 and NO_x. *Tellus B*, **39B**, 271–285.

Iversen, T., 1984: On the atmospheric transport of pollution to the Arctic. *Geophys. Res. Lett.*, **11**, 457–460.

Iversen, T. and E. Joranger, 1985: Arctic air pollution and large scale atmospheric flows. *Atmospheric Environment (1967)*, **19**, 2099–2108.

Jacob, D., 2000: Heterogenous chemistry and tropospheric ozone. *Atmospheric Environment*, **34**, 2131–2159.

Jacob, D., Q. B.D. Field, D. Blake, J. de Gouw, C. Warneke, A. Hansel, A. Wisthaler, H. B. Singh, and A. Guenther, 2005: Global budget of methanol: Constraints from atmospheric observations. *Journal of Geophysical Research*, **110**, D08303.

Jacob, D. J., 1999a: *Introduction to Atmospheric Chemistry*. Princeton University Press, Princeton, New Jersey.

Jacob, D. J., 1999b: *Ozone Pollution in Introduction to Atmospheric Chemistry*, Princeton University Press, Princeton, New Jersey., chapter 12. 237.

Jacob, D. J., 1999c: *Tropospheric Chemistry in Introduction to Atmospheric Chemistry*, Princeton University Press, Princeton, New Jersey., chapter 11. 200–219.

Jacob, D. J., J. H. Crawford, H. Maring, A. D. Clarke, J. E. Dibb, L. K. Emmons, R. A. Ferrare, C. A. Hostetler, P. B. Russell, H. B. Singh, A. M. Thompson, G. E. Shaw, E. McCauley, J. R. Pederson, and J. A. Fisher, 2010: The Arctic Research of the Composition of the Troposphere from Aircraft and Satellites (ARCTAS) mission: design, execution, and first results. *Atmospheric Chemistry and Physics*, **10**, 5191–5212.

Jacob, D. J., B. D. Field, E. M. Jin, I. Bey, Q. Li, J. A. Logan, R. M. Yantosca, and H. B. Singh, 2002: Atmospheric budget of acetone. *J. Geophys. Res.*, **107**, doi:10.1029/2001JD000694.

Jaeglé, L., D. J. Jacob, P. O. Wennberg, C. M. Spivakovsky, T. F. Hanisco, E. J. Lanzendorf, E. J. Hintsa, D. W. Fahey, E. R. Keim, M. H. Proffitt, E. L. Atlas, F. Flocke, S. Schauffler, C. T. McElroy, C. Midwinter, L. Pfister, and J. C. Wilson, 1997: Observed OH and HO_2 in the upper troposphere suggest a major source from convective injection of peroxides. *Geophys. Res. Lett.*, **24**, 3181–3184.

Jaeglé, L., D. A. Jaffe, H. U. Price, P. Weiss-Penzias, P. I. Palmer, M. J. Evans, D. J. Jacob, and I. Bey, 2003: Sources and budgets for CO and O_3 in the northeastern Pacific during the spring of 2001: Results from the PHOBEA–II Experiment. *J. Geophys. Res.*, **108**, 8802–, doi:10.1029/2002JD003121.

Jaffe, D., T. Anderson, D. Covert, R. Kotchenruther, B. Trost, J. Danielson, W. Simpson, T. Berntsen, S. Karlsdottir, D. Blake, J. Harris, G. Carmichael, and I. Uno, 1999: Transport of Asian air pollution to North America. *Geophys. Res. Lett.*, **26**, 711–714.

Jaffe, D. A., R. E. Honrath, J. A. Herring, S.-M. Li, and J. D. Kahl, 1991: Measurements of Nitrogen Oxides at Barrow, Alaska During Spring: Evidence for Regional and Northern Hemispheric Sources of Pollution. *J. Geophys. Res.*, **96**, 7395–7405.

JMA, 2009: Annual report on atmospheric and marine environment monitoring: Executive summary.

Johannessen, O., L. Bengtsson, M. Miles, S. Kuzmina, V. Semenov, G. Alekseev, A. Nagurnyi, V. Zakharov, L. Bobylev, L. Pettersson, K. Hasselmann, and H. Cattle, 2004: Arctic climate change: observed and modelled temperature and sea–ice variability. *Tellus A*, **56**, 328–341.

Julian, P. and R. Chervin, 1978: Study of Southern Oscillation and Walker Circulation Phenomenon. *Mon. Weather Rev.*, **106**, 1433–1451.

Kaiser, A., H. Scheifinger, W. Spangl, A. Weiss, S. Gilge, W. Fricke, L. Ries, D. Cemas, and B. Jesenovec, 2007: Transport of nitrogen oxides, carbon monoxide and ozone to the Alpine Global Atmosphere Watch stations Jungfraujoch (Switzerland), Zugspitze and Hohenpeissenberg (Germany), Sonnblick (Austria) and Mt. Krvavec (Slovenia). *Atmospheric Environment*, **41**, 9273 – 9287.

Kasischke, E. S., E. J. Hyer, P. C. Novelli, L. P. Bruhwiler, N. H. F. French, A. I. Sukhinin, J. H. Hewson, and B. J. Stocks, 2005: Influences of boreal fire emissions on Northern Hemisphere atmospheric carbon and carbon monoxide. *Global Biogeochem. Cycles*, **19**, GB1012.

Khalil, M. and R. Rasmussen, 1994: Global decrease in atmospheric carbon monoxide concentration. *Nature*, **370**, 639–641.

Khalil, M. A. K. and R. A. Rasmussen, 1984a: Carbon monoxide in the Earth's atmosphere: Increasing trend. *Science*, **224**, 54–56.

Khalil, M. A. K. and R. A. Rasmussen, 1984b: Statistical analysis of trace gases in Arctic haze. *Geophys. Res. Lett.*, **11**, 437–440.

Kiley, C. and H. Fuelberg, 2006: An examination of summertime cyclone transport processes during Intercontinental Chemical Transport Experiment (INTEX–A). *J. Geophys. Res.*, **111**, doi:10.1029/2006JD007115.

Kinnison, D. E., G. P. Brasseur, S. Walters, R. R. Garcia, D. R. Marsh, F. Sassi, V. L. Harvey, C. E. Randall, L. Emmons, J. F. Lamarque, P. Hess, J. J. Orlando, X. X. Tie, W. Randel, L. L. Pan, A. Gettelman, C. Granier, T. Diehl, U. Niemeier, and A. J. Simmons, 2007: Sensitivity of chemical tracers to meteorological parameters in the MOZART-3 chemical transport model. *J. Geophys. Res.*, **112**, D20302.

Kitzberger, T., T. W. Swetnam, and T. T. Veblen, 2001: Inter-hemispheric synchrony of forest fires and the El Nio–Southern Oscillation. *Global Ecology and Biogeography*, **10**, 315–326.

Klonecki, A., P. Hess, L. Emmons, L. Smith, J. Orlando, and D. Blake, 2003: Seasonal changes in the transport of pollutants into the Arctic troposphere–model study. *J. Geophys. Res.*, **108**, doi:10.1029/2001JD001390.

Koch, D. and J. Hansen, 2005: Distant origins of Arctic black carbon: A Goddard Institute for Space Studies ModelE experiment. *J. Geophys. Res.*, **110**, D04204.

Kopacz, M., D. J. Jacob, J. A. Fisher, J. A. Logan, L. Zhang, I. A. Megretskaia, R. M. Yantosca, K. Singh, D. K. Henze, J. P. Burrows, M. Buchwitz, I. Khlystova, W. W. McMillan, J. C. Gille, D. P. Edwards, A. Eldering, V. Thouret, and P. Nedelec, 2010: Global estimates of CO sources with high resolution by adjoint inversion of multiple satellite datasets (MOPITT, AIRS, SCIAMACHY, TES). *Atmospheric Chemistry and Physics*, **10**, 855–876.

Krol, M., P. J. van Leeuwen, and J. Lelieveld, 1998: Global OH trend inferred from methylchloroform measurements. *J. Geophys. Res.*, **103**, 10697–10711.

Kumar, K. K., B. Rajagopalan, and M. A. Cane, 1999: On the Weakening Relationship Between the Indian Monsoon and ENSO. *Science*, **284**, 2156–2159.

Lamarque, J.-F., T. Bond, V. E. C.Granier, A. Heil, Z. Klimont, D. Lee, C. Liousse, A. Mieville, B. Owen, M. Schultz, D. Shindel, S. Smith, E. Stehfest, J. Aardenne, O. Cooper, M. Kainuma, N. Mahowald, J. McConnell, V.Naik, K. Riahi, and D. van Vuuren, 2010: Historical (1850–2000) gridded anthropogenic and biomass burning emissions of reactive trace gases and aerosols: methodology and application. *Atmos. Chem. Phys.*, **10**, 7017–7039.

Landsea, C. W., 2000: *El Nino/Southern Oscillation and the Seasonal Predictability of Tropical Cyclones*, Cambridge University Press, chapter 5. 149–181.

Law, K., P.-H. Plantevin, D. Shallcross, H. Rogers, J. Pyle, C. Grouhel, V. Thouret, and A. Marenco, 1998: Evaluation of modeled O_3 using measurements of ozone by airbus in-service aircraft (MOZAIC) data. *J. Geophys. Res.*, **103**, 25721–25737.

Law, K. S. and A. Stohl, 2007: Arctic air pollution: Origins and impacts. *Science*, **315**, 1537–1540, doi:10.1126/science.1137695.

Lawrence, M., 2004: *Export of Air Pollution from Southern Asia and its Large Scale Effects in Intercontinental Transport of Air Pollution*, Springer-Verlag Berlin Heidelberg New York, chapter 6. 131–172.

Lawrence, M. G., P. Jöckel, and R. von Kuhlmann, 2001: What does the global mean OH concentration tell us? *Atmospheric Chemistry and Physics*, **1**, 37–49.

Le Goff, H., M. D. Flannigan, and Y. Bergeron, 2009: Potential changes in monthly fire risk in the eastern Canadian boreal forest under future climate change. *Canadian Journal of Forest Research*, **39**, 2369–2380.

Leathers, D., B. Yarnal, and M. Palecki, 1991: The Pacific/North American Teleconnection Pattern and United States Climate. Part I: Regional Temperature and Precipitation Associations. *Journal of Climate*, **4**, 517–528.

Lee, J. D., S. J. Moller, K. A. Read, A. C. Lewis, L. Mendes, and L. J. Carpenter, 2009: Year-round measurements of nitrogen oxides and ozone in the tropical North Atlantic marine boundary layer. *J. Geophys. Res.*, **114**, D21302.

Legrand, M., M. De Angelis, T. Staffelbach, A. Neftel, and B. Stauffer, 1992: Large perturbations of ammonium and organic acids content in the summit Greenland Ice Core. Fingerprint from forest fires? *Geophys. Res. Lett.*, **19**, 473–475.

Levy, I., H., W. J. Moxim, and R. S. Kasibhatla, 1996: A global three-dimensional time-dependent lightning source of tropospheric NO_x. *J. Geophys. Res.*, **101**, 22911–22922.

Li, J., R. Yu, and T. Zhou, 2008: Teleconnection between NAO and Climate Downstream of the Tibetan Plateau. *J. Climate*, **21**, 4680–4690.

Liang, Q., A. R. Douglass, B. N. Duncan, R. S. Stolarski, and J. C. Witte, 2009: The governing processes and timescales of stratosphere–to–troposphere transport and its contribution to ozone in the Arctic troposphere. *Atmospheric Chemistry and Physics*, **9**, 3011–3025.

Liang, Q., J. M. Rodriguez, A. R. Douglass, J. H. Crawford, E. Apel, H. Bian, D. R. Blake, W. Brune, M. Chin, P. R. Colarco, A. da Silva, G. S. Diskin, B. N. Duncan, L. G. Huey, D. J. Knapp, D. D. Montzka, J. E. Nielsen, J. R. Olson, S. Pawson, A. J. Weinheimer, and D. D. Reimer, 2011: Reactive nitrogen, ozone and ozone production in the Arctic troposphere and the impact of stratosphere–troposphere exchange. *Atmospheric Chemistry and Physics Discussions*, **11**, 10721–10767.

Liu, H., D. J. Jacob, I. Bey, R. M. Yantosca, B. N. Duncan, and G. W. Sachse, 2003: Transport pathways for Asian pollution outflow over the Pacific: Interannual and seasonal variations. *Journal of Geophysical Research*, **108**, doi:10.1029/2002JD003102.

Liu, S. C., M. Trainer, F. C. Fehsenfeld, D. D. Parrish, E. J. Williams, D. W. Fahey, G. Hbler, and P. C. Murphy, 1987: Ozone Production in the Rural Troposphere and the Implications for Regional and Global Ozone Distributions. *Journal of Geophysical Research*, **92**, 4191–4207.

Logan, J. A., 1985: Tropospheric ozone: Seasonal behavior, trends, and anthropogenic influence. *Journal of Geophysical Research*, **90**, 10463–10482.

Logan, J. A., I. Megretskaia, R. Nassar, L. T. Murray, L. Zhang, K. W. Bowman, H. M. Worden, and M. Luo, 2008: Effects of the 2006 El Nino on tropospheric composition as revealed by data from the Tropospheric Emission Spectrometer (TES). *Geophys. Res. Let.*, **35**, doi:10.1029/2007GL031698.

Logan, M. J. P. S. C. W., J. A. and M. B. McElroy, 1981: Tropospheric Chemistry: A Global Perspective. *Journal of Geophysical Research*, **86**, 7210–7254.

Macintyre, H., 2010: *Heterogeneous Chemistry in the Troposphere: A Chemical Indirect Effect*. Ph.D. thesis, University of Leeds.

Macintyre, H. and M. Evans, 2010: Sensitivity of a global model to the uptake of N_2O_5 by tropospheric aerosol. *Atmospheric Chemistry and Physics*, **10**, 7409–7414.

Mann, G., K. S. Carslaw, D. V. Spracklen, D. A. Ridley, P. T. Manktelow, M. P. Chipperfield, S. J. Pickering, , and C. E. Johnson, 2010: Description and evaluation of GLOMAP–mode: a modal global aerosol microphysics model for the UKCA composition-climate model. *Geoscientific Model Development*, **3**, 519–551.

Mao, J., D. J. Jacob, M. J. Evans, J. R. Olson, X. Ren, W. H. Brune, J. M. S. Clair, J. D. Crounse, K. M. Spencer, M. R. Beaver, P. O. Wennberg, M. J. Cubison, J. L. Jimenez, A. Fried, P. Weibring, J. G. Walega, S. R. Hall, A. J. Weinheimer, R. C. Cohen, G. Chen, J. H. Crawford, C. McNaughton, A. D. Clarke, L. Jaeglé, J. A. Fisher, R. M. Yantosca, P. Le Sager, and C. Carouge, 2010: Chemistry of hydrogen oxide radicals (HO_x) in the Arctic troposphere in spring. *Atmospheric Chemistry and Physics*, **10**, 5823–5838.

McCabe, G., M. Clark, and M. Serreze, 2001: Trends in Northern Hemisphere surface cyclone frequency and intensity. *Journal of Climate*, **14**, 2763–2768.

McKenzie, D., Z. Gedalof, D. Peterson, and P. Mote, 2004: Climatic change, wildfire, and conservation. *Conservation Biology*, **18**, 890–902.

McPhaden, M. J., S. E. Zebiak, and M. H. Glantz, 2006: ENSO as an Integrating Concept in Earth Science. *Science*, **314**, 1740–1745.

Meehl, G., T. Stocker, W. Collins, P. Friedlingstein, A. Gaye, J. Gregory, A. Kitoh, R. Knutti, J. Murphy, A. Noda, S. Raper, I. Watterson, A. Weaver, and Z.-C. Zhao, 2007: *Global Climate Projections. In: Climate Change 2007: The Physical Science Basis. Contribution of Working Group I to the Fourth Assessment Report of the Intergovernmental Panel on Climate Change.*, Cambridge University Press, Cambridge, United Kingdom and New York, NY, USA., chapter 10.

Mogili, P. K., P. D. Kleiber, M. A. Young, and V. H. Grassian, 2006: N_2O_5 hydrolysis on the components of mineral dust and sea salt aerosol: Comparison study in an environmental aerosol reaction chamber. *Atmospheric Environment*, **40**, 7401 – 7408.

Monks, P. S., 2000: A review of the observations and origins of the spring ozone maximum. *Atmospheric Environment*, **34**, 3545 – 3561.

Montzka, S. A., M. Krol, E. Dlugokencky, B. Hall, P. Jckel, and J. Lelieveld, 2011: Small interannual variability of global atmospheric hydroxyl. *Science*, **331**, 67–69.

Moxim, W. J., I. Levy, H., and P. S. Kasibhatla, 1996: Simulated global tropospheric PAN: Its transport and impact on NO_x. *Journal of Geophysical Research*, **101**, 12621–12638.

Müller, J.-F. and G. Brasseur, 1999: Sources of upper tropospheric HO_x: A three–dimensional study. *Journal of Geophysical Research*, **104**, 1705–1715.

Murayama, S., S. Taguchi, and K. Higuchi, 2004: Interannual variation in the atmospheric CO_2 growth rate: Role of atmospheric transport in the Northern Hemisphere. *Journal of Geophysical Research*, **109**, doi:10.1029/2003JD003729.

Nassar, R., J. A. Logan, I. A. Megretskaia, L. T. Murray, L. Zhang, and D. B. A. Jones, 2009: Analysis of tropical tropospheric ozone, carbon monoxide, and water vapor during the 2006 El Nino using TES observations and the GEOS–Chem model. *Journal of Geophysical Research*, **114**, doi:10.1029/2009JD011760.

Nedelec, P., J.-P. Cammas, V. Thouret, G. Athier, J.-M. Cousin, C. Legrand, C. Abonnel, F. Lecoeur, G. Cayez, and C. Marizy, 2003: An improved infrared carbon monoxide analyser for routine measurements aboard commercial Airbus aircraft: technical validation and first scientific results of the MOZAIC III programme. *Atmospheric Chemistry and Physics*, **3**, 1551–1564.

Nicholls, N., 2004: The Changing Nature of Australian Droughts. *Climatic Change*, **63**, 323–336.

Novelli, P., K. Masarie, and P. Lang, 1998: Distributions and recent changes of carbon monoxide in the lower troposphere. *Journal of Geophysical Research*, **103**, 19015–19033.

Ohara, T., H. Akimoto, J. Kurokawa, N. Horii, K. Yamaji, X. Yan, and T. Hayasaka, 2007: An Asian emission inventory of anthropogenic emission sources for the period 1980–2020. *Atmospheric Chemistry and Physics*, **7**, 4419–4444.

Oltmans, S., A. Lefohn, J. Harris, I. Galbally, H. Scheel, G. Bodeker, E. Brunke, H. Claude, D. Tarasick, B. Johnson, P. Simmonds, D. Shadwick, K. Anlauf, K. Hayden, F. Schmidlin, T. Fujimoto, K. Akagi, C. Meyer, S. Nichol, J. Davies, A. Redondas, and E. Cuevas, 2006: Long–term changes in tropospheric ozone. *Atmospheric Environment*, **40**, 3156 – 3173, doi:10.1016/j.atmosenv.2006.01.029.

Oltmans, S., R. Schnell, P. Sheridan, R. Peterson, S.-M. Li, J. Winchester, P. Tans, W. Sturges, J. Kahl, and L. Barrie, 1989: Seasonal surface ozone and filterable bromine relationship in the high arctic. *Atmospheric Environment (1967)*, **23**, 2431–2441.

Oltmans, S. J., A. S. Lefohn, H. E. Scheel, J. M. Harris, I. Levy, H., I. E. Galbally, E. Brunke, C. P. Meyer, J. A. Lathrop, B. J. Johnson, D. S. Shadwick, E. Cuevas, F. J. Schmidlin, D. W. Tarasick, H. Claude, J. B. Kerr, O. Uchino, and V. Mohnen, 1998: Trends of ozone in the troposphere. *Geophys. Res. Lett.*, **25**, 139–142.

Pacyna, J. and B. Ottar, 1989: Origin of natural constituents in the Arctic aerosol. *Atmospheric Environment (1967)*, **23**, 809 – 815.

Pacyna, J. M., 1995: The origin of Arctic air pollutants: lessons learned and future research. *Science of The Total Environment*, **160-161**, 39 – 53.

Pacyna, J. M. and B. Ottar, 1985: Transport and chemical composition of the summer aerosol in the Norwegian Arctic. *Atmospheric Environment (1967)*, **19**, 2109 – 2120.

Page, S. E., F. Siegert, J. O. Rieley, H.-D. V. Boehm, A. Jaya, and S. Limin, 2002: The amount of carbon released from peat and forest fires in Indonesia during 1997. *Nature*, **420**, 61–65.

Paris, J.-D., P. Ciais, P. Nedelec, M. Ramonet, B. D. Belan, M. Y. Arshinov, G. S. Golitsyn, I. Granberg, A. Stohl, G. Cayez, G. Athier, F. Boumard, and J.-M. Cousin, 2008: The YAK–AEROSIB transcontinental aircraft campaigns: new insights on the transport of CO_2, CO and O_3 across Siberia. *Tellus B*, **60**, 551–568.

Paris, J.-D., A. Stohl, P. Nédélec, M. Y. Arshinov, M. V. Panchenko, V. P. Shmargunov, K. S. Law, B. D. Belan, and P. Ciais, 2009: Wildfire smoke in the Siberian Arctic in summer: source characterization and plume evolution from airborne measurements. *Atmospheric Chemistry and Physics*, **9**, 9315–9327.

Park, M., W. J. Randel, L. K. Emmons, and N. J. Livesey, 2009: Transport pathways of carbon monoxide in the Asian summer monsoon diagnosed from Model of Ozone and Related Tracers (MOZART). *Journal of Geophysical Research*, **114**, D08303.

Parrish, D. D., J. S. Holloway, M. Trainer, P. C. Murphy, F. C. Fehsenfeld, and G. L. Forbes, 1993: Export of North American Ozone Pollution to the North Atlantic Ocean. *Science*, **259**, 1436–1439.

Patra, P. K., S. Houweling, M. Krol, P. Bousquet, D. Belikov, D. Bergmann, H. Bian, P. Cameron-Smith, M. P. Chipperfield, K. Corbin, A. Fortems-Cheiney, A. Fraser, E. Gloor, P. Hess, A. Ito, S. R. Kawa, R. M. Law, Z. Loh, S. Maksyutov, L. Meng, P. I. Palmer, R. G. Prinn, M. Rigby, R. Saito, and C. Wilson, 2011: TransCom model simulations of CH_4 and related species: linking transport, surface flux and chemical loss with CH_4 variability in the troposphere and lower stratosphere. *Atmospheric Chemistry and Physics Discussions*, **11**, 18767–18821.

Penkett, S. and K. Brice, 1986: The spring maximum in photo-oxidants in the Northern Hemisphere troposphere. *Nature*, **319**, 655 – 657.

Phadnis, M. J., I. Levy, Hiram, and W. J. Moxim, 2002: On the evolution of pollution from South and Southeast Asia during the winter-spring monsoon. *Journal of Geophysical Research*, **107**, doi:10.1029/2002JD002190.

Pöschl, U., R. von Kuhlmann, N. Poisson, and P. J. Crutzen, 2000: Development and intercomparison of condensed isoprene oxidation mechanisms for global atmospheric modeling. *Journal of Atmospheric Chemistry*, **37**, 29–52.

Prather, M., 1986: Numerical advection by conservation of second–order moments. *Journal of Geophysical Research*, **91**, 6671–6681.

Price, C. and D. Rind, 1994: Possible implications of global climate change on global lightning distributions and frequencies. *Journal of Geophysical Research*, **99**, 10823–10831.

Prinn, R. G., J. Huang, R. F. Weiss, D. M. Cunnold, P. J. Fraser, P. G. Simmonds, A. McCulloch, C. Harth, P. Salameh, S. O'Doherty, R. H. J. Wang, L. Porter, and B. R. Miller, 2001: Evidence for substantial variations of atmospheric hydroxyl radicals in the past two decades. *Science*, **292**, 1882–1888.

Prinn, R. G., R. F. Weiss, B. R. Miller, J. Huang, F. N. Alyea, D. M. Cunnold, P. J. Fraser, D. E. Hartley, and P. G. Simmonds, 1995: Atmospheric Trends and Lifetime of CH_3CCI_3 and Global OH Concentrations. *Science*, **269**, 187–192.

Przybylak, R., 2003: *Air Pollution In The Climate of the Arctic*, Kluwer Academic Publishers, Dordrecht, Boston and London., chapter 8. 141–148.

Purvis, R. M., A. C. Lewis, R. A. Carney, J. B. McQuaid, S. R. Arnold, J. Methven, H. Barjat, K. Dewey, J. Kent, P. S. Monks, L. J. Carpenter, N. Brough, S. A. Penkett, and C. E. Reeves, 2003: Rapid uplift of nonmethane hydrocarbons in a cold front over central Europe. *Journal of Geophysical Research*, **108**, 4224–.

Quinn, P., T. Bates, N. Baum, E. Doubleday, M. Fiore, A.M. Flanner, A. Fridlind, T. Garrett, D. Koch, D. Menon, S. Shindell, A. Stohl, and S. Warren, 2008: Short-lived pollutants in the Arctic: their climate impact and possible mitigation strategies. *Atmospheric Chemistry and Physics*, **8**, 1723–1735.

Quinn, P. K., G. Shaw, E. Andrews, E. G. Dutton, T. Ruoho-Ailrola, and S. L. Gong, 2007: Arctic haze: current trends and knowledge gaps. *Tellus B*, **59**, 99–114, doi:10.1111/j.1600-0889.2006.00238.x.

Raatz, W. E., 1989: An anticyclonic point of view on low-level tropospheric long–range transport. *Atmospheric Environment (1967)*, **23**, 2501 – 2504.

Raatz, W. E. and G. E. Shaw, 1984: Long-Range Tropospheric Transport of Pollution Aerosols into the Alaskan Arctic. *Journal of Climate and Applied Meteorolgy*, **23**, 1052–1064.

Rahmstorf, S., 2000: The Thermohaline Ocean Circulation: A System with Dangerous Thresholds? *Climatic Change*, **46**, 247–256.

Rahn, K., 1981: The Mn/V ratio as a tracer of large-scale sources of pollution aerosol for the Arctic. *Atmospheric Environment (1967)*, **15**, 1457 – 1464.

Rahn, K. A., 1985: Progress in Arctic air chemistry, 1980-1984. *Atmospheric Environment (1967)*, **19**, 1987 – 1994, doi:DOI: 10.1016/0004-6981(85)90107-6.

Ravishankara, A. R., 1997: Heterogeneous and multiphase chemistry in the troposphere. *Science*, **276**, 1058–1065.

Rayner, N. A., D. E. Parker, E. B. Horton, C. K. Folland, L. V. Alexander, D. P. Rowell, E. C. Kent, and A. Kaplan, 2003: Global analyses of sea surface temperature, sea ice, and night marine air temperature since the late nineteenth century. *Journal of Geophysical Research*, **108**, doi:10.1029/2002JD002670.

Read, K. A., A. S. Mahajan, L. J. Carpenter, M. J. Evans, B. V. E. Faria, D. E. Heard, J. R. Hopkins, J. D. Lee, S. J. Moller, A. C. Lewis, L. Mendes, J. B. McQuaid, H. Oetjen, A. Saiz-Lopez, M. J. Pilling, and J. M. C. Plane, 2008: Extensive halogen-mediated ozone destruction over the tropical Atlantic Ocean. *Nature*, **453**, 1232–1235.

Real, E., K. S. Law, B. Weinzierl, M. Fiebig, A. Petzold, O. Wild, J. Methven, S. Arnold, A. Stohl, H. Huntrieser, A. Roiger, H. Schlager, D. Stewart, M. Avery, G. Sachse, E. Browell, R. Ferrare, and D. Blake, 2007: Processes influencing ozone levels in Alaskan forest fire plumes during long-range transport over the North Atlantic. *Journal of Geophysical Research*, **112**, D10S41.

Reynolds, R., 2004: *Global Weather In Guide To Weather*, Phillips, chapter 2. 24–55.

Ridley, B., T. Zeng, Y. Wang, E. Atlas, E. Browell, P. Hess, J. Orlando, K. Chance, and A. Richter, 2007: An ozone depletion event in the sub-arctic surface layer over hudson bay, canada. *Journal of Atmospheric Chemistry*, **57**, 255–280, 10.1007/s10874-007-9072-z.

Rogers, J. and H. Van Loon, 1979: Seesaw in winter temperatures between Greenland and northern Europe .2. some oceanic and atmospheric effects in middle and high-latitudes. *Monthly Weather Review*, **107**, 509–519.

Roiger, A., H. Aufmhoff, P. Stock, F. Arnold, and H. Schlager, 2011a: An aircraft-borne chemical ionization; ion trap mass spectrometer (CI-ITMS) for fast PAN and PPN measurements. *Atmospheric Measurement Techniques*, **4**, 173–188.

Roiger, A., H. Schlager, A. Schäfler, H. Huntrieser, M. Scheibe, H. Aufmhoff, O. R. Cooper, H. Sodemann, A. Stohl, J. Burkhart, M. Lazzara, C. Schiller, K. S. Law, and F. Arnold, 2011b: In-situ observation of Asian pollution transported into the Arctic lowermost stratosphere. *Atmospheric Chemistry and Physics Discussions*, **11**, 16265–16310.

Ropelewski, C. and M. Halpert, 1986: North-American precipitation and temperature patterns associated with the El Niño Southern Oscillation (ENSO). *Monthly Weather Review*, **114**, 2352–2362.

Schnell, R. C., 1984: Arctic haze and the Arctic Gas and Aerosol Sampling Program (AGASP). *Geophys. Res. Lett.*, **11**, 361–364.

Schnell, R. C. and W. E. Raatz, 1984: Vertical and horizontal characteristics of Arctic haze during AGASP: Alaskan Arctic. *Geophys. Res. Lett.*, **11**, 369–372.

Seiler, W. and P. Crutzen, 1980: Estimates of gross and net fluxes of carbon between the biosphere and the atmosphere from biomass burning. *Climatic Change*, **2**, 207–247.

Seinfeld, J. H. and S. N. Pandis, 2006: *Chemistry of the Troposhere In Atmospheric Chemistry and Physics - From Air Pollution to Climate Change*, Wiley-Interscience Publications, chapter 6. 2nd edition, 205–283.

Serreze, M. and R. Barry, 2005: *Physical characteristics and basic climatic feactures in The Arctic Climate System*, Cambridge University Press, Cambridge., chapter 2. 17–54.

Serreze, M. and J. Francis, 2006: The Arctic amplification debate. *Climatic Change*, **76**, 241–264.

Sharma, S., E. Andrews, L. A. Barrie, J. A. Ogren, and D. Lavoue, 2006: Variations and sources of the equivalent black carbon in the high Arctic revealed by long-term observations at Alert and Barrow: 1989-2003. *Journal of Geophysical Research*, **111**, doi:10.1029/2005JD006581.

Shaw, G. E., 1995: The Arctic Haze Phenomenon. *Bulletin of the American Meteorological Society*, **76**, 2403–2413.

Shindell, D., 2007: Local and remote contributions to Arctic warming. *Geophys. Res. Lett.*, **34**, L14704.

Shindell, D. and G. Faluvegi, 2009: Climate response to regional radiative forcing during the twentieth century. *Nature Geoscience*, **2**, 294–300.

Shindell, D., G. Faluvegi, A. Lacis, J. Hansen, R. Ruedy, and E. Aguilar, 2006a: Role of tropospheric ozone increases in 20th-century climate change. *Journal of Geophysical Research*, **111**, D08302.

Shindell, D. T., M. Chin, F. Dentener, R. M. Doherty, G. Faluvegi, A. M. Fiore, P. Hess, D. M. Koch, I. A. MacKenzie, M. G. Sanderson, M. G. Schultz, M. Schulz, D. S. Stevenson, H. Teich, C. Textor, O. Wild, D. J. Bergmann, I. Bey, H. Bian, C. Cuvelier, B. N. Duncan, G. Folberth, L. W. Horowitz, J. Jonson, J. W. Kaminski, E. Marmer, R. Park, K. J. Pringle, S. Schroeder, S. Szopa, T. Takemura, G. Zeng, T. J. Keating, and A. Zuber, 2008: A multi-model assessment of pollution transport to the Arctic. *Atmospheric Chemistry and Physics*, **8**, 5353–5372.

Shindell, D. T., G. Faluvegi, D. S. Stevenson, M. C. Krol, L. K. Emmons, J.-F. Lamarque, G. Ptron, F. J. Dentener, K. Ellingsen, M. G. Schultz, O. Wild, M. Amann, C. S. Atherton, D. J. Bergmann, I. Bey, T. Butler, J. Cofala, W. J. Collins, R. G. Derwent, R. M. Doherty, J. Drevet, H. J. Eskes, A. M. Fiore, M. Gauss, D. A. Hauglustaine, L. W. Horowitz, I. S. A. Isaksen, M. G. Lawrence, V. Montanaro, J.-F. Mller, G. Pitari, M. J. Prather, J. A. Pyle, S. Rast, J. M. Rodriguez, M. G. Sanderson, N. H. Savage, S. E. Strahan, K. Sudo, S. Szopa, N. Unger, T. P. C. van Noije, and G. Zeng, 2006b: Multimodel simulations of carbon monoxide: Comparison with observations and projected near-future changes. *Journal of Geophysical Research*, **111**, D19306.

Simpson, W. R., R. von Glasow, K. Riedel, P. Anderson, P. Ariya, J. Bottenheim, J. Burrows, L. J. Carpenter, U. Frieß, M. E. Goodsite, D. Heard, M. Hutterli, H.-W. Jacobi, L. Kaleschke, B. Neff, J. Plane, U. Platt, A. Richter, H. Roscoe, R. Sander, P. Shepson, J. Sodeau, A. Steffen,

T. Wagner, and E. Wolff, 2007: Halogens and their role in polar boundary-layer ozone depletion. *Atmospheric Chemistry and Physics*, **7**, 4375–4418.

Singh, H. B., D. O'Hara, D. Herlth, J. D. Bradshaw, S. T. Sandholm, G. L. Gregory, G. W. Sachse, D. R. Blake, P. J. Crutzen, and M. A. Kanakidou, 1992: Atmospheric Measurements of Peroxyacetyl Nitrate and other Organic Nitrates at High Latitudes: Possible Sources and Sinks. *Journal of Geophysical Research*, **97**, 16511–16522.

Sodemann, H., M. Pommier, S. R. Arnold, S. A. Monks, K. Stebel, J. F. Burkhart, J. W. Hair, G. S. Diskin, C. Clerbaux, P. F. Coheur, D. Hurtmans, H. Schlager, A. M. Blechschmidt, J. E. Kristjansson, and A. Stohl, 2011: Episodes of cross-polar transport in the Arctic troposphere during July 2008 as seen from models, satellite, and aircraft observations. *Atmospheric Chemistry and Physics*, **11**, 3631–3651.

Soja, A. J., N. M. Tchebakova, N. H. French, M. D. Flannigan, H. H. Shugart, B. J. Stocks, A. I. Sukhinin, E. Parfenova, F. S. C. III, and P. W. S. Jr., 2007: Climate-induced boreal forest change: Predictions versus current observations. *Global and Planetary Change*, **56**, 274 – 296.

Solberg, S., N. Schmidbauer, A. Semb, F. Stordal, and . Hov, 1996: Boundary-layer ozone depletion as seen in the norwegian arctic in spring. *Journal of Atmospheric Chemistry*, **23**, 301–332.

Solomon, S., D. Qin, M. Manning, R. Alley, T. Berntsen, N. Bindoff, Z. Chen, A. Chidthaisong, J. Gregory, G. Hegerl, M. Heimann, B. Hewitson, B. Hoskins, F. Joos, J. Jouzel, V. Kattsov, U. Lohmann, T. Matsuno, M. Molina, N. Nicholls, J. Overpeck, G. Raga, V. Ramaswamy, J. Ren, M. Rusticucci, R. Somerville, T. Stocker, P. Whetton, R. Wood, and D. Wratt, 2007: *Technical Summary. In: Climate Change 2007: The Physical Science Basis. Contribution of Working Group I to the Fourth Assessment Report of the Intergovernmental Panel on Climate Change.*, Cambridge University Press, Cambridge, United Kingdom and New York, NY, USA.

Spivakovsky, C. M., J. A. Logan, S. A. Montzka, Y. J. Balkanski, M. Foreman-Fowler, D. B. A. Jones, L. W. Horowitz, A. C. Fusco, C. A. M. Brenninkmeijer, M. J. Prather, S. C. Wofsy, and M. B. McElroy, 2000: Three-dimensional climatological distribution of tropospheric OH: Update and evaluation. *Journal of Geophysical Research*, **105**, 8931–8980.

Staudt, A., D. Jacob, J. Logan, D. Bachiochi, T. Krishnamurti, and G. Sachse, 2001: Continental sources, transoceanic transport, and interhemispheric exchange of carbon monoxide over the Pacific. *Journal of Geophysical Research*, **106**, 32571–32589.

Stephenson, D., V. Pavan, M. Collins, M. Junge, R. Quadrelli, and , 2006: North Atlantic Oscillation response to transient greenhouse gas forcing and the impact on European winter climate: a CMIP2 multi-model assessment. *Climate Dynamics*, **27**, 401–420, 10.1007/s00382-006-0140-x.

Stevenson, D. S., F. J. Dentener, M. G. Schultz, K. Ellingsen, T. P. C. van Noije, O. Wild, G. Zeng, M. Amann, C. S. Atherton, N. Bell, D. J. Bergmann, I. Bey, T. Butler, J. Cofala, W. J. Collins, R. G. Derwent, R. M. Doherty, J. Drevet, H. J. Eskes, A. M. Fiore, M. Gauss, D. A. Hauglustaine, L. W. Horowitz, I. S. A. Isaksen, M. C. Krol, J.-F. Lamarque, M. G. Lawrence, V. Montanaro, J.-F. Mller, G. Pitari, M. J. Prather, J. A. Pyle, S. Rast, J. M. Rodriguez, M. G. Sanderson, N. H. Savage, D. T. Shindell, S. E. Strahan, K. Sudo, and S. Szopa, 2006: Multimodel ensemble simulations of present-day and near-future tropospheric ozone. *Journal of Geophysical Research*, **111**, D08301.

Stocks, B., 1993: Global warming and forest fires in Canada. *The Forestry Chronicle*, **69**, 290–293.

Stocks, B., M. A. Fosberg, T. Lynham, L. Mearns, B. Wotton, Q. Yang, J.-Z. Jin, K. Lawrence, G. Hartley, J. A. Mason, and D. W. McKenny, 1998: Climate change and forest fire potential in Russian and Canadian boreal forests. *Climatic Change*, **38**, 1–13.

Stockwell, D. and M. Chipperfield, 1999: A tropospheric chemical-transport model: Development and validation of the model transport schemes. *Quarterly Journal of the Royal Meteorological Society*, **125**, 1747–1783.

Stockwell, D., C. Giannakopoulos, P. Plantevin, G. Carver, M. Chipperfield, K. Law, J. Pyle, D. Shallcross, and K. Wang, 1999: Modelling NO_x from lightning and its impact on global chemical fields. *Atmospheric Environment*, **33**, 4477–4493.

Stohl, A., 2001: A 1–year Lagrangian climatology of airstreams in the Northern Hemisphere troposphere and lowermost stratosphere. *Journal of Geophysical Research*, **106**, 7263–7279.

Stohl, A., 2006: Characteristics of atmospheric transport into the Arctic troposphere. *Journal of Geophysical Research*, **111**, D11306.

Stohl, A., T. Berg, J. F. Burkhart, A. M. Fjraa, C. Forster, A. Herber, Ø. Hov, C. Lunder, W. W. McMillan, S. Oltmans, M. Shiobara, D. Simpson, S. Solberg, K. Stebel, J. Ström, K. Tørseth, R. Treffeisen, K. Virkkunen, and K. E. Yttri, 2007: Arctic smoke; record high air pollution levels in the European Arctic due to agricultural fires in Eastern Europe in spring 2006. *Atmospheric Chemistry and Physics*, **7**, 511–534.

Stohl, A. and S. Eckhardt, 2004: *Intercontinental Transport of Air Pollution: An Introduction in Intercontinental Transport of Air Pollution*, Springer-Verlag Berlin Heidelberg New York, volume 4 of *The Handbook of Environmental Chemistry*, chapter 1. 1–11.

Stohl, A., S. Eckhardt, C. Forster, P. James, and N. Spichtinger, 2002: On the pathways and timescales of intercontinental air pollution transport. *Journal of Geophysical Research*, **107**, doi:10.1029/2001JD001396.

Stohl, A. and T. Trickl, 1999: A textbook example of long-range transport: Simultaneous observation of ozone maxima of stratospheric and North American origin in the free troposphere over Europe. *Journal of Geophysical Research*, **104**, 30445–30462.

Straus, D. M. and J. Shukla, 2002: Does ENSO Force the PNA? *Journal of Climate*, **15**, 2340–2358.

Stroud, C., S. Madronich, E. Atlas, C. Cantrell, A. Fried, B. Wert, B. Ridley, F. Eisele, L. Mauldin, R. Shetter, B. Lefer, F. Flocke, A. Weinheimer, M. Coffey, B. Heikes, R. Talbot, and D. Blake, 2004: Photochemistry in the Arctic Free Troposphere: Ozone Budget and Its Dependence on Nitrogen Oxides and the Production Rate of Free Radicals. *Journal of Atmospheric Chemistry*, **47**, 107–138.

Stroud, C., S. Madronich, E. Atlas, B. Ridley, F. Flocke, A. Weinheimer, B. Talbot, A. Fried, B. Wert, R. Shetter, B. Lefer, M. Coffey, B. Heikes, and D. Blake, 2003: Photochemistry in the arctic free troposphere: NO_x budget and the role of odd nitrogen reservoir recycling. *Atmospheric Environment*, **37**, 3351 – 3364.

Sturges, W., R. Schnell, S. Landsberger, S. Oltmans, J. Harris, and S.-M. Li, 1993: Chemical and meteorological influences on surface ozone destruction at barrow, alaska, during spring 1989. *Atmospheric Environment. Part A. General Topics*, **27**, 2851–2863.

Szopa, S., D. A. Hauglustaine, and P. Ciais, 2007: Relative contributions of biomass burning emissions and atmospheric transport to carbon monoxide interannual variability. *Geophys. Res. Let.*, **34**, L18810.

Thompson, A. M., K. E. Pickering, R. R. Dickerson, W. G. Ellis, D. J. Jacob, J. R. Scala, W.-K. Tao, D. P. McNamara, and J. Simpson, 1994: Convective transport over the central United States and its role in regional CO and ozone budgets. *Journal of Geophysical Research*, **99**, 18,703–18,711.

Tie, X., G. Brasseur, L. Emmons, L. Horowitz, and D. Kinnison, 2001: Effects of aerosols on tropospheric oxidants: A global model study. *Journal of Geophysical Research*, **106**, 22931–22964.

Tie, X., L. Emmons, L. Horowitz, G. Brasseur, B. Ridley, E. Atlas, C. Stround, P. Hess, A. Klonecki, S. Madronich, R. Talbot, and J. Dibb, 2003: Effect of sulfate aerosol on tropospheric NO_x and ozone budgets: Model simulations and TOPSE evidence. *Journal of Geophysical Research*, **108**, doi:10.1029/2001JD001508.

Tie, X., R. Zhang, G. Brasseur, and W. Lei, 2002: Global NO_x Production by Lightning. *Journal of Atmospheric Chemistry*, **43**, 61–74.

Tiedtke, M., 1989: A comprehensive mass flux scheme for cumulus parameterization in large–scale models. *Monthly Weather Review*, **117**, 1779–1800.

Trenberth, K., 1997: The definition of El Niño. *Bulletin of the American Meteorological Society*, **78**, 2771–2777.

Turquety, S., J. Logan, D. J. Jacob, R. C. Hudman, F. Y. Leung, C. L. Heald, R. M. Yantosca, S. Wu, L. K. Emmons, D. P. Edwards, and G. W. Sachse, 2007: Inventory of boreal fire emissions for North America in 2004: Importance of peat burning and pyroconvective injection. *Journal of Geophysical Research*, **112**, doi:10.1029/2006JD007281.

Tyrlis, E. and B. J. Hoskins, 2008: Aspects of a Northern Hemisphere Atmospheric Blocking Climatology. *Journal of Atmospheric Science*, **65**, 1638–1652.

van de Werf, G., J. Randerson, G. Collatz, and L. Giglio, 2003: Carbon emissions from fires in tropical and subtropical ecosystems. *Global Change Biology*, **9**, 547–562.

van de Werf, G., J. Randerson, G. Collatz, L. Giglio, P. Kasibhatla, A. Arellano, S. Olsen, and E. Kasischke, 2004: Continental-scale partitioning of fire emissions during the 1997 to 2001 El Niño/La Niña period. *Science*, **303**, 73–76.

van de Werf, G., J. Randerson, L. Giglio, G. Collatz, P. Kasibhatla, and A. Arellano, 2006: Interannual variability in global biomass burning emissions from 1997 to 2004. *Atmospheric Chemistry and Physics*, **6**, 3423–3441.

van de Werf, G., J. Randerson, L. Giglio, G. Collatz, M. Mu, P. Kasibhatla, D. Morton, R. DeFries, Y. Jin, and T. van Leeuwen, 2010: Global fire emissions and the contribution of deforestation, savanna, forest, agricultural, and peat fires (19972009). *Atmospheric Chemistry and Physics*, **10**, 11707–11735.

van der Werf, G. R., J. T. Randerson, L. Giglio, N. Gobron, and A. J. Dolman, 2008: Climate controls on the variability of fires in the tropics and subtropics. *Global Biogeochemical Cycles*, **22**, GB3028.

Van Loon, H. and J. Rogers, 1978: Seesaw in winter temperatures between Greenland and northern Europe .1. general description. *Monthly Weather Review*, **106**, 296–310.

Vingarzan, R., 2004: A review of surface ozone background levels and trends. *Atmospheric Environment*, **38**, 3431 – 3442, doi:10.1016/j.atmosenv.2004.03.030.

von Glasow, R., 2008: Atmospheric chemistry: Sun, sea and ozone destruction. *Nature*, **453**, 1195–1196.

Voulgarakis, A., P. Hadjinicolaou, and J. A. Pyle, 2011: Increases in global tropospheric ozone following an el niño event: examining stratospheric ozone variability as a potential driver. *Atmospheric Science Letters*, **12**, 228–232.

Wallace, J. and D. Gutzler, 1981: Teleconnections in the geopotential height field during the Northern Hemisphere winter. *Monthly Weather Review*, **109**, 784–812.

Wang, K., J. Pyle, M. Sanderson, and C. Bridgeman, 1999: Implementation of a convective atmospheric boundary layer scheme in a tropospheric chemistry transport model. *Journal of Geophysical Research*, **104**.

Wang, Y. and D. J. Jacob, 1998: Anthropogenic forcing on tropospheric ozone and OH since preindustrial times. *Journal of Geophysical Research*, **103**, 31123–31135.

Wang, Y., B. Ridley, A. Fried, C. Cantrell, D. Davis, G. Chen, J. Snow, B. Heikes, R. Talbot, J. Dibb, F. Flocke, A. Weinheimer, N. Blake, D. Blake, R. Shetter, B. Lefer, E. Atlas, M. Coffey, J. Walega, and B. Wert, 2003: Springtime photochemistry at northern mid and high latitudes. *Journal of Geophysical Research*, **108**, doi:10.1029/2003JD003592.

Warneke, C., K. D. Froyd, J. Brioude, R. Bahreini, C. A. Brock, J. Cozic, J. A. de Gouw, D. W. Fahey, R. Ferrare, J. S. Holloway, A. M. Middlebrook, L. Miller, S. Montzka, J. P. Schwarz, H. Sodemann, J. R. Spackman, and A. Stohl, 2010: An important contribution to springtime Arctic aerosol from biomass burning in Russia. *Geophys. Res. Lett.*, **37**, L01801.

Webster, P. J. and S. Yang, 1992: Monsoon and ENSO: Selectively Interactive Systems. *Quarterly Journal of the Royal Meteorological Society*, **118**, 877–926.

Wespes, C., L. Emmons, D. P. Edwards, J. Hannigan, D. Hurtmans, M. Saunois, P.-F. Coheur, C. Clerbaux, M. T. Coffey, R. Batchelor, R. Lindenmaier, K. Strong, A. J. Weinheimer, J. B. Nowak, T. B. Ryerson, J. D. Crounse, and P. O. Wennberg, 2011: Analysis of ozone and nitric acid in spring and summer Arctic pollution using aircraft, ground–based, satellite observations and MOZART–4 model: source attribution and partitioning. *Atmospheric Chemistry and Physics Discussions*, **11**, 23707–23760.

Westerling, A. L., H. G. Hidalgo, D. R. Cayan, and T. W. Swetnam, 2006: Warming and Earlier Spring Increase Western U.S. Forest Wildfire Activity. *Science*, **313**, 940–943.

White, W., J. Anderson, D. Blumenthal, R. Husar, N. Gillani, J. Husar, and W. Wilson, 1976: Formation and transport of secondary air pollutants: ozone and aerosols in the St. Louis urban plume. *Science*, **194**, 187–189.

Whitlow, S., P. Mayewski, J. Dibb, G. Holdsworth, and M. Twickler, 1994: An ice-core-based record of biomass burning in the Arctic and Subarctic, 17501980. *Tellus B*, **46**, 234–242.

Wiedinmyer, C., S. K. Akagi, R. J. Yokelson, L. K. Emmons, J. A. Al-Saadi, J. J. Orlando, and A. J. Soja, 2011: The Fire INventory from NCAR (FINN): a high resolution global model to estimate the emissions from open burning. *Geoscientific Model Development*, **4**, 625–641.

Wiedinmyer, C., B. Quayle, C. Geron, A. Belote, D. McKenzie, X. Zhang, S. O'Neill, and K. Wynne, 2006: Estimating emissions from fires in North America for Air Quality Modeling. *Atmospheric Environment*, **40**, 3419–3432.

Wild, O., 2007: Modelling the global tropospheric ozone budget: exploring the variability in current models. *Atmospheric Chemistry and Physics*, **7**, 2643–2660.

Wild, O. and H. Akimoto, 2001: Intercontinental transport of ozone and its precursors in a three–dimensional global CTM. *Journal of Geophysical Research*, **106**, 27,729–27,744.

Williams, A. and D. Karoly, 1999: Extreme fire weather in Australia and the impact of the El Niño–Southern Oscillation. *Australian Meteorological Magazine*, **48**, 15–22.

Wofsy, S. C., G. W. Sachse, G. L. Gregory, D. R. Blake, J. D. Bradshaw, S. T. Sandholm, H. B. Singh, J. A. Barrick, R. C. Harriss, R. W. Talbot, M. A. Shipham, E. V. Browell, D. J. Jacob, and J. A. Logan, 1992: Atmospheric Chemistry in the Arctic and Subarctic: Influence of Natural Fires, Industrial Emissions, and Stratospheric Inputs. *Journal of Geophysical Research*, **97**, 16731–16746.

Wolter, K. and M. S. Timlin, 1998: Measuring the strength of ENSO events: How does 1997/98 rank? *Weather*, **53**, 315–324.

Wotawa, G., P. Novelli, M. Trainer, and C. Granier, 2001: Inter-annual variability of summertime CO concentrations in the Northern Hemisphere explained by boreal forest fires in North America and Russia. *Geophys. Res. Let.*, **28**, 4575–4578.

Xiao, Y., J. A. Logan, D. J. Jacob, R. C. Hudman, R. Yantosca, and D. R. Blake, 2008: Global budget of ethane and regional constraints on U.S. sources. *Journal of Geophysical Research*, **113**, D21306.

Young, P., 2007: *The influence of biogenic isoprene emissions on atmospheric chemistry: A model study for present and future atmospheres*. Ph.D. thesis, University of Cambridge.

Yurganov, L., W. McMillan, E. Grechko, and A. Dzhola, 2010: Analysis of global and regional CO burdens measured from space between 2000 and 2009 and validated by ground-based solar tracking spectrometers. *Atmospheric Chemistry and Physics*, **10**, 3479–3494.

Zeng, G. and J. Pyle, 2005: Influence of El Niño Southern Oscillation on stratosphere/troposphere exchange and the global tropospheric ozone budget. *Geophys. Res. Let.*, **32**, doi:10.1029/2004GL021353.

Zhang, Q., D. Streets, G. Carmichae, K. He, H.Huo, A. Kannari, Z. Klimont, I. Park, S. Reddy, J. Fu, D. Chen, L. Duan, Y. Lei, L. Wang, and Z. Yao, 2009: Asian emissions in 2006 for the NASA INTEX-B mission. *Atmospheric Chemistry and Physics*, **9**, 5131–5153.

Ziereis, H., H. Schlager, P. Schulte, P. F. J. van Velthoven, and F. Slemr, 2000: Distributions of NO, NO_x , and NO_y in the upper troposphere and lower stratosphere between 28°and 61°N during POLINAT 2. *Journal of Geophysical Research*, **105**, 3653–3664.

Zumbrunnen, T., H. Bugmann, M. Conedera, and M. Brgi, 2009: Linking Forest Fire Regimes and ClimateA Historical Analysis in a Dry Inner Alpine Valley. *Ecosystems*, **12**, 73–86.

Zveryaev, I. I. and R. P. Allan, 2010: Summertime precipitation variability over Europe and its links to atmospheric dynamics and evaporation. *Journal of Geophysical Research*, **115**, D12102.